Hoch- und zeitaufgelöste optische Methoden zur spektralen Analyse von individuellen Cyanobakterien und sphäroiden Zellverbänden

Dissertation

der Mathematisch-Naturwissenschaftlichen Fakultät

der Eberhard Karls Universität Tübingen

zur Erlangung des Grades eines

Doktors der Naturwissenschaften

(Dr. rer. nat.)

vorgelegt von

Tim David Rammler

aus Stuttgart

Tübingen

2022

Gedruckt mit Genehmigung der Mathematisch-Naturwissenschaftlichen Fakultät der Eberhard Karls Universität Tübingen.

Tag der mündlichen Qualifikation:	16.03.2023
Dekan:	Prof. Dr. Thilo Stehle
1. Berichterstatter:	Prof. Dr. Alfred J. Meixner
2. Berichterstatter:	Prof. Dr. Klaus Harter
3. Berichterstatterin:	PD Dr. Dai Zhang
4. Berichterstatterin:	Prof. Dr. Monika Fleischer

Copyright

Diese Dissertation wurde in der Gruppe von Prof. Dr. Alfred J. Meixner am Institut für Physikalische und Theoretische Chemie der Eberhard Karls Universität Tübingen zwischen Februar 2018 und Januar 2022 angefertigt.

Danksagung

Besonderer Dank gebührt Professor Dr. Alfred J. Meixner für die stetige Unterstützung, die wertvollen Anregungen und das mir entgegengebrachte Vertrauen in das Gelingen dieses interdisziplinären Projekts.

Des Weiteren danke ich PD Dr. Dai Zhang, die sich freundlicherweise bereit erklärt hat, als Gutachterin für diese Arbeit zu fungieren.

Professor Dr. Klaus Harter danke ich für sein Vertrauen bei diesem umfassenden Projekt, seine inspirierende Begeisterung und seine umfassende Unterstützung.

Weiterhin danke ich Professor Dr. Karl Forchhammer für die konstruktiven Gespräche sowie die interdisziplinäre Hilfestellung.

Dieses Projekt zeigt, wie fruchtbar die Zusammenarbeit zwischen IPTC, ZMBP und IMIT sein kann.

Mein Dank gilt auch Dr. Sven zur Oven-Krockhaus, der meine Forschung seit meiner Bachelorarbeit engagiert begleitet hat.

Dr. Frank Wackenhut danke ich für die vielen Paper-Korrekturen, MATLAB-Skripte und Mikroresonator-Hilfestellungen.

Dr. Johanna Rapp danke ich für den biologischen Input und die kontinuierliche Versorgung mit Cyanobakterien.

Dr. Caprice Doerbeck, die mich in meiner Forschung stets bestärkt hat, danke ich für ihre Unterstützung.

Mein ganz besonderer Dank gilt schließlich meinen Eltern, die mich nicht nur während meiner Promotion in jeder erdenklichen Weise unterstützt haben. Ihnen ist diese Arbeit gewidmet.

Zusammenfassung

Diese Arbeit behandelt einen Teilaspekt der Photosynthese. Sie liefert einen Erklärungsansatz dafür, dass photosynthetische Organismen nicht nur die newtonsche Mechanik und Thermodynamik, sondern auch nicht-triviale Quanteneffekte nutzen und davon profitieren. Ein neuartiger quantenoptischen Ansatz soll dies ermöglichen. In einem eigens für diese Arbeit optimierten Fabry-Pérot-ähnlichen Mikroresonator und einem dafür gebauten zeitaufgelösten konfokalen Mikroskop werden lebende Cyanobakterien der Art *Synechococcus elongatus* unter physiologischen Bedingungen untersucht. Parameter wie die Fluoreszenzlebensdauer des Photosystems, die quantenoptische Kopplung von individuellen Cyanobakterien mit einem Mikroresonator und die optisch ausgelesene photosynthetische Aktivität liefern starke Hinweise auf die Existenz nicht-trivialer Quanteneffekte im Photosystem. Ein zweiter Schwerpunkt dieser Arbeit ist die Aufnahme und Analyse von Fluoreszenzlebensdauern von Farbstoffen in Tumorsphäroiden sowie von Quanten Dots in einer speziellen chemischen Umgebung.

Abstract (in english)

This work addresses one aspect of photosynthesis. It provides an explanation that photosynthetic organisms use and benefit from not only Newtonian mechanics and thermodynamics, but also from non-trivial quantum effects. A novel quantum optical approach is expected to make this possible. In a purpose-optimized Fabry-Pérot-like microcavity and a time-resolved confocal microscope built for this work, living cyanobacteria of the species *Synechococcus elongatus* are studied under physiological conditions. Parameters such as the fluorescence lifetime of the photosystem, the quantum optical coupling of individual cyanobacteria with a microcavity, and the optically read-out photosynthetic activity provide strong evidence for the existence of non-trivial quantum effects in the photosystem. A second focus of this work is the acquisition and analysis of fluorescence lifetimes of dyes in tumor spheroids and of quantum dots in a special chemical environment.

Inhaltsverzeichnis

1. Einleitung und Motivation

Die Photosynthese ist einer der fundamentalsten biologischen Prozesse der Welt und der einzige, welcher Sonnenenergie in chemische Energie umwandelt. Für chemotrophe Organismen, zu denen alle Tiere sowie der Mensch gehören, ist die Photosynthese nicht nur Grundlage der Nahrungsaufnahme, sondern auch essenziell für die Fixierung von atmosphärischem CO_2 und die Synthese von Sauerstoff aus Wasser.[1] Durch die evolutionäre Optimierung der Photosynthese über 3,5 Ga (Milliarden Jahre) existiert bis heute kein effizienterer synthetischer Lichtsammelprozess.[1] Zum Vergleich: Moderne Solarzellen erreichen unter optimalen Laborbedingungen eine Effizienz von ca. 47 % (Galliumarsenid-Zellen)[2].[3] Neben der immensen wissenschaftlichen Bedeutung besteht auch ein großes industrielles Interesse daran, den photosynthetischen Prozess in Gänze zu verstehen, um ihn beeinflussen und nachbilden zu können. Vor dem Hintergrund der globalen Energie- und Klimakrise ist es zudem aus ökologischer Sicht notwendig, die Forschung auf diesem Gebiet auszubauen (Nutzung des Sonnenlichtes und Fixierung des Treibhausgases CO_2).[4] Zwar ist der grundlegende Ablauf der Photosynthese bereits gut erforscht, es fehlt jedoch an detaillierten Untersuchungen bestimmter Teilaspekte. Insbesondere der Energietransfermechanismus, welcher die fast schon extreme Effizienz des Prozesses verursacht, ist für die wissenschaftliche Gemeinde noch ein Rätsel. Diverse Forschungsgruppen vermuten hier den Einfluss von Quanteneffekten, welche von der Evolution bevorzugt und selektiert wurden.[5] Leider flachte der anfängliche Hype um die quantenbiologische Beschreibung der Photosynthese einige Jahre nach ihrem dritten Aufschwung im Jahre 2007[6] wieder ab, da bis heute eindeutige und biologisch relevante Beweise fehlen. Um die wissenschaftlichen Bemühungen erneut anzukurbeln, wird mit dieser Arbeit eine neue Analysenmethode vorgestellt, welche Quanteneffekte im Photosystem *in vivo*, unter physiologischen Bedingungen und unter sonnenähnlichen (d.h. unter polychromatischen und inkohärenten) Lichtbedingungen nachweisen und deren biologische Relevanz zeigen soll. Hierzu werden photoautotrophe Cyanobakterien in einen optischen Mikroresonator, bestehend aus zwei nah beieinanderstehenden halbdurchlässigen Spiegeln eingebettet und unter den dort herrschenden „quantenoptischen“ Bedingungen untersucht. Mit einem eigens dafür gebauten konfokalen Mikroskop (auch für Durchlicht geeignet) sollen durch eine Einzelzell-Analyse unter Zuhilfenahme des Kautsky-Effekts[7] zur Quantifizierung photosynthetischer Parameter die letzten Mysterien der Funktionswiese des Photosystems aufgeklärt werden.

Die Mikroresonator-Technologie bietet über die Analyse der Photosysteme hinaus auch großes Potential in anderen Gebieten. Schon heute kommt sie als optischer Filter[8] bzw. Reflexionsschutz[9], in Interferenzspiegeln (z.B. wichtig in der EUV-Lithografie[10]) oder als Laserresonator[11] zum Einsatz. Sie ist darüber hinaus auch in der chemischen Synthese äußerst vielversprechend. Durch die Beeinflussung der Absorption und Emission von Molekülen im Resonator ist eine effizientere lichtgetriebene chemische Reaktion denkbar[12,13,14]. Die Resonatoren könnten die Aktivierungsenergie von Reaktionen herabsetzen (Funktion als optische Katalysatoren) und sogar das Reaktionsgleichgewicht verändern, wozu herkömmliche Katalysatoren nicht in der Lage sind.[15,16] Auch im Hinblick auf die für die wissenschaftliche Industrie bedeutsamer werdenden Quantencomputer sind optische Mikroresonatoren von Interesse.[17] Da in einem Mikroresonator die Zustandsdichte bei Raumtemperatur verringert werden kann, könnten zukünftige Quantencomputer vielleicht sogar auf eine Betriebstemperatur nahe dem absoluten Nullpunkt verzichten.[18]

Der zweite wichtige Teil dieser Arbeit ist die mikroskopische Untersuchung von multizellulären Tumorsphäroiden, die mit Hypericin eingefärbt wurden. Krebserkrankungen waren laut statistischem Bundesamt 2019 für ein Viertel aller Todesfälle in Deutschland verantwortlich (ca. 231 000 Menschen).[19] Oft ist bei einer Krebsdiagnose nur eine operative Entfernung des Karzinoms möglich. Eine der Schwierigkeiten bei der Entfernung von Tumoren ist jedoch die Unterscheidung von erkranktem zu gesundem Gewebe. Es hat sich gezeigt, dass Hypericin die Eigenschaft besitzt, sich in Tumoren zu akkumulieren und somit als Marker für erkranktes Gewebe eingesetzt werden kann.[20,21] Die Forschung am Hypericin-Molekül und sein Einsatz in der Medizin steht noch ganz am Anfang. Diese Arbeit dient daher auch zur besseren Charakterisierung des Moleküls in Tumoren. Bildgebende Verfahren wie die Fluoreszenzlebensdaueranalyse gekoppelt mit konfokaler Mikroskopie sollen Aufschluss über die Eindringtiefe und Verteilung des Moleküls im Tumor liefern.

Um eine interdisziplinäre Grundlage auf dem Gebiet der Photosynthese-Forschung zu schaffen und damit für Chemiker, Biologen und Physiker gleichermaßen nützlich zu sein, wurde bewusst auf quantenmechanische Beschreibungen in der Bra-Ket-Notation (Dirac Schreibweise) verzichtet.

Stellvertretend für sämtliche photoautotrophen Organismen wird in dieser Arbeit zumeist das Cyanobakterium *Synechococcus Elongatus* als Modelorganismus herangezogen. Die meisten Experimente im photosynthetischen Bereich sind jedoch auch auf andere photoautotrophe Organismen anwendbar.

2. Grundlagen Interferometrie und Licht-Materie-Wechselwirkung

Das applikative Herzstück dieser Arbeit ist, neben dem verwendeten konfokalen Mikroskop ein durchstimmbares Fabry-Pérot-Interferometer. Ein Interferometer nutzt die Fähigkeit zur Überlagerung bzw. Interferenz von elektromagnetischen Wellen aus.[22] Ursächlich für die Interferenz sind Gangunterschiede der einzelnen elektromagnetischen Wellen, welche zu Phasenverschiebungen der einzelnen Teilwellen führen. Im Gegensatz zu den klassischen Interferometern (z.B. das Michelson Interferometer) wird beim Fabry-Pérot-Interferometer der Primärstrahl nicht durch einen Strahlteiler in zwei kohärente Sekundärstrahlen aufgeteilt, die durch unterschiedliche Wegstrecken anschließend konstruktiv oder destruktiv überlagert werden können.[23] Ein Fabry-Pérot-Interferometer besteht nur aus zwei parallel angeordneten, halbdurchlässigen Silberspiegeln, deren Abstand präzise mittels eines Piezo-Aktuators eingestellt werden kann.[22] Durch Reflexion an den nach innen gerichteten Spiegeloberflächen können aufgrund von konstruktiver und destruktiver Interferenz nur elektromagnetische Wellen existieren, die die Resonanzbedingung der Kavität erfüllen.[23] Die wellenlängenselektierenden Eigenschaften kommen u.a. in optischen Filtern zum Einsatz.[9] Der Effekt wird zudem in Anti-Reflex-Beschichtungen von Brillen eingesetzt.[9]

2.1 Interferenz

Das Phänomen der Interferenz ist hauptsächlich dafür verantwortlich, dass sich in Interferometern die Amplituden zweier kohärenter Teilstrahlen bei einer Überlagerung ändern können. Voraussetzung für eine zeitlich stabile Interferenz ist, dass beide Teilstrahlen eine zeitlich feste Phasenbeziehung zueinander haben.[9] Sie müssen also kohärent zueinander sein. Die Amplitude der Teilstrahlen muss dabei nicht identisch sein. Im Falle der Inkohärenz addieren sich bei Überlagerung nicht die Amplituden, sondern nur die Intensitäten (das Quadrat der Amplitude) der beiden Teilstrahlen.[9] Welche Art der Interferenz (konstruktive oder destruktive) entsteht, ist abhängig von der Phasenverschiebung der beiden Teilstrahlen. Von konstruktiver Interferenz spricht man, wenn die Phasenverschiebung 0 oder $n \cdot \lambda/2$ ($n \in \mathbb{N}$) ist.[9]

Im Folgenden werden beispielhaft die Interferenzeffekte an zwei planparallelen teildurchlässigen Spiegeln, welche mit monochromatisch (Wellenlänge λ) divergentem Licht bestrahlt werden, erläutert. Die spiegelnden Flächen sind dabei nach innen gerichtet. Das Medium zwischen den Spiegelflächen hat einen Brechungsindex n. Der Träger der Spiegelschicht besitzt denselben Brechungsindex n_1 wie das Medium, welches das Interferometer umgibt. Es wird zuerst das reflektierte Zweistrahl-Interferenzmuster beschrieben

(Abbildung 2-1A). Hierzu wird der Gangunterschied Δs von zwei Teilstrahlen bestimmt. Δs ist abhängig vom Einfallswinkel α der eintreffenden Wellen, dem Abstand d und dem Brechungsindex n zwischen den beiden reflektierenden Schichten:[9]

$$\Delta s = 2d\sqrt{n^2 - \sin^2(\alpha)} \tag{2-1}$$

Die Phasendifferenz Δφ der reflektierten Teilstrahlen wird wie folgt unter Berücksichtigung des Phasensprungs um π an der Spiegeloberfläche beschrieben:[9]

$$\Delta\varphi = \frac{2\pi}{\lambda}\Delta s - \pi \tag{2-2}$$

Da es auch höhere Interferenzordnungen m gibt, gilt für konstruktive Interferenz $\Delta\varphi = m \cdot 2\pi$ und für destruktive Interferenz $\Delta\varphi = (2m+1)\pi$. Das Interferenzmuster des reflektierten Lichts bildet um die Einfallsnormale ein Muster aus abwechselnd hellen und dunklen konzentrischen Ringen (Abbildung 2-1B). Für alle Einfallswinkel α, welche folgende Gleichung erfüllen:[9]

$$2d\sqrt{n^2 - \sin^2(\alpha)} = (m + 1/2)\lambda \tag{2-3}$$

entsteht ein Intensitätsmaxium in Form eines hellen Ringes. Das transmittierte Zweistrahl-Interferenzmuster ähnelt dem des reflektierten stark. Da jedoch kein Phasensprung an der Spiegelfläche auftritt, wird die Phasendifferenz Δφ nicht um -π korrigiert. Dies hat zur Folge, dass ein Transmissionsmaximum immer auf ein Reflexionsminimum fällt.[23]

Das in dieser Arbeit verwendete Fabry-Pérot-Interferometer besitzt jedoch stärker reflektierende Spiegelschichten. Das bedeutet, ein einfallender Lichtstrahl kann nicht sofort wieder aus dem Interferometer austreten, sondern wird mehrfach reflektiert, bis er schließlich transmittiert wird.

2.2 Vielstrahlinterferenz

Zunächst wird der Gerad der Reflexion und Transmission eines teildurchlässigen Spiegels definiert. Der Reflexionsgrad R ergibt sich aus dem Verhältnis zwischen reflektierter Leistung P_r und eingestrahlter Leistung P_e in Bezug auf dessen Intensität. Reflexionsfaktor r

hingegen bezieht sich auf die Amplitude der Strahlen und ist somit als Quadrat des Reflexionsgrades definiert:

$$R = \frac{P_r}{P_e} = r^2 \tag{2-4}$$

Wird nun die Reflektivität der Spiegel aus dem vorherigen Kapitel stark erhöht, können die einzelnen Teilstrahlen das System erst nach mehrmaliger Reflexion verlassen. Das Zweistrahl-Experiment muss also um die Überlagerung vieler Teilstrahlen erweitert werden, die bei Transmission miteinander interferieren können. Die Herleitung der quantitativen Interferenz erfolgt analog zur Herleitung der Zweistrahl-Interferenz und wird hier nicht näher erläutert. Die Herleitung führt zu den sogenannten Airy-Formeln, welche die reflektierte und transmittierte Intensität des Interferometers bestimmen:

Reflektierte Intensität:[23]

$$I_R = I_0 \cdot \frac{f \cdot \sin^2\left(\frac{\Delta\varphi}{2}\right)}{1 + f \cdot \sin^2\left(\frac{\Delta\varphi}{2}\right)} \tag{2-5}$$

Transmittierte Intensität:[23]

$$I_T = I_0 \cdot \frac{1}{1 + f \cdot \sin^2\left(\frac{\Delta\varphi}{2}\right)} \tag{2-6}$$

Beschreibung des Finesse-Koeffizienten:[23]

$$f = \frac{4\mathrm{R}}{(1 - \mathrm{R})^2} \tag{2-7}$$

Der Finesse-Koeffizient ist ausschließlich von der Reflektivität der Spiegel abhängig und beschreibt den Kontrast des entstehenden Ringmusters.[23] Die Phasendifferenz $\Delta\varphi$ ist dabei sowohl abhängig vom Einfallswinkel α und der Wellenlänge λ (oder dem Wellenlängenbereich) des einfallenden Lichtes als auch vom Spiegelabstand d. Abbildung 2-1C zeigt die Transmission des Systems in Abhängigkeit der Phasendifferenz für verschieden

große R. Da es in der Praxis oft einfacher ist, die Halbwertsbreite ε einer Transmissionskurve statt der Reflektivität der Spiegel zu messen, wird ε zur Charakterisierung herangezogen. Der Zusammenhang lässt sich wie folgt darstellen:[9]

$$\varepsilon = \frac{4}{\sqrt{f}} = \frac{2(1-R)}{\sqrt{R}} \tag{2-8}$$

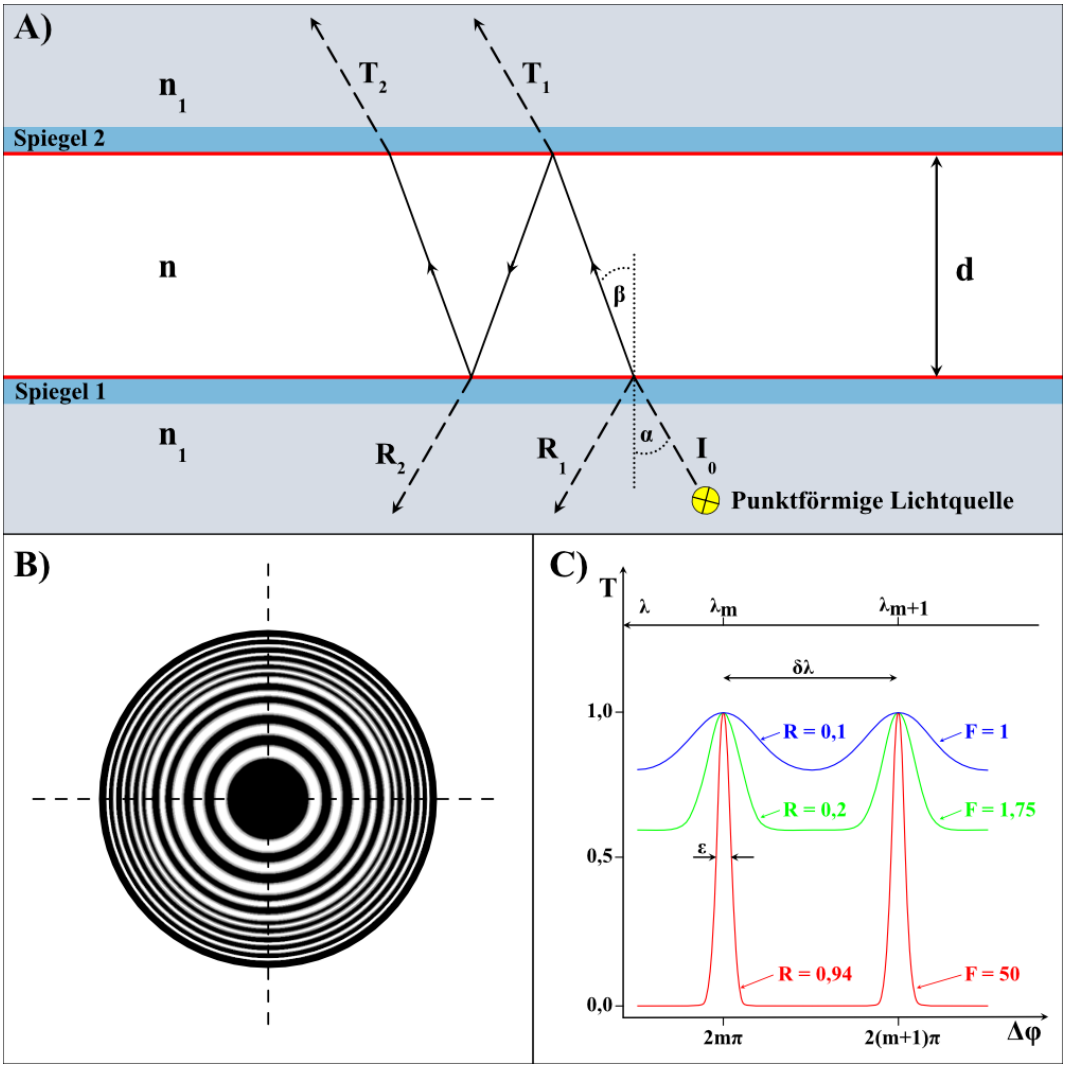

Abbildung 2-1: **(A)** Strahlengang in einem aus zwei planaren halbdurchlässigen Spiegeln bestehenden Interferometer am Beispiel der Zweistrahl-Interferenz. **(B)** Transmittiertes Zweistrahl-Interferenzmuster des reflektierten monochromatischen Lichts an einem aus zwei planaren halbdurchlässigen Spiegeln bestehenden Interferometer. **(C)** Transmissionsmuster als Funktion der Phasendifferenz am Beispiel von drei Interferometern mit verschiedenen Reflektivitäten der Spiegel (ähnlich [23]).

Das Fabry-Pérot-Interferometer lässt sich mittels Vielstrahlinterferenzanalyse sehr gut beschreiben. Da ein Fabry-Pérot-Interferometer aber durch eine Linse kollimiertes Licht

verwendet, fallen alle Teilstrahlen genau senkrecht auf die Spiegel. Durch diese Vereinfachung kann die Filtereigenschaft eines Fabry-Pérot-Interferometers ganz einfach durch folgende Abhängigkeit beschreiben werden:[9]

$$\lambda_{transmittiert,m} = \frac{2nd}{m} \tag{2-9}$$

Wird ein Weißlichttransmissionsspektrum eines Fabry-Pérot-Interferometers aufgenommen, so ist die Anzahl der Transmissionsmaxima abhängig vom Spiegelabstand. Der Abstand dieser Maxima wird freier Spektralbereich genannt:[9]

$$\delta\lambda = \frac{\lambda_m}{m+1} \tag{2-10}$$

Fabry-Pérot-Interferometer (mit planaren Spiegeln) werden durch die Finesse F (nicht zu verwechseln mit dem Finesse Koeffizient f) charakterisiert, die das Verhältnis zwischen freiem Spektralbereich δλ und Halbwertsbreite ε der Transmissionsmaxima beschreibt und als Maß für die Anzahl der interferierenden Teilstrahlen angesehen werden kann:[9]

$$F = \frac{\delta\lambda}{\varepsilon} = \frac{\pi\sqrt{R}}{1-R} \tag{2-11}$$

2.3 Aufbau und Herstellung des verwendeten Resonators

Der für diese Arbeit verwendete Mikroresonator ähnelt dem oben beschriebenen Fabry-Pérot-Interferometer und wurde in der Arbeitsgruppe Meixner der Universität Tübingen entwickelt.[24] Der Unterschied zum klassischen Fabry-Pérot-Interferometer besteht darin, dass im verwendeten Mikroresonator nicht zwei Planspiegel verwendet wurden, sondern ein verspiegeltes Deckglas (Dicke ca. 170 µm) und eine verspiegelte konvexe Linse (Brennweite 150 mm). Die zwei Spiegel können parallel angenähert und anschließend in einem Stangensystem fixiert werden. Die verspiegelte Linse kann durch einen Piezo-Aktuator dem verspiegelten Deckglas sehr präzise angenähert werden, eine Metallfeder fixiert die Linse in die entgegengesetzte Richtung. Im Zentrum der Linse ist der Abstand zum Deckglas am geringsten. Der Abstand zwischen den Spiegeln steigt zum Rand der Linse. Gemäß der in Kapitel 2.2 beschriebenen Vielstrahlinterferenz werden also im verwendeten Resonator beim

Durchleuchten mit Weißlicht ortsabhängig verschiedene Wellenlängen transmittiert. Das so transmittierte Muster aus konzentrisch angeordneten farbigen Ringen wird Newton-Ringe genannt. Abbildung 2-2A zeigt die Auswirkungen eines Resonators aus planaren Spiegeln mit zwei verschiedenen Abständen auf das Transmissionsmuster bzw. die transmittierten Farben im Vergleich zum Transmissionsmuster eines plankonvexen Resonators. Vom Zentrum der Linse aus zeigen die Newton-Ringe einen Farbverlauf vom blauen bis zum roten Farbspektrum. Mit zunehmender Annäherung an den Rand der Linse ist eine häufigere Wiederhohlung des Farbverlaufs von blau nach rot wahrnehmbar. Die Farbdurchlaufswiederholungen werden als Ordnung bezeichnet und entsprechen im Wesentlichen den Interferenzordnungen (siehe Abbildung 2-2B/C).[9] Beträgt der Abstand der beiden Spiegel weniger als die halbe Wellenlänge von gerade noch erkennbarem Licht (ca. 400 nm), was meist im Linsenzentrum der Fall ist, wird kein Licht mehr vom Resonator transmittiert. Deshalb ist das Zentrum der Newton-Ringe schwarz.

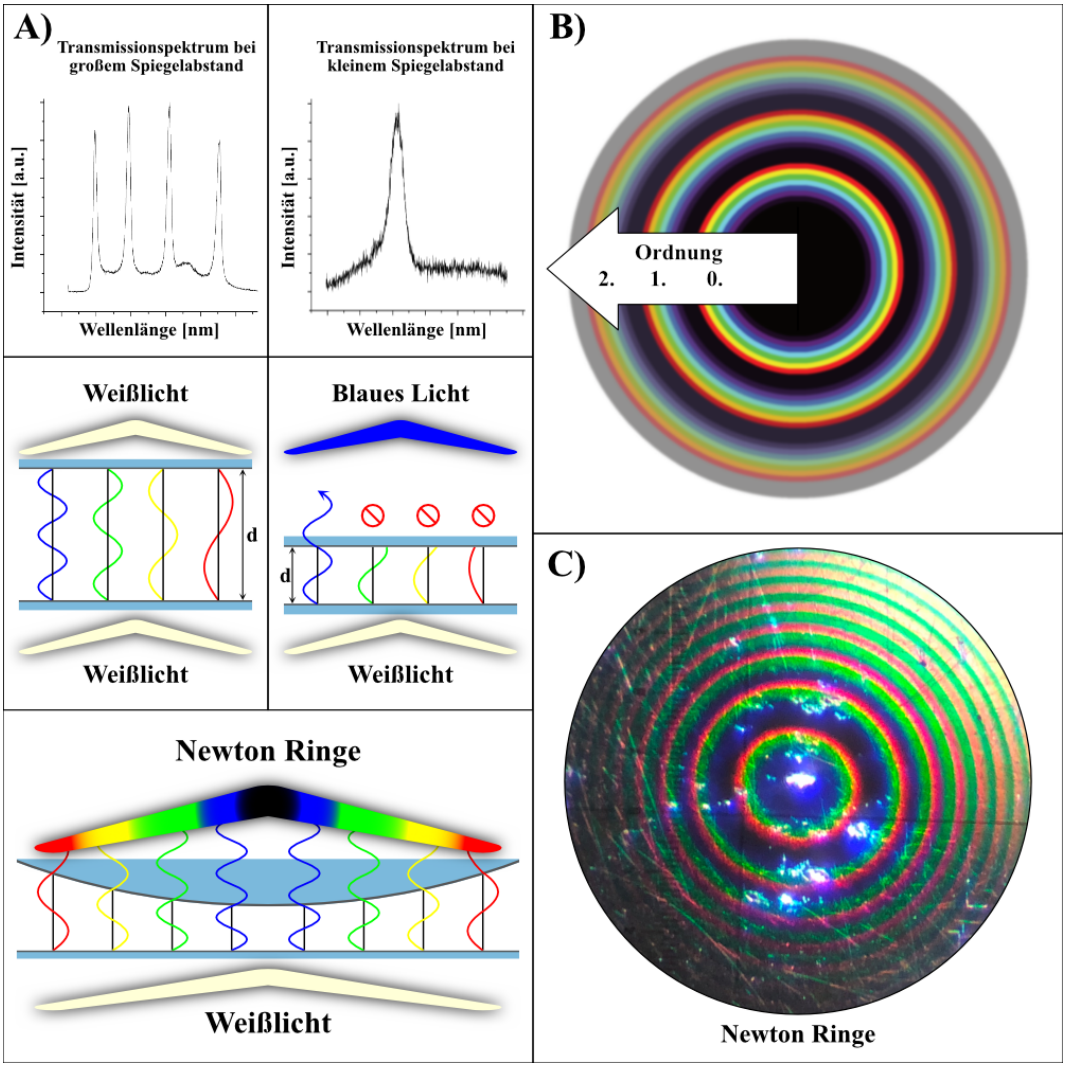

Abbildung 2-2: **(A)** Interferenzeffekte am Beispiel für einen großen (Mitte links) und einen kleinen (Mitte rechts) Spiegelabstand d und die daraus resultierenden Transmissionsspektren bei Durchleuchtung mit Weißlicht (oben). Unten: Ursache des Interferenzmusters aus B/C aufgrund der verspiegelten Linse im Mikroresonator. **(B)** Schematische Darstellung von Newton-Ringen in Transmission beim Durchleuchten eines Mikroresonators mit Weißlicht. **(C)** Experimentell erstelltes Newton-Ring-Muster des in dieser Arbeit verwendeten Mikroresonators.

Die Herstellung der Spiegel erfolgte durch Elektronenstrahl-Verdampfung von Metallen und deren Abscheidung an der Glasoberfläche von Deckgläsern und Linsen. Die Schichtdickenbestimmung ermöglicht ein oszillierender Quarzkristall, dessen Schwingfrequenz sich ändert, wenn er durch die aufgedampften Schichten schwerer wird. Zur Vorbereitung der Glasoberfläche wurden die Glasträger für mindestens 24 h in ein Chrom-Schwefelsäure-Bad (H_2SO_4+CrO_3) eingelegt. Das Säurebad reinigt und aktiviert dabei die Glasoberfläche. Zunächst wird eine ca. 3 nm dicke Chromschicht aufgedampft. Das Chrom dient als Haftvermittlung für die folgende Silberschicht, welche die eigentlichen reflektiven Eigenschaften besitzt.[24] Die Silberschichtdicke auf dem Deckglas beträgt ca. 30 nm und auf der

Linse ca. 60 nm. Da Silber jedoch bakterizid[25] und anfällig für mechanische Schäden ist, wurde anschließend eine 5 nm dicke Goldschicht und zusätzlich eine 20 nm dicke Siliziumdioxid-Schicht aufgedampft. Aufgrund der Linse handelt es sich um einen instabilen Resonator. Die Strahlen können seitlich aus dem Resonator herauslaufen. Daher wird zur Charakterisierung nicht die Finesse, welche nur für planare Resonatoren verwendet wird, sondern der Güte- bzw. Q-Faktor angegeben.[17] Q beschreibt die mittlere Verweildauer der Photonen im Mikroresonator und berechnet sich aus dem Verhältnis der Resonanzwellenlänge zur Halbwertsbreite der Hohlraumresonanz. Die Schichtdicken des verwendeten Resonators ergeben einen Qualitätsfaktor von Q=98. Der Resonatoraufbau wurde so entworfen, dass er genau auf das verwendete konfokale Mikroskop passt und Emissions- sowie (Weißlicht-) Transmissionsspektren von derselben Stelle aufgenommen werden können.

2.4 Molekül-Resonator-Kopplung

Das spezielle optische Feld in einem Mikroresonator kann genutzt werden, um eine Fluorophor-Resonator-Wechselwirkung hervorzurufen. Ein Molekül erfährt hierbei nicht mehr die konstante und unendlich große Modendichte des Vakuums, an welche ein emittiertes Photon immer koppeln kann, sondern die eingeschränkte Modendichte eines optischen Resonators. Es wird die Annahme zugrunde gelegt, dass ein Farbstoff, der in den Resonator gebracht wird, die dort wiederholt reflektierten Photonen sowohl absorbieren als auch emittieren kann. Normalerweise ist dies bei klassischen organischen Farbstoffen aufgrund des Stokes-Shifts nicht der Fall. Emittierte Photonen haben aufgrund der thermischen Äquilibrierung eine geringere Energie als die absorbierten. Eine Ausnahme stellt das Chlorophyll-Molekül im Photosystem von Pflanzen und Cyanobakterien dar. Wird der Spiegelabstand so eingestellt, dass die Resonatormode resonant zur Fluoreszenz bzw. Absorption des Farbstoffes ist, kann eine Wechselwirkung stattfinden. In diesem Fall wechseln die Photonen zwischen Resonatormode und Molekül hin und her. Die Stärke der Wechselwirkung ist dabei von drei Parametern abhängig: Der Photonenzerfallsrate κ, der nichtresonanten Zerfallsrate γ und dem Resonator-Molekül-Kopplungssparameter g_0.[17] γ beschreibt die Rate, mit der Photonen aus dem Resonator ohne erneute Reflexion austreten, da sie z.B. senkrecht zur Spiegelanordnung (bzw. zur Hohlraummode) emittiert werden oder das Molekül nichtradiativ in den Grundzustand übergeht. κ hingegen beschreibt die Photonen, welche ohne Reflexion von einem der Spiegel transmittiert werden und ist somit hauptsächlich von der Güte des Resonators abhängig. Die beiden irreversiblen Zerfallsraten stehen dem Kopplungsparameter g_0 gegenüber: Wird κ und/oder γ größer, sinkt g_0. Der Kopplungsparameter g_0 ist hauptsächlich

abhängig vom Dipolmoment des Moleküls μ_{12}, dem Modenvolumen V und der Frequenz des Resonators ω.[17]

Im Allgemeinen kann die Wechselwirkung eines Quantensystems mit dem optischen Feld in einem Mikroresonator in zwei Regime unterteilt werden: In das starke ($g_{0>>}\kappa,\gamma$) und das schwache Kopplungsregime ($g_{0<<}\kappa,\gamma$).[17]

Im schwachen Kopplungsregime beeinflusst der Resonator die irreversible spontane Emissionsrate bzw. Übergangswahrscheinlichkeiten von elektronischen Übergängen aufgrund der geänderten Photonenzustandsdichte im Hohlraum des Resonators.[26] Dieser Effekt wird Purcell-Effekt (benannt nach Edward Mills Purcell) genannt. Die spontane Emissionsrate wird dabei um den Purcell-Faktor F_P erhöht:[27]

$$F_P = \frac{3Q}{4\pi^2 V}\left(\frac{\lambda_{em}}{n}\right)^3 \tag{2-12}$$

Der Purcell-Faktor ist also abhängig von der Wellenlänge der emittierten Strahlung λ_{em}, dem Modenvolumen V, der Güte des Resonators Q und dem Brechungsindex in dem Resonator n.[28] Ist der Purcell-Faktor größer eins, steigt die spontane Emissionsrate, ist er kleiner eins, sinkt die Rate. Ist der Resonator jedoch nicht resonant zur Molekülemission, wird die Emission unterdrückt, da keine Resonatormoden vorhanden sind, an die das Emissionsphoton koppeln kann. Die Auswirkungen des Purcell-Effektes werden in Kapitel 7.1 näher beleuchtet.

Im starken Kopplungsregime ist die Molekül-Resonator-Wechselwirkung viel schneller als der irreversible Verlust von Photonen aus dem Resonator.[17] Das Molekül kann also emittierte Photonen reabsorbieren, was zu einem kohärenten Energieaustausch zwischen Resonator und Molekül führt. Dieser Energieaustausch kann als kohärente Überlagerung bzw. Superposition der Resonatormode mit dem elektronischen Zustand des Moleküls betrachtet werden und hat eine Hybridmode, auch Polariton genannt, zur Folge (siehe Abbildung 2-3A, Polariton in blau).[29] Polaritonen treten immer paarweise auf. Es entstehen also bei einer Kopplung zwei neue Energiezustände. Die quantenelektrodynamische Beschreibung dieser Wechselwirkung wird durch das Jaynes-Cummings-Modell beschrieben (benannt nach Edwin Thompson Jaynes und Fred Cummings).[17] Das Modell beschreibt die Wechselwirkung vollquantisiert, wohingegen das Rabi-Modell einen halbklassischen Ansatz beschreibt, bei dem das elektromagnetische Feld klassisch betrachtet wird.[30]

Bei einer Wechselwirkung eines Resonators mit einem einzigen Molekül wird die Aufspaltung (auch vacuum Rabi splitting ΔE^{vac} genannt) wie folgt berechnet:[17]

$$\Delta E^{vac} = 2\hbar g_0 = 2\hbar \left(\frac{\mu_{12}^2 \omega}{2\varepsilon_0 \hbar V} \right)^{1/2} \tag{2-13}$$

Die Berechnung des Vakuum Rabi splittings gilt für eine Anregung mit einer großen Anzahl an Photonen (n). Wird im Spektrum Rabi splitting observiert, ist dies eine starkes und fast immer zutreffendes Indiz für starke Kopplung.[18] Die tatsächliche Aufspaltung ist jedoch abhängig von der Anzahl N der an der Kopplung teilnehmenden kohärenten Molekülen. Im Jaynes-Cummings-Modell wird daher die Aufspaltungsenergie ΔE_N^{vac} allgemein für Experimente mit mehreren Molekülen (z.B. mit einem biologischen Photosystem) um einen Faktor der Molekülanzahl angepasst:[17,18]

$$\Delta E_N^{vac} = \sqrt{N} 2\hbar g_0 \tag{2-14}$$

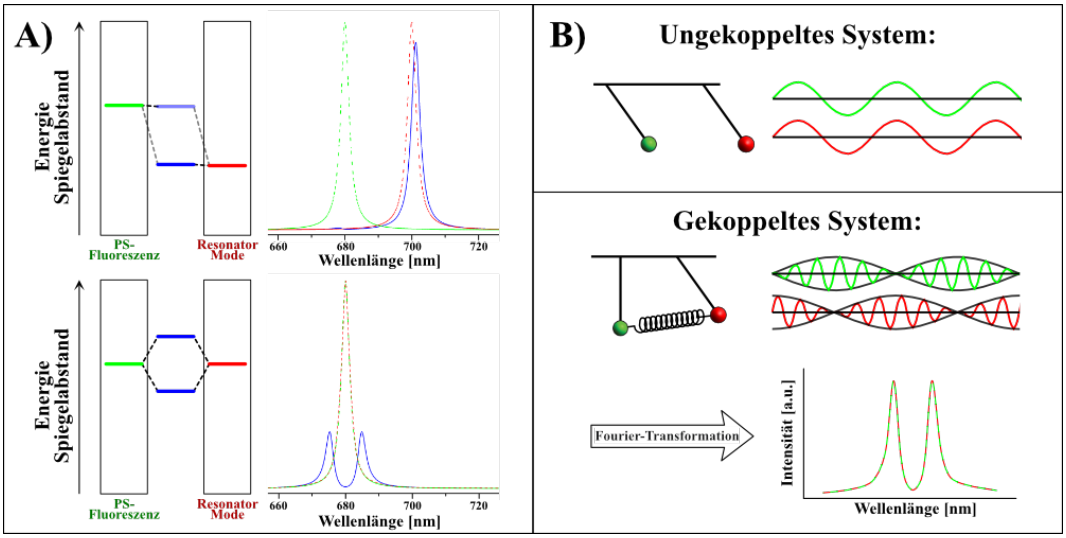

Abbildung 2-3: **(A)** Energieniveauschema einer Kopplung zwischen einem Mikroresonator und dem Photosystem von *S. Elongatus* und das daraus resultierende Spektrum (blau). Zur Veranschaulichung sind die beiden ungekoppelten Spektren (Resonator und Photosystem) als grün bzw. rot gestrichelte Linien dargestellt. Oben: Nicht resonanter Fall. Es herrscht eine nur sehr geringe Kopplung. Die Aufspaltung ist nur sehr schwer zu erkennen. Unten: Resonanter Fall. Hier ist die Kopplung maximal ausgeprägt. **(B)** Oben: Ungekoppelte Federpendel und deren zeitliche Bewegungsverläufe. Unten: Klassische Beschreibung einer starken Kopplung am Beispiel eines gekoppelten harmonischen und gedämpften Federpendels im Schwebungsfall. Durch Fourier-Transformation wird die Bewegung der Pendel aus der Zeitdomäne in die Frequenzdomäne (also in ein Spektrum) überführt.[31]

Um eine starke Kopplung zu simulieren, ist es jedoch effizienter, das Modell komplett klassisch zu beschreiben. Eine klassische Beschreibung durch ein gekoppeltes harmonisches und gedämpftes Federpendel im Schwebungsfall liefert dieselben Ergebnisse wie eine quantisierte Beschreibung des Systems (siehe Abbildung 2-3B).[17] Die Ursache kann jedoch nur durch eine quantisierte Beschreibung des Vakuum-Feldes im Resonator erklärt werden. Die Bewegungsgleichungen[31] der Pendel x_1 und x_2 erhält man durch das Einsetzen der Dämpfungskonstanten κ und γ, der Resonanzfrequenz der Pendel bzw. des Resonators und des Moleküls ω_1 und ω_2 sowie des Kopplungsparameters g:

$$\ddot{x_1}(t) + \gamma_1 \dot{x_1}(t) + \omega_1^2 x_1(t) + g x_2(t) = 0 \qquad (2\text{-}15)$$

$$\ddot{x_2}(t) + \gamma_2 \dot{x_2}(t) + \omega_2^2 x_2(t) + g x_1(t) = 0 \qquad (2\text{-}16)$$

Die Simulation einer starken Kopplung am Beispiel des Photosystems von *S. Elongatus* in einem Mikroresonator wird in Kapitel 7.1 genauer beschrieben.

3. Biologische Grundlagen

Dieses Kapitel beleuchtet kurz die beiden in dieser Arbeit verwendeten biologischen Proben. *Synechococcus Elongatus* PCC 7942 wurde als Modellorganismus stellvertretend für photoautotrophe einzellige Organismen ausgewählt, um die ablaufenden Mechanismen der Photosynthese genauer zu erforschen.[32] Des Weiteren wurden multizelluläre Tumorsphäroide eingesetzt, um *in vitro* Studien zum Verhalten des Fluoreszenzfarbstoffes Hypericin in biologischem Gewebe durchzuführen. Das Augenmerk dieser Arbeit lag jedoch auf der Analyse des photosynthetischen Apparats.

3.1 Cyanobakterium *S. Elongatus* PCC 7942

Der Modellorganismus *S. Elongatus* (Pasteur Culture collection of Cyanobacteria, PCC 7942) ist ein stäbchenförmiges, einzelliges Cyanobakterium, das im Schnitt ca. 1-2 µm entlang der großen Achse misst (siehe Abbildung 4-1B, alle länglichen Zellen sind zum Zeitpunkt der Aufnahme im Begriff sich zu teilen, vgl. Cytokinese).[33] *S. Elongatus* wurde für diese Arbeit ausgewählt, da es bereits sehr gut erforscht wurde und aufgrund seiner Robustheit den extremen Bedingungen in einem Mikroresonator standhält. Außerdem ermöglicht seine schnelle Wachstumsrate[33] eine effiziente Durchführung der Experimente. Eine genetische Veränderung des Bakteriums ist ebenfalls möglich, welche in Zukunft tiefergehende Forschung an der Einzelzell-Analyse in Mikroresonatoren ermöglicht. Die einzelnen Photosysteme von *S. Elongatus* sind in der Thylakoidmembran lokalisiert, welche sich in 2-3 Lagen unter der Zellmembran befindet.[33] Aufgrund der Größe der Zellen und der pflanzenähnlichen Photosynthese (siehe Kapitel 3.3.1, Endosymbiontentheorie[34]) eignet sich *S. Elongatus* hervorragend für Untersuchungen in einem Mikroresonator. Die Kultivierungsbedingungen sind in Kapitel 7.1 und 7.2 beschrieben.

3.2 Multizelluläre Tumorsphäroide inkubiert mit Hypericin

Das zweite in dieser Arbeit behandelte biologische Gewebe sind multizelluläre Tumorsphäroide. Tumorsphäroide sind kugelartige Zellgebilde, bestehend aus einer Vielzahl von Tumorzellen.[35] In der Zellbiologie werden solche Aggregate zur *in vitro* Untersuchung von Krebserkrankungen eingesetzt.[35] In Kapitel 7.4 wird beschrieben, wie die Tumorsphäroide mit dem Fluoreszenzfarbstoff Hypericin inkubiert werden, da er die Eigenschaft besitzt, in Tumoren zu akkumulieren[20]. Hier wurden Querschnitte der Sphäroide auf ein Deckglas aufgezogen und in einem Einbettmedium fixiert. Eine bildgebende Analyse der Fluoreszenzlebensdauer (Fluorescence liftime imaging, FLIM, siehe Kapitel 4.3 für die Theorie

und Kapitel 7.4 für die praktische Anwendung) soll Aufschluss über die Verteilung von Hypericin und den Einfluss des umgebenden Gewebes im Sphäroid geben. Das in Kapitel 4.1 erläuterte konfokale Mikroskop wurde für diese Analyse verwendet.

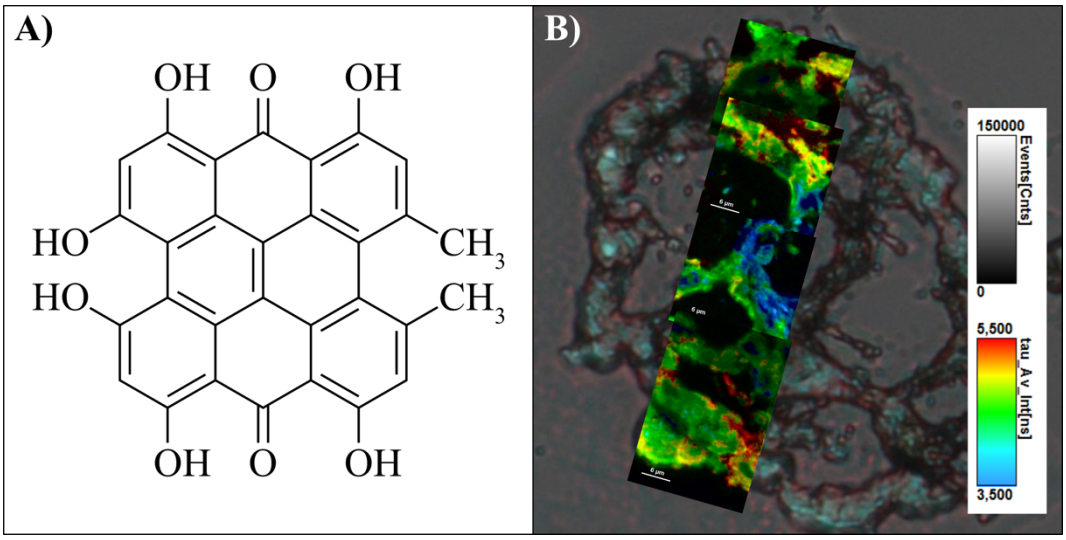

Abbildung 3-1: **(A)** Molekülstruktur von Hypericin.[20] **(B)** Hellfeldaufnahme eines multizellulären Tumorsphäroids inkubiert mit Hypericin (Hintergrund). Im Vordergrund: konfokale Fluoreszenzlebensdauer-Aufnahmen einzelner Bildausschnitte. Farblich gekennzeichnet sind die intensitätsgewichteten durchschnittlichen Fluoreszenzlebensdauern FLT (vgl. Kapitel 4.3). Blau kennzeichnet eine kurze und rot eine längere FLT.

3.3 Oxygene Photosynthese

3.3.1 Der photosynthetische Prozess

Photoautotrophe Organismen, wie Pflanzen, Algen oder Cyanobakterien, nutzen Licht (z.B. von der Sonne), um komplexe organische Moleküle, hauptsächlich Kohlenhydrate und andere energiespeichernde Substanzen, aus Kohlenstoffdioxid (CO_2) und Wasser (H_2O) physiologisch zu synthetisieren.[36] Dieser Vorgang wird Photosynthese genannt und ist nicht nur für photoautotrophe Organismen, sondern auch für chemotrophe Lebewesen, welche auf die photosynthetisch hergestellten organischen Nährstoffe angewiesen sind, die Grundlage des Lebens.[37] Überdies erzeugt die oxygene Photosynthese Sauerstoff (O_2), welcher über die Atmosphäre von chemotrophen Organismen zur oxidativen Phosphorylierung aufgenommen wird.[38]

Der Sauerstoff wird dabei nicht aus CO_2, sondern aus H_2O gewonnen, welches unter Abgabe von Elektronen (e^-) und Aufbau eines Protonengradienten über die Thylakoidmembran durch die absorbierte Strahlungsenergie gespalten wird.[39] Dieser Prozess und die anschließende

Synthese von Nicotinsäureamid-Adenin-Dinukleotid-Phosphat (reduzierte Form: NADPH, Reduktion von $NADP^+$ durch die Elektronen) und Adenosintriphosphat (ATP, chemiosmotische und enzymkatalysierte Hydrolyse von Adenosindiphosphat ADP) wird Lichtreaktion genannt.[40] Die anschließende CO_2-Assimilation, welche durch Reoxidation von NADPH zu $NADP^+$ und Abspaltung eines Phosphatrests (P_i) von ATP im Calvin-Zyklus angetrieben wird, wird als Dunkelreaktion bezeichnet, da sie nur indirekt von Strahlungsenergie abhängig ist.[41] Dem Calvin-Zyklus wird kontinuierlich Glycerinaldehyd-3-phosphat (GAP) entzogen, welches schlussendlich in vielen weiteren Schritten zu den lebensnotwendigen Zuckermolekülen umgewandelt wird.[41]

Teilreaktionsgleichung der Lichtreaktion:

$$2H_2O + 2NADP^+ + 3ADP + 3P_i \xrightarrow{Lichtreaktion} O_2 + 2\,NADPH/H^+ + 3ATP + 2H_2O$$

Teilreaktionsgleichung der Dunkelreaktion:

$$3CO_2 + 6\,NADPH/H^+ + 6H^+ + 9ATP + 5H_2O \rightarrow GAP + 6NADP^+ + 9ADP + 8P_i$$

In eukaryotischen Zellen (z.B. in Pflanzen) läuft die Lichtreaktion in der Thylakoidmembran in abgetrennten Organellen, den Chloroplasten ab. In prokaryotischen Zellen (z.B. den Cyanobakterien) sitzt die Thylakoidmembran, die nicht durch eine Organelle abgetrennt ist, unter der Zellmembran.[41] Aufgrund der Ähnlichkeit von Chloroplasten zu Cyanobakterien werden diese als evolutionäre Vorgänger der Chloroplasten angesehen (vgl. Endosymbiontentheorie[34]).

3.3.2 Aufbau des Photosystems

Im Folgenden wird der Aufbau und die Anordnung der für die Photosynthese verantwortlichen Superproteinkomplexe erläutert (vgl. dazu Abbildung 3-2A). Trotz langjähriger Forschung ist noch nicht abschließend geklärt, wie genau die räumliche Anordnung und die molekulare Struktur der Photosynthesekomplexe in der Thylakoidmembran aussehen.

Der Photosyntheseapparat der meisten Cyanobakterien besteht aus großen membranständigen Superproteinkomplexen, auf der Membran sitzenden Antennenproteinen und kleineren beweglichen Komplexen für den Elektronentransfer.[42] In Richtung des Elektronenflusses

beginnt die Photosynthese mit dem Photosystem 2 (PS2, Nummerierung aufgrund der zeitlichen Entdeckung). Das PS2 besteht aus 25 Untereinheiten und ist für den nichtzyklischen Elektronentransport von der Wasserspaltung zum Plastochinonpool (PQ) verantwortlich.[43] Die Untereinheiten des PS2 lassen sich in die peripheren und inneren Lichterntekomplexe (LHC2) und den Kernkomplex mit dem wasserspaltenden Mangankomplex einteilen.[43] Im Kernkomplex befinden sich die meisten Farbpigmente und das Reaktionszentrum P680 (Lichtabsorption bis 680 nm möglich), bestehend aus vermutlich zwei parallel angeordneten Chlorophyll a Molekülen, welche von zwei Polypeptiden (D1 und D2) gebunden sind. Oxidiertes Plastochinon (Q_B) kann an die Bindungsstelle im Polypeptid D1 binden und dort durch ein Elektron, welches im Reaktionszentrum (P680) aus Wasser erzeugt wurde, reduziert werden.[39] Dies ist nur möglich, da ein mit Lichtenergie angeregtes Reaktionszentrum ($P680^+$) ein so starkes Oxidationsmittel ist, dass es in der Lage ist, Wasser oxidativ zu spalten. Anschließend kann das reduzierte Plastochinon in den Plastochinonpool zurückdiffundieren und schließlich unter Abgabe eines Elektrons an den Cytochrom-b_6-f-Komplex (Cyt b_6-f) wieder reoxidiert werden.[44] Die Reoxidation ist vermutlich der langsamste Schritt des gesamten Elektronentransportes.[45] Die Redoxreaktion des Plastochinonpools erzeugt dabei einen Protonengradienten über die Thylakoidmembran[46], welcher von der ATP-Synthase zur chemiosmotischen und enzymkatalysierten Hydrolyse von ADP genutzt wird.[47]

Um den Elektronentransport vom PS2 zu Cyt b_6-f zu unterbinden, kann 3-(3,4-Dichlorphenyl)-1,1-dimethylharnstoff (DCMU) eingesetzt werden, welcher die D1 Bindungsstelle blockiert.[48] Die Unterbrechung des Energietransportes im Photosystem kann gezielt eingesetzt werden, um die photochemischen und physikalischen Eigenschaften des Systems zu analysieren (siehe Kapitel 3.3.5 ff.).

Das an den Cyt b_6-f Komplex abgegebene Elektron wird nun zur Reduktion von Plastocyanin (PC) verwendet (Reduktion des Zentralions Cu^{2+} zu Cu^+).[46] Das PC-Protein kann in der Thylakoidmembran diffundieren und transportiert das Elektron vom Cyt b_6-f Komplex zum PS1.[46] Das periphere Protein Ferredoxin (Fd) transferiert das vom PS1 aufgenommene Elektron auf die Ferredoxin-NADP-Oxidoreduktase (FNR), wo es zur Reduktion von $NADP^+$ zu $NADPH/H^+$ eingesetzt wird.[49] Mit der Reduktion von $NADP^+$ endet der lineare Elektronentransport und somit die Lichtreaktion.

Viele Cyanobakterien besitzen zusätzlich zu den Lichtsammelkomplexen der PS1 und 2 große Antennenproteine, welche sich auf der Thylakoidmembran befinden und sich dort eingeschränkt bewegen können (vgl. state transition, wobei sie jedoch hauptsächlich über dem PS2 lokalisiert sind[50,51]). Diese Antennen werden Phycobilisome (PBS) genannt und enthalten Farbpigmente (Phycobiline), welche das Absorptionsspektrum des gesamten Photosystems erweitern sollen (Abdeckung der Grünlücke).[52] Absorbierte Energie wird dabei direkt an das P680 weitergeleitet.

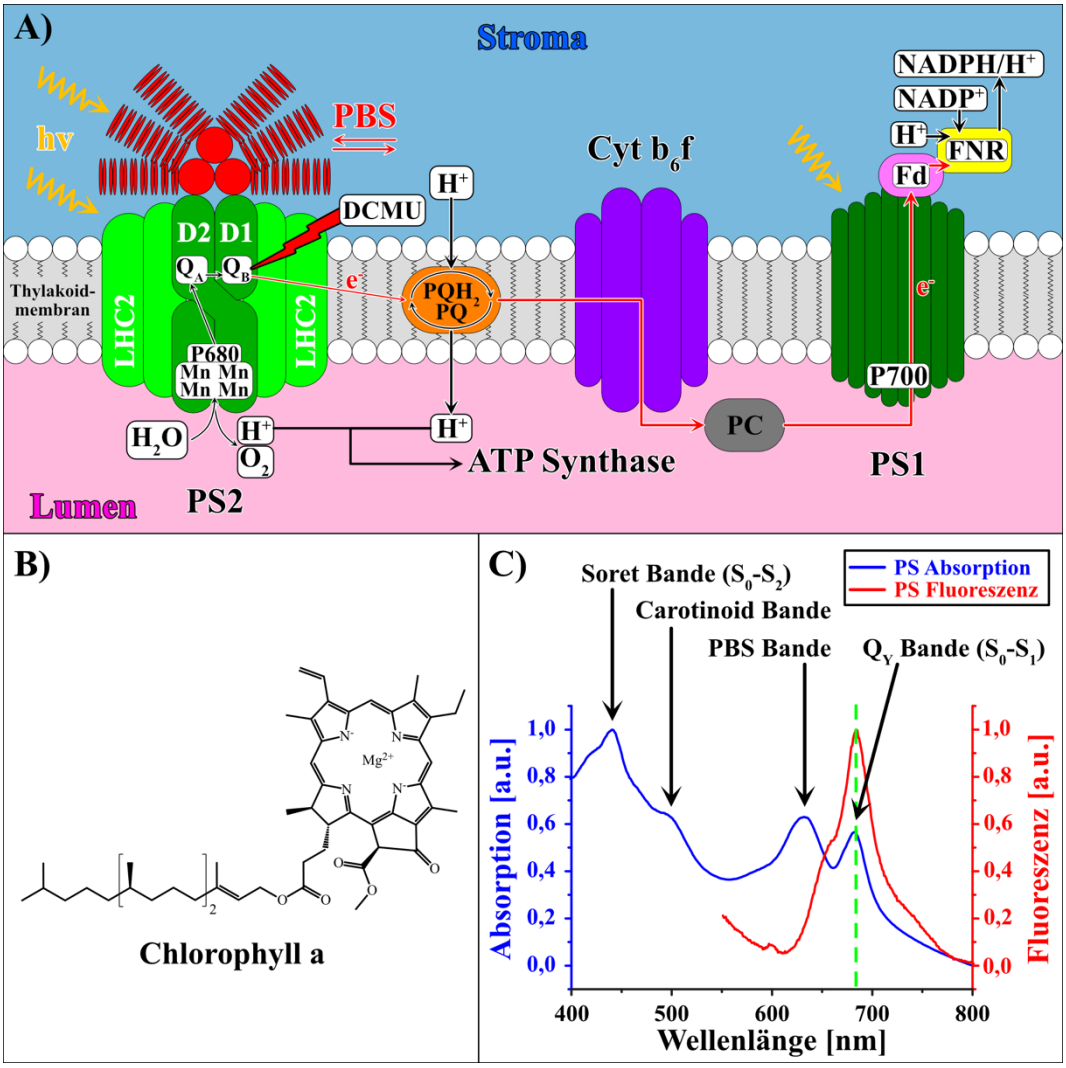

Abbildung 3-2: **(A)** Schematische Darstellung des Photosystems in der Thylakoidmembran (weiß) von Cyanobakterien.[37] Hellblau: Stroma; rosarot: Lumen; gelb: Sonnenlicht; hellgrün: Photosystem 2 (PS2), Lichtsammelkomplex 2 (LHC2), Polypeptidgerüst des PS2 (D1, D2), Reaktionszentrum des PS2 (P680), reduziertes Plastochinon (Q_A), oxidiertes Plastochinon (Q_B) Angriffsstelle für 3-(3,4-Dichlorphenyl)-1,1-dimethylharnstoff (DCMU); rot: Phycobilisome (PBS); orange: Plastochinonpool (reduzierte Form: PQH_2, oxidierte Form: PQ); violett: Cytochrom-b_6-f-Komplex (Cyt b_6-f); grau: Elektronentransferprotein Plastocyanin (PC); dunkelgrün: Photosystem 1 (PS1), Reaktionszentrum des PS1 (P700); pink: Elektronentransferprotein

Ferredoxin (Fd); gelb: Ferredoxin-NADP-Oxidoreduktase (FNR) wandelt Nicotinsäureamid-Adenin-Dinukleotid-Phosphat um (reduzierte Form: NADPH, oxidierte Form: $NADP^+$). **(B)** Molekülstruktur von Chlorophyll a.[53] **(C)** Absorptions- und Fluoreszenzspektrum von *S. Elongatus* in BG11-Medium. Da *S. Elongatus* nur das Chlorophyllderivat a enthält, spiegeln die Spektren, abgesehen von der Carotinoid- und PBS-Bande, sehr gut das Spektrum des Chlorophylls a wider.

Dabei gibt es mehr PS2 als PS1 (PS2-Heterogenität). Diese Heterogenität und die asymmetrische Verteilung der PS über die Thylakoidmembran verhindern einen unkontrollierten Elektronenfluss.[54]

3.3.3 Energietransfer im Photosystem

Gegenstand aktueller Forschung und wissenschaftlichen Diskurses ist der Energietransfer von der Absorption eines Photons im PS2 bis hin zum Reaktionszentrum P680.[55] In diesem Kapitel wird dieser Energietransfer vorerst als klassischer Hüpfprozess beschrieben. Eine quantenmechanische Beschreibung folgt in Kapitel 5 ff. zur Quantenbiologie. Der elektronenvermittelte bzw. chemische Energietransfer nach dem Reaktionszentrum wird ebenfalls klassisch beschrieben.

Der Energietransfer im PS2 erfolgt durch Dipol-Dipol-Wechselwirkung und somit strahlungslos zwischen den Chlorophyll-Molekülen, welche im PS2-Proteingerüst nichtkovalent in einer ganz bestimmten Anordnung zueinander gebunden sind. Die Anregungsenergie wird durch diese evolutionär optimierte Anordnung der Pigmente mit einer Effizienz von fast 100 % übertragen.[56] Dieser Anregungsübertrag, zumeist als klassischer FRET-Transfer (Förster Resonanz Energietransfer) beschrieben, wird bis zum P680 nicht durch einen Elektronentransfer vermittelt. Erst ab dem P680 wird durch eine Kaskade von Redoxreaktionen verschiedener Proteine, Energie in Form von Elektronen transportiert (vgl. Z-Schema der Lichtreaktion, welches in Abhängigkeit des Standardredoxpotentials den Verlauf des chemischen Energietransfers beschreibt[57]). Dabei ist zu berücksichtigen, dass die physikalischen Prozesse Absorption, Fluoreszenz und Energietransfer in Form von Dipol-Dipol-Wechselwirkung sehr viel schneller ablaufen, als ein chemischer Elektronentransport durch Redoxreaktionen und Diffusion.[45] Physikalische Energietransfers laufen im Bereich von Nanosekunden ab. Um einen optimalen Energietransfer zum P680 zu gewährleisten, kommt es auf die Schnelligkeit der Dipol-Dipol-Wechselwirkung an, welche in direkter Konkurrenz zur nicht photosynthesetreibenden Fluoreszenz steht. Elektronentransporte durch Redoxreaktionen

und Diffusionsprozesse laufen viel langsamer (im Mikro- bis Millisekunden-Bereich) ab. Diesen zeitlichen Unterschied kann man sich in der Photosyntheseanalyse zu Nutze machen (siehe Kapitel 3.3.5 ff.).

3.3.4 Spektrale Eigenschaften

Photoautotrophe Organismen verwenden Farbstoffe, um Strahlungsenergie zu absorbieren und zu transportieren. Neben Carotinoiden und den Farbstoffen der peripheren Antennenpigmente in Cyanobakterien (Phycobiline) ist das Chlorophyll der wichtigste Farbstoff in der Photosynthese (Chlorophyll a: Abbildung 3-2B). Die Molekülstruktur des Chlorophylls ähnelt der des Häms, besteht jedoch aus einem derivatisierten Porphyrin-Ring mit einem Mg^{2+} als Zentralion.[53]

Mg^{2+} hat sich vermutlich evolutionär aufgrund der hohen biologischen Verfügbarkeit, seiner passenden Größe für Porphyrin-Ringe (Ionenradius bei einer Koordinationszahl von 7 ist 72 pm) und seiner hohen Präferenz zu regulären Oktaedern (die zwei nicht durch das Porphyrin besetzten, axialen Positionen werden zu einer geordneten und starren 3D-Struktur im Proteingitter des Photosystems besetzt) durchgesetzt.[58] Außerdem neigt Mg^{2+} nicht zu unkontrollierten und unproduktiven Redoxreaktionen bzw. Elektronentransferprozessen und ist ein vergleichsweise leichtes Element, welches durch eine geringe Spin-Bahn-Kopplung weniger dazu neigt, spinverbotene Übergänge (z.B. in den Triplettzustand) einzugehen.[59]

In der Natur gibt es mehrere Chlorophyll-Derivate mit leicht unterschiedlichen optischen Eigenschaften, welche sich in den Resten der Seitenkette des Porphyrins unterscheiden. In anoxygenen phototrophen Organismen (z.B. Purpurbakterien oder grüne Schwefelbakterien), welche keinen Sauerstoff bei der Photosynthese produzieren, werden die Porphyrin Derivate Bakteriochlorophyll genannt.[41]

Im Folgenden wird das Absorptionsspektrum von *S. Elongatus* spektral charakterisiert. Da *S. Elongatus* nur das Derivat Chlorophyll a enthält, ist eine eindeutige Trennung der verschiedenen photosynthetischen Pigmente möglich. Das Absorptionsspektrum weist vier breite Banden auf (siehe: Abbildung 3-2C):

1. Die Soret-Bande von Chlorophyll a im blauen Spektralbereich bei 440 nm:[60] Bei Anregung der Soret-Bande werden die π-Elektronen des Chlorophylls direkt in das

S_2-Niveau angehoben.[41] Nach der thermischen Äquilibrierung in das S_1-Niveau kann die absorbierte Energie weitergeleitet (oder als Konkurrenzprozess radiativ in Form von Fluoreszenz emittiert) und anschließend im Reaktionszentrum in photochemische Arbeit umgesetzt werden.[61] Die Anregung der Soret-Bande bietet die Vorteile, dass sie sehr effizient und spektral weit von der Emission abgetrennt ist (großer Stokes-Shift).

2. Die Carotinoid-Bande bei 500 nm im gelben Spektralbereich:[62] Carotinoide erweitern das Absorptionsspektrum des ganzen Photosystems um den blau-grünen Spektralbereich. Sie schützen außerdem die Chlorophyll-Moleküle vor photooxidativer Zerstörung durch Sauerstoffradikale.[37,63]
3. Die Phycobilisom (PBS) -Bande bei 630 nm im grün-orangenen Spektralbereich:[64] Phycobiline ermöglichen es photoautotrophen Organismen die sogenannte Grünlücke des photosynthetischen Spektrums auszunutzen. Algen und Cyanobakterien sind dadurch in der Lage, tiefer unter der Wasseroberfläche zu existieren.[41]
4. Die Q_y-Bande von Chlorophyll a bei 680 nm:[65] Der Bereich zwischen der Soret- und der Q_y-Bande wird als Grünlücke bezeichnet. Bei einer Anregung der Q_y-Bande werden die π-Elektronen des Chlorophylls in das S_1-Niveau angehoben. Nach der thermischen Äquilibrierung in den vibronischen Grundzustand des S_1-Niveaus (vgl. Kashas Regel) erfolgt kongruent zur Anregung der Soret-Bande der Energietransfer oder die Fluoreszenz.

Die Dissipation der Anregungsenergie kann dabei auf verschiedene, konkurrierende Arten stattfinden. Neben der oben bereits erwähnten Fluoreszenz und eines Transfers der Energie auf ein anderes Chlorophyll-Molekül kann die Anregungsenergie auch durch thermische Äquilibrierung an die Umgebung abgegeben werden (internal conversion). Auch der spinverbotene Übergang vom S_1-Singuletniveau in das T_1-Triplettniveau (intersystem crossing), welcher anschließend radiativ in Form von Phosphoreszenz dissipiert, ist eine, wenn auch sehr unwahrscheinliche, Form der Energieabgabe.[41] Nur der Energietransfer auf ein anderes Chlorophyll-Molekül bzw. am Ende des Transfers auf das Reaktionszentrum ist ein Prozess, der die Photosynthese vorantreibt. Alle anderen Arten der Dissipation verhindern bzw. mindern den Ablauf der Photosynthese.[37] Da die Fluoreszenz, im Vergleich zur Analyse des emittierten Sauerstoffs, am einfachsten zu messen ist und sie abhängig von der Stärke der Konkurrenzprozesse ist (also nicht direkt proportional zu absorbierten Lichtmenge, vgl. Kapitel 3.3.5), wird sie häufig zur Analyse des Photosystems herangezogen. Insbesondere bei der

Analyse einzelner Individuen, welche bei der Sauerstoff-Analyse eine nicht zu messende Menge an Stauersoff emittieren würden.

Bei einer Anregung der Soret-Bande (440 nm) ist das Fluoreszenzspektrum von *S. Elongatus* stark von der Chlorophyll a Emission bei 680 nm dominiert.[37] Chlorophyll b ist nicht vorhanden und andere Pigmente (z.B. Carotinoide und die Phycobiline) werden bei 440 nm nicht angeregt. Die Emission bei 680 nm stammt dabei hauptsächlich vom inneren Antennensystem des PS2.[66] Der Fluoreszenzanteil des PS1 beträgt bei einer Anregung mit 440 nm und der Emission bei 685 nm ca. 2 % und bei 720 nm ca. 5 %.[66] Die Eigenschaft der Cyanobakterien, bei 680 nm sowohl ein Absorptions- als auch ein Emissionsmaximum zu besitzen, ermöglicht es ihnen, ihre selbst emittierten Photonen wieder zu reabsorbieren. Dies hat gleich zwei Vorteile: Energie, welche durch Fluoreszenz nicht für die Photosynthese verwendet wurde, kann durch eine Reabsorption doch noch verwendet werden. Außerdem sind sie durch diese Eigenschaft in der Lage, eine Interaktion bzw. Kopplung mit einem Mikroresonator einzugehen. Wird der Resonator auf das Fluoreszenz- bzw. Absorptionsmaximum eingestellt, können Photonen zwischen der Hohlraummode und den Photosystemen hin und her wandern.[67] Ob dies einen physiologischen Einfluss auf die Cyanobakterien hat, wird in Kapitel 7.1 und 7.2 genauer erörtert.

3.3.5 Kautsky-Effekt

In diesem Kapitel wird der Effekt, der den nichtlinearen zeitlichen Fluoreszenzverlauf nach Dunkeladaption des Photosystems beschreibt, kurz beleuchtet. Dieser sogenannte Kautsky-Effekt (benannt nach Hans Kautsky) wurde bereits 1931 entdeckt[7], fand aber erst Ende der 1990er Jahre Einzug in die kommerzielle Photosynthese-Analyse.

Wird das Blatt einer Landpflanze oder Cyanobakterien für eine gewisse Zeit unter Ausschluss jeglicher optischen Strahlung dunkeladaptiert, tritt nach einer abrupten Beleuchtung mit aktinischem (photosynthesetreibendem) Licht, ein Fluoreszenzeffekt auf, welcher normalerweise bei molekularen Farbstoffen nicht auftritt. Wird ein normaler Farbstoff optisch angeregt, ist seine Fluoreszenzintensität bei gleichbleibender Anregungsenergie konstant. Wird jedoch nach Dunkeladaption ein Photosystem angeregt, steigt bei gleichbleibender Anregungsenergie die Fluoreszenzintensität bis zu einem bestimmten Wert und sinkt anschließend wieder bis zu einem terminalen Intensitätswert (siehe Abbildung 3-3A). Der Kautsky-Effekt erklärt diesen zeitlichen Fluoreszenzverlauf.[7] Im Folgenden wird dieser Verlauf

am Beispiel der cyanobakteriellen Photosynthese kurz beschrieben und einige charakteristische Punkte nach dem Modell von van Kooten und Snel[68] erläutert.

Wird das Photosystem von Cyanobakterien mit aktinischem Licht angeregt, startet die Chlorophyll-Fluoreszenz innerhalb weniger Pikosekunden. Das anfängliche Fluoreszenzniveau wird minimale oder Grundfluoreszenz genannt und mit F_0 abgekürzt. Der Grund für die Existenz des F_0-Niveaus wurde bereits kurz in Kapitel 3.3.3 erwähnt: Physikalische Energietransfers, wie z.B. die Energieweiterleitung des Sonnenlichts zum Reaktionszentrum P680, verlaufen sehr viel schneller als Energietransfers in Form eines Elektronentransports durch eine Reihe von Redoxreaktionen. Ist nun die Anregungsenergie so hoch, dass die Fluoreszenz das F_0-Niveau übersteigt, werden mehr Photonen zum P680 transferiert als Elektronen durch das reduzierte Plastochinon Q_A transferiert werden können. Es entsteht eine Art Elektronenrückstau und die überschüssige, absorbierte Energie wird vorerst in Form von Fluoreszenz abgegeben.[37] F_0 ist also die maximale Fluoreszenz, die ohne Elektronenrückstau emittiert wird. Wird das Photosystem konstant mit einer Intensität angeregt, die keinen Elektronenrückstau zur Folge hat, bleibt F_0 nach dem Einschalten des aktinischen Lichts konstant. Man kann deshalb F_0 als unabhängig von allen (photo-)chemischen Prozessen betrachten.[37] Um das maximale F_0-Niveau genau bestimmen zu können, müssen entweder alle P680 im offenen bzw. im Grundzustand vorliegen (Q_A ist oxidiert) oder es muss mit sehr hoher zeitlicher Auflösung gemessen werden. Da eine hohe zeitliche Auflösung schwer zu realisieren ist, werden alle P680 durch Dunkeladaption in den offenen Zustand überführt, was bedeutet, dass der Protonengradient über die Thylakoidmembran abgebaut wird und der zyklische Elektronentransport zum Erliegen kommt. Da eine zu lange Dunkeladaption F_0 verringern (photoinhibitorische Fluoreszenzlöschung, Erhöhung der thermischen Äquilibrierung) und eine zu kurze Dunkeladaption F_0 erhöhen kann, wurden Studien durchgeführt, die als optimalen Kompromiss 15 Minuten Dunkeladaption bestimmt haben.[37,69,66] Der Fluoreszenzverlauf steigt anschließend, nach dem abrupten Anstieg auf F_0, bis zu einem Maximalwert F_M an. Der Verlauf bis F_M wird variable Fluoreszenz F_V genannt und lässt Rückschlüsse auf den Zustand des Photosystems zu. F_V wird bei der Hälfte kurz von einem intermediären Plateau $F_{I/D}$ unterbrochen, was sich jedoch sehr schlecht zeitlich auflösen lässt und ohnehin keine Relevanz für diese Arbeit hat. F_V steigt zeitlich gesehen nicht so schnell an wie F_0, da nach der Erzeugung von Elektronen (aus der Wasserspaltung) im P680 der chemische Energietransport deutlich langsamer ist als der physikalische Energietransport in den Antennen. Ein weiterer verlangsamender Faktor ist der zeitlich verzögerte Start des Kohlenstoffreduktionszyklusses,

der die Reduktion von $NADPH/H^+$ vorerst verhindert. Da jedoch kontinuierlich Lichtenergie zugeführt wird, kann die überschüssige Energie nur in Form von Fluoreszenz (und zu einem kleinen Teil in Form von Wärme durch die Carotinoide) abgeleitet werden. Während des Anstiegs von F_0 auf F_M befindet sich Q_A also teilweise im reduzierten Zustand, was zur Folge hat, dass die variable Fluoreszenz den Redoxzustand von Q_A indiziert. Die maximale Fluoreszenz F_M wird nur erreicht, wenn die Lichtintensität des aktinischen Lichts alle PS2 vollständig sättigt. Nur dann befinden sich alle P680 im sogenannten geschlossenen Zustand wobei alle Q_A vollständig reduziert sind. Ist die Lichtintensität nicht ausreichend hoch, wird nicht die maximal mögliche Fluoreszenz emittiert, sondern nur ein anregungsintensitätsabhängiges Peak-Maximum F_P. Der wahre F_M-Wert kann außerdem nur dann bestimmt werden, wenn das Fluoreszenzmaximum nach wenigen Millisekunden erreicht wird. Ist die Anregungsintenistät etwas höher als die sättigende Intensität, können schnell Lichtschutzmechanismen in Kraft treten, welche die Intensität des F_M-Wertes verfälschen und das zeitliche Erreichen des F_M-Wertes hinauszögern (vgl. Kapitel 7.2). Je nach Anregung kann ein Fluoreszenzmaximum auch erst nach Sekunden erreicht werden, was dem Bakterium Zeit gibt, mit Schutzmechanismen auf das optische Überladen des Photosystems zu reagieren. Um eine Verzögerung von F_M zu unterbinden, kann das Herbizid 3-(3,4-Dichlorphenyl)-1,1-dimethylharnstoff (DCMU)[70] eingesetzt werden. DCMU blockiert den Elektronentransport zwischen P680 und Q_A, was zur Folge hat, dass das PS1 nicht weiter mit Elektronen versorgt wird.[48] Die absorbierte Energie im PS2 muss also nach dem ersten erzeugten Elektron vollständig (abgesehen von der thermischen Äquilibrierung der Carotinoide) radiativ emittiert werden. Wird DCMU zugegeben, sinkt die variable Fluoreszenz nach Erreichen des F_M-Wertes nicht mehr ab (siehe Abbildung 3-3B). Ohne DCMU jedoch sinkt die Fluoreszenzemission nach F_M wieder, da der Elektronentransport zu PS1 und die anschließende Reduktion zu $NADPH/H^+$ beginnt (siehe Abbildung 3-3A). Die Fluoreszenz sinkt (ebenfalls unterbrochen von einem für diese Arbeit irrelevanten intermediären Plateau F_{inter}) bis zum terminalen Wert F_T ab und bleibt anschließend konstant. Da sich der Anstieg bis F_M im Millisekunden-Bereich abspielt, wird dieser auch die schnelle Fluoreszenzkinetik (SFK, siehe Abbildung 3-3A/B/C, blauer Bereich) genannt und der Abnahme ab F_M wird langsame Fluoreszenzkinetik (LFK, siehe Abbildung 3-3A/B/C, grüner Bereich) genannt, da er einige Sekunden bis Minuten dauert.[71]

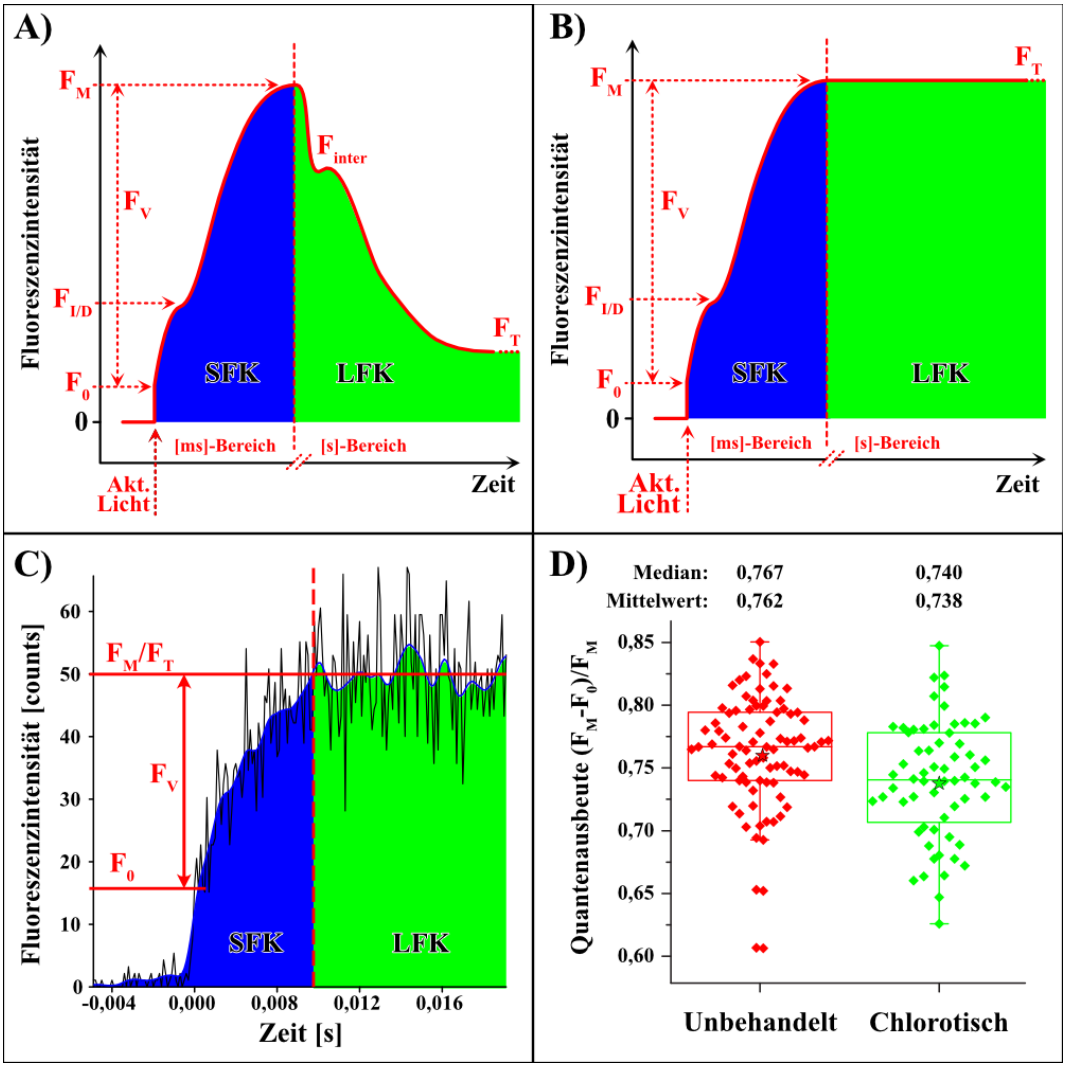

Abbildung 3-3: **(A)** Schematisch dargestellter zeitlicher Verlauf der Fluoreszenzintensität (rote Kurve), angeregt mit sättigender Lichtintensität gemäß dem Kautsky-Effekt.[37] Der blaue Bereich zeigt die schnellen Fluoreszenzkinetik (im Millisekunden-Bereich), der grüne Bereich die langsamen Fluoreszenzkinetik (im Sekunden- bis Minuten-Bereich). **(B)** Schematisch dargestellter zeitlicher Verlauf der Fluoreszenzintensität aus (A) jedoch unter Zugabe von DCMU. **(C)** Experimentell bestimmter zeitlicher Verlauf der Fluoreszenzintensität (Messwerte in schwarz, geglättete Messkurve in blau) von *S. Elongatus* unter Zugabe von DCMU. Farbliche Unterscheidung der Bereiche wie in (A)/(B), entnommen aus Kapitel 7.2. **(D)** Boxplot der Quantenausbeute ($(F_M-F_0)/F_M$) von *S. Elongatus* fixiert in einer Agarose-Matrix. In rot: unbehandelte Zellen, in grün: unter stickstoffarmen Bedingungen gewachsene Zellen, entnommen aus Kapitel 7.2.

3.3.6 Chlorophyllfluoreszenz-Analyse

Die Chlorophyllfluoreszenz-Analyse (CFA) nutzt u.a. den Kautsky-Effekt, um schnell und nichtinvasiv Informationen über das Photosystem *in vivo* zu erhalten.[37] Obwohl nicht mehr als die Fluoreszenzintensität in Abhängigkeit der Zeit aufgenommen wird, können durch die CFA erstaunlich viele und komplexe Informationen über den Zustand des Photosystems von allen photoautorophen Organismen, welche Chlorophyll als Hauptpigment enthalten, gewonnen

werden. Damit bietet die CFA einen tiefen Einblick in die photosynthetische Aktivität von Pflanzen und Cyanobakterien.[37]

In den letzten 40 Jahren wurden verschiedene Techniken entwickelt, um die Chlorophyllfluoreszenz optimal zu analysieren.[37] In dieser Arbeit wird eine der weniger komplexen Methoden verwendet, da die Messung an einzelnen Zellen extrem hohe Anforderungen, im Bezug auf Sensitivität, an den Messaufbau stellt. Es hat sich herausgestellt, dass die Analyse der schnellen Fluoreszenzkinetik durch direkte Anregung des PS2, mit einem fokussierten Laserstrahl der Wellenlänge 440 nm (direkte Anregung des Absorptionsmaximum von Chlorophyll a), die effektivste Methode ist, um Einzelzellanalysen durchzuführen. Da einzelne Zellen nur sehr wenig Fluoreszenz emittieren, ist eine OJIP-Analyse[71] der einzelnen intermediären Plateaus in der SFK nicht möglich, da diese nicht aufgelöst werden können. Die Analyse der langsamen Fluoreszenzkinetik ist ebenfalls ungeeignet, da sie sehr ungenau und anfällig für alle Arten von Messfehlern ist. Die Methode der Puls-Amplituden-Modulation (PAM) bietet zwar den Vorteil, dass Messungen außerhalb des Labors (z.B. im Freiland, vgl. kommerzielle Geräte der Firma Walz in Effeltrich) sehr detailliert und genau durchgeführt werden können, stellt jedoch größere Anforderungen an den apparativen Aufbau, da verschiedene Lichtquellen (teilweise im kHz-Bereich gepulst) eingesetzt werden müssen. Da die in dieser Arbeit verwendeten Cyanobakterien jedoch unter kontrollierten Bedingungen im Labor gezüchtet wurden, besteht keine Notwendigkeit eine PAM einzusetzen. Ebenfalls ungeeignet sind bildgebende CFA Systeme, da die Cyanobakterien nur ca. doppelt so groß wie die Auflösungsgrenze eines konfokalen Mikroskops sind und somit keine zusätzlichen Informationen gewonnen werden können.

3.3.7 Analyse der schnellen Fluoreszenzkinetik

In der Analyse der SFK werden die F_0- und F_M-Werte verwendet, um Rückschlüsse auf den Zustand des Photosystems von Cyanobakterien zu ziehen. Da die absoluten Werte jedoch von mehreren Faktoren (z.B. Zellgröße, Pigmentanzahl oder der Aufbau der Messapparatur) abhängen, wird F_0 zur Normierung von F_V (Differenz aus F_M und F_0) herangezogen. Der Quotient wird als Quantenausbeute des PS2 (Φ_{maxPS2}) bezeichnet:[71,72]

$$\Phi_{maxPS2} = \frac{F_M - F_0}{F_M} = \frac{F_V}{F_M} \tag{3-1}$$

Die Quantenausbeute kann als Maß für die Effizienz angesehen werden, mit der die absorbierte Lichtenergie in das Reaktionszentrum geleitet wird.[72] Studien haben überdies gezeigt, dass die Quantenausbeute eine reliable Näherung der maximalen Elektronentransportwirksamkeit bzw. der maximalen photochemischen Effizienz des PS2 ist.[73] Das Paradebeispiel für den Einsatz der SFK-Analyse ist die Untersuchung von Stresssituationen. Beispielhaft wird in Kapitel 7.2 die Quantenausbeute von lebenden Cyanobakterien mit den Quantenausbeuten von durch Stickstoffmangel gestressten (chlorotischen) Cyanobakterien verglichen. Die Ergebnisse sind in Abbildung 3-3D in einem Box-Plot zusammengefasst. Deutlich zu erkennen ist, dass chlorotische Zellen im Schnitt eine geringere Quantenausbeute haben als ungestresste Zellen.

4. Grundlagen konfokaler Fluoreszenzmikroskopie

Das erste konfokale Mikroskop wurde in den 1950er Jahren von Marvin Minsky entwickelt und patentiert.[74] Jedoch wurde die Anwendung erst in den 1980er Jahren mit der Verbreitung von Laser- und Computersystemen der allgemeinen Forschung zugänglich.[74]

Alle Messungen in dieser Arbeit (wenn nicht anders beschreiben) wurden mit einem selbstgebauten konfokalen Fluoreszenzmikroskop durchgeführt. Dabei wurde die Variante des inversen bzw. Auflichtmikroskops eingesetzt. Hier wird das Objektiv zur Laserfokussierung und zur Detektion verwendet. Konfokale Mikroskope zählen zu den Lichtmikroskopen, beleuchten jedoch, im Gegensatz zur konventionellen Lichtmikroskopie, nicht die ganze Probe, sondern nur einen kleinen Teil der Probe. Je nach Variante wird die Probe über den Lichtfleck (*sample* bzw. *stage scanning*) oder der Lichtfleck über die Probe (*laser* bzw. *beam scanning*) gerastert. Die Fluoreszenz der durch den Lichtfleck angeregten Farbstoffe wird anschließend Punkt für Punkt zu einem Bild zusammengesetzt. Dieses Abrastern der Probe ermöglicht zudem, Bilder in axialer Richtung aufzunehmen. Eine Lochblende (oder vergleichbares optisches Element) filtert dabei das Licht, welches nicht aus der Fokusebene stammt, heraus.[74] Das Zentrum der Lochblende und das Zentrum des in die Probe abgebildeten Lichtfleckes befinden sich dabei gleichzeitig im Fokus. Sie sind also konfokal (siehe Abbildung 4-1A, das konfokale Prinzip).[74] Dies ermöglicht das für die konfokale Mikroskopie typische kontrastreiche und scharfe Bild.

4.1 Aufbau des verwendeten konfokalen Fluoreszenzmikroskops

Abbildung 4-1C zeigt den schematischen Aufbau des verwendeten konfokalen Mikroskops. Als Anregungslichtquelle diente eine Laserdiode (LDH-D-C-440, PicoQuant GmbH, Deutschland), welche gepulst oder im Dauerstrichbetrieb (continous wave) mit einer Anregungswellenlänge von 440 nm verwendet wurde. Der Strahl wird durch einen Bandpassinterferenzfilter (MaxDiode™ LD01-439/8-12.5, Semrock Inc., USA) durch eine Linse auf eine Singlemode-Glasfaser (P1-405 BPM-FC-2, Thorlabs Inc., USA) fokussiert. Nach dem Auskoppeln des Laserstrahls durch eine weitere Linse hinter der Glasfaser, kann zur Weitfeldbeleuchtung eine Linse in den Strahlengang eingesetzt werden, welche den Laser auf die Rückapertur des Objektivs fokussiert. Vor dem Objektiv wird der Strahl von einen dichroitischen Strahlteiler reflektiert (Reflexion unterhalb von 488 nm und Transmission über 488 nm), der in einem Winkel von 45° zur Ausbreitungsrichtung angeordnet ist (F48-487 Laserstrahlteiler zt 488, AHF Analysentechnik AG, Deutschland). Der reflektierte Strahl wird nun durch ein

Ölimmersionsobjektiv (Zeiss Plan-Apochromat, 100x, 1,4 Oil DIC, Carl Zeiss AG, Deutschland) auf die Probe fokussiert. Die Probe kann durch Mikrometerschrauben grob positioniert werden. Das eigentliche Abrastern der Probe erfolgt jedoch durch einen piezogesteuerten Scanningtisch (P-733.3CD, Physik Instrumente (PI) GmbH & Co. KG, Deutschland), welcher ein Scannen der Probe in drei Raumrichtungen erlaubt. *Stage-scanning* ist im Gegensatz zu *Beam-scanning* zwar langsamer, jedoch ist der Aufbau eines *Stage-scanning* Mikroskops günstiger, leichter zu justieren und der Beleuchtungspunkt ist an jeder Stelle in der Probe gleich intensiv. Das von der Probe emittierte Fluoreszenzlicht wird anschließend wieder vom selben Objektiv aufgefangen und passiert anschließend den Strahlteiler. Ein zusätzlicher Langpassfilter (488 LP Edge Basic Langpassfilter, BLP01-488R-25, Semrock Inc., USA) und ein Bandpassfilter (BrightLine® FF01-676/29-25, Semrock Inc., USA) gewährleisten, dass das detektierte Signal ausschließlich von der Probe bzw. in diesem Fall vom PS2 stammt. Eine thermoelektrisch gekühlte *Electron Multiplying Charge-Coupled Device* Kamera (EMCCD) (iXon+ DU-888 E-C00-#BV, Andor Technology Ltd., Großbritannien) wird zur Orientierung innerhalb der Probe und für das Erstellen von Echtzeit-Weitfeldaufnahmen eingesetzt. Konfokale Aufnahmen wurden durch eine Einzelphotonen-Avalanche-Dioden-Detektor (engl. *single-photon avalanche diode* (SPAD); PDM-Serie, Micro Photon Devices, Italien) realisiert. Durch die Kopplung der SPAD mit einer zeitkorrelierten Einzelphotonenzähleinheit (engl. *time-correlated single photon counting unit* (TCSPC); HydraHarp 400, PicoQuant GmbH, Deutschland) und der gepulsten Laserdiode können zeitaufgelöste Messungen wie Fluoreszenzlebensdauer-Messungen (TCSPC *measurements*) und Bilder (*fluorescence lifetime imaging*, FLIM) und Einzelmolekülspektroskopie durchgeführt werden. Fluoreszenzspektren (mit geeigneten Laserquellen und Filtern auch Ramanspektren) werden mit einem Spektrometer (Acton SP300i, Princeton Instruments, USA) mit einer thermoelektrisch gekühlten CCD-Kamera (PIXIS 100, Princeton Instruments, USA) aufgenommen. Die Weitfeldaufnahmen werden von einer EMCCD-Kamera mit der Software Andor Solis (Andor Technology Ltd., Großbritannien) aufgenommen und verarbeitet. Der Scanningtisch, die SPAD, die Laserdiode und die TCSPC-Einheit werden von der Software SymphoTime® (PicoQuant GmbH, Deutschland) gesteuert. Fluoreszenz- und Einzelmolekülspektren werden mit der Software Winspec® (Princeton Instruments, USA) aufgenommen. Die Software steuert dabei den Monochromator und die CCD-Kamera.

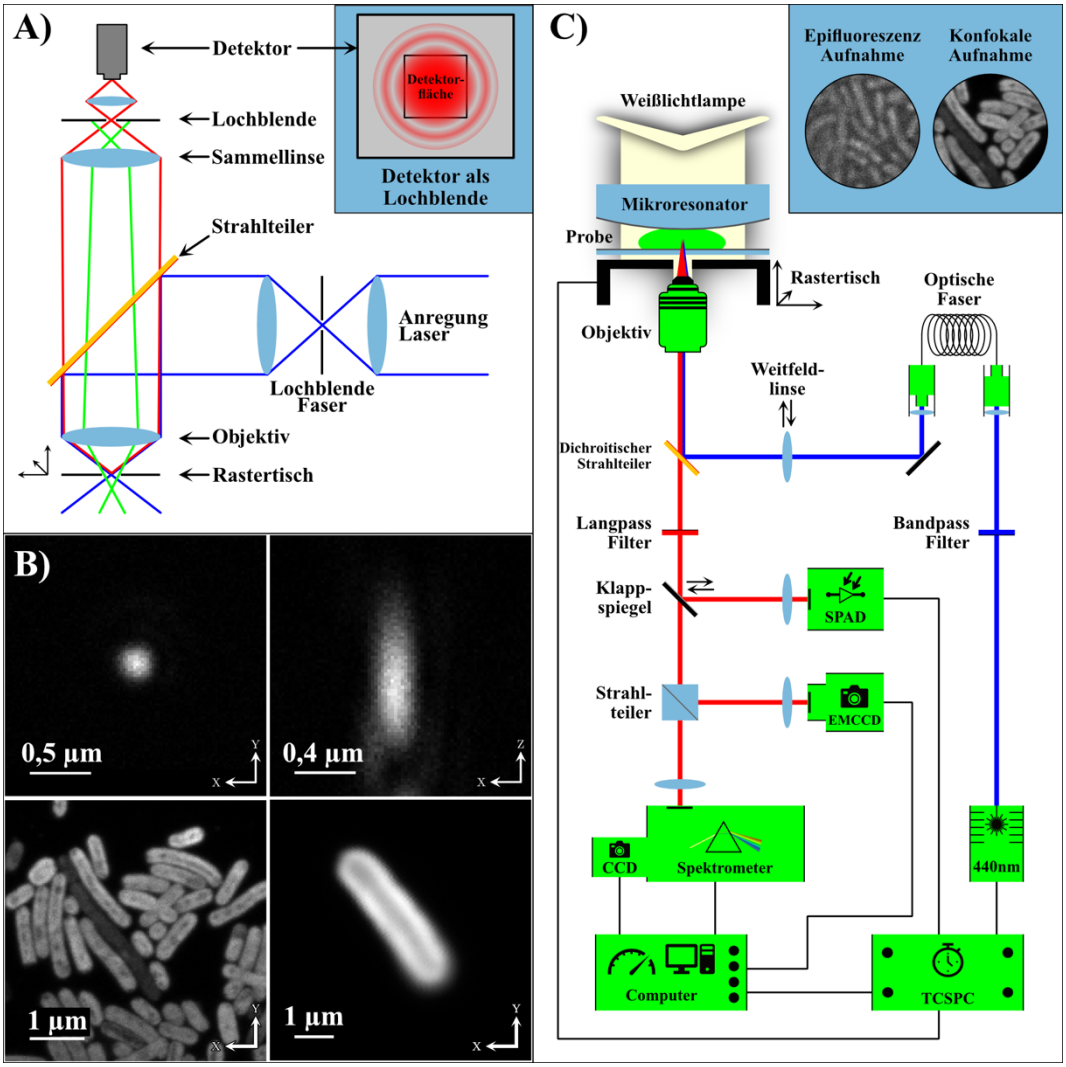

Abbildung 4-1: **(A)** Das konfokale Prinzip.[74] Blau: Anregungs- bzw. Laserlicht. Rot: Fluoreszenzlicht aus der Fokusebene. Grün: Fluoreszenzlicht nicht aus der Fokusebene. Oben rechts: Illustration der Detektorfläche der SPAD als Lochblende. Die Linse vor dem Detektor wurde so gewählt, dass die PSF in XY-Richtung so groß ist, dass sie die Detektorfläche leicht überstrahlt. **(B)** Oben: Rayleigh Streuung des Laserstrahls an einer Goldkugel (Durchmesser ca. 40 nm) links in der XY-Ebene und rechts in der XZ-Ebene. Da die Goldkugel kleiner als die Dimensionen der Punktspreizfunktion (PSF) ist, wird im konfokalen Bild die wahre Größe der PSF dargestellt. Unten: Beispiel für konfokale Bilder von *S. Elongatus*. Links: Übersichtsbild, rechts: Detailbild. **(C)** Schematischer Aufbau des verwendeten konfokalen Mikroskops. Als Probe wurde der Mikroresonator auf dem Probentisch illustriert. Oben rechts: Vergleich einer Epifluoreszenzaufnahme (Weitfeldbeleuchtung) mit einer konfokalen Aufnahme von *S. Elongatus*.

4.2 Die Punktspreizfunktion und Auflösung

Unter optischer Auflösung eines optischen Mikroskops versteht man im Allgemeinen den kleinstmöglichen Abstand, den zwei Objekte haben dürfen, um noch als getrennt voneinander wahrgenommen zu werden. Dieser Abstand wird Abbe-Limit (benannt nach Ernst Abbe) genannt und ist hauptsächlich durch die Beugung am freien Raum begrenzt.[75] Das Abbe-Limit

gilt jedoch nur für beleuchtete Objekte, welche das einfallende Licht zum Detektor hin beugen. In der konfokalen Fluoreszenzmikroskopie leuchten jedoch die untersuchten Objekte nach der Anregung von allein und können deshalb als punktförmige Lichtquellen betrachtet werden. Aus diesem Grund wird hier zur Bestimmung der Auflösung das heuristische Rayleigh-Kriterium (benannt nach John William Strutt, 3. Baron Rayleigh)[76] herangezogen.[77] Dieses Kriterium beschreibt das Auflösungslimit über die Intensitätsverteilung zweier Beugungsscheiben. Eine Beugungsscheibe ist dabei das mikroskopische Abbildungsmuster einer punktförmigen Lichtquelle. Dieses wird durch die Punktspreizfunktion (PSF) beschrieben.[78] Theoretisch besagt das Rayleigh-Kriterium, dass zwei Objekte gerade noch als getrennt wahrgenommen werden können, wenn das Intensitätsmaximum der einen Beugungsscheibe genau auf das erste Intensitätsminimum der anderen Beugungsscheibe fällt.[76] Da dieses heuristische Kriterium experimentell nur schwer messbar ist, wird zumeist die Halbwertsbreite (engl. full width at half maximum, FWHM) der PSF verwendet, wenn auch die tatsächliche Auflösung von weiteren Faktoren, wie z.B. vom Signal-Rausch-Verhältnis, abhängt.[78]

Die theoretisch größte beugungsbegrenzte Auflösung kann durch die Berechnung der theoretisch kleinsten Halbwertsbreite der PSF bestimmt werden. Der berechnete Wert ist nur theoretisch, da er nur für unendlich kleine Lochblenden, eine ideal punktförmige Lichtquelle, bei vollständiger Ausleuchtung der Rückapertur des Objektivs und bei ausreichend großem Kontrast (also genug Fluoreszenzlicht von der Probe) gilt. Da in der konfokalen Mikroskopie nicht die ganze Probe beleuchtet wird, werden bei der Berechnung die Anregungs- und Detektions-PSFs berücksichtigt. Dies äußert sich in der Auflösungsgleichung um eine fixe Auflösungsverbesserung um den Faktor $1/\sqrt{2}$. Zur Berechnung werden als variable Größen die Numerische Apertur NA (beschreibt den Öffnungswinkel eines Objektivs bzw. das Vermögen eines Objektivs Licht zu fokussieren) und der Durchschnitt aus Anregungs- und Emissionswellenlänge (λ) eingesetzt.[79] Der Faktor 0,37 berücksichtigt bereits die beiden PSFs:

$$FWHM_{x,y} = \frac{0{,}37\lambda}{NA} \tag{4-1}$$

Da die Detektionslochblende hauptsächlich lateral (in der XY-Ebene) das Emissionslicht filtert, ist die axiale (in Z-Richtung) Auflösung geringer:

$$FWHM_z = \frac{0{,}67\lambda}{n - \sqrt{n^2 - NA^2}} \quad (4\text{-}2)$$

Im Falle eines Immersionsölobjektivs ist der Brechungsindex n=1,518 und entspricht somit ungefähr dem des Deckglases.

Das in dieser Arbeit verwendete konfokale Mikroskop wurde ohne Anregungslochblende und ohne Detektionslochblende verwendet. Die Funktion der Anregungslochblende wurde von einer Einmoden-Glasfaser übernommen, welche ausschließlich die sogenannte Gauß-Mode transmittiert (das laterale Strahlprofil gleicht dabei einer Gaußkurve) und den Vorteil bietet, verschiedene Laserwellenlängen in das Mikroskop einzukoppeln, ohne das komplette System neu zu justieren. Eine Detektionslochblende erhöht zwar die Auflösung des Systems, verringert aber die Fluoreszenzintensität, welche am Detektor aufgenommen wird. Die in dieser Arbeit behandelten Proben neigten jedoch dazu, nur sehr wenig Fluoreszenzintensität zu emittieren, außerdem bestand keine Notwendigkeit, die Auflösung zu maximieren. Deshalb wurde die Detektorfläche als Lochblende verwendet, indem das Maximum des Detektionsstrahls minimal die Fläche des Detektors überstrahlt. Dies und die Tatsache, dass in Cyanobakterien sehr viele Farbstoffe sehr nah beieinander liegen (Emissionsmaximum 680 nm), was den Kontrast stark verschlechtert, erzielte das verwendete konfokale Mikroskop in lateraler Ebene eine Auflösung von ca. 190 nm und in axialer Ebene ca. 510 nm. Die zur Bestimmung der Auflösung verwendeten PSFs, welche durch Streuung des 440 nm Lasers an 40 nm großen Goldkugeln aufgenommen wurde, sind in Abbildung 4-1B (oben rechts und links) dargestellt.[78]

4.3 Fluoreszenzlebensdauern

Eine sehr umfangreiche Analysenmethode, welche häufig in Verbindung mit konfokaler Fluoreszenzmikroskopie eingesetzt wird, ist die Analyse der Fluoreszenzlebensdauer (FLT).[77] Das in dieser Arbeit verwendete Mikroskop ist dabei in der Lage, die FLT punktweise (örtliche Auflösung begrenzt durch die PSF) aufzunehmen oder ein komplettes konfokales Bild um die FLT-Dimension (Darstellung der FLT durch Fehlfarben) zu erweitern (Bsp: siehe Abbildung 3-1B).[77]

Die FLT (τ) ist die Zeitkonstante des exponentiellen Fluoreszenzzerfalls und ist ein Maß für die mittlere Verweildauer von Molekülen im angeregten Zustand. Sie ist die Zeit, nach der sich 1/e der Moleküle noch im angeregten Zustand (z.B. im S_1-Niveau) befinden. Der Zerfall des

angeregten Niveaus wird als exponentielle Abnahme, bei einem unendlich kurzen Anregungspuls zur Zeit t = 0, beschrieben:[77]

$$I(t) = I_0 e^{-t/\tau} \tag{4-3}$$

t: vergangene Zeit nach der Anregung
I(t): Fluoreszenzintensität nach der Zeit t
I_0: Fluoreszenzintensität direkt nach der Anregung

Kompetitive Prozesse wie internal conversion, thermische Äquilibrierung, intersystem crossing oder alle Arten von Energietransfers, die statt der Fluoreszenz stattfinden können, reduzieren die mittlere Fluoreszenzlebensdauer. Normalerweise liegt die Fluoreszenzlebensdauer von Farbstoffen (wie z.B. Hypericin[21], siehe Kapitel 7.4) im unteren Nanosekunden-Bereich (1-10 ns). Im Beispiel der Cyanobakterien ist jedoch nur der Energietransfer zum Reaktionszentrum photosynthetisch produktiv, weshalb dieser Prozess evolutionär stark selektiert wurde. Der Grund dafür ist nicht abschließend geklärt, wird jedoch in dieser Arbeit genauer untersucht. Je schneller einer der konkurrierenden Prozesse abläuft, desto wahrscheinlicher ist er. Der Energietransfer im Photosystem läuft im unteren Picosekunden-Bereich ab, was bedeutet, dass nur die Fluoreszenz zu messen ist, welche noch schneller abläuft, also nur ein kleiner Teil der absorbierten (Sonnen-) Energie.[80]

Um Fluoreszenzlebensdauern zu bestimmen, wurde die Methode der zeitkorrelierten Einzelphotonenzählung (TCSPC) angewendet (vgl. Abbildung 4-2).[77] Dabei wird die Probe mit sehr kurzen Laserpulsen (ca. 100 ps) und einer Pulsrate von 40 oder 80 MHz angeregt. Die Pulsrate wird abhängig von der zu messenden FLT eingestellt, da sie das Zeitfenster begrenzt, in der ein Histogramm des Fluoreszenzzerfalls aufgenommen werden kann. Das Prinzip der TCSPC-Messung (im Folgenden auf Basis von Lakowicz[77] erläutert), stellt große Anforderungen an die Genauigkeit der verwendeten Messinstrumente. Der Laser startet durch Aussenden eines Pulses die Stoppuhr in der TCSPC-Einheit. Der Laserpuls regt die Probe zur Fluoreszenz an, welche wiederum von der Einzelphotonen-Avalanche-Diode (SPAD) detektiert wird und ein Stoppsignal in der TCSPC-Einheit auslöst. Die ermittelten und statistisch verteilten Zeiten werden nun mittels Computer in einem Histogramm aufgezeichnet und mit einer Exponentialfunktion angepasst. Der beobachtete exponentielle Vorgang des Zerfalls in der Zeitdomänenmessung ist eine Faltung des wahren Zerfallsvorgangs mit der

Instrumentenantwortfunktion (engl. instrument response function, IRF). Durch eine Faltung der IRF mit iterativ veränderten Parametern und einem anschließenden Vergleich mit den Rohdaten, kann die wahre Fluoreszenzlebensdauer aus der gemessenen Zerfallskurve bestimmt werden. Die IRF wird vor jedem Experiment durch Analysieren der Laserstreuung an einer Spiegeloberfläche bestimmt als eine Art von Hintergrundkorrektur.

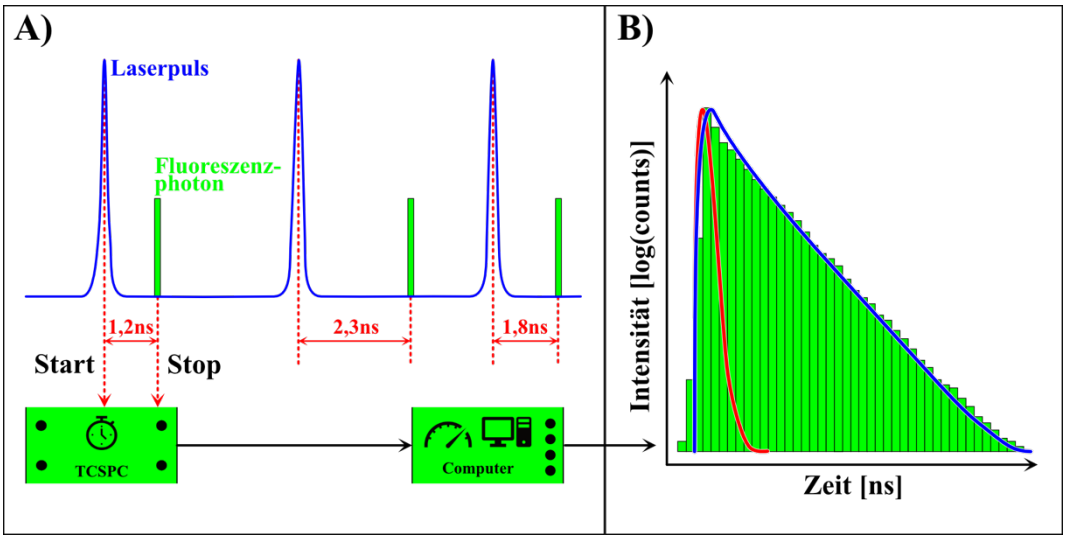

Abbildung 4-2: **(A)** Fluoreszenzlebensdauermessung nach der zeitkorrelierten Einzelphotonenzählmethode. Der Laser sendet zeitgleich mit dem Aussenden eines Photons (blau) ein Startsignal (rot) an die Einzelphotonenzähleinheit (TCSPC-unit). Das dadurch erzeugte Fluoreszenzphoton wird vom Einzelphotonen-Avalanche-Dioden-Detektor (SPAD) detektiert und sendet zeitgleich ein Stoppsignal (rot) an die TCSPC-Einheit. Die gemessenen Lebensdauern werden durch einen Computer verarbeitet und in einem Histogramm dargestellt: **(B)** Das Fluoreszenzlebensdauern-Histogramm zeigt die Häufigkeit der gemessenen Fluoreszenzlebensdauern (grün). Durch eine exponentielle Regression (blau) mit anschließender Faltung der Instrumentenantwortfunktion (IRF, rot) kann auf die Fluoreszenzlebensdauer geschlossen werden.

Die FLT an sich ist eine substanzspezifische Eigenschaft, die ohne Umgebungseinflüsse an jedem Punkt der Probe den gleichen Wert annimmt.[77] Da biologische Proben jedoch sehr komplexe Umgebungen darstellen, wird die FLT auch stark beeinflusst. Zu diesen Einflüssen zählen z.B. die Farbstoff-Konzentration, das Bleichverhalten und die chemische Umgebung (z.B. pH-Wert der Umgebung, vgl. Kapitel 7.4) des Farbstoffs. Diese Einflüsse sind für Messungen an lebenden Cyanobakterien oder Messungen in biologischen Geweben von großer Bedeutung. Es ist nicht einfach festzustellen, wie viele Farbstoffe ein einzelnes Bakterium enthält, was passiert, wenn einzelne Farbstoffe des Photosystems durch eine Messung ausgebleicht werden oder in welcher chemischen Umgebung sich die Farbstoffe befinden. Auch

die Geräteanordnung, Gerätestabilität und Temperatur sind maßgebliche Faktoren. Diese Einflüsse führen dazu, dass in der Literatur oft sehr unterschiedliche FLTs zu denselben Proben gemessen werden. Die in dieser Arbeit gemessenen FLTs sollen jedoch nur als Vergleich zwischen den Messreihen dienen. Dem absoluten Wert wird hier weniger Relevanz beigemessen, zumal die gemessene Fluoreszenzlebensdauer des Photosystems extrem kurz ist: Für eine Energietransport-Effizienz von ca. 95 % ergaben Berechnungen, dass die Fluoreszenzlebensdauer des PS2 im Femtosekunden-Bereich liegen muss, da nur die emittierte Energie gemessen werden kann, welche nicht das Reaktionszentrum erreicht.[56] Die komplexe Struktur des Photosystems hat unweigerlich sehr verschiedene chemische Umgebungen der einzelnen Farbstoffe zur Folge. Daraus folgen komplexere Zerfallseigenschaften als nur ein simpler monoexponentieller Zerfall. Der Zerfall muss deshalb durch eine Summe von Exponentialfunktionen dargestellt werden:

$$I(t) = \sum_i A_i \, e^{-t/\tau_i} \tag{4-4}$$

A_i repräsentiert die Amplitude bzw. Gewichtung der einzelnen Exponenten. Aus dieser Gleichung kann nun die mittlere intensitätsgewichtete FLT τ_I bestimmt werden:[81]

$$\tau_I = \frac{\sum_i A_i \, \tau_i^2}{\sum_i A_i \, \tau_i} \tag{4-5}$$

Untersuchungen haben gezeigt, dass τ_I (im Gegensatz zur, hier nicht näher erläuterten, mittleren amplitudengewichteten FLT, τ_A) weitgehend unabhängig von der Summe der Exponentialfunktionen ist und somit, aufgrund der unbekannten Anzahl an Zerfallsspezies ein genaueres Ergebnis liefert.[81] τ_I kann deshalb als eine intrinsische Eigenschaft des Fluoreszenzabfalls angesehen werden. Neben den obengenannten Einflussfaktoren auf die FLT wird im Zusammenhang mit dieser Arbeit ein weiterer Einfluss, welcher normalerweise bei FLT-Messungen keine Relevanz hat, vorgestellt. Ein Mikroresonator ist in der Lage die spontane Emissionsrate und damit die FLT zu beeinflussen. Dieser Effekt wird Purcell-Effekt genannt und besagt, dass die Wahrscheinlichkeit der spontanen Emission höher ist, wenn sich die fluoreszierende Probe in einem Mikroresonator befindet.[27] Die Emissionsrate hängt dabei vom Purcell-Faktor ab. Je höher der Purcell-Faktor, desto höher die Emissionsrate, was eine geringere FLT zur Folge hat.[17] Dies gilt jedoch nur, wenn der Mikroresonator resonant zur Fluoreszenz des Farbstoffes ist. Nur im resonanten Fall hat das Fluoreszenzphoton eine Mode

außerhalb des Photosystems, an das es koppeln kann. Im nicht resonanten Fall passiert genau das Gegenteil: Die Emissionsrate fällt und somit steigt die FLT. Dem Photosystem wird quasi „verboten“ zu fluoreszieren, da außerhalb des Photosystems keine Mode existiert, an die das Fluoreszenzphoton koppeln kann. Das Wort „verboten“ wurde vorliegend im quantenmechanischen Sinne verwendet und bedeutet damit „sehr unwahrscheinlich“. Ein anschauliches Beispiel für den Purcell-Effekt ist in Kapitel 7.1 aufgezeigt.

4.4 Messung der schnellen Fluoreszenzkinetik

Die Messung der schnellen Fluoreszenzkinetik aus Kapitel 3.3.5 ff. stellt große Anforderungen an das verwendete konfokale Mikroskop. Da ein einzelnes Bakterium die absorbierte Lichtenergie hauptsächlich zur Photosynthese nutzt, emittieren sie nur sehr wenige Fluoreszenzphotonen. Werden diese dann zeitlich hoch aufgelöst registriert, treffen im Schnitt, bei einer sättigenden Anregungsleistung von ca. 2 nW (440 nm), nur 60 Photonen im Fluoreszenzmaximum pro 0,2 ms auf die SPAD. Eine höhere zeitliche Auflösung wäre theoretisch möglich, hätte aber zur Folge, dass die zeitliche Integration über einen Datenpunkt nur ein Photon zählen würde und keine Kurve mehr erkennbar wäre. Selbst bei einer zeitlichen Auflösung von 0,2 ms streuen die Messwerte aufgrund des Hintergrundrauschens immens (siehe bspw. Abbildung 3-3D und vgl. Kapitel 7.2). Eine reproduzierbare Auswertung aller Daten ist nur durch einen Glätt-Algorithmus und ein MATLAB-Skript (vgl. Kapitel 7.2 in der Supplementary information) möglich, welches auf mathematischer Basis den F_0- und F_M-Wert bestimmt. Die Methode der Einzelzell-SFK-Messung hat somit eine große Streuung der Quantenausbeute zur Folge. Dies deutet darauf hin, dass einzelne Cyanobakterien nicht eine einheitliche (wie von kommerziellen CFK-Geräten suggeriert), sondern individuell unterschiedliche Quantenausbeuten zeigen. Die Einzelzell-SFK-Methode ist also in der Lage, Effekte zu zeigen, welche normalerweise in einer Ensemble-Messung im Rauschen untergehen. Außerdem ermöglicht sie die ortsaufgelöste Messung an einzelnen Zellen in einem Mikroresonator an einer Stelle, an der das optische Feld resonant (oder zum Vergleich nichtresonant) zur PS2-Fluoreszenz ist (siehe Kapitel 7.2).

5. Die Quantenbiologie

Nach der Geburt der Quantentheorie im frühen 20. Jahrhundert entstand in den darauffolgenden Jahren die Idee, dass sich nicht nur die Menschheit Quanten-Phänomene zunutze machen kann, sondern dass die Natur selbst Quanteneffekte evolutionär einsetzte, um ein effizienteres Dasein von lebenden Organismen zu entwickeln.[82] Tatsächlich wurden schon kurz nach der Entdeckung der Quantentheorie Vermutungen zu biologisch signifikanten und nicht trivialen Quanteneffekten publiziert. Schon vor dem vermeintlichen Begründer der Quantenbiologie (Erwin Schrödinger) vermuteten der deutsche Physiker Pascual Jordan[82] und der dänische Physiker Nils Bohr[83] einen Einfluss von Quanteneffekten auf die Biologie. Anschließend erst spekulierte Erwin Schrödinger 1944 in seiner wissenschaftlichen Abhandlung „What is life?“, dass Quanteneffekte einen direkten Einfluss auf die Evolution haben.[84] Es wurden überdies sogar Vermutungen angestellt, dass der Indeterminismus der Quantenmechanik Auswirkungen auf einen makroskopischen Organismus haben und der Ursprung des freien Willens der Menschen sein könnte.[85] Es folgten weitere quantenbiologische Theorien, wie z.B. das Protonentunneln in Bioproteinen[86], das Elektronentunneln in Enzymen[87], die quantenmechanische Funktion des Magnetsinns einiger Tiere[88,89,90,91], die quantenmechanische Funktion des Sehsinnes[92] und die langlebige Quantenkohärenz im Photosystem von photoautotrophen Organismen[6].

Ganz dem wissenschaftlichen Geiste des Diskurses entsprechend gab es auch Vertreter der Nichtquantenbiologie. Alexander Sergejewitsch Davydovs positionierte sich beispielsweise in „Biology and Quantum Mechanics“ 1982 im Lager der quantenevolutionären Kritiker.[93] Er vermutete, dass Quanteneffekte ausschließlich für rein isolierte Systeme relevant sind und auf biologische Systeme keinen signifikanten Einfluss nehmen würden. Quanteneffekte seien äußerst empfindliche Phänomene und nicht relevant für „warme, nasse und laute“ Lebewesen.[56]

Da die wissenschaftlichen Methoden bis zum Ende des 20. Jahrhunderts nicht ausreichend genaue Ergebnisse liefern konnte, erlebte die Forschung erst Anfang des 21. Jahrhunderts einen erneuten Aufschwung. Durch die Entwicklung hochsensitiver und ultraschneller Messmethoden können nun Quanteneffekte in hochkomplexen biologischen Systemen untersucht werden. Allen voran entwickelte sich die Photosynthese als Modellprozess für die Quantenbiologie. So wird auch in dieser Arbeit der Einfluss von nichttrivialen Quanteneffekten auf die Photosynthese durch einen neuartigen Analysenansatz untersucht werden.

5.1 Forschungsstand der quantenbiologischen Beschreibung der Photosynthese

Die Entstehung des photosynthetischen Prozesses stellt Forscher seit Jahrhunderten vor ein großes Rätsel. Es wird vermutet, dass die anoxygene Photosynthese vor ca. 3,5 Ga[94] entstand und erst nach dem großen Anstieg der Sauerstoffkonzentration (vgl. Große Sauerstoffkatastrophe) in der Erdatmosphäre (vor ca. 2,4 Milliarden Jahren)[95] die oxygene Photosynthese. Es ist daher äußerst schwer, an verlässliche Informationen zu gelangen, die so lange in der Vergangenheit liegen. Zum Vergleich: Das Sonnensystem entstand vermutlich vor ca. 4,56 Milliarden Jahren[96] und die ersten einzelligen und alle ausschließlich maritimen Organismen vor ca. 3,77-4,28 Milliarden Jahren[97]. Es gibt zahlreiche Theorien, wie die Photosynthese entstand, jedoch soll in dieser Arbeit nur eine neue und noch unbelegte Theorie angesprochen werden, welche nicht für sich beansprucht, ausschließliche Gültigkeit zu besitzen.

Es wäre denkbar, dass vor 3,5 Milliarden Jahren die ersten einzelligen Organismen in hauchdünne Gesteinsrisse diffundierten und sich dort abgesetzt haben. Da zu dieser Zeit die Erde noch von vielen Rissen in der Erdkruste durchzogen war[98] und heiße Ströme oder Lava viele Organismen abtöteten, könnten sich Organsimen durch das Absetzten in geschützten Gesteinsrissen, einen Vorteil verschafft haben. Bestand nun das Gestein zufällig aus Hämatit/Eisenglanz (z.B. im pazifischen und mittelatlantischen Meer), welches aufgrund seiner reflektierenden Eigenschaften[98] schon in der Antike als Spiegel eingesetzt wurde, könnten Risse als eine Art Mikroresonator fungiert haben. Wie bereits in Kapitel 2 erläutert, herrschen in einem Mikroresonator ganz spezielle optische Bedingungen. Die in die Risse diffundierten Organismen, könnten diese speziellen optischen Bedingungen ausgenutzt haben, um aus einfallendem Sonnenlicht, welches in den Rissen kohärent hin und her reflektiert wurde, den photosynthetischen Prozess zu entwickeln. Gemäß dieser Überlegung wurden in dieser Arbeit die Nachfahren der damaligen Einzeller, die Cyanobakterien, in einem Mikroresonator untersucht (vgl. Kapitel 7.1 und 7.2).

Der aktuelle Stand der quantenbiologischen Überlegungen zur Photosynthese behandelt den Energietransfer aus Kapitel 3.3.3. Es wird versucht die Übertragungseffizienz von fast 100%[56,41] der Energie, von der Absorption eines Photons bis hin zum Reaktionszentrum (z.B. dem P680), zu erklären. In der klassischen Beschreibung wird der Transfer als eine Art „Energie-Hüpfen“ auf einer ganz diskreten Route von einem zum anderen Chlorophyll-Molekül in Form einer Dipol-Dipol-Wechselwirkung oder einfach als klassischer FRET-

Transfer beschrieben (siehe Abbildung 5-1A).[99] Ein klassischer FRET-Transfer über mehrere Moleküle kann jedoch nicht mit einer nahezu perfekten Effizienz stattfinden, da jeder einzelne Transfer von mehreren Faktoren abhängt (z.B. Abstand, Ausrichtung der Übergangsdipolmomente und Überlapp von Absorptions- und Emissionsspektren der Chlorophyll-Moleküle)[99,41], welche das Photosystem nicht über einen so großen Weg hinweg leisten kann. Es hat sich herausgestellt, dass es bei der Photosynthese nur wenige Prozessschritte gibt, welche durch einen klassischen FRET-Transfer beschrieben werden können.[56] Durch die weitgehend starre Anordnung des Proteingerüstes wird ein Energietransfer begünstigt, der sich nicht ausschließlich durch die optischen Eigenschaften von Donor-Chlorophyll und Akzeptor-Chlorophyll beschreiben lässt.[56] Es wurde daraufhin versucht, eine quantenmechanische Erklärung für die hohe Transfereffizienz zu finden. Befürworter des quantenbiologischen Ansatzes gehen inzwischen davon aus, dass sich durch das relativ starre Proteingerüst des Photosystems die einzelnen Chromophore wie elektronisch delokalisierte Zustände verhalten, obwohl sie getrennt voneinander existieren.[100] Die Eigenschaften der delokalisierten Zustände werden also hauptsächlich durch Wechselwirkungen mit der Umgebung / dem Proteingerüst (vgl. umgebungsabhängige Einzelmolekülspektroskopie) bestimmt.[101] Eine Charakterisierung des Transfers (z.B. Bestimmung der Transferrate, Transfermechanismus, etc.) ist jedoch nicht einfach zu verwirklichen. Triviale Spektroskopiemethoden liefern hierzu keine ausreichenden Informationen.

Erste Ansätze zur quantenmechanischen Beschreibung liefert das System-Umgebungsphonon-Modell. Diesem liegt die Förster-Theorie zugrunde und es beschreibt im Prinzip zwei Grenzfälle:

1. Besteht eine große exzitonische Kopplung der Chromophore an Phononen (kollektive Anregung von Gitterschwingungen im Proteingerüst) der Umgebung (Kopplung der Chromophore untereinander klein), werden die Anregungszustände von Donor- und Akzeptor-Chlorophyll klassisch nach der Förster-Theorie beschrieben.
2. Ist die exzitonische Kopplung an die Umgebung jedoch viel kleiner als die Kopplung der Chromophore untereinander, müssen die Exzitonen delokalisiert beschrieben werden. Das Ergebnis sind die Redfield-Gleichungen.

Die aus diesen Überlegungen resultierende moderne multichromophorische FRET-Theorie (MFRET-Theorie) betrachtet Donor und Akzeptor jeweils als eine kleine Gruppe von

Molekülen, die kohärent angeregt werden.[102] Nach dieser Theorie besteht demnach Kohärenz zwischen den Exzitonenzuständen der Chromophore.[102] Ein wellenartiger Energiefluss, dessen genauer Weg nicht lokalisiert werden kann, ist die Folge. Dies ist der wesentliche Unterschied zum klassischen, inkohärenten und diffusionsartigen Transport, welcher den klassischen Geschwindigkeitsgesetzen folgt. Jedoch versagt auch die MFRET-Theorie bei einer langanhaltenden Quantenkohärenz, welche im Photosystem von grünen Schwefelbakterien (genauer im Fenna–Matthews–Olson-Komplex, welcher die Anregungsenergie der Antennenpigmente in das Reaktionszentrum leitet) entdeckt wurde, da sie nur die Grenzfälle beschreibt.[56]

Es ist bis heute nicht abschließend geklärt, ob eine Kohärenz im Photosystem wirklich existiert und den photosynthetischen Prozess unterstützt oder ob sie nur ein irrelevantes Nebenprodukt der Evolution ist. Hätte jedoch die Kohärenz einen biologisch relevanten Einfluss, hätte die Evolution Jahrmilliarden Zeit, um den Kohärenzgrad präzise an das System anzupassen, um einen optimalen Energietransfer zu gewährleisten. Denn wäre das System vollständig kohärent, würde es einfach oszillieren und kein Populationstransfer stattfinden.[103] Wenn andererseits die Kopplung an das Proteingerüst zu groß ist, würde die Transfereffizienz ebenfalls sinken. Eine somit vollständige Lokalisierung der Energie hätte zur Folge, dass die Population den angeregten Zustand nicht verlassen kann.[103] Es wird daher vermutet, dass ein Optimum des Kohärenzgrades zwischen diesen beiden Extremen existiert.[56] Daraufhin entstanden viele weitere Theorien, welche den FRET-Transfer um die elektronische Energieübertragungsdynamik und die auf die Superposition von Exzitonenzuständen zurückzuführenden exzitonischen Kohärenzeffekte erweiterten.[104] Überdies wurde festgestellt, dass dieselben Energietransfer-Wechselwirkungen, welche zur Photosynthese genutzt werden, auch dazu eingesetzt werden, um überschüssige (Sonnen-)Energie abzuleiten und Schäden durch übermäßige Anregung zu verhindern.[101]

Sollte die Kohärenz im Photosystem einen relevanten Zweck besitzen, würde sie jedoch ein Werkzeug darstellen, um Einfluss auf das System zu ermöglichen. Diese Arbeit zielt genau auf eine solche Einflussnahme und deren biologischer Relevanz ab (vgl. Kapitel 7.1 und 7.2).

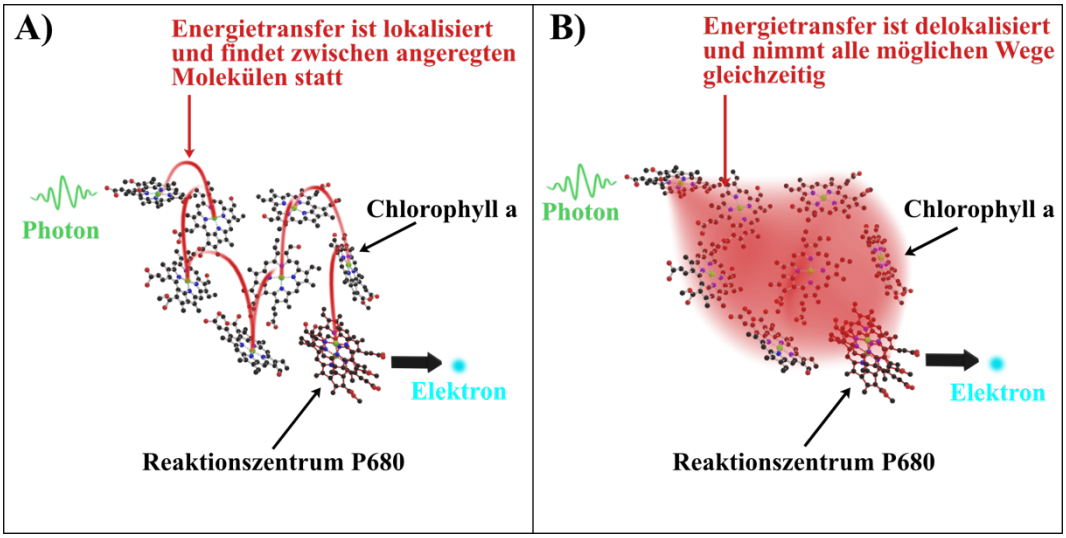

Abbildung 5-1: **(A)** Schematische Darstellung des Energietransfers im Photosystem 2 von der Absorption eines Photons bis zum Reaktionszentrum P680. In der klassischen Beschreibung des Transfers ist die Energie zu jedem Zeitpunkt in einem Chlorophyll-Molekül lokalisiert (entnommen aus Kapitel 7.1). **(B)** Quantenelektrodynamische Beschreibung des Energietransfers aus (A). Die Energie des Photons ist delokalisiert und wird zu einem gewissen Grad kohärent zum Reaktionszentrum P680 transportiert (entnommen aus Kapitel 7.1).

Zunächst wird jedoch die jüngere Geschichte der die Photosynthese behandelnden Quantenbiologie zusammengefasst. Die ersten konkreten Vermutungen zu einem kohärenten Energietransfer im Photosystem wurden 2004 von Fleming und Scholes publiziert.[101] Dem folgten 2007 Experimente an isolierten Lichtsammelkomplexen bei 77 K.[6] Nur drei Jahre später konnte von Collini[105] und Panitchayangkoon[106] in lebenden photosynthetischen Organismen unter physiologischen Bedingungen eine signifikant lang anhaltende Kohärenz beobachten. Hierbei wurde mit ultrakurzen Laserpulsen im Femptosekunden-Bereich eine Kohärenz im Photosystem erzeugt und deren Zerfall über die Zeit hinweg beobachtet. Die biologische Relevanz wurde jedoch nicht untersucht. Da sie jedoch die Existenzberechtigung der Quantenbiologie darstellt, bedarf es zwingend weitergehender Untersuchungen. Ebenfalls konnte nicht abschließend geklärt werden, ob die Kohärenz nicht alleine durch die Messmethode von Collini *et al.*[105] und Panitchayangkoon *et al.*[106] mit kohärenten Laserpulsen im Femtosekunden-Bereich induziert wurde. Hierzu schreibt Fleming jedoch, dass die Pulse nur zur anfänglichen zeitlichen Koordinierung dienen und anschließend Einblicke in die Dynamik des Kohärenzzerfalls geben.[56] Eine Messung im makroskopischen Maßstab scheint ihm jedoch noch nicht realisierbar.[56] 2009 wurden außerdem Vermutungen angestellt, dass eine langlebige Kohärenz im Photosystem der Grund für das Retten aus sogenannten „Trap-States“ ist. Befindet sich zum Beispiel die Energie in einem Chlorophyll-Molekül, welches sich in der

Energielandschaft ganz unten befindet (Trap-state), wäre ein Übertrag auf ein anderes Chlorophyll-Molekül, welches energetisch höher liegt, nicht möglich (siehe Abbildung 5-2A).[107] Das Chlorophyll-Molekül müsste die Energie irgendwann in Form von Fluoreszenz oder Wärmeabgabe an die Umgebung emittieren.[108] Die Kohärenz im System wäre jedoch in der Lage, diese Energiebarriere zu überwinden und den Energietransport dadurch erhöhen (von Fleming als „Energietransfer-Gleichrichter“ bezeichnet, siehe Abbildung 5-2B).[107] 2017 sahen Scholes *et. al.* in einem Artikel[109] die Existenz von langlebiger Kohärenz im Photosystem neben anderen chemischen und biologischen Prozessen als ausreichend bewiesen an. Sie forderten, dass sich die zukünftige Forschung mehr mit der Funktion der Kohärenz beschäftigen solle, also mit der biologischen Relevanz der Kohärenz. Als gutes Beispiel wurden Experimente mit Attosekunden-Laserpulsen[110] erwähnt und der Einsatz von zeitaufgelöster Röntgenspektroskopie[111].

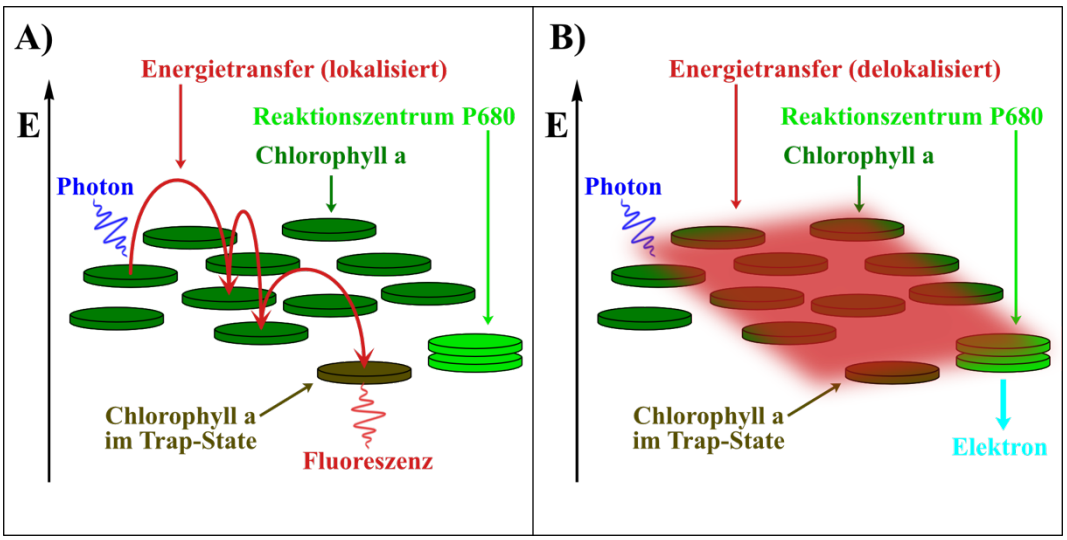

Abbildung 5-2: **(A)** Befindet sich ein Chlorophyll a-Molekül in der Energielandschaft ganz unten (Trap-state), wäre ein Übertrag auf das energetisch höher liegende Reaktionszentrum P680 nicht möglich. Das Chlorophyll a-Molekül müsste fluoreszieren. **(B)** Langlebige Kohärenz im Photosystem könnte ein Grund für das Retten aus dem Trap-State sein. Ein delokalisierter Energietransfer könnte diese Energiebarriere überwinden und den Energietransport zum Reaktionszentrum P680 ermöglichen.

2020 fasste Cao *et. al* die letzten 10 Jahre der Forschung im Bereich der Quantenbiologie zusammen. Sie kamen zu dem Ergebnis, dass es noch immer keine ausreichenden Beweise für die Existenz von biologisch relevanten, nichttrivialen Quanteneffekte gibt.[55] Die Existenz einer langlebigen Kohärenz im Photosystem wird nicht direkt bestritten, vielmehr wird gefordert, dass die Wechselwirkungen zwischen den Chromophoren und dem Proteingerüst genauer

untersucht werden. Experimente mit Femptosekunden-Pulsen werden kritisch gesehen. Ebenfalls 2020 berichtete Mančal[112] das die Quantenrevolution der Biologie (vorerst) gescheitert sei. Er führte das Scheitern jedoch auf das Problem der Interdisziplinarität zurück, dass die unterschiedlichen Fachbereiche jeweils ihre eigene Fachsprache benutzen und somit Verständnisprobleme aufgetreten sind. Auch das Problem, dass die Qualität einer wissenschaftlichen Arbeit am Impact-Faktor eines Journals gemessen wird, wurde als Grund angeführt. Mančal fordert eine Rückkehr zu den physikalischen Grundlagen und das Entwickeln neuer Ansätze, Theorien und Methoden.

Trotz der Uneinigkeit in der Wissenschaft sollte die Forschung im Bereich der Quantenbiologie nicht eingestellt werden. Es ist aus wissenschaftlicher Sicht fast schon zwingend notwendig, die Photosynthese als einen der wichtigsten Prozesse des Lebens genau zu verstehen. Dass dieser Prozess nicht klassisch beschrieben werden kann, steht inzwischen außer Frage, deshalb wird in dieser Arbeit ein neuer Weg aufgezeigt, der hoffentlich in naher Zukunft seinen Teil zur Aufklärung der letzten Unklarheiten der Photosynthese beitragen wird. Denn auch abgesehen von der Wichtigkeit der wissenschaftlichen Grundlagenforschung besteht in der industriellen Forschung großes Potential, wenn der photosynthetische Energietransfer auf moderne (biologische oder sogar nachwachsende) Solarzellen übertragen werden könne. Zudem ist die Existenz langlebiger Quantenkohärenzen von großer Bedeutung für die Forschung an Quantencomputern, welche immer bedeutender für die Industrie und die Forschung werden, da sie bei bestimmten mathematischen Problemstellungen um ein Vielfaches effizienter arbeiten als herkömmliche Computer. Eine Vermeidung von Dekohärenz spielt für die Quanteninformationsverarbeitung eine wesentliche Rolle.[113]

5.2 Zentrale Aufgabe: Detektierbarkeit

Die Detektierbarkeit von Quanteneffekten stellt die Forschung vor große Herausforderungen. Bis heute beruht die Quantenbiologie größtenteils auf theoretischen Simulationen. Es mangelt an experimentell eindeutigen Ergebnissen, die im besten Falle zusätzlich einen biologisch signifikanten Einfluss aufzeigen. Es wird vermutet, dass Quanteneffekte für eine Vielzahl von Phänomenen ursächlich sein könnten. Der photosynthetische Prozess ist darunter jedoch der wohl am häufigsten untersuchte und am besten zu untersuchende Prozess. Vielversprechende Methoden, wie die Exziton-Exziton-Interaktions-zwei-dimensionale-(EEI2D)-Spektroskopie[114], die oben bereits erwähnten Attosekunden-Laserpulse[110] und die zeitaufgelöste Röntgenspektroskopie[111] sowie der Einsatz optischer Mikroresonatoren (vgl.

Kapitel 7.1) könnten neue Erkenntnisse über die Auswirkungen von Kohärenz in biologischen Systemen enthüllen. Da ein Nachweis von Quanteneffekten jedoch nicht notwendigerweise biologische Signifikanz nachweist, bedarf es außerdem eines reliablen Nachweises der Relevanz. Diese Arbeit schlägt eine Methode vor, welche den Energietransfer im Photosystem 2 *in vivo* und unter physiologischen Bedingungen quantifiziert (vgl. Kapitel 3.3.6 zur Theorie und Kapitel 7.2 zur Praxis). Dabei ist jedoch zu berücksichtigen, dass kohärente Einflüsse auf den Energietransfer nicht notwendigerweise eine erhöhte photosynthetische Aktivität zur Folge haben. Umgebungsbedingungen oder nachgelagerte Prozesse (wie z.B. die CO_2-Fixierung) könnten limitierende Faktoren darstellen.

5.3 Weitere quantenbiologische Theorien

Neben der Photosynthese könnten nichttriviale Quanteneffekte ursächlich für weitere biologische Prozesse sein. Nah mit dem Energietransfer verwandt ist beispielsweise die katalytische Beschleunigung von Reaktionen durch Enzyme. Es wird vermutet, dass Enzyme Protonen oder Hydride durch den quantenmechanischen Tunneleffekt transportieren.[86] Da diese Transfers meist die geschwindigkeitsbestimmenden Schritte einer enzymatischen Reaktion sind, würde das Tunneln der Protonen zur Steigerung des katalytischen Effektes beitragen. Hier spielen die Umgebungseffekte, ähnlich wie im Photosystem eine wichtige Rolle, um einen quantenmechanischen Transfer zu gewährleisten. Solche nukularen Quanteneffekte sind sehr empfindlich gegenüber Umgebungseinflüssen (z.B. Abstandsänderungen im Enzym).[56] Dies resultiert daraus, dass ein Proton, mit seiner vergleichsweise großen Masse, eine sehr kurze de-Broglie-Wellenlänge besitzt.[56] Es wurde bereits versucht, über eine Abstandsänderung im Enzym die Quantentunnelereignisse bzw. die katalytischen Reaktionsrate zu beeinflussen.[115,116] Möglicherweise ist die anomale Temperaturabhängigkeit von Enzymen auf die geänderte Tunnelrate durch Abstandsänderung zurückzuführen.[56] Auch das Elektronentunneln in Proteinen wird intensiv untersucht.[117]

Ein weiteres viel diskutiertes Phänomen ist die Magnetrezeption verschiedener Organismen. Magnetotaktische Bakterien, Amphibien, Insekten, Vögel, Fische und auch einige Säugetiere sind durch ihren Magnetsinn in der Lage, sich am Erdmagnetfeld zu orientieren.[118] Früher wurde der Magnetsinn, basierend auf dem klassischen Modell des Elektromagnetismus, ohne Zuhilfenahme der Quantenmechanik beschrieben. Inzwischen ist allerdings davon auszugehen, dass durch Lichtinduktion ein kurzweiliges Radikalpaar entsteht.[119] Das Modell wurde „Radikalpaar-Modell“[92] genannt. Das Radikalpaar ist in der Lage, zwischen zwei möglichen

Quantenzuständen hin und her zu wechseln (Singulett-/Triplettzustand). Je nachdem, ob das Paar im Singulett- oder Triplettzustand zerfällt, entstehen unterschiedliche Moleküle. Das Verhältnis der unterschiedlichen Moleküle wird durch den Neigungswinkel der Erdmagnetfeldlinien beeinflusst. Das Verhältnis der Zerfallsprodukte gibt den Organismen die Orientierungsinformation.[120]

Zudem gibt es weitere quantenbiologische Theorien zu biologischen Prozessen, auf die hier nicht näher eingegangen wird, die deshalb aber nicht weniger interessant sind. Unter anderem ist der Einfluss der Quantenmechanik auf den Geruchssinn[121], Sehsinn[122] und das Gehirn[123] Gegenstand der aktuellen quantenbiologischen Forschung.

6. Literaturverzeichnis

1. Hohmann-Marriott, M. F. & Blankenship, R. E. Evolution of Photosynthesis. *Annu. Rev. Plant Biol.* **62**, 515–548 (2011).
2. Green, M. A. *et al.* Solar cell efficiency tables (Version 55). *Prog. Photovolt. Res. Appl.* **28**, 3–15 (2020).
3. Wagemann, H.-G. & Eschrich, H. *Photovoltaik*. (Vieweg + Teubner, 2013).
4. Archer, D., Rahmstorf, S. & Library, E. *The Climate Crisis: An Introductory Guide to Climate Change*. (Cambridge University Press, 2010).
5. Kim, Y. *et al.* Quantum Biology: An Update and Perspective. *Quantum Rep.* **3**, 80–126 (2021).
6. Engel, G. S. *et al.* Evidence for wavelike energy transfer through quantum coherence in photosynthetic systems. *Nature* **446**, 782–786 (2007).
7. Kautsky, H. & Hirsch, A. Neue Versuche zur Kohlensäureassimilation. *Naturwissenschaften* **19**, 964–964 (1931).
8. Gradmann, U. Gekoppelte Interferenzfilter. *Opt. Acta Int. J. Opt.* **3**, 30–35 (1956).
9. Demtröder, W. & Demtröder, W. *Elektrizität und Optik: mit 11 Farbtafeln, 17 Tabellen, zahlreichen durchgerechneten Beispielen und 143 Übungsaufgaben mit ausführlichen Lösungen*. (Springer, 2004).
10. Madey, T. E., Faradzhev, N. S., Yakshinskiy, B. V. & Edwards, N. V. Surface phenomena related to mirror degradation in extreme ultraviolet (EUV) lithography. *Appl. Surf. Sci.* **253**, 1691–1708 (2006).
11. Corzine, S. W., Geels, R. S., Scott, J. W., Yan, R.-H. & Coldren, L. A. Design of Fabry-Perot surface-emitting lasers with a periodic gain structure. *IEEE J. Quantum Electron.* **25**, 1513–1524 (1989).
12. Schäfer, C., Ruggenthaler, M., Appel, H. & Rubio, A. Modification of excitation and charge transfer in cavity quantum-electrodynamical chemistry. *Proc. Natl. Acad. Sci.* **116**, 4883–4892 (2019).
13. Lather, J., Bhatt, P., Thomas, A., Ebbesen, T. W. & George, J. Cavity Catalysis by Cooperative Vibrational Strong Coupling of Reactant and Solvent Molecules. *Angew. Chem. Int. Ed.* **58**, 10635–10638 (2019).
14. Vergauwe, R. M. A. *et al.* Modification of Enzyme Activity by Vibrational Strong Coupling of Water. *Angew. Chem. Int. Ed.* **58**, 15324–15328 (2019).
15. Galego Pascual, J. Theory of Polaritonic Chemistry. in *Polaritonic Chemistry* 87–98 (Springer International Publishing, 2020). doi:10.1007/978-3-030-48698-3_4.

16. Herrera, F. & Owrutsky, J. Molecular polaritons for controlling chemistry with quantum optics. *J. Chem. Phys.* **152**, 100902 (2020).

17. Fox, M. *Quantum optics: an introduction*. (Oxford University Press, 2006).

18. Kyaw, T. H. Ultrastrong Light–Matter Interaction. in *Towards a Scalable Quantum Computing Platform in the Ultrastrong Coupling Regime* 33–45 (Springer International Publishing, 2019). doi:10.1007/978-3-030-19658-5_3.

19. Krebsfälle Deutschland. *Pressemitteilung Nr. N 010 vom 3. Februar 2021* https://www.destatis.de/DE/Presse/Pressemitteilungen/2021/02/PD21_N010_231.html (2021).

20. Agostinis, P., Vantieghem, A., Merlevede, W. & de Witte, P. A. M. Hypericin in cancer treatment: more light on the way. *Int. J. Biochem. Cell Biol.* **34**, 221–241 (2002).

21. Liu, Q. *et al.* Hypericin: Single Molecule Spectroscopy of an Active Natural Drug. *J. Phys. Chem. A* **124**, 2497–2504 (2020).

22. Reider, G. A. *Photonik*. (Springer Vienna, 2012). doi:10.1007/978-3-7091-1521-3.

23. Demtröder, W. *Laserspektroskopie 1*. (Springer Berlin Heidelberg, 2011). doi:10.1007/978-3-642-21306-9.

24. Konrad, A., Metzger, M., Kern, A. M., Brecht, M. & Meixner, A. J. Controlling the dynamics of Förster resonance energy transfer inside a tunable sub-wavelength Fabry–Pérot-resonator. *Nanoscale* **7**, 10204–10209 (2015).

25. Lalueza, P., Monzón, M., Arruebo, M. & Santamaría, J. Bactericidal effects of different silver-containing materials. *Mater. Res. Bull.* **46**, 2070–2076 (2011).

26. Agranovich, V. M. Microcavity Polaritons in Materials with Weak Intermolecular Interaction. 9 (2002).

27. Purcell, E. M. Spontaneous Emission Probabilities at Radio Frequencies. in *Confined Electrons and Photons: New Physics and Applications* (eds. Burstein, E. & Weisbuch, C.) 839–839 (Springer US, 1995). doi:10.1007/978-1-4615-1963-8_40.

28. Kern, A. M. *et al.* Enhanced single-molecule spectroscopy in highly confined optical fields: from λ/2-Fabry–Pérot resonators to plasmonic nano-antennas. *Chem Soc Rev* **43**, 1263–1286 (2014).

29. Yamamoto, Y., Tassone, F. & Cao, H. *Semiconductor cavity quantum electrodynamics*. (Springer, 2000).

30. Gerry, C. & Knight, P. Introductory Quantum Optics. 333.

31. Junginger, A. *et al.* Tunable strong coupling of two adjacent optical λ/2 Fabry-Pérot microresonators. *Opt. Express* **28**, 485 (2020).

32. Nick, P. *et al. Modellorganismen*. (Springer Berlin Heidelberg, 2019). doi:10.1007/978-

3-662-54868-4.

33. Yu, J. *et al.* Synechococcus elongatus UTEX 2973, a fast growing cyanobacterial chassis for biosynthesis using light and CO2. *Sci. Rep.* **5**, (2015).

34. Sagan, L. On the Origin of Mitosing Cdls. 56.

35. Mueller-Klieser, W. Three-dimensional cell cultures: from molecular mechanisms to clinical applications. *Am. J. Physiol.-Cell Physiol.* **273**, C1109–C1123 (1997).

36. Christen, P., Jaussi, R. & Benoit, R. *Biochemie und Molekularbiologie*. (Springer Berlin Heidelberg, 2016). doi:10.1007/978-3-662-46430-4.

37. Matyssek, R. & Herppich, W. B. Experimentelle Pflanzenökologie: Chlorophyllfluoreszenzanalyse. in *Handbuch der Geodäsie* (eds. Freeden, W. & Rummel, R.) 1–56 (Springer Berlin Heidelberg, 2018). doi:10.1007/978-3-662-53493-9_13-1.

38. *Löffler/Petrides Biochemie und Pathobiochemie*. (Springer Berlin Heidelberg, 2014). doi:10.1007/978-3-642-17972-3.

39. Vinyard, D. J., Ananyev, G. M. & Charles Dismukes, G. Photosystem II: The Reaction Center of Oxygenic Photosynthesis. *Annu. Rev. Biochem.* **82**, 577–606 (2013).

40. Ort, D. R. & Yocum, C. F. *Oxygenic Photosynthesis: The Light Reactions*. (Springer Netherlands, 2006).

41. Heldt, H. W. & Piechulla, B. *Pflanzenbiochemie*. (Springer Berlin Heidelberg, 2015). doi:10.1007/978-3-662-44398-9.

42. Dekker, J. P. & Boekema, E. J. Supramolecular organization of thylakoid membrane proteins in green plants. *Biochim. Biophys. Acta BBA - Bioenerg.* **1706**, 12–39 (2005).

43. Caffarri, S., Tibiletti, T., Jennings, R. & Santabarbara, S. A Comparison Between Plant Photosystem I and Photosystem II Architecture and Functioning. *Curr. Protein Pept. Sci.* **15**, 296–331 (2014).

44. Baniulis, D., Yamashita, E., Zhang, H., Hasan, S. S. & Cramer, W. A. Structure-Function of the Cytochrome b_6f Complex †. *Photochem. Photobiol.* **84**, 1349–1358 (2008).

45. Hope, A. B. Electron transfers amongst cytochrome f, plastocyanin and photosystem I: kinetics and mechanisms. *Biochim. Biophys. Acta BBA - Bioenerg.* **1456**, 5–26 (2000).

46. Kurisu, G. Structure of the Cytochrome b6f Complex of Oxygenic Photosynthesis: Tuning the Cavity. *Science* **302**, 1009–1014 (2003).

47. Graan, T. & Ort, D. R. Initial events in the regulation of electron transfer in chloroplasts. The role of the membrane potential. *J. Biol. Chem.* **258**, 2831–2836 (1983).

48. Komenda, J., Koblížek, M. & Prašil, O. Characterization of processes responsible for the distinct effect of herbicides DCMU and BNT on Photosystem II photoinactivation in cells

of the cyanobacterium Synechococcus sp. PCC 7942. 10.

49. Busch, A. & Hippler, M. The structure and function of eukaryotic photosystem I. *Biochim. Biophys. Acta BBA - Bioenerg.* **1807**, 864–877 (2011).

50. Mullineaux, C. W. State transitions: an example of acclimation to low-light stress. *J. Exp. Bot.* **56**, 389–393 (2004).

51. Mullineaux, C. W. Excitation energy transfer from phycobilisomes to Photosystem I in a cyanobacterium. *Biochim. Biophys. Acta BBA - Bioenerg.* **1100**, 285–292 (1992).

52. Grossman, A. R., Schaefer, M. R., Chiang, G. G. & Collier, J. L. The Phycobilisome, a Light-Harvesting Complex Responsive to Environmental Conditionst. *MICROBIOL REV* **57**, 25 (1993).

53. Hoober, J. K., Eggink, L. L. & Chen, M. Chlorophylls, ligands and assembly of light-harvesting complexes in chloroplasts. *Photosynth. Res.* **94**, 387–400 (2007).

54. Albertsson, P.-Å. A quantitative model of the domain structure of the photosynthetic membrane. *Trends Plant Sci.* **6**, 349–354 (2001).

55. Cao, J. *et al.* Quantum biology revisited. *Sci. Adv.* **6**, eaaz4888 (2020).

56. Fleming, G. R., Scholes, G. D. & Cheng, Y.-C. Quantum effects in biology. *Procedia Chem.* **3**, 38–57 (2011).

57. Govindjee, Björn, L. O. & Nickelsen, K. Evolution of the Z-Scheme of Electron Transport in Oxygenic Photosynthesis. in *Photosynthesis Research for Food, Fuel and the Future* 827–833 (Springer Berlin Heidelberg, 2013). doi:10.1007/978-3-642-32034-7_175.

58. Zass, E. Untersuchungen zum Einbau des Magnesiums in Liganden der Chlorophyll-Reihe. 184 S. (ETH Zurich, 1977). doi:10.3929/ETHZ-A-000126354.

59. Kaim, W. & Schwederski, B. Metalle im Zentrum der Photosynthese: Magnesium und Mangan. in *Bioanorganische Chemie: Zur Funktion chemischer Elemente in Lebensprozessen* 58–86 (Vieweg+Teubner Verlag, 2005). doi:10.1007/978-3-663-01605-2_4.

60. Kondou, Y., Nakazawa, M., Higashi, S., Watanabe, M. & Manabe, K. Equal-quantum Action Spectra Indicate Fluence-rate-selective Action of Multiple Photoreceptors for Photomovement of the Thermophilic Cyanobacterium Synechococcus elongatus¶. *Photochem. Photobiol.* **73**, 90–95 (2007).

61. Barber, J. Photosynthetic energy conversion: natural and artificial. *Chem Soc Rev* **38**, 185–196 (2009).

62. Kennis, J. T. M. *et al.* Light Harvesting by Chlorophylls and Carotenoids in the Photosystem I Core Complex of *Synechococcus elongatus* : A Fluorescence Upconversion Study. *J. Phys. Chem. B* **105**, 4485–4494 (2001).

63. Wormit, M. & Dreuw, A. Quantum chemical insights in energy dissipation and carotenoid radical cation formation in light harvesting complexes. *Phys. Chem. Chem. Phys.* **9**, 2917 (2007).

64. Lahmi, R. *et al.* Alanine Dehydrogenase Activity Is Required for Adequate Progression of Phycobilisome Degradation during Nitrogen Starvation in Synechococcus elongatus PCC 7942. *J. Bacteriol.* **188**, 5258–5265 (2006).

65. Damjanović, A., Vaswani, H. M., Fromme, P. & Fleming, G. R. Chlorophyll Excitations in Photosystem I of *Synechococcus elongatus*. *J. Phys. Chem. B* **106**, 10251–10262 (2002).

66. Krause, G. H. & Weis, E. Chlorophyll Fluorescence and Photosynthesis: The Basics. 37.

67. Coles, D. *et al.* A Nanophotonic Structure Containing Living Photosynthetic Bacteria. *Small* **13**, 1701777 (2017).

68. van Kooten, O. & Snel, J. F. H. The use of chlorophyll fluorescence nomenclature in plant stress physiology. *Photosynth. Res.* **25**, 147–150 (1990).

69. Herppich, W. B. *et al.* Photosynthetic responses to CO2 concentration and photon fluence rates in the CAM-cycling plant Delosperma tradescantioides (Mesembryanthemaceae). *New Phytol.* **138**, 433–440 (1998).

70. Tóth, S. Z., Schansker, G. & Strasser, R. J. In intact leaves, the maximum fluorescence level (FM) is independent of the redox state of the plastoquinone pool: A DCMU-inhibition study. *Biochim. Biophys. Acta BBA - Bioenerg.* **1708**, 275–282 (2005).

71. *Chlorophyll a fluorescence: a signature of photosynthesis*. (Kluwer Academic, 2004).

72. Baker, N. R. A possible role for photosystem II in environmental perturbations of photosynthesis. *Physiol. Plant.* **81**, 563–570 (1991).

73. Björkman, O. & Demmig, B. Photon yield of O2 evolution and chlorophyll fluorescence characteristics at 77 K among vascular plants of diverse origins. *Planta* **170**, 489–504 (1987).

74. *Confocal microscopy methods and protocols*. (Humana Press, 1999).

75. Cremer, C. Lichtmikroskopie unterhalb des Abbe-Limits. Lokalisationsmikroskopie. *Phys. Unserer Zeit* **42**, 21–29 (2011).

76. Jodl, H.-J. *Rayleigh-Kriterium: Das Auflösungsvermögen optischer Instrumente*. (2007).

77. Lakowicz, J. R. *Principles of fluorescence spectroscopy*. (Springer, 2006).

78. Cole, R. W., Jinadasa, T. & Brown, C. M. Measuring and interpreting point spread functions to determine confocal microscope resolution and ensure quality control. *Nat. Protoc.* **6**, 1929–1941 (2011).

79. Cox, G. & Sheppard, C. J. R. Practical limits of resolution in confocal and non-linear microscopy. *Microsc. Res. Tech.* **63**, 18–22 (2004).

80. Bhatti, A. F., Choubeh, R. R., Kirilovsky, D., Wientjes, E. & van Amerongen, H. State transitions in cyanobacteria studied with picosecond fluorescence at room temperature. *Biochim. Biophys. Acta BBA - Bioenerg.* **1861**, 148255 (2020).

81. Fišerová, E. & Kubala, M. Mean fluorescence lifetime and its error. *J. Lumin.* **132**, 2059–2064 (2012).

82. Jordan, P. Die Quantenmechanik und die Grundprobleme der Biologie und Psychologie. *Naturwissenschaften* **20**, 815–821 (1932).

83. Bohr, N. *Foundations of quantum physics II (1933-1958)*. vol. 7 (North-Holland Publishing Company, 1996).

84. Schrödinger, E. *What Is Life?* (Cambridge University Press, 1944).

85. McFadden, J. & Al-Khalili, J. The origins of quantum biology. *Proc. R. Soc. Math. Phys. Eng. Sci.* **474**, 20180674 (2018).

86. Löwdin, P.-O. Proton Tunneling in DNA and its Biological Implications. *Rev. Mod. Phys.* **35**, 724–732 (1963).

87. De Vault, D. & Chance, B. Studies of Photosynthesis Using a Pulsed Laser. *Biophys. J.* **6**, 825–847 (1966).

88. Wiltschko, W. & Wiltschko, R. Magnetic Compass of European Robins. *Science* **176**, 62–64 (1972).

89. Emlen, S. T., Wiltschko, W., Demong, N. J., Wiltschko, R. & Bergman, S. Magnetic Direction Finding: Evidence for Its Use in Migratory Indigo Buntings. *Science* **193**, 505–508 (1976).

90. Schulten, K., Staerk, H., Weller, A., Werner, H.-J. & Nickel, B. Magnetic Field Dependence of the Geminate Recombination of Radical Ion Pairs in Polar Solvents. *Z. Für Phys. Chem.* **101**, 371–390 (1976).

91. Schulten, K. & Weller, A. Exploring fast electron transfer processes by magnetic fields. *Biophys. J.* **24**, 295–305 (1978).

92. Ritz, T., Adem, S. & Schulten, K. A Model for Photoreceptor-Based Magnetoreception in Birds. *Biophys. J.* **78**, 707–718 (2000).

93. Davydov, A. S. (Aleksandr S., 1912-. *Biology & quantum mechanics / by A.S. Davydov ; translated by D. Oliver*. (Pergamon Press, 1982).

94. Nisbet, E. G. & Nisbet, R. E. R. Methane, oxygen, photosynthesis, rubisco and the regulation of the air through time. *Philos. Trans. R. Soc. B Biol. Sci.* **363**, 2745–2754 (2008).

95. Buick, R. When did oxygenic photosynthesis evolve? *Philos. Trans. R. Soc. B Biol. Sci.* **363**, 2731–2743 (2008).

96. Pfalzner, S. *et al.* The formation of the solar system. *Phys. Scr.* **90**, 068001 (2015).

97. Dodd, M. S. *et al.* Evidence for early life in Earth's oldest hydrothermal vent precipitates. *Nature* **543**, 60–64 (2017).

98. Pernklau, E. Mineralogie; Eine einführung in die spezielle mineralogie, petrologie und lagerstättenkunde. *Earth-Sci. Rev.* **23**, 65–66 (1986).

99. Forster, Th. Energiewanderung und Fluoreszenz. *Naturwissenschaften* **33**, 166–175 (1946).

100. Leonas Valkunas, Herbert Van Amerongen, & Rienk Van Grondelle. *Photosynthetic Excitons*. (World Scientific, 2000).

101. Fleming, G. R. & Scholes, G. D. Quantum mechanics for plants. *Nature* **431**, 256–257 (2004).

102. Jang, S., Newton, M. D. & Silbey, R. J. Multichromophoric Förster Resonance Energy Transfer from B800 to B850 in the Light Harvesting Complex 2: Evidence for Subtle Energetic Optimization by Purple Bacteria †. *J. Phys. Chem. B* **111**, 6807–6814 (2007).

103. Ishizaki, A. & Fleming, G. R. On the adequacy of the Redfield equation and related approaches to the study of quantum dynamics in electronic energy transfer. *J. Chem. Phys.* **130**, 234110 (2009).

104. Novoderezhkin, V. I. & van Grondelle, R. Physical origins and models of energy transfer in photosynthetic light-harvesting. *Phys. Chem. Chem. Phys.* **12**, 7352 (2010).

105. Collini, E. *et al.* Coherently wired light-harvesting in photosynthetic marine algae at ambient temperature. *Nature* **463**, 644–647 (2010).

106. Panitchayangkoon, G. *et al.* Long-lived quantum coherence in photosynthetic complexes at physiological temperature. *Proc. Natl. Acad. Sci.* **107**, 12766–12770 (2010).

107. Ishizaki, A. & Fleming, G. R. Theoretical examination of quantum coherence in a photosynthetic system at physiological temperature. *Proc. Natl. Acad. Sci.* **106**, 17255–17260 (2009).

108. Hussels, M. & Brecht, M. Effect of Glycerol and PVA on the Conformation of Photosystem I. *Biochemistry* **50**, 3628–3637 (2011).

109. Scholes, G. D. *et al.* Using coherence to enhance function in chemical and biophysical systems. *Nature* **543**, 647–656 (2017).

110. Calegari, F. *et al.* Charge migration induced by attosecond pulses in bio-relevant molecules. *J. Phys. B At. Mol. Opt. Phys.* **49**, 142001 (2016).

111. Mukamel, S., Healion, D., Zhang, Y. & Biggs, J. D. Multidimensional Attosecond Resonant X-Ray Spectroscopy of Molecules: Lessons from the Optical Regime. *Annu. Rev. Phys. Chem.* **64**, 101–127 (2013).

112. Mančal, T. A decade with quantum coherence: How our past became classical and the future turned quantum. *Chem. Phys.* **532**, 110663 (2020).

113. Ishizaki, A. & Fleming, G. R. Quantum superpositions in photosynthetic light harvesting: delocalization and entanglement. *New J. Phys.* **12**, 055004 (2010).

114. Dostál, J. *et al.* Direct observation of exciton–exciton interactions. *Nat. Commun.* **9**, 2466 (2018).

115. Kamerlin, S. C. L. & Warshel, A. An analysis of all the relevant facts and arguments indicates that enzyme catalysis does *not* involve large contributions from nuclear tunneling: DOES TUNNELING *REALLY* CONTRIBUTE TO ENZYME CATALYSIS? *J. Phys. Org. Chem.* **23**, 677–684 (2010).

116. Bothma, J. P., Gilmore, J. B. & McKenzie, R. H. The role of quantum effects in proton transfer reactions in enzymes: quantum tunneling in a noisy environment? *New J. Phys.* **12**, 055002 (2010).

117. Trixler, F. Quantum Tunnelling to the Origin and Evolution of Life. *Curr. Org. Chem.* **17**, 1758–1770 (2013).

118. Wiltschko, W. & Wiltschko, R. Migratory orientation of European Robins is affected by the wavelength of light as well as by a magnetic pulse. *J. Comp. Physiol. A* **177**, (1995).

119. Wiltschko, W., Munro, U., Ford, H. & Wiltschko, R. Red light disrupts magnetic orientation of migratory birds. *Nature* **364**, 525–527 (1993).

120. Kerpal, C. *et al.* Chemical compass behaviour at microtesla magnetic fields strengthens the radical pair hypothesis of avian magnetoreception. *Nat. Commun.* **10**, 3707 (2019).

121. Lloyd, S. Quantum coherence in biological systems. *J. Phys. Conf. Ser.* **302**, 012037 (2011).

122. Chakravarthi, R., Rajagopal, A. K. & Devi, A. R. U. Quantum Mechanical Basis of Vision. *ArXiv08040190 Q-Bio* (2008).

123. Adams, B. & Petruccione, F. Quantum effects in the brain: A review. *AVS Quantum Sci.* **2**, 022901 (2020).

7. Manuskripte und Veröffentlichungen in wissenschaftlichen Fachzeitschriften

7.1 Strong coupling between an optical microcavity and photosystems in single living cyanobacteria (veröffentlicht)

Received: 22 April 2021 | Revised: 15 October 2021 | Accepted: 8 November 2021

DOI: 10.1002/jbio.202100136

RESEARCH ARTICLE

JOURNAL OF BIOPHOTONICS

Strong coupling between an optical microcavity and photosystems in single living cyanobacteria

Tim Rammler[1,2] | Frank Wackenhut[1*] | Sven zur Oven-Krockhaus[1,2] | Johanna Rapp[3] | Karl Forchhammer[3] | Klaus Harter[2] | Alfred J. Meixner[1*]

[1]Institute of Physical and Theoretical Chemistry, University of Tübingen, Tübingen, Germany

[2]Center for Plant Molecular Biology, University of Tübingen, Tübingen, Germany

[3]Interfaculty Institute of Microbiology and Infection Medicine, University of Tübingen, Tübingen, Germany

***Correspondence**
Frank Wackenhut and Alfred J. Meixner, Institute of Physical and Theoretical Chemistry, University of Tübingen, Tübingen, Germany.
Email: frank.wackenhut@uni-tuebingen.de (F. W.) and alfred.meixner@uni-tuebingen.de (A. J. M.)

Funding information
Deutsche Forschungsgemeinschaft, Grant/Award Numbers: SFB 1101/Z02, SFB 1101/D02, HA 2146/23-1, ME 1600/13-3; VW foundation

Abstract

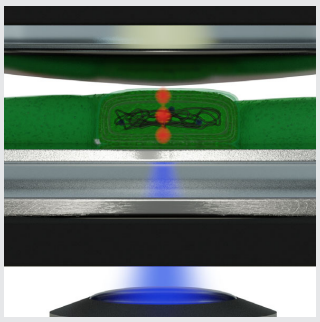

The first step in photosynthesis is an extremely efficient energy transfer mechanism that led to the debate to which extent quantum coherence may be involved in the energy transfer between the photosynthetic pigments. In search of such a coherent behavior, we have embedded living cyanobacteria between the parallel mirrors of an optical microresonator irradiated with low intensity white light. As a consequence, we observe vacuum Rabi splitting in the transmission and fluorescence spectra as a result of strong light matter coupling of the chlorophyll *a* molecules in the photosystems (PSs) and the cavity modes. The Rabi-splitting scales with the number of the PSs chlorophyll *a* pigments involved in strong coupling indicating a delocalized polaritonic state. Our data provide evidence that a delocalized polaritonic state can be established between the chlorophyll *a* molecule of the PSs in living cyanobacterial cells at ambient conditions in a microcavity.

1 | INTRODUCTION

In photosynthesis, light energy is absorbed and converted into relatively stable chemical products by well organized, dynamic, membrane-integral pigment-protein complexes called photosystems for long-term chemical energy storage.[1,2] Photosynthetic complexes are optimized to capture photons from solar light and transmit the excitation energy from peripheral pigments to the photosynthetic reaction center with an extremely high efficiency (close to 100%[3]). They consist of a collection of pigment molecules, such as chlorophylls and carotenoids that are arranged by a protein scaffold in a way that near-field dipole coupling is possible.[3] When interacting with light they no longer act as independent excited molecules, but coupling between them results in collective excitations called excitons, whose wave function extends over several pigment units.[4,5]

The observation of oscillatory intensity modulations of ultrafast photon echoes from isolated photosynthetic complexes of *Chlorobium* at cryogenic temperatures and under almost physiological conditions led to the hypothesis that quantum coherence could be a possible explanation for the efficient energy transfer.[4,6–10] Recent investigations

have revealed that both electronic and vibrational coherences are involved in primary energy transfer in bacterial reaction centers.[11,12] However, excitation in ultrafast time-resolved laser spectroscopy, as it was done in the experiments mentioned above, is pulsed and coherent, while perception of white light under ambient conditions occurs continuously over the course of minutes to hours via incoherent photons. As a consequence, the energy transfer in the photosynthetic machinery must operate on the basis of independent single photons. A possible alternative way to ultrashort laser pulses in time domain spectroscopy is to observe coherent light-matter interaction in the frequency domain by placing the respective chromophores in a resonant optical microresonator to achieve hybrid light-matter states.[13] Thus, we have enclosed living cyanobacteria (*Synechococcus elongatus*) in the confined electromagnetic field between the two mirrors of the microresonator to probe their optical properties in vivo. Using low intensity white light irradiation, we actually observe a symmetric splitting of the transmission band, which is a consequence of coherent excitonic coupling between the chlorophyll *a* pigments within photosystems (PSs) and the cavity field via the formation of a delocalized polaritonic state in vivo. We suspect that this coupling could lead to an explanation for the very efficient photosynthetic energy transfer within the PSs of cyanobacteria.

2 | RESULTS

To study possible quantum effects in the PSs of living organisms at ambient conditions, we embedded cells of *S. elongatus* (strain PCC 7942) in an optical microcavity. In contrast to sulfur bacteria,[4,14] *S. elongatus* performs oxygenic photosynthesis. The photosynthesis of this cyanobacterial species is intensively studied with respect to biochemistry, structural organization and dynamics

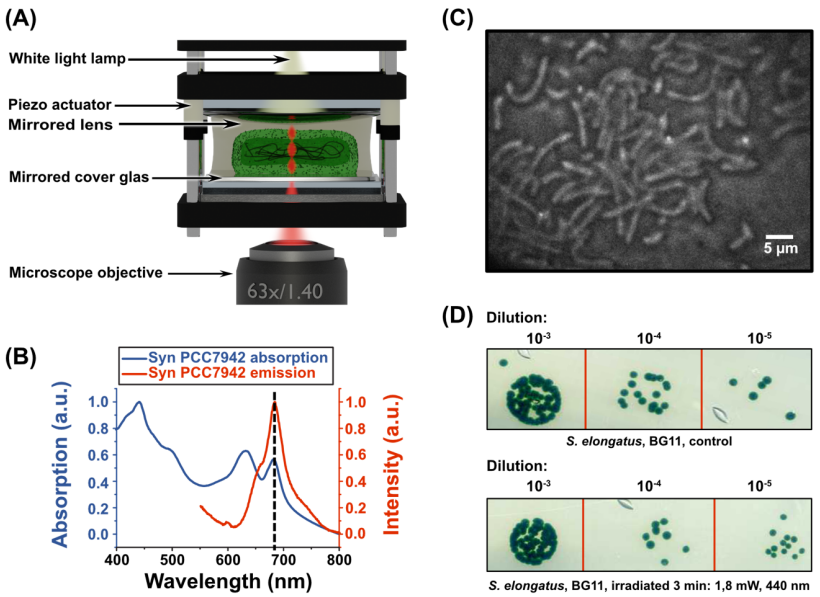

FIGURE 1 The spectral properties of the photosynthetic pigments of *S. elongatus* cells and a Fabry-Pérot microresonator. The survival of *S. elongatus* cells is not impaired by the light conditions prevailing in the microcavity. (A) Scheme of the Fabry-Pérot microcavity, which consists of two partially transparent mirrors. The distance between the mirrors can be fine-tuned with piezoelectric actuators. Due to constructive and destructive interference, only wavelengths fulfilling the resonance condition of the cavity are transmitted. The bacteria are placed in an agarose matrix inside the cavity. (B) Normalized absorption (blue) and fluorescence (red) spectra ($\lambda_{ex} = 440$ nm) of *S. elongatus* cells located inside the microcavity. The dashed black line indicates the wavelength where the bacteria emit and absorb photons of the same wavelength. (C) Light microscopy image of *S. elongatus* cells inside the microcavity. (D) Spot assay[16] of *S. elongatus* cells in BG11 medium. Top: Non-irradiated control in a dilution series (1:10), initial concentration: $OD_{750} = 0.5$. Below: Irradiated sample in a dilution series (1:10), initial concentration: $OD_{750} = 0.5$. The bacteria were irradiated with an expanded laser beam at adjusted intensity before the preparation of a spot assay. The irradiation conditions were comparable to those in the microcavity. The comparable growth rate indicates a negligible impact of the typical irradiation during the experiments

of the photosynthetic machinery[1,15] and therefore well-suited for the study of quantum physical processes in vivo at ambient conditions.

Our Fabry-Pérot optical microresonator (quality factor, $Q = 98$) consists of two partially transparent mirrors (Figure 1A). Their distance can be precisely adjusted with a piezo actuator to control the resonance condition of the microcavity. Compared to previous works,[14] we have chosen silver mirrors with a large layer thickness to achieve a stronger interaction between the microcavity and the cyanobacteria. More details about the experimental set up are given in the supporting information (Appendix S1). Transmission spectra were acquired from below via a high numerical aperture (NA) objective lens (NA = 1.4), while the microcavity was irradiated by a continuously emitting white light source from above (Figure 1A). Additionally, we irradiated the sample with a laser from below to detect strong coupling in the emission spectrum of individual bacteria, which is made possible by the small focal spot size of the high NA objective. As shown in Figure 1B, the in vivo absorption (blue line) shows the typical chlorophyll *a* maximum at around 680 nm due to a red-shift of protein-bound chlorophyll.[17] The emission spectrum at 440 nm excitation reveals again a maximum at around 680 nm. This fluorescence emission can be predominantly assigned to the chlorophyll *a* pigments of the PSs as the fluorescence of the phycobilisomes is almost completely quenched in vivo.[15,18,19] However, the observed fluorescence emission can predominantly be attributed to the chlorophyll *a* molecules of photosystem 2 (PS2), as the photosystem 1 (PS1) acts as a very efficient energy trap at ambient temperature.[20] The cavity resonance can be tuned across the absorption and emission maximum (see Figure S1), allowing efficient optical coupling between the cavity modes and the cyanobacteria. Remarkably, the absorption and emission spectra of the photosynthetic pigments largely overlap in the 680 nm region (Figure 1B), demonstrating that the cyanobacteria are able to reabsorb their own emitted light. This photophysical feature of *S. elongatus* is a prerequisite for the potential coupling of the photosynthetic pigments to an optical field confined in a microcavity.

The survival rate of the cyanobacteria in the microcavity was assayed to examine the possible impact of the laser irradiation on the embedded organisms (Figure 1C). Since only a single bacterium is exposed to the focused laser irradiation inside the cavity at a time, which cannot be isolated after the experiment, we have designed an assay to analyze comparable irradiation conditions by embedding a cyanobacterial culture in a low-melting agarose matrix outside the cavity. The cyanobacteria were then exposed to light conditions (440 *nm*, 1000 µmol photons s^{-1} m^{-2}, 3 minutes) similar to those prevailing in the cavity, while a non-irradiated culture served as a control and the survivability was analyzed by a spot assay (see supporting information [Appendix S1] for details). No growth difference between the irradiated and non-irradiated sample was observed (Figure 1D), indicating that the light conditions in the microcavity have no discernible impact on the cyanobacterial survivability.

To determine whether the microcavity influences the cyanobacterial photosynthetic system in vivo, fluorescence lifetimes (FLTs)[21] of its pigments in single bacteria were acquired.

The light-harvesting pigments of the PSs serve to rapidly and efficiently transfer light energy from the peripheral pigments to the reaction center, therefore, the fluorescence signal of cyanobacteria is weak. Transfer and trapping of the excitation energy in the PSs lead to a fast non-exponential fluorescence decay, which can be observed from live cyanobacteria with a wide distribution of FLT components from short ones in the low and mid picosecond range and slow components in the low nanosecond range.[22] The spontaneous emission rate of a chromophore can be increased or decreased by placing it in a microcavity and tuning it in-resonance or off-resonance with the chromophore emission. This is known as Purcell effect[23,24] leading to shorter or longer FLTs, respectively. The long-lived FLT component originates from particularly those PS2 chlorophyll *a* pigments where the excitation energy is trapped in an emitting state and can therefore be analyzed in vivo for three cases: (a) free space (outside of the cavity), (b) inside the cavity in off-resonance mode and (c) inside the cavity in resonance mode. Due to the extreme efficient energy transfer of PS1, its FLT is around 20 ps,[25] which is much shorter than the temporal resolution of the used time correlated single photon counting equipment. Hence, we assume that the observed FLTs are those of PS2. Short laser pulses ($\lambda_{ex} = 440$ nm) with pulse durations of less than 80 ps and a pulse rate of 80 MHz were used. The PS2 chlorophyll *a* pigments irradiated in free space (i) reveal a FLT value of $\tau_I = (0.26 \pm 0.006)$ ns ((i) in Figure 2) and a slightly larger value of $\tau_I = (0.29 \pm 0.016)$ ns in the off-resonant microcavity ((ii) in Figure 2). In contrast, the FLT of the PS2 pigments in the resonant microcavity (iii) decreased to $\tau_I = (0.16 \pm 0.006)$ ns and was significantly shorter compared with the data obtained in free space or in the off-resonant cavity. This result is consistent with the Purcell effect[23] of isolated pigments and demonstrates that the microcavity has a noticeable impact on the PS2 photosynthetic processes in single living cyanobacteria.

In general, the interaction of a quantum system with the optical field in a microcavity can be separated in the weak and strong coupling regime. In the weak coupling regime, the individual damping constants of the cavity

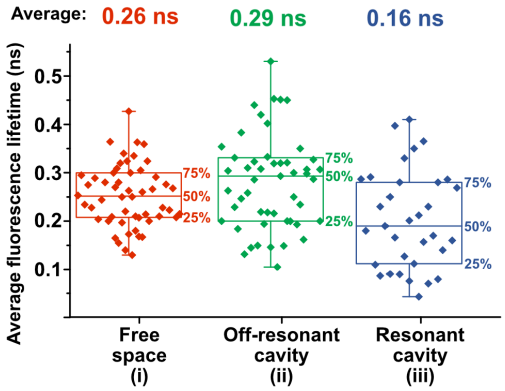

FIGURE 2 The FLT of *S. elongatus* chlorophyll *a* pigments is influenced in vivo by the microcavity. The bacteria were embedded in low-melting agarose and irradiated with short laser pulses ($\lambda_{ex} = 440$ nm) with a duration of less than 80 ps and a repetition rate of 80 MHz. The average intensity-weighted FLTs were recorded in free space ([a], red, n = 53), inside the off-resonance cavity ([b], green, n = 50) or inside the cavity in resonance with the light emission of the cyanobacteria ([c], blue, n = 33). The center line in the box plot indicates the median, box edges show the 75th and 25th percentiles, and whiskers cover the full range of values. A two-tailed t-test confirms a significant difference between the PS2 chlorophyll *a* FLTs for the off-resonant (and without) cavity and the resonant cavity, $p = 2.05 \times 10^{-5}$, ($p = 3.20 \times 10^{-6}$)

and the chlorophyll *a* pigments are larger than the coupling constant. In this case, the microcavity only influences the spontaneous emission rate via the Purcell effect as observed in the FLT analysis (Figure 2). However, if the coupling constant exceeds the individual damping constants, the energy of a photon can be coherently cycled back and forth between the oscillating electromagnetic field in the microcavity and the induced polarization formed by a large number of coherent electronically excited chromophores enclosed between the cavity mirrors before it escapes from the cavity; this condition reflects the strong coupling regime.[26] The energy of the photon, which is dispersed in the whole mode volume and shared between the cavity mode and the polarization, is described in quantum electrodynamics as a hybrid light-matter state or polariton.[27–29] In our case, these so-called polaritonic modes are a coherent superposition of the cavity mode and the electronically excited state of the chlorophyll *a* pigments in the PSs. As shown in Figure S2, the back and forth cycling of the photon energy between the electromagnetic field in the microcavity and the polarization in the time domain leads to a splitting in the spectral domain that manifests itself as a double-peaked cavity transmission spectrum with a peak separation referred to as vacuum Rabi splitting, as schematically illustrated in Figure 3A,B.

To study vacuum Rabi splitting, due to a polaritonic mode in the PSs of a living cyanobacterium and the optical field in the microcavity, we simulated and experimentally investigated the dispersive behavior of the coupled system.

The dashed lines in Figure 3A,B illustrate the simulated uncoupled emission of the cyanobacteria PSs (green) and the cavity mode (red). Figure 3A illustrates the case when there is no spectral overlap between them. The transmission spectrum of such a coupled, but off-resonant system, is similar to that of the uncoupled cavity mode. Conversely, when the cavity mode approaches the spectral position of the chlorophyll *a* emission, a splitting into two polaritonic modes is visible (Figure 3B, blue line). Figure 3C represents the simulated spectral shift $\Delta\lambda$ of the coupled modes relative to the uncoupled modes. The shift caused by strong coupling is largest when the cavity is in resonance with the chlorophyll *a* emission, leading to a symmetric double-peaked cavity transmission spectrum. The occurrence of such a spectral gap between the two polaritonic modes is called vacuum Rabi splitting. Mathematically, such a coupled system can be modeled by two coupled damped harmonic oscillators, as described in the supporting information (Appendix S1) or in Reference 30. First, we want to illustrate in Figure 3D, E the results of the calculation without coupling between the cavity mode and the chlorophyll *a* emission ($\kappa = 0\,eV$). Each line in Figure 3D represents a cavity transmission spectrum, as indicated by the spectrum number, and its intensity is given by the color map. In this simulation, the cavity length gradually increased from top to bottom, leading to a spectral red shift of the cavity resonance. The dashed lines in Figure 3D,E represent the spectral position of the uncoupled chlorophyll *a* emission and the cavity mode, respectively. In the absence of strong coupling, no splitting is observed, even when both modes were tuned to the same resonance wavelength; the chlorophyll *a* emission was only influenced by the Purcell effect (Figure 3E). This changes with strong coupling between the cavity mode and the chlorophyll *a* pigments, with a calculated coupling constant of $\kappa = 0.14$ eV in Figure 3F,G. The calculated cavity transmission spectra in Figure 3F show a clear anti-crossing behavior when the cavity resonance approaches the spectral position of the chlorophyll *a* emission at 680 nm. In the calculated emission spectra in Figure 3G, the mode splitting is less obvious, because it is obscured by the spectrally broad fluorescence background of the chlorophyll *a* pigments that are not strongly coupled to the cavity mode. The uncoupled chlorophyll *a* pigments have their electronic transition dipole moments oriented perpendicular to the polarization and constitute about 2/3 of the total number of chlorophyll *a* pigments. By comparing the simulations in Figure 3D,E with Figure 3F,G, it is

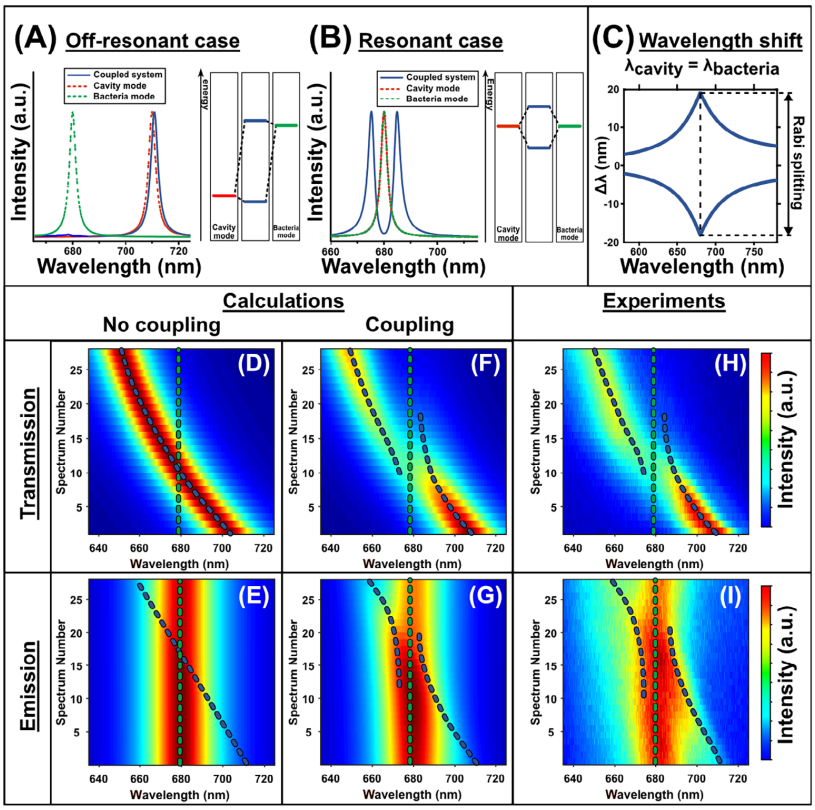

FIGURE 3 Strong coupling between a microcavity and the chlorophyll *a* pigments in living cyanobacteria. (A) represents where the bacteria absorption/emission and the cavity are spectrally separated. The dashed green and red spectra represent the uncoupled bacteria absorption/emission mode and cavity mode. The blue spectrum illustrates the cavity transmission spectrum for the nonresonant but coupled case and is similar to the uncoupled system. The graph on the right illustrates the corresponding energy level scheme. (B) Illustration of the resonant case, where the cavity mode is spectrally overlapping with the emission of the PSs, and two polaritonic modes (blue lines) are clearly visible in the double-peaked cavity transmission spectrum. (C) Spectral shift Δλ of the coupled modes relative to the uncoupled ones. The largest splitting, that is, vacuum Rabi splitting, is observed when the cavity and the chlorophyll *a* pigments of the cyanobacterial PSs are in resonance. (D,E) Simulated cavity transmission/ bacteria emission spectra without coupling as a function of the decreasing mirror distance (indicated by the spectrum number). The dashed green and blue lines are the spectral position of the uncoupled bacteria emission/ cavity resonance, respectively. No anti-crossing can be observed when the cavity mode is tuned across the chlorophyll *a* emission. (F,G) Simulated cavity transmission/ chlorophyll *a* emission spectra including strong coupling between the cavity mode and the emission. Strong coupling is visible in (F,G) by the anti-crossing dispersion, when the cavity mode is close to the emission of the cyanobacterial PSs. (H,I) Experimental cavity transmission/ chlorophyll *a* emission spectrum. Strong coupling can be observed in (H,I) by the anti-crossing dispersion and is in perfect agreement with the simulation in (F,G)

possible to experimentally distinguish between no/weak and strong coupling in the microcavity-cyanobacterial system. Notably, the experimental white light transmission spectra derived from the PSs of living cyanobacteria show a clear anti-crossing behavior when the cavity resonance is tuned over the chlorophyll *a* emission at 680 *nm* (Figure 3H). In the emission spectra (Figure 3I) the splitting is less obvious since it is composed of two types of photons, those that participate in the strong coupling process with the cavity mode and those that escape from the resonator without coupling due to the Purcell effect. The experimental results fit perfectly to the calculated spectra in Figure 3F,G and prove that strong coupling between the microcavity and the chlorophyll *a* pigments is achievable in living cyanobacteria.

According to the Jaynes-Cummings model, the energy splitting ΔE is given by Equation (1) and is proportional to the square root of the number n of chlorophyll *a* pigments that coherently couple to the cavity mode with a coupling constant g_0.[26]

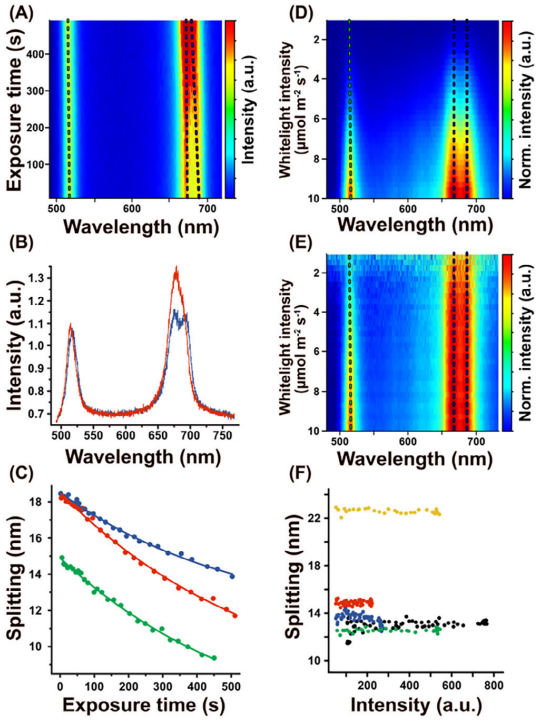

FIGURE 4 Reducing the number of chlorophyll *a* pigments in a cyanobacterium by photobleaching reduces vacuum Rabi splitting and shows that the chlorophyll *a* pigments are coherently coupled in living cyanobacterial cells. (A) Cavity transmission spectra with two cavity modes as a function of the exposure time. One mode shows vacuum Rabi splitting (dashed blue line), while the other is not coupled (dashed green line). The splitting energy, and thus the coupling, is reduced by the continuous irradiation and photobleaching the chlorophyll *a* pigments of the bacterium. (B) First (blue line, $t = 0$ s) and last (red line, $t = 500$ s) spectrum of A. (C) Rabi splitting between the two intensity maxima around 680 nm as a function of the exposure time. Three different, individual bacteria (red, green and blue) in the cavity show the decrease of the vacuum Rabi splitting with increasing bleaching of the chlorophyll a pigments. (D) Cavity transmission spectra with two resonances as a function of the illumination intensity of the white light lamp of 10 μmol photons s^{-1} m^{-2} to 1 μmol photons s^{-1} m^{-2} (corresponding to 28 – 2.8 mWcm^{-2} at 680 nm) from bottom to top. The coupling remains constant while the intensity of the white light lamp is reduced. (E) Intensity normalized version of (D), where each spectrum is normalized to its maximum intensity, to better visualize the constant splitting. (F) Splitting as a function of the white light intensity. At low illumination intensity, five different, individual bacteria in the cavity show that the vacuum Rabi splitting is independent of the light intensity

$$\Delta E = 2\sqrt{n}\hbar g_o \quad (1)$$

Therefore, the splitting energy should decrease when the number of pigments is reduced. This can indeed be achieved in a living cyanobacterium by photobleaching a fraction of the functional chlorophyll *a* pigments by increasing the laser intensity by a factor of 100 as compared to the previous experiments.

As shown in Figure 4A at the beginning the cavity mode at $\lambda = 680$ nm had a spectral dip at the center due to vacuum Rabi splitting. As the photobleaching of the chlorophyll *a* molecules proceeded (Figure 4A, blue dashed line), the energy splitting between the two peaks reduced and disappeared. In contrast, at the same time for the cavity mode at $\lambda = 546$ nm, which has no coupling to the chlorophyll *a* pigments, no changes in intensity or spectral position were visible. This is further illustrated in Figure 4B, where the first (blue line) and the last (red line) spectrum of the spectral series in Figure 4A are shown.

The number of molecules (n in Equation (1)) decreased exponentially by photobleaching as tested at three different locations in the cavity, resulting in a decreased splitting of the coupled modes, which can be fitted to the square root of an exponential decay (Figure 4C). These results demonstrate that the extent of the Rabi splitting depends on the number of chlorophyll *a* pigments effectively participating in polaritonic coupling to the optical mode throughout the entire focal volume.

To reveal the light intensity dependence, white-light transmission spectra were acquired with different excitation intensities of 10 μmol photons s^{-1} m^{-2} down to 1 μmol photons s^{-1} m^{-2} (corresponding to 28.0 – 2.8 mWcm^{-2} measured at 680 nm) in single living cyanobacteria as shown in Figure 4D,E, where the *y*-axis corresponds to different excitation intensities. The resonance mode at $\lambda = 680$ nm, which is strongly coupled to chlorophyll *a*, showed Rabi splitting which remained constant with decreasing white light irradiation intensity (Figure 4D). This was even more obvious in the normalized spectra (Figure 4E), where each spectrum along the *y*-axis was normalized to its maximum intensity. This constant Rabi splitting was observed for different individual cyanobacteria in the sample, as shown in Figure 4F by plotting the Rabi splitting against the intensity of the cavity mode. As a consequence, since the photons used for white-light illumination are completely incoherent, strong coupling must occur even at very low light intensity; or in other words, one resonant photon is already sufficient to induce a polaritonic state between the microcavity and the chlorophyll *a* pigments in vivo.

3 | DISCUSSION

The emission and transmission spectra presented here suggest that there is in vivo strong coupling between the microcavity and the chlorophyll *a* pigments of the

cyanobacterial photosystem. Photo-bleaching experiments confirm that the microcavity couples to about 4.8×10^5 chlorophyll *a* molecules (calculated from the measured splitting and assuming that a chlorophyll molecule has a transition dipole moment of $5.39\,D$ and that the average refractive index of its surroundings is $n = 1.34$,[31] see supporting information [Appendix S1] for calculation) at the same time to form a delocalized polaritonic state. Considering that each PS2 monomer contains 35 chlorophyll *a* molecules and each PS1 monomer 96 chlorophyll *a* molecules[32,33] the experimentally determined coupling of 4.8×10^5 chlorophyll *a* molecules suggests that the majority of the PS bound chlorophyll *a* pigments in the thylakoid membrane of a cyanobacterial cell participate to the interaction with the microcavity. The term vacuum Rabi splitting refers to number of photons in the resonator, which can be zero, indicating that it works at very low light intensities and for the formation of a polaritonic state one single photon is sufficient. The wide delocalization of the polaritonic state suggests that each PS reaction center is optimally supplied with photons also in a low-light environment. To be able to take advantage of the long-range polaritonic state, a complex and dynamic spatial and structural organization of the PS complexes appears to be required, which compensates or makes use of the thermodynamic fluctuations occurring in the ambient environment. The functional implications on the physiology of oxygenic photosynthetic organisms have to be determined in future, involving molecular genetic approaches. However, our observation of strong coupling between the photosynthetic light harvesting machinery of living cyanobacteria and an optical microcavity at ambient conditions makes it worth investigating other biological processes, which are difficult to be explained by classical thermodynamics with respect to quantum electrodynamics effects.[3,34] Future experiments will show if and to what degree the semi-classical model of energy "hopping" in the light-harvesting machinery of PSs must be expanded by a delocalized wave-like energy transfer under natural irradiation conditions.

4 | METHODS

4.1 | Preparation of cavity mirrors

The mirrors were produced by evaporating a 3 nm thick chromium layer on a glass surface serving as an adhesion layer for the following silver layer, which has a thickness of 30 nm or 60 nm for the lower and upper mirror, respectively. Since silver is bactericidal and very susceptible to damage and oxidation, it was coated with a gold layer (5 nm) and an SiO_2 layer (20 nm).[35] These layer thicknesses result in a microcavity with a quality factor of $Q = 98$. The microcavity was assembled in a custom-built holder with piezo actuators and mounted on a stage scanning confocal microscope for the collection of both white light transmission and fluorescence spectra from the same spatial position.

4.2 | Light intensity measurements

The light intensity was measured with a Li-Cor Li-189 radiometer from Heinz Walz GmbH (Germany).

4.3 | Bacterial cultivation conditions

Synechococcus elongatus PCC 7492 cells were cultivated under photoautotrophic conditions with continuous illumination at around 30 µmol photons s^{-1} m^{-2} (Lumilux de Lux, Daylight, Osram) at 28°C. The cultures were grown in 100 mL Erlenmeyer flasks, filled with 40 mL BG11[36] medium, supplemented with 5 mM $NaHCO_3$ and shaken at 120 − 130 rpm.

4.4 | The survivability after laser irradiation analyzed by a spot assay

The *S. elongatus* cultures of both treatments were adjusted to an optical density $OD_{750} = 0.5$, and a dilution series to the power of 10 was made in BG11 medium ($10^0 - 10^{-5}$). Five microliters of each dilution was dropped on BG11-agar plates and cultivated at 28°C[37] under constant light with the intensity of 30 µmol photons s^{-1} m^{-2} for 7 days. All experiments are shown in Figure 1D. Top: Non-irradiated control in a dilution series (1:10), three replicates. Figure 1D below: Irradiated sample in a dilution series (1:10), three replicates. The bacteria were irradiated with a lens widened laser beam at adjusted intensity ($\lambda_{ex} = 440$ nm, power: 1.8 mW) for 3 minutes before preparation of a spot assay. Representative results are shown in Figure 1D.

4.5 | The spectral properties of *S. elongatus*

To characterize the spectral properties of the photosynthetic pigments, absorption and emission spectra were recorded from 20 µL of a cyanobacterial suspension, embedded in a low-melting agarose matrix to prevent cell movement (Figure 1C). The absorption spectrum shown in Figure 1B features four distinct bands: the soret band of chlorophyll *a* at 440 nm,[38] the carotenoid band at

500 nm,[39] the PBS band at 630 nm[40] and the Q_y band of chlorophyll *a* at 680 nm.[41] Excitation of the soret band is very efficient, taking additional advantage of the large Stokes shift to separate the laser reflection at the cavity mirrors from the emission signal, which is dominated by the chlorophyll *a* emission at 680 nm.[39]

ACKNOWLEDGMENTS

The authors would like to thank F. de Courcy for English proofreading of the manuscript, M. Kittelberger for initial experiments and M. Harter for the hint of trying quantum biology. Alfred J. Meixner, Frank Wackenhut and Klaus Harter acknowledge support by the VW foundation (project title: A quantum beat for life) and the Deutsche Forschungsgemeinschaft (ME 1600/13-3; HA 2146/23-1; SFB 1101/D02, SFB 1101/Z02). Open access funding enabled and organized by Projekt DEAL.

AUTHOR CONTRIBUTIONS

Sven zur Oven-Krockhaus, Klaus Harter and Alfred J. Meixner designed the project. Tim Rammler and Johanna Rapp performed experiments. Tim Rammler and Frank Wackenhut analyzed the data and wrote the manuscript with input and proofreading from Karl Forchhammer, Klaus Harter, Alfred J. Meixner, Sven zur Oven-Krockhaus and Johanna Rapp.

DATA AVAILABILITY STATEMENT

Data are available in the main text or the supplementary materials. Further material is available from the corresponding author upon reasonable request.

ORCID

Frank Wackenhut https://orcid.org/0000-0001-6554-6600

REFERENCES

[1] S. Casella, F. Huang, D. Mason, G. Y. Zhao, G. N. Johnson, C. W. Mullineaux, L. N. Liu, *Mol. Plant* **2017**, *10*, 1434.
[2] A. Stirbet, D. Lazár, Y. Guo, G. Govindjee, *Ann. Bot.* **2020**, *126*, 511.
[3] G. R. Fleming, G. D. Scholes, Y.-C. Cheng, *Proc. Chem.* **2011**, *3*, 38.
[4] G. S. Engel, T. R. Calhoun, E. L. Read, T. K. Ahn, T. Mančal, Y. C. Cheng, R. E. Blankenship, G. R. Fleming, *Nature* **2007**, *446*, 782.
[5] J. Strümpfer, M. Şener, K. Schulten, *J. Phys. Chem. Lett.* **2012**, *3*, 536.
[6] E. Collini, *Chem. Soc. Rev.* **2013**, *42*, 4932.
[7] E. Collini, C. Y. Wong, K. E. Wilk, P. M. G. Curmi, P. Brumer, G. D. Scholes, *Nature* **2010**, *463*, 644.
[8] Y.-C. Cheng, G. R. Fleming, *Annu. Rev. Phys. Chem.* **2009**, *60*, 241.
[9] R. Hildner, D. Brinks, J. B. Nieder, R. J. Cogdell, N. F. van Hulst, *Science* **2013**, *340*, 1448.
[10] P. D. Dahlberg, G. J. Norris, C. Wang, S. Viswanathan, V. P. Singh, G. S. Engel, *J. Chem. Phys.* **2015**, *143*, 101101.
[11] J. Cao, R. J. Cogdell, D. F. Coker, H. G. Duan, J. Hauer, U. Kleinekathöfer, T. L. C. Jansen, T. Mančal, R. J. D. Miller, J. P. Ogilvie, V. I. Prokhorenko, T. Renger, H. S. Tan, R. Tempelaar, M. Thorwart, E. Thyrhaug, S. Westenhoff, D. Zigmantas, *Sci. Adv.* **2020**, *6*, eaaz4888.
[12] F. Ma, E. Romero, M. R. Jones, V. I. Novoderezhkin, R. van Grondelle, *Nat. Commun.* **2019**, *10*, 933.
[13] T. W. Ebbesen, *Acc. Chem. Res.* **2016**, *49*, 2403.
[14] D. Coles, L. C. Flatten, T. Sydney, E. Hounslow, S. K. Saikin, A. Aspuru-Guzik, V. Vedral, J. K. H. Tang, R. A. Taylor, J. M. Smith, D. G. Lidzey, *Small* **2017**, *13*, 1701777.
[15] S. Rexroth, M. M. Nowaczyk, M. Rögner, Cyanobacterial Photosynthesis: The Light Reactions. in *Modern Topics in the Phototrophic Prokaryotes: Metabolism, Bioenergetics, and Omics* (Ed: P. C. Hallenbeck), Springer International Publishing, Cham, Switzerland **2017**, p. 163.
[16] A. Doerrich, A. Wilde, *BIO-Protoc.* **2015**, *5*, e1574.
[17] C. S. French, J. S. Brown, M. C. Lawrence, *Plant Physiol.* **1972**, *49*, 421.
[18] I. N. Stadnichuk, P. M. Krasilnikov, D. V. Zlenko, *Microbiology* **2015**, *84*, 101.
[19] A. F. Bhatti, R. R. Choubeh, D. Kirilovsky, E. Wientjes, H. van Amerongen, *Biochim. Biophys. Acta BBA Bioenerg.* **2020**, *1861*, 148255.
[20] G. H. Krause, E. Weis, Chlorophyll Fluorescence and Photosynthesis: The Basics, *37*.
[21] J. R. Lakowicz, *Principles of Fluorescence Spectroscopy*, Springer, NewYork **2006**.
[22] M. Byrdin, I. Rimke, E. Schlodder, D. Stehlik, T. A. Roelofs, *Biophys. J.* **2000**, *79*, 992.
[23] E. M. Purcell, Spontaneous Emission Probabilities at Radio Frequencies. in *Confined Electrons and Photons: New Physics and Applications* (Eds: E. Burstein, C. Weisbuch), Springer, Boston, MA **1995**, p. 839.
[24] A. I. Chizhik, A. M. Chizhik, D. Khoptyar, S. Bär, A. J. Meixner, J. Enderlein, *Nano Lett.* **2011**, *11*, 1700.
[25] E. G. Andrizhiyevskaya, D. Frolov, R. van Grondelle, J. P. Dekker, *Biochim. Biophys. Acta BBA—Bioenerg.* **2004**, *1656*, 104.
[26] M. Fox, *Quantum Optics: An Introduction*, Oxford University Press, New York **2006**.
[27] J. A. Hutchison, T. Schwartz, C. Genet, E. Devaux, T. W. Ebbesen, *Angew. Chem. Int. Ed.* **2012**, *51*, 1592.
[28] J. Dintinger, S. Klein, F. Bustos, W. L. Barnes, T. W. Ebbesen, *Phys. Rev. B* **2005**, *71*, 035424-1 - 035424-5.
[29] K. A. Atlasov, K. F. Karlsson, A. Rudra, B. Dwir, E. Kapon, *Opt. Express* **2008**, *16*, 16255.
[30] A. Junginger, F. Wackenhut, A. Stuhl, F. Blendinger, M. Brecht, A. J. Meixner, *Opt. Express* **2020**, *28*, 485.
[31] R. S. Knox, B. Q. Spring, *Photochem. Photobiol.* **2003**, *77*, 497.
[32] P. Jordan, P. Fromme, H. T. Witt, O. Klukas, W. Saenger, N. Krauû, Three-dimensional structure of cyanobacterial photosystem I at 2.5 AÊ resolution. **2001**, *411*, 9.
[33] Y. Umena, K. Kawakami, J.-R. Shen, N. Kamiya, *Nature* **2011**, *473*, 55.
[34] A. Marais, B. Adams, A. K. Ringsmuth, M. Ferretti, J. M. Gruber, R. Hendrikx, M. Schuld, S. L. Smith, I. Sinayskiy, T. P.

J. Krüger, F. Petruccione, R. Van Grondelle, *J. R. Soc. Interface* **2018**, *15*, 20180640.
[35] A. Konrad, M. Metzger, A. M. Kern, M. Brecht, A. J. Meixner, *Nanoscale* **2015**, *7*, 10204.
[36] R. Rippka, R. Y. Stanier, J. Deruelles, M. Herdman, J. B. Waterbury, *Microbiology* **1979**, *111*, 1.
[37] B. Watzer, P. Spät, N. Neumann, M. Koch, R. Sobotka, B. Macek, O. Hennrich, K. Forchhammer, *Front. Microbiol.* **2019**, *10*, 1428.
[38] Y. Kondou, M. Nakazawa, S. Higashi, M. Watanabe, K. Manabe, *Photochem. Photobiol.* **2007**, *73*, 90.
[39] J. T. M. Kennis, B. Gobets, I. H. M. Van Stokkum, J. P. Dekker, R. Van Grondelle, G. R. Fleming, *J. Phys. Chem. B* **2001**, *105*, 4485.
[40] R. Lahmi, E. Sendersky, A. Perelman, M. Hagemann, K. Forchhammer, R. Schwarz, *J. Bacteriol.* **2006**, *188*, 5258.
[41] A. Damjanović, H. M. Vaswani, P. Fromme, G. R. Fleming, *J. Phys. Chem. B* **2002**, *106*, 10251.

SUPPORTING INFORMATION

Additional supporting information may be found in the online version of the article at the publisher's website.

How to cite this article: T. Rammler, F. Wackenhut, S. zur Oven-Krockhaus, J. Rapp, K. Forchhammer, K. Harter, A. J. Meixner, *J. Biophotonics* **2021**, e202100136. https://doi.org/10.1002/jbio.202100136

Rammler, T., Wackenhut, F., zur Oven-Krockhaus, S., Rapp, J., Forchhammer, K., Harter, K., Meixner, A. J., J. Biophotonics 2021, e202100136.

https://doi.org/10.1002/jbio.202100136

Anteil an gemeinschaftlicher Veröffentlichung:

Es handelt sich hierbei um eine Nebenveröffentlichung. Wie auch diese Arbeit behandelt sie Mikroresonatoren. Die wissenschaftliche Grundidee dieser Veröffentlichung hatten Saeed Nosrati, Alfred J. Meixner und Frank Wackenhut. Die Projektplanung wurden von Saeed Nosrati durchgeführt. Bei der Datenaufnahme war ich beratend tätig. Der Aufbau einer der verwendeten Messinstrumente erfolgte durch mich. Die Datenverarbeitung wurde von Saeed Nosrati und Frank Wackenhut durchgeführt. Die Daten wurden von Saeed Nosrati und Frank Wackenhut evaluiert. Das Manuskript wurde von Saeed Nosrati, Alfred J. Meixner und Frank Wackenhut erstellt, wobei ich inhaltlich unterstützend und beratend tätig war.

7.2 Analysis of Fast Fluorescence Kinetics of a Single Cyanobacterium Trapped in an Optical Microcavity (veröffentlicht)

plants

MDPI

Article

Analysis of Fast Fluorescence Kinetics of a Single Cyanobacterium Trapped in an Optical Microcavity

Tim Rammler [1,2], Frank Wackenhut [1], Johanna Rapp [3], Sven zur Oven-Krockhaus [1,2], Karl Forchhammer [3], Alfred J. Meixner [1,*] and Klaus Harter [2,*]

[1] Institute for Physical and Theoretical Chemistry, University of Tübingen, 72076 Tübingen, Germany
[2] Center for Plant Molecular Biology (ZMBP), University of Tübingen, 72076 Tübingen, Germany
[3] Interfaculty Institute of Microbiology and Infection Medicine, University of Tübingen, 72076 Tübingen, Germany
* Correspondence: alfred.meixner@uni-tuebingen.de (A.J.M.); klaus.harter@uni-tuebingen.de (K.H.); Tel.: +49-(0)-7071-2976903 (A.J.M.); +49-(0)-7071-2972605 (K.H.)

Abstract: Photosynthesis is one the most important biological processes on earth, producing life-giving oxygen, and is the basis for a large variety of plant products. Measurable properties of photosynthesis provide information about its biophysical state, and in turn, the physiological conditions of a photoautotrophic organism. For instance, the chlorophyll fluorescence intensity of an intact photosystem is not constant as in the case of a single fluorescent dye in solution but shows temporal changes related to the quantum yield of the photosystem. Commercial photosystem analyzers already use the fluorescence kinetics characteristics of photosystems to infer the viability of organisms under investigation. Here, we provide a novel approach based on an optical Fabry–Pérot microcavity that enables the readout of photosynthetic properties and activity for an individual cyanobacterium. This approach offers a completely new dimension of information, which would normally be lost due to averaging in ensemble measurements obtained from a large population of bacteria.

Keywords: cyanobacteria; photosystem; fast fluorescence kinetics; optical microcavity; fluorescence microscopy

Citation: Rammler, T.; Wackenhut, F.; Rapp, J.; zur Oven-Krockhaus, S.; Forchhammer, K.; Meixner, A.J.; Harter, K. Analysis of Fast Fluorescence Kinetics of a Single Cyanobacterium Trapped in an Optical Microcavity. *Plants* **2023**, *12*, 607. https://doi.org/10.3390/plants12030607

Academic Editors: Vasily Ptushenko and Alexei Solovchenko

Received: 9 November 2022
Revised: 25 January 2023
Accepted: 25 January 2023
Published: 30 January 2023

1. Introduction

Photosynthesis by cyanobacteria is one of the most important processes on earth. It was responsible for the oxygenation of the Earth about 2.4 billion years ago, which enabled the subsequent development of multicellular life forms [1]. Even today, cyanobacterial photosynthesis significantly contributes to oxygen (O_2) generation during the process of carbon fixation typically from CO_2 [2]. Furthermore, ancient cyanobacteria were the precursors of endosymbiotic chloroplasts [3] that enable all photosynthetic eukaryotes (including higher plants) to produce O_2 and the chemical energy equivalents needed to fix CO_2. Due to the importance of this process, and with the hope of replicating this process in organic solar cells, it is compelling to understand this process in its entirety. Although there is much already known, there are still unexplained phenomena in the photosynthetic process. One example is the energy transfer in photosystem 2 (PS2) from the absorption of a photon in the peripheral pigments to the reaction center, where the energy is used to split water. It is still not conclusively understood why the efficiency of this process is as high as 99% and whether this is related to non-trivial quantum optical effects [4].

The study of photosynthetic organisms by chlorophyll fluorescence kinetics has become an effective method for detecting even small changes in the photosynthetic process [5]. Among other techniques, this non-invasive method is already routinely used for the analysis of photosynthetic microorganisms, plant cell cultures and whole plants [6]. In this work, we present a novel method to study the photosynthetic efficiency in a living individual cyanobacterium on the basis of the well-studied Kautsky effect. In it, the kinetic behavior

of the fluorescence emission is used to determine the quantum yield [7]. In contrast to previous analyses performed at the population level, our method enables one to determine the photosynthetic activity of an individual cell, exposing effects that are usually lost due to population averaging.

To enable the very detailed analysis of the Kautsky effect, and thus, the photosynthetic efficiency at the single cell level, living cyanobacteria were placed in an optical Fabry–Pérot microcavity, as in our earlier work [8]. There, we focused more on the design of the experimental system, to which we would refer the reader for more technical details on the microcavity. In short, such a microresonator is composed of two semi-transparent mirrors, with a mirror separation of ~2 µm giving rise to microcavity resonances in the visible spectral range. In addition to strong coupling, a microcavity can also increase or decrease the spontaneous emission rate of a chromophore by tuning the resonance of the microcavity to the fluorescence of the chromophore or away from the fluorescence. This effect is called the Purcell effect [9–11] and shortens the fluorescence lifetime (FLT) of the chromophore for an on-resonant microcavity and prolongs it for an off-resonant microcavity [8]. Due to the small space inside the microcavity, it is difficult or impossible to use near-probe dependent means, such as O_2 detectors, to determine the quantum yield in vivo. In order to capture the true photosynthetic efficiency of PS2, the experimental setup was designed as to minimize and eliminate residual phycobilisome (PBS) and photosystem 1 (PS1) fluorescence signals [12]. Our experimental approach offers a completely new way of obtaining knowledge about the PS2 activity, which would normally be lost due to averaging in ensemble measurements using a large cyanobacterial population.

2. Results

2.1. Theoretical Introduction and Technical Challenges

In our experiments, we investigated the unicellular cyanobacterium *Synechocccus elongatus* strain PCC 7942 (*S. elongatus*), a widely used model organism for photosynthetic research [13,14]. We have determined the quantum yields of individual cyanobacteria by analyzing the fast fluorescence kinetics (FFK) of PS2. The principle is based on the Kautsky effect [7], which describes the variable fluorescence (F_V) after dark adaptation as a function of the irradiation time with actinic light (photosynthesis activating light) (see Figure 1A). The Kautsky effect divides the temporal evolution of the fluorescence signal into two regions: a short, initial time window of the fast fluorescence increase in intensity (fast fluorescence kinetics, FFK) occurring in microseconds (see Figure 1A,C,D, blue area), and the subsequent region of slow fluorescence kinetics (SFK), which describes the slow decrease occurring in seconds to minutes (see Figure 1A,C,D, green area). The photosystem of *S. elongatus* was spectrally analyzed to ensure that, according to the Kautsky effect, only the PS2 core antenna chlorophyll fluorescence was measured. The absorption spectrum of *S. elongatus* cells has four distinct bands: the chlorophyll a soret band at 440 nm [15], the carotenoid band at 500 nm [16], the PBS band at 630 nm [17], and the Q_y band of chlorophyll a at 680 nm [18] (Figure 1B).

Excitation with 440 nm laser light as an actinic source (exciting the soret band) was most efficient and guaranteed almost exclusive fluorescence of chlorophyll a (compare to Figure 1B). Note that the laser source was operated in continuous wave mode, as pulsed laser sources might introduce undesired effects/damage. Conveniently, the soret band is spectrally distant from the chlorophyll a emission, which simplifies the separation of the laser scattering at 440 nm and the emission signal at 680 nm. In addition, a bandpass filter (676/29 nm) was placed in front of the detector to ensure that almost only photons emitted by PS2 were detected, since PS1 fluorescence occurs above 700 nm [19] and PBS fluorescence under 660 nm. Under these conditions, we can assume that only the fluorescence emission of the core antenna complex of PS2 was detected [20]. As the only type of chlorophyll in *S. elongatus* is chlorophyll a [21], the detected signal is dominated by chlorophyll a from PS2.

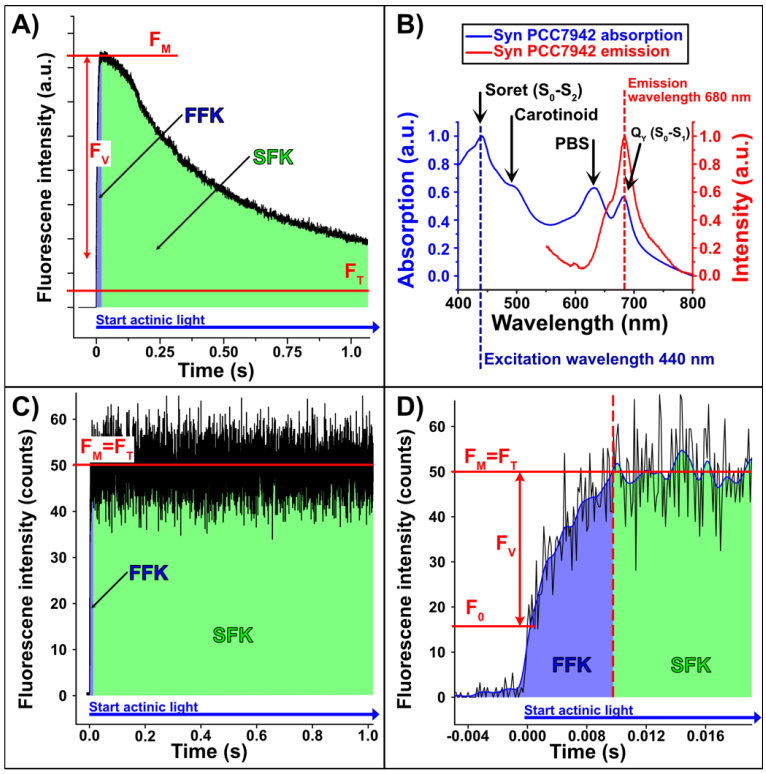

Figure 1. (**A**) Illustrative example of a fluorescence intensity time trace of a *S. elongatus* population (without any special treatment) excited with saturating light intensity (blue arrow). Shown in red: the maximum fluorescence intensity (F_M) and the terminal fluorescence (F_T) intensity according to the Kautsky effect. The blue area indicates the temporal range of the fast fluorescence kinetics (FFK), and the green area indicates the range of the slow fluorescence kinetics (SFK). (**B**) Normalized fluorescence (red) and absorption (blue) spectra of *S. elongatus* measured in BG11 medium, taken from [8]. The bacteria were excited with 440 nm light (blue dashed line). This spectrum was acquired with a conventional UV/VIS spectrometer. In contrast to the following measurements, no spectral filters were used for wavelength selection. The bacteria have both absorption and emission maxima at approx. 680 nm (red dashed line). (**C**) Fluorescence intensity time trace of *S. elongatus* after treatment with 3-(3,4-dichlorophenyl)-1,1-dimethylurea (DCMU). By spiking with DCMU, F_T no longer decreases to the same level as shown in (**A**), because electron transport between PS2 and PS1 is blocked, and the excitation energy is released almost exclusively by fluorescence. In this case, the terminal fluorescence (F_T) is equal to the maximum fluorescence (F_M). (**D**) Expanded section of (**C**) to determine the sudden fluorescence increase F_0 and the maximum fluorescence F_M. These values are used to quantify the quantum yield (Φ_{maxPS2} = 0.7 for this particular example).

In the following, we briefly explain the temporal evolution of a typical fluorescence signal (F_V) and introduce three important parameters: minimum fluorescence (F_0), maximum fluorescence intensity (F_M), and terminal fluorescence (F_T) [22]. Almost instantly, within a few picoseconds after actinic light irradiation, the photosynthetic chlorophyll fluorescence reaches an initial level called minimum fluorescence, F_0 (Figure 1D). Since the transfer of the photon energy via dipole–dipole interaction is much faster than the electron transfer by a sequence of redox reactions, a kind of energy pile-up occurs in the physical to the chemical energy transformation. The absorbed energy initially leads to a fast increase in the fluorescence intensity to the level F_M. F_0 is thereby the maximum energy

that can be emitted without an electron backlog. If the photosystem is irradiated with an intensity too low to induce closure of PS2 centers, F_0 remains constant after the abrupt increase to the F_0-level [20]. To reliably determine the maximal F_0 value, all PS2 reaction centers must be open and the corresponding electron acceptor (i.e., first stable acceptor, plastoquinone, Q_A) oxidized. This state can be achieved by 15 min of dark adaptation of the cyanobacterial cells [23]. After the abrupt rise to F_0, the variable fluorescence (F_V) rises to the maximum fluorescence F_M, since there is a temporal delay between the first absorption of a photon after dark adaptation and the start of the carbon reduction cycle. During the rise from F_0 to F_M, the electron acceptor Q_A becomes increasingly reduced [24] and an electron backlog occurs because reduced quinone (QH_2) cannot be re-oxidized fast enough and excess energy is released via fluorescence. Therefore, F_V reflects the redox state of Q_A. F_M is only achieved when the actinic light intensity completely saturates all photosystems. In this case, all PS2 reaction centers are assumed to be in a closed state, and all associated Q_A are completely reduced. If the actinic light is not saturating, the peak intensity does not reflect the maximum possible fluorescence of the system. Here, it is important to ensure that F_M is reached after a few milliseconds. To prevent the delay of F_M, the experiments were carried out in the presence of 3-(3,4-dichlorophenyl)-1,1-dimethylurea (DCMU). DCMU blocks the plastoquinone binding site (Q_B) and thereby prevents electron transport from Q_A to Q_B [25]. Consequently, all Q_A sites become completely reduced after the onset of actinic light (Figure S1). This procedure enables one to determine the true F_M value, since the energy absorbed by PS2 is completely emitted radiatively due to blocking of further electron transport. In the absence of DCMU, F_V decreases again as soon as Q_A becomes re-oxidized due to electron transport towards $NADPH/H^+$, essentially driven by PS1 activity. After a few minutes, it reaches the steady-state level F_T, as illustrated in Figure 1A. This decrease is not possible in the presence of DCMU, and F_M remains constant. In this case, F_M and F_T are technically the same (Figure 1C).

The analysis of the FFK enables us to obtain precise information about the intactness and efficiency of PS2 [26]. A good approximation for the current photochemical efficiency can be calculated by using F_0 and F_M:

$$\Phi_{maxPS2} = \frac{F_M - F_0}{F_M} = \frac{F_V}{F_M} \quad (1)$$

The current photochemical efficiency or quantum yield of PS2 Φ_{maxPS2} is a measure of the efficiency with which the excitation energy from the internal antenna pigments is used for photochemical reactions in the open P680 reaction centers [26]. Experiments that have determined the amount of oxygen produced as a function of light intensity show that Φ_{maxPS2} reflects, to a good approximation, the maximum relative electron transport efficiency [27]. In most plant species, Φ_{maxPS2} of about 0.83 can be expected [28]. However, determining Φ_{maxPS2} in cyanobacteria is not as straightforward as in plants, since additional antenna proteins, such as PBS, interfere with the measurement, distort the result and are the main reason for lower Φ_{maxPS2} yields [29]. After careful elimination of all interfering factors described above (DCMU application, narrow-band 440 nm laser excitation, use of a bandpass filter), a value for Φ_{maxPS2} of around 0.8 can also be expected for *S. elongatus* [29,30].

The major challenge of the current work is to detect the fluorescence signal of a single cyanobacterium which is embedded in an optical microcavity. For this reason, the microcavity with the embedded cyanobacterium was mounted on the scanning stage of a confocal microscope, and one bacterium was centered in the focal volume of the high numerical aperture (NA) objective lens. The large NA ensures that a large fraction of the photons emitted by the excited bacterium can be collected. At a laser power of 1.28 nW, a single bacterial cell emitted statistically only 60 photons per millisecond at the fluorescence maximum (F_M), measured after the objective lens was put in place but before the cover slip was, on which the cyanobacterium was placed. Only about half of the bacterium was illuminated by the diffraction limited excitation spot. In addition, to resolve the

sudden fluorescence increase (F_0) in the time domain, highly sensitive and fast-responding detectors must be used (rise time < 2 ns; for more details, see Material and Methods). Due to the low photon emission rate (compare Figure 1D), a computer-assisted evaluation was necessary to carry out the data analysis. To determine the fast increase in the F_0 emission, the raw data set was therefore smoothed by a Gaussian filter (Figure 1D, blue line). The maxima of the first and second derivatives of the smoothed data set indicate F_0, since it is located in between these two extrema. The fluorescence maximum, F_M, was obtained by averaging all values in a temporal window ranging from 0.08 to 1.00 s after F_0 (Figure 1D, red dashed line indicates the start of a temporal window).

2.2. Measurement Results

The quantum yield of individual cyanobacteria was measured and analyzed via their individual fluorescence responses. For this purpose, the 440 nm laser (continuous wave mode) was precisely focused on one bacterium. The cross-section of a bacterium was approximated by a 1 × 2 µm ellipse. As a guide for the optimal light intensity for the following experiments, we used the standard setting for commercial chlorophyll fluorescence curve analysis devices of approx. 3000 µmol photons $\cdot s^{-1} \cdot m^{-2}$ [28], which is equivalent to a 440 nm laser power of 1.28 nW per bacterium. To test for any effect in the variations of irradiation intensity on the quantum yield, FFK curves of different individual bacteria from the same growth culture were measured with different laser intensities (see Figure 2B,C; 3 and 90 nW).

As shown in Figure 2B, the quantum yields of individual bacteria were the same for laser exposure of 90 and 3 nW, as the difference in their medians lies within the two statistical distributions (two-tailed *t*-test, $p = 0.343$). This indicates that the difference in the quantum yield cannot be attributed to unequal irradiation conditions. Under these conditions, a change in the quantum yield could therefore only be caused by the nature of the surrounding electromagnetic field. In order to test the lower limitation of the FFK in a single cell, the quantum yield of chlorotic cyanobacteria was recorded. The chlorosis of the cyanobacteria was induced by nitrogen starvation, which induces the degradation of photosynthetic pigments, in particular, those of the PCBs, whilst the bulk of the photosystems stays intact [31]. As shown in Figure 2D,E, the quantum yield (excitation 440 nm, 1.28 nW) in chlorotic cyanobacteria was significantly lower ($\Phi_{maxPS2} = 0.74$), compared to the yield from non-chlorotic cells ($\Phi_{maxPS2} = 0.77$).

An advantage of the single-bacterium experiment over the classical population approach is that also the distribution of the quantum yields can be analyzed statistically and individually. The possibility of determining the quantum yield of a single bacterium allows one to investigate extreme examples (outliers) in more detail. In a population experiment, small-scale differences of individual cells would be averaged.

An example in which a single-bacterium approach is advantageous for FFK analysis is a situation where the photosynthetic light conditions vary on a small spatial scale, which is the case in an electromagnetic Fabry–Pérot microcavity. Here, each cyanobacterium experiences a different optical field. Fabry–Pérot microcavities consist of two semitransparent mirrors (quality factor, Q = 98) with an optical path length allowing resonances in the visible spectral range. Since the upper mirror is curved, the mirror spacing varies depending on the spatial location, which is why the individual cyanobacteria experience different electromagnetic fields. For analysis in the microcavity, the cyanobacteria were embedded in a BG-11 agarose matrix to restrict spatial drift [8]. In the set-up, the cyanobacteria located in the microcavity were irradiated with 440 nm laser light from below and the residual fluorescence recorded through a high-NA objective lens (NA = 1.4) (see Figure 3A). More details about the experimental setup were published before [8] and are also given in Materials and Methods.

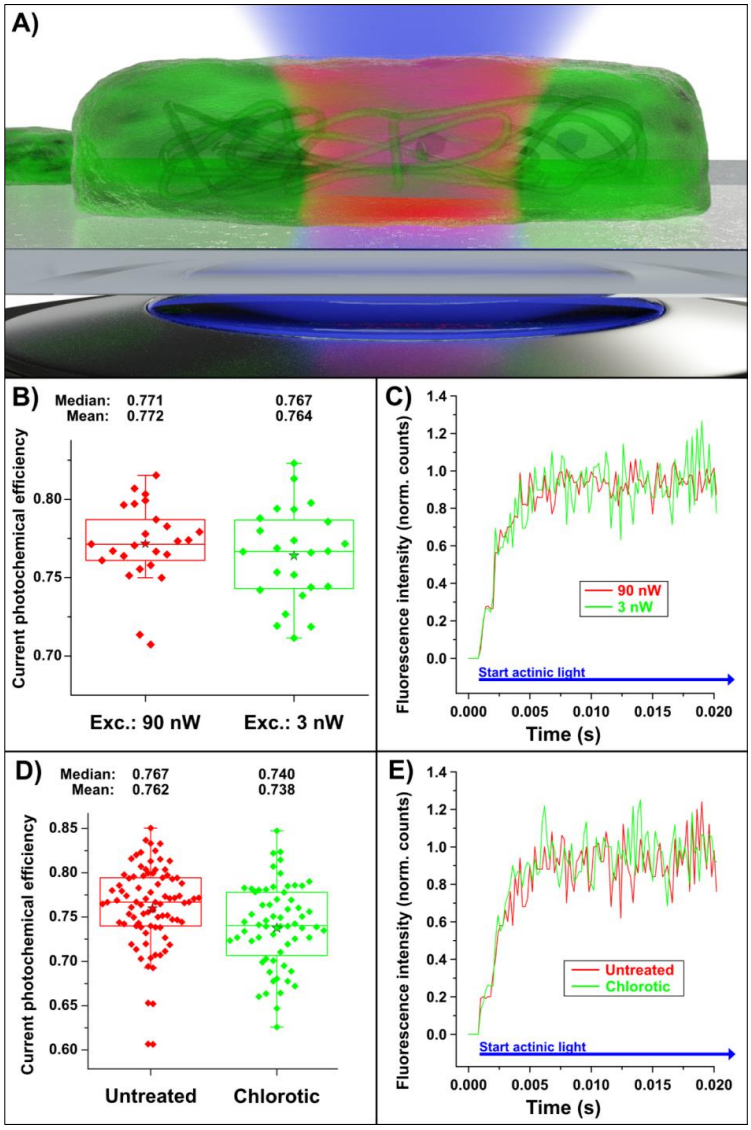

Figure 2. (**A**) Schematic illustration of a single bacterium on a glass coverslip in the focal volume of a high-numerical-aperture (NA = 1.4) objective lens. (**B**) Box plot of the quantum yield of *S. elongatus* irradiated by 90 nW (red dots) and 3 nW (green dots) laser power to prove the independence of the photosynthetic efficiency from the laser power. There is no significant difference between 90 and 3 nW (two-tailed *t*-test, $p = 0.343$). (**C**) Two representative fluorescence curves recorded with a laser excitation intensity of 90 nW (red curve) or 3 nW (green curve). The curves were normalized to F_M because different amounts of chlorophyll were measured due to different bacterial sizes, allowing a direct comparison. (**D**) Box plot of the effective quantum yield of *S. elongatus* in free space (red curve) and chlorotic cells (nitrogen starved) in free space (green curve). Statistically, the median of the quantum yields of the free space and the chlorotic bacteria differ significantly (two-tailed *t*-test $p = 3.10 \times 10^{-3}$). (**E**) Two representative fluorescence curves (normalized to F_M) of untreated cyanobacteria (red curve) and cyanobacteria grown under chlorotic conditions (green curve). The star in (**B**) and (**D**) represents the mean.

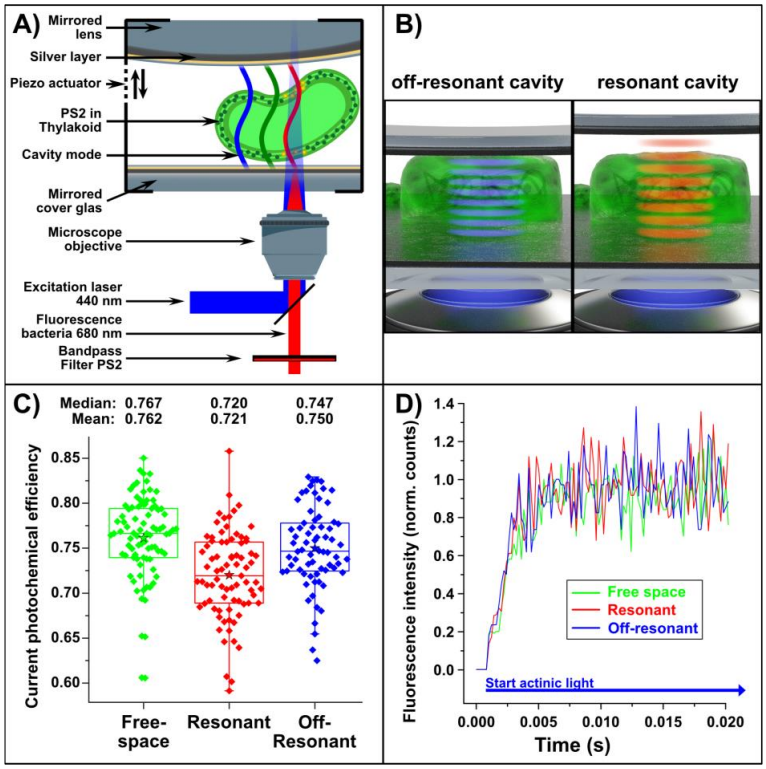

Figure 3. (**A**) Layout of the experimental set-up. A laser (440 nm, continuous wave) is focused by an objective lens onto a single bacterium in the microcavity that consists of two semi-transparent silver mirrors. The fluorescent light of the bacterium is transmitted by the beam splitter and directed to a detector. (**B**) Illustration of *S. elongatus* in a microcavity (consisting of two very close silver mirrors). On the right, bacterial fluorescence is resonant with the microcavity mode (red waves), which leads to strong coupling and splitting of the energy levels. For detailed measurements, please refer to: [8]. On the left, *S. elongatus* is illustrated in an off-resonant microcavity. (**C**) Box plot of the quantum yield of *S. elongatus* in free space (green dots), in a resonant (red dots) and an off-resonant (blue dots) microcavity. The quantum yield drops significantly inside the resonant microcavity (two-tailed *t*-test: compared to free space: $p = 7.54 \times 10^{-8}$; compared to off-resonant microcavity: $p = 1.52 \times 10^{-4}$), with otherwise equal ambient conditions in both series of measurements. Statistically, the free space and off-resonant measurement series do not differ (two-tailed *t*-test, $p = 0.12$). (**D**) Three representative fluorescence curves (normalized to F_M) of cyanobacteria in free space (green curve), in a resonant microcavity (red curve) and an off-resonant cavity (blue curve). The star in (**C**) represents the mean.

In the first series, the FFK measurements were performed in free space (see Figure 3C,D, green). The second series was recorded in a microcavity resonant to the absorption/emission at 680 nm (see Figure 3C,D, red; and illustration in Figure 3B, right) and in the third series in an off-resonant microcavity (see Figure 3C/D, blue and illustration in Figure 3B, left) with resonance set to approx. 500 nm. The excitation energy was 1.28 nW laser intensity). The largest quantum yield was observed in free space and in the off-resonant microcavity. In contrast, there was a significant difference between the quantum yield in the off-resonance and the on-resonance ($p = 1.52 \times 10^{-4}$) microcavity, and between free space and the resonant ($p = 7.54 \times 10^{-8}$) microcavity (Figure 3C). Detailed values of the absolute, F_0-normalized, and F_M-normalized data of quantum yield measurements in free space, resonant, and off-resonant microcavity are given in the supplementary information, Table S1. Hence, only the resonant microcavity had a significant reductive impact on the

quantum yield of single cyanobacteria, which also corresponds to previous fluorescence lifetime measurements of microcavity-enclosed cyanobacteria [8]. Since the same ambient conditions prevail in the free space and resonant microcavity, we can assume that the quantum yield is solely influenced by the special light conditions, i.e., the coherence of the optical field inside the resonant microcavity.

3. Discussion

We have developed a method to reliably determine the quantum yield of individual living cyanobacteria and demonstrated the reliability of the method. Moreover, we showed that the measurements tolerate slight variations in the excitation intensity of the actinic light. To our opinion, the approach applied here and in our previous publication [8] are the first examples showing that an optical cavity enables the interrogation of biological systems in terms of quantum physical phenomena, as theoretically proposed recently [32].

An especially interesting scenario is observed when the microcavity resonance coincides with the fluorescence and absorption maxima of the cyanobacterium (see Figure 1B), where the excitation energy can coherently oscillate back and forth between the electromagnetic field in the microcavity and the photosynthetic pigments. This leads to so called strong light–matter coupling, resulting in a polaritonic state, which manifests itself as a double-peaked microcavity transmission spectrum with a peak spacing called vacuum Rabi splitting [33].

The spread in the single-cell experimental data most likely originated from the biological variation in the photosynthetic quantum yields of individual whole cyanobacteria. Impressively, our method can be used to show such differences. The magnitude of the spread might also allow deriving inferences about other biological effects, such as non-obvious deficiency symptoms or suboptimal environmental conditions of a bacterial culture. Our highly spatially resolved and direct measurements also demonstrate that cyanobacteria differ in their photosynthetic activity in the optical microcavity. Since the quantum yields differ significantly between a resonant and an off-resonant microcavity, it is reasonable to propose that the coherent optical field in the microcavity has a significant effect on the energy transfer in PS2 in vivo.

Our method allows us to study the microcavity's influences on a single cyanobacterium. We are of the opinion that such a method will be helpful for future researchers to unravel remaining open questions of photosynthesis, e.g., about the efficiency of optical-to-chemical energy conversion.

4. Materials and Methods

4.1. Experimental Set-Up

A home-built confocal scanning microscope was used for the measurements in this work (compare Figure 4). The excitation light source is a laser diode (LDH-D-C-440, PicoQuant GmbH, Berlin, Germany) operated in continuous wave mode with an excitation wavelength of 440 nm. The beam is directed via two mirrors through a clean-up interference filter (MaxDiode™ LD01-439/8-12.5, Semrock Optical Filters, Rochester, NY, USA) onto a lens, which combines the beams into a single-mode glass fiber (P1-405 BPM-FC-2, Thorlabs Inc., Newton, NJ, USA). After the decoupling unit, the excitation light is passed through various gray filters and then onto a swiveling lens. This lens can be used to focus on the back aperture of the objective lens to acquire widefield images. After the lens, the beam is reflected by a dichroic beam splitter, which is positioned at a 45° angle to the propagation direction (F48-487 Laser Beam Splitter zt 488, AHF Analysentechnik AG, Tübingen, Germany). The beam splitter reflects light with wavelengths below 488 nm, whereas it transmits light with longer wavelengths. The reflected beam is now focused on the sample through an oil objective lens (Zeiss Plan-Apochromat, 100×, 1.4 Oil DIC, Carl Zeiss Jena GmbH, Jena, Germany). Micrometer screws are used for coarse positioning of the sample, and a piezo-controlled scanning stage (P-733.3CD, Physik Instrumente (PI) GmbH & Co. KG, Karlsruhe, Germany) allows sample scanning in three spatial dimensions.

The fluorescent light emitted by the sample is collected by the same objective lens and transmitted through a beam splitter. An additional long-pass filter (488 LP Edge Basic long-pass filter, BLP01-488R-25, Semrock Inc., USA) and a band-pass filter (BrightLine® FF01-676/29-25, Semrock Inc., USA) are used to filter the detected signal. Confocal images of the fluorescence intensity are acquired by a single photon avalanche diode (SPAD) (PDM Series, Micro Photon Devices, Bolzano, Italy). The SPAD is coupled with a TCSPC unit (HydraHarp 400, PicoQuant GmbH, Berlin, Germany) for the acquisition of time-correlated fluorescence traces. Spectra are acquired with a spectrometer (Acton SP300i, Princeton Instruments, Trenton, NJ, USA) with a thermoelectrically cooled CCD camera (PIXIS 100, Princeton Instruments, Trenton, NJ, USA). With widefield illumination, videos or images can be recorded in real time. The scanning stage, the SPAD, the laser diode and the TCSPC unit are controlled by SymphoTime® software 64 (PicoQuant GmbH, Berlin, Germany). Fluorescence spectra are acquired with the software Winspec® (Princeton Instruments, Trenton, NJ, USA). This software controls the monochromator and the corresponding CCD camera.

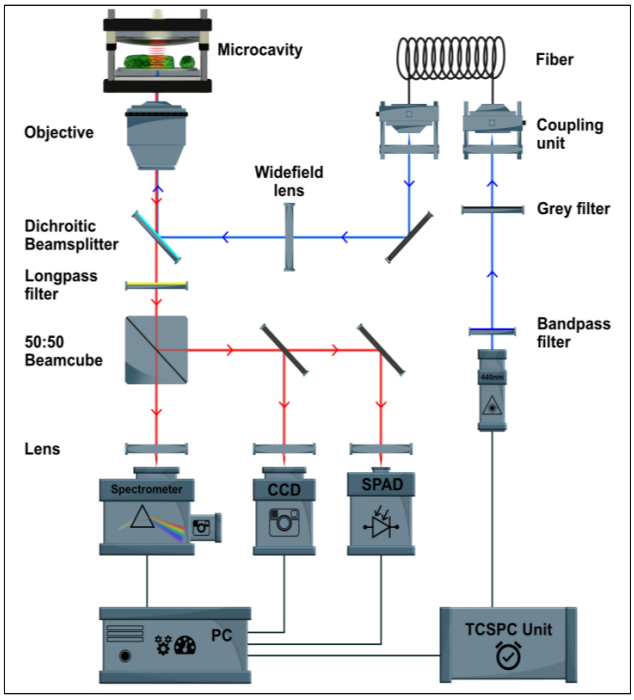

Figure 4. Home-built semi confocal microscope.

4.2. Preparation of Microcavity Mirrors

The mirror preparation was achieved by evaporating a 3 nm chromium layer on a glass cover slip to ensure that the following layers adhere well. Next, the reflective silver layer with a thickness of 30 or 60 nm—for the lower and upper mirrors, respectively—was vapor-deposited. A gold layer (5 nm) and an SiO_2 layer (20 nm) served as a coating layer, since silver is very susceptible to oxidation and damage and is bactericidal [34]. The structure of these layers created a microcavity with a quality factor of Q = 98. The distance between the two mirrors was adjusted very precisely by a piezo actuator. The custom-built holder was mounted on the stage of a scanning confocal microscope to measure the fluorescence of cyanobacteria one at a time.

4.3. Light Intensity Measurements

The light intensity for the cultivation for *S. elongatus* was measured with a Li-Cor Li-189 radiometer from Heinz Walz GmbH (Pfullingen, Germany). The laser power was measured with an Optical Power Meter Model 1830-C and a Sensor Model 818-SL, both from Newport Corporation (Irvine, CA, USA).

4.4. Bacterial Cultivation Conditions

Synechococcus elongatus PCC 7492 was cultivated under photoautotrophic conditions under continuous light with an intensity of around 30 µmol photons $\cdot s^{-1} \cdot m^{-2}$ (Lumilux de Lux, Daylight, Osram, Munich, Germany). The cultivation was performed in 50 mL BG11 medium [35] supplemented with 5 mM $NaHCO_3$ in 100 mL Erlenmeyer flasks at 28 °C and continuous shaking (120–130 rpm).

Nitrogen-starved, chlorotic cells were obtained as previously described [36] with slight modifications. Exponentially grown *S. elongatus* cells in BG11 were harvested by centrifugation at room temperature (3500× *g*, 10 min), the supernatant was discarded, and the cell pellet was washed twice with 50 mL $NaNO_3$-free BG11-medium (BG11-0). After that, the cultures were cultivated in BG11-0 at light intensities of 50–60 µmol photons $\cdot s^{-1} \cdot m^{-2}$ for 1 day.

4.5. Bacteria Preparation

The cyanobacteria were treated with a 10 µmol 3-(3,4-dichlorophenyl)-1,1-dimethylurea (DCMU) solution. Then, 20 µL of a *S. elongatus* suspension was embedded in a low-melting agarose matrix (prepared with BG11 [35] medium) to prevent cell movement.

Supplementary Materials: The following supporting information can be downloaded at: https://www.mdpi.com/article/10.3390/plants12030607/s1. Figure S1: (A) Confocal microscopy image of *S. elongatus* cells inside the microcavity. (B) Boxplot of the current photochemical efficiency of *S. elongatus* measured in free space, treated with DCMU (red) and untreated (green); Figure S2: (A) Two representative fluorescence curves of cyanobacteria in free space (red curve), in a resonant microcavity (green curve). Both measurements were carried out with a pulsed laser (repetition rate: 80 MHz, pulse duration: 80 ps) and an excitation intensity of 30 µW. The part on the left is zoomed. Table S1: Absolute, F_0-normalized and F_M-normalized F_0 and F_M values of quantum yield measurements in free space, resonant and off-resonant microcavity.

Author Contributions: T.R. and J.R. performed the experiments and analyzed the data with input from K.F., K.H., A.J.M., and S.z.O.-K., T.R. and F.W. wrote the manuscript with proofreading input from K.F., K.H., A.J.M., S.z.O.-K. and J.R. All authors have read and agreed to the published version of the manuscript.

Funding: A.J.M., F.W., and K.H. acknowledge support by the VW foundation (project title: A quantum beat for life) and the Deutsche Forschungsgemeinschaft (ME 1600/13-3; HA 2146/23-1; SFB 1101/D02 and Z02).

Institutional Review Board Statement: Not applicable.

Informed Consent Statement: Not applicable.

Data Availability Statement: Data are available in the main text or the Supplementary Materials. Further material is available from the corresponding author upon request.

Acknowledgments: The authors would like to thank the native English speaker Kenneth Berendzen for English proofreading of the manuscript.

Conflicts of Interest: The authors declare no conflict of interest.

References

1. Schirrmeister, B.E.; de Vos, J.M.; Antonelli, A.; Bagheri, H.C. Evolution of Multicellularity Coincided with Increased Diversification of Cyanobacteria and the Great Oxidation Event. *Proc. Natl. Acad. Sci. USA* **2013**, *110*, 1791–1796. [CrossRef]
2. Holland, H.D. The Oxygenation of the Atmosphere and Oceans. *Philos. Trans. R. Soc. B* **2006**, *361*, 903–915. [CrossRef] [PubMed]

3. Keeling, P.J. The Number, Speed, and Impact of Plastid Endosymbioses in Eukaryotic Evolution. *Annu. Rev. Plant Biol.* **2013**, *64*, 583–607. [CrossRef]
4. Mančal, T. A Decade with Quantum Coherence: How Our Past Became Classical and the Future Turned Quantum. *Chem. Phys.* **2020**, *532*, 110663. [CrossRef]
5. Maxwell, K.; Johnson, G.N. Chlorophyll Fluorescence—A Practical Guide. *J. Exp. Bot.* **2000**, *51*, 659–668. [CrossRef]
6. Küpper, H.; Benedikty, Z.; Morina, F.; Andresen, E.; Mishra, A.; Trtílek, M. Analysis of OJIP Chlorophyll Fluorescence Kinetics and Q_A Reoxidation Kinetics by Direct Fast Imaging. *Plant Physiol.* **2019**, *179*, 369–381. [CrossRef]
7. Kautsky, H.; Hirsch, A. Neue Versuche zur Kohlensäureassimilation. *Naturwissenschaften* **1931**, *19*, 964. [CrossRef]
8. Rammler, T.; Wackenhut, F.; zur Oven-Krockhaus, S.; Rapp, J.; Forchhammer, K.; Harter, K.; Meixner, A.J. Strong Coupling between an Optical Microcavity and Photosystems in Single Living Cyanobacteria. *J. Biophotonics* **2022**, *15*, e202100136. [CrossRef] [PubMed]
9. Purcell, E.M. Spontaneous Emission Probabilities at Radio Frequencies. In *Confined Electrons and Photons: New Physics and Applications*; Burstein, E., Weisbuch, C., Eds.; Springer: Boston, MA, USA, 1995; p. 839. ISBN 978-1-4615-1963-8.
10. Chizhik, A.I.; Chizhik, A.M.; Khoptyar, D.; Bär, S.; Meixner, A.J.; Enderlein, J. Probing the Radiative Transition of Single Molecules with a Tunable Microresonator. *Nano Lett.* **2011**, *11*, 1700–1703. [CrossRef]
11. Chizhik, A.; Schleifenbaum, F.; Gutbrod, R.; Chizhik, A.; Khoptyar, D.; Meixner, A.J.; Enderlein, J. Tuning the Fluorescence Emission Spectra of a Single Molecule with a Variable Optical Subwavelength Metal Microcavity. *Phys. Rev. Lett.* **2009**, *102*, 073002. [CrossRef]
12. Simis, S.G.H.; Huot, Y.; Babin, M.; Seppälä, J.; Metsamaa, L. Optimization of Variable Fluorescence Measurements of Phytoplankton Communities with Cyanobacteria. *Photosynth. Res.* **2012**, *112*, 13–30. [CrossRef] [PubMed]
13. Casella, S.; Huang, F.; Mason, D.; Zhao, G.-Y.; Johnson, G.N.; Mullineaux, C.W.; Liu, L.-N. Dissecting the Native Architecture and Dynamics of Cyanobacterial Photosynthetic Machinery. *Mol. Plant* **2017**, *10*, 1434–1448. [CrossRef] [PubMed]
14. Rexroth, S.; Nowaczyk, M.M.; Rögner, M. Cyanobacterial Photosynthesis: The Light Reactions. In *Modern Topics in the Phototrophic Prokaryotes: Metabolism, Bioenergetics, and Omics*; Hallenbeck, P.C., Ed.; Springer International Publishing: Cham, Switzerland, 2017; pp. 163–191, ISBN 978-3-319-51365-2.
15. Kondou, Y.; Nakazawa, M.; Higashi, S.; Watanabe, M.; Manabe, K. Equal-Quantum Action Spectra Indicate Fluence-Rate-Selective Action of Multiple Photoreceptors for Photomovement of the Thermophilic Cyanobacterium *Synechococcus Elongatus*. *Photochem. Photobiol.* **2007**, *73*, 90–95. [CrossRef]
16. Kennis, J.T.M.; Gobets, B.; van Stokkum, I.H.M.; Dekker, J.P.; van Grondelle, R.; Fleming, G.R. Light Harvesting by Chlorophylls and Carotenoids in the Photosystem I Core Complex of *Synechococcus Elongatus*: A Fluorescence Upconversion Study. *J. Phys. Chem. B* **2001**, *105*, 4485–4494. [CrossRef]
17. Lahmi, R.; Sendersky, E.; Perelman, A.; Hagemann, M.; Forchhammer, K.; Schwarz, R. Alanine Dehydrogenase Activity Is Required for Adequate Progression of Phycobilisome Degradation during Nitrogen Starvation in *Synechococcus Elongatus* PCC 7942. *J. Bacteriol.* **2006**, *188*, 5258–5265. [CrossRef]
18. Damjanović, A.; Vaswani, H.M.; Fromme, P.; Fleming, G.R. Chlorophyll Excitations in Photosystem I of *Synechococcus Elongatus*. *J. Phys. Chem. B* **2002**, *106*, 10251–10262. [CrossRef]
19. Pfündel, E.E.; Klughammer, C.; Meister, A.; Cerovic, Z.G. Deriving Fluorometer-Specific Values of Relative PSI Fluorescence Intensity from Quenching of F_0 Fluorescence in Leaves of *Arabidopsis Thaliana* and *Zea Mays*. *Photosynth. Res.* **2013**, *114*, 189–206. [CrossRef]
20. Krause, G.H.; Weis, E. Chlorophyll Fluorescence and Photosynthesis: The Basics. *Annu. Rev. Plant Biol.* **1991**, *42*, 313–349. [CrossRef]
21. Zouni, A.; Witt, H.-T.; Kern, J.; Fromme, P.; Krauss, N.; Saenger, W.; Orth, P. Crystal Structure of Photosystem II from *Synechococcus Elongatus* at 3.8 Å Resolution. *Nature* **2001**, *409*, 739–743. [CrossRef]
22. van Kooten, O.; Snel, J.F.H. The Use of Chlorophyll Fluorescence Nomenclature in Plant Stress Physiology. *Photosynth. Res.* **1990**, *25*, 147–150. [CrossRef]
23. Lohscheider, J.N.; Strittmatter, M.; Küpper, H.; Adamska, I. Vertical Distribution of Epibenthic Freshwater Cyanobacterial *Synechococcus* Spp. Strains Depends on Their Ability for Photoprotection. *PLoS ONE* **2011**, *6*, e20134. [CrossRef]
24. Papageorgiou, G.C.; Govindjee (Eds.) *Chlorophyll a Fluorescence: A Signature of Photosynthesis*; Advances in Photosynthesis and Respiration; Kluwer Academic: Dordrecht, The Netherlands, 2004; ISBN 978-1-4020-3217-2.
25. Komenda, J.; Koblížek, M.; Prašil, O. Characterization of Processes Responsible for the Distinct Effect of Herbicides DCMU and BNT on Photosystem II Photoinactivation in Cells of the Cyanobacterium *Synechococcus* Sp. PCC 7942. *Photosynth. Res.* **2000**, *63*, 135–144. [CrossRef]
26. Baker, N.R. A Possible Role for Photosystem II in Environmental Perturbations of Photosynthesis. *Physiol. Plant* **1991**, *81*, 563–570. [CrossRef]
27. Björkman, O.; Demmig, B. Photon Yield of O_2 Evolution and Chlorophyll Fluorescence Characteristics at 77 K among Vascular Plants of Diverse Origins. *Planta* **1987**, *170*, 489–504. [CrossRef] [PubMed]
28. Matyssek, R.; Herppich, W.B. Experimentelle Pflanzenökologie: Chlorophyllfluoreszenzanalyse. In *Handbuch der Geodäsie*; Freeden, W., Rummel, R., Eds.; Springer Reference Naturwissenschaften; Springer: Berlin/Heidelberg, Germany, 2018; pp. 1–56. ISBN 978-3-662-46900-2.

29. Ogawa, T.; Sonoike, K. Effects of Bleaching by Nitrogen Deficiency on the Quantum Yield of Photosystem II in *Synechocystis* sp. PCC 6803 Revealed by Chl Fluorescence Measurements. *Plant Cell Physiol.* **2016**, *57*, 558–567. [CrossRef] [PubMed]
30. Santabarbara, S.; Villafiorita Monteleone, F.; Remelli, W.; Rizzo, F.; Menin, B.; Casazza, A.P. Comparative Excitation-emission Dependence of the F_V/F_M Ratio in Model Green Algae and Cyanobacterial Strains. *Physiol. Plant.* **2019**, *166*, 351–364. [CrossRef]
31. Görl, M.; Sauer, J.; Baier, T.; Forchhammer, K. Nitrogen-Starvation-Induced Chlorosis in *Synechococcus* PCC 7942: Adaptation to Long-Term Survival. *Microbiology* **1998**, *144*, 2449–2458. [CrossRef]
32. Caruso, F.; Saikin, S.K.; Solano, E.; Huelga, S.F.; Aspuru-Guzik, A.; Plenio, M.B. Probing Biological Light-Harvesting Phenomena by Optical Cavities. *Phys. Rev. B* **2012**, *85*, 125424. [CrossRef]
33. Boca, A.; Miller, R.; Birnbaum, K.M.; Boozer, A.D.; McKeever, J.; Kimble, H.J. Observation of the Vacuum Rabi Spectrum for One Trapped Atom. *Phys. Rev. Lett.* **2004**, *93*, 233603. [CrossRef]
34. Konrad, A.; Metzger, M.; Kern, A.M.; Brecht, M.; Meixner, A.J. Controlling the Dynamics of Förster Resonance Energy Transfer inside a Tunable Sub-Wavelength Fabry—Pérot-Resonator. *Nanoscale* **2015**, *7*, 10204–10209. [CrossRef]
35. Rippka, R.; Stanier, R.Y.; Deruelles, J.; Herdman, M.; Waterbury, J.B. Generic Assignments, Strain Histories and Properties of Pure Cultures of Cyanobacteria. *Microbiology* **1979**, *111*, 1–61. [CrossRef]
36. Klotz, A.; Georg, J.; Bučinská, L.; Watanabe, S.; Reimann, V.; Januszewski, W.; Sobotka, R.; Jendrossek, D.; Hess, W.R.; Forchhammer, K. Awakening of a Dormant Cyanobacterium from Nitrogen Chlorosis Reveals a Genetically Determined Program. *Curr. Biol.* **2016**, *26*, 2862–2872. [CrossRef]

Rammler, T.; Wackenhut, F.; Rapp, J.; zur Oven-Krockhaus, S.; Forchhammer, K.; Meixner, A.J.; Harter, K. Analysis of Fast Fluorescence Kinetics of a Single Cyanobacterium Trapped in an Optical Microcavity. Plants **2023**, *12*, 607.

https://doi.org/10.3390/plants12030607

Anteil an gemeinschaftlicher Veröffentlichung:

Es handelt sich bei diesem noch nicht veröffentlichten Manuskript um den zweiten Hauptteil dieser Arbeit. Die wissenschaftliche Grundidee stammt von mir. Anregungen dazu stammen von meinen Co-Autoren. Die Projektplanung, der Aufbau der verwendeten Messinstrumente und die Datenaufnahme wurden von mir durchgeführt. Die Daten wurden von Frank Wackenhut und mir verarbeitet. Das Züchten der Cyanobakterien übernahm Johanna Rapp. Die Datenevaluation wurde von Frank Wackenhut, Karl Forchhammer, Klaus Harter, Alfred J. Meixner und mir durchgeführt. Das Manuskript wurde ebenfalls von Frank Wackenhut, Karl Forchhammer, Klaus Harter, Alfred J. Meixner und mir erstellt.

7.3 Combining Optical Strong Mode Coupling with Polaritonic Coupling in a λ/2 Fabry Pérot Microresonator (veröffentlicht)

THE JOURNAL OF PHYSICAL CHEMISTRY C
A JOURNAL OF THE AMERICAN CHEMICAL SOCIETY

pubs.acs.org/JPCC Article

Combining Optical Strong Mode Coupling with Polaritonic Coupling in a λ/2 Fabry−Pérot Microresonator

Saeed Nosrati, Tim Rammler, Alfred J. Meixner,* and Frank Wackenhut*

Cite This: J. Phys. Chem. C 2021, 125, 13024−13032 Read Online

ACCESS | Metrics & More | Article Recommendations | Supporting Information

ABSTRACT: Strong coupling has attracted much research interest motivated by the possibility to tune the energy levels of molecules enabling to control and modify chemical reactions. Strong coupling leads to the formation of new hybrid modes and is caused by coherent energy exchange between the individual constituents. Such a coherent energy exchange occurs when the coupling rate exceeds the damping rate of the individual components and has been observed for highly diverse systems. Here, we present a strongly coupled hybrid system consisting of a thin TDBC J-aggregate film inside an optical subwavelength microresonator coupled to a second microresonator. This hybrid structure combines strong coupling of purely optical modes with strong light−matter interaction. The coupling strength and damping sensitively depend on the position and concentration of the coupled molecules in the microresonator structure. Such a coupled system can be modeled by coupled damped oscillators, which allows to determine the coupling and damping constants. We show that the individual components making up the coupled hybrid system cannot be treated individually, but the coupled system needs to be considered as a whole. As a consequence, altering one parameter does influence the whole coupled system, and the individual components need to be carefully adapted to each other to achieve efficient coupling. These results can have important consequences for the field of optoelectronics or polaritonic chemistry.

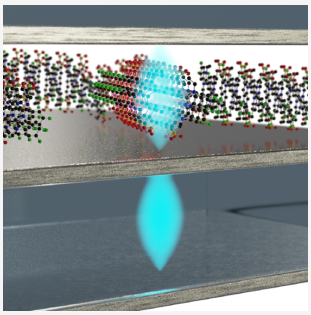

INTRODUCTION

The ability of optical microresonators to confine light to subwavelength dimensions and to control light−matter interaction has drawn considerable research attention during the past decades. The interaction between an emitter and a confined optical field can be classified into weak and strong coupling,[1,2] which is defined by the ratio of the damping and coupling rates of the emitter and the microresonator. The coupled system is in the weak coupling regime when the individual damping rates are larger than the coupling rate. In this case, the emission properties of the emitter are exclusively altered by the Purcell effect,[3−8] which has been reported in plasmonic antennas,[9] microcavities,[10−12] or photonic crystals[13,14] and can be used to control Förster resonant energy transfer and photobleaching in optical environments.[15−20] In contrast, strong coupling occurs when the coupling rate exceeds the individual damping rates, and the individual modes are hybridized into new polaritonic modes[21] or supermodes.[22] The hybridized modes are spectrally separated by the Rabi splitting, and strong coupling manifests itself by anticrossing of the coupled modes in the dispersion of the coupled hybrid system.[23,24] This is a very attractive aspect of strong coupling because it enables to tune the energy levels of the hybrid system and to modify and control chemical reactivity.[25−27] In general, strong coupling can be achieved in a variety of diverse systems, which can be subdivided into coupling of purely optical modes and coupling of an optical mode with matter. Strong coupling of purely optical modes, leading to the formation of supermodes, has been observed in phase-locked semiconductor laser arrays,[28] coupled optical or photonic fibers,[29,30] or photonic crystal cavities,[31−33] just to mention a few. On the other hand, strong light−matter coupling has been studied extensively and was realized for microresonators,[1,34−40] photonic crystals,[41−43] micropillars,[44,45] microdisks,[46] microtubes,[47] and plasmonic systems.[48−54] Especially λ/2 Fabry−Pérot microresonators are attractive to achieve strong coupling due to their ease of fabrication, flexible geometry, and accessibility; hence, many examples have been reported in the literature, for example, microresonators containing photonic molecules,[55−58] polymers,[59,60] inorganic quantum wells,[61−64] quantum dots,[45,65] or organic semiconductors.[66−68] More recently, studies of organic materials have been focused on J-aggregates of cyanine dye molecules due to the fact that they possess narrow and sharp peaks in their absorption and photoluminescence spectra, making them ideal to achieve strong light−matter coupling.[69−74]

Received: April 3, 2021
Revised: May 22, 2021
Published: June 4, 2021

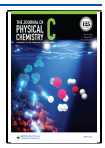

https://doi.org/10.1021/acs.jpcc.1c03004
J. Phys. Chem. C 2021, 125, 13024−13032

In this paper, we focus on strong coupling between a thin TDBC J-aggregate film and a pair of optically coupled $\lambda/2$ Fabry–Pérot microresonators. We demonstrate that two types of strong coupling occur simultaneously in the coupled system. The first type is strong coupling of two purely optical modes of the adjacent microresonators, in which the coupling strength can be tuned by varying the thickness of the central shared mirror and is described in detail in our previous work.[2] The second type is strong coupling between matter, that is, the TDBC J-aggregate molecules and the optical modes of the coupled microresonators. We demonstrate that the coupling strength and damping of the hybrid system can be tuned by the optical microresonator modes, the lateral position of the TDBC film, and the TDBC concentration in the film. Additionally, we show that the hybrid system can be modeled by a coupled harmonic oscillator approach, which allows to determine all important parameters, that is, the coupling and damping constants. These results prove that such a coupled system is well suited to investigate the basic concepts of strong coupling between optical modes and electronically excited molecules because it enables to have full control over all parameters. Finally, we point out the importance to precisely control the systems' geometry, which needs to be taken carefully into account in the fields of polaritonic chemistry or long-range coupling of two emitters.

EXPERIMENTAL SECTION

Preparation of TDBC–PVA Film. A thin film of 5,6-dichloro-2-[[5,6-dichloro-1-ethyl-3-(4-sulfobutyl)-benzimidazol-2-ylidene]propenyl]-1-ethyl-3-(4-sulfobutyl)-benzimidazolium hydroxide, inner salt, sodium salt (TDBC; purchased from FEW Chemicals, Germany, and used without further purification), in a poly(vinyl alcohol) (PVA) matrix was deposited by spin-coating on the SiO_2 spacer layer covering the central mirror. TDBC molecules are dissolved in a solution of PVA (1 wt %) in water, where they are forming J-aggregates.[75] The TDBC J-aggregate solution was prepared at a concentration of 10^{-2} mol/L, if no other concentration is explicitly mentioned. The solution was sonicated for 20 min, and a 5 μL droplet of the TDBC J-aggregate/PVA solution was spin-coated on top of the SiO_2 layer for 30 s at 1700 rpm angular velocity. This procedure has been precisely repeated for all microresonators. The average thickness of obtained film is 30 nm as measured with an atomic force microscope (AFM).

Coupled Microresonator Preparation. The layers forming the microresonator structure are deposited by electron beam evaporation. The lower microresonator with a fixed optical path length consists of two silver mirrors, where a 50 nm thick silver layer is evaporated on a clean glass cover slide, followed by a 10 nm gold and a dielectric SiO_2 layer of 148 nm. The thickness of this SiO_2 layer is chosen to tune the resonance of the fixed resonator and to spectrally overlap it with the maximum absorption peak of TDBC J-aggregate molecules at 590 nm (Figure 1a). Afterward, the central shared mirror is created by evaporating a 24 nm silver layer on top of this SiO_2 layer. In addition, the central mirror is coated with a 10 nm gold layer and a SiO_2 spacer layer with variable thicknesses ranging from 50 to 185 nm. This dielectric SiO_2 spacer layer allows to control the spatial position of a thin TDBC–PVA film inside the upper microresonator. The topmost mirror is a lens coated with an 80 nm silver layer, a 10 nm thick gold layer, and a 10 nm SiO_2 layer and forms, together with the central mirror, the tunable microresonator.

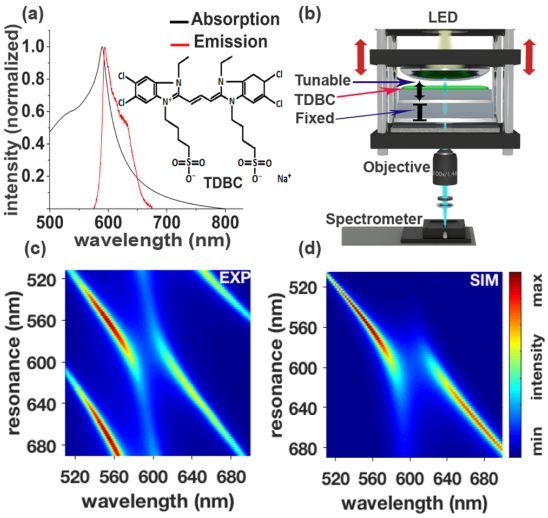

Figure 1. (a) Absorption and emission spectra of a TDBC J-aggregate film including the chemical structure of TDBC. (b) Graphic sketch of two adjacent Fabry–Pérot microresonators, where the upper resonator is tunable and the lower one is fixed. The two resonators are separated by a shared central silver mirror. A white light LED is used to record the transmission spectrum of the coupled microresonators. (c) Experimental transmission spectra of the strongly coupled microresonators with an anticrossing dispersion of the two resonator modes. The horizontal axis is the wavelength of the transmitted light as recorded by the spectrometer, and the vertical axis indicates the resonance of the tunable resonator. (d) Corresponding simulation using coupled harmonic oscillators, where the resonance frequencies are fitted to the experimental data. In (c) two additional resonator modes are visible, which have not been considered in the simulations. The color map illustrates the intensity of the transmission spectra.

Experimental Setup. A home-built holder and a piezo actuator (8302 Picomotor Actuator, Newport) are used to assemble the coupled microresonators.[2] The two coupled microresonators consist of three silver mirrors, where the central silver mirror is shared between the two microresonators. In this geometry, the topmost mirror (a silver-coated lens) can be moved toward the shared mirror to reach the $\lambda/2$ region of the visible spectral range. A white light LED is mounted on top of the microresonator holder to acquire transmission spectra. The transmitted light is collected via an oil immersion objective lens (NA = 1.4) from below, and the detected signal is guided to a spectrometer with a thermoelectrically cooled CCD camera (PIXIS 100, Princeton Instruments, USA).

RESULTS AND DISCUSSION

The molecular structure of TDBC is shown in Figure 1a, together with the experimental absorption and emission spectra of TDBC J-aggregate film that have a small Stokes shift between the absorption and emission maximum. A schematic drawing of the experimental setup consisting of two adjacent Fabry–Pérot microresonators and a home-built confocal microscope is shown in Figure 1b. It consists of two adjacent microresonators with an additional thin TDBC film on top of a SiO_2 spacer layer deposited on the central mirror. The optical path length of the upper resonator can be

https://doi.org/10.1021/acs.jpcc.1c03004
J. Phys. Chem. C 2021, 125, 13024–13032

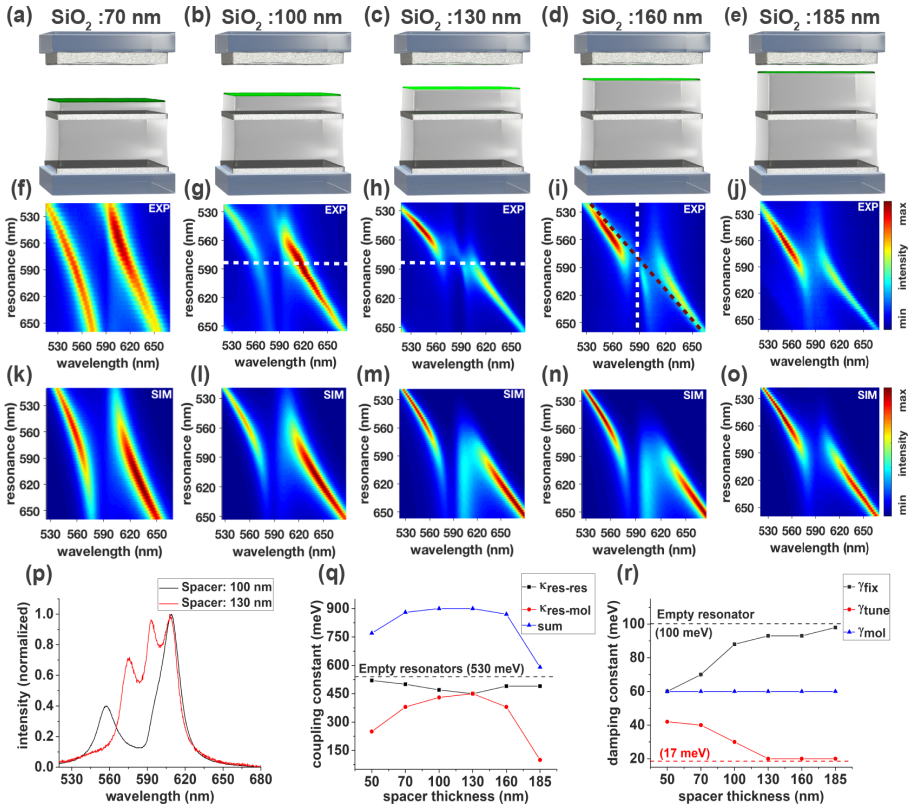

Figure 2. (a–e) Schematic drawings of five different experimental situations showing two coupled microresonators, where a thin TDBC J-aggregate film is deposited on a SiO_2 spacer layer inside the upper resonator. The thickness of the spacer layer is indicated on top of the respective scheme. (f–j) Experimental white light transmission spectra of coupled microresonators with the enclosed TDBC J-aggregate film. (k–o) Corresponding simulated transmission spectra. (p) Two exemplary experimental transmission spectra of the coupled system (marked by the white dashed line in (g, h)) with a spacer thickness 100 nm (black line) and 130 nm (red line). (q) Coupling constants between two microresonators ($\kappa_{res-res}$, black squares) and between the tunable resonator and the molecules ($\kappa_{res-mol}$, red dots) as a function of the TDBC film position. Sum of both coupling constants (blue triangles) to show the maximum coupling strength of the whole system. (r) Damping constants of the coupled system for different positions of the TDBC film. The individual components are TDBC molecules (γ_{mol}, blue triangles), fixed microresonator (γ_{fix}, black squares), and tunable microresonator (γ_{tune}, red dots).

tuned by piezo actuators, while it is fixed for the lower one. In the following, we will refer to the upper and lower microresonator as the tunable and fixed microresonator. The transmission spectra of the empty coupled microresonator are shown in Figure 1c.

Strong coupling between the purely optical microresonator modes results in the formation of supermodes and frequency splitting,[22] which can be seen in Figure 1c at ~600 nm. The vertical axis in Figure 1c represents the resonance wavelengths of the tunable microresonator. The two transmitted peaks show an anticrossing dispersion at ~600 nm and are separated by the Rabi splitting when the resonances of the fixed and tunable microresonator coincide. The Rabi splitting obtained from the experimental data is ~23 nm. Figure 1d shows the corresponding calculations based on two coupled harmonic oscillators, which are described in detail in ref 2 and in the Supporting Information. An additional higher and lower order mode is observed in the experimental spectra, which are not considered in the calculations. This model enables to reproduce the experimental data in Figure 1c and allows to determine the resonator–resonator coupling constant $\kappa_{res-res}$ and the corresponding damping constants of the fixed γ_{fix} and tunable γ_{tune} microresonator. The respective damping and coupling constants of the coupled microresonator shown in Figure 1c are γ_{fix} = 100 meV, γ_{tune} = 17 meV, and $\kappa_{res-res}$ = 530 meV. The coupling constant is larger than the individual damping constants; hence, the two microresonators are within the strong coupling regime. The next step is to investigate coupling between a thin TDBC film with such a coupled microresonator structure. In this case, there are two types of strong coupling mechanisms: first, strong coupling of the two purely optical modes of the microresonators and, second, strong light–matter coupling between the optical microresonator modes and the TDBC J-aggregates. As we have shown in ref 2, strong coupling between the two microresonators can be tuned by varying the thickness of the central mirror, which is kept constant for all experiments presented here. First, we want to show that coupling between the TDBC film and the optical modes sensitively depends on the spatial position of the film within the tunable microresonator. This can be achieved by varying the thickness of the dielectric SiO_2

https://doi.org/10.1021/acs.jpcc.1c03004
J. Phys. Chem. C 2021, 125, 13024–13032

spacer layer deposited on the central mirror, as schematically illustrated in Figures 2a–e.

The transmission spectra of these five microresonators are shown in Figures 2f–j for dielectric layer thicknesses ranging from 70 nm in (f) to 185 nm in (j). The resonance frequency of the lower microresonator is fixed and is adjusted to be close to the absorption maximum of the TDBC J-aggregate film at 590 nm, as marked by the white dashed line in Figure 2i. Each line along the vertical axis in Figure 2 represents a transmission spectrum recorded for a distinct optical path length of the tunable microresonator, and the respective resonance wavelength is shown exemplarily by the black dashed line in Figure 2i and on the vertical axis. Clear anticrossing can be observed when the resonance of the tunable microresonator is spectrally overlapping with the resonance of the fixed one or the absorption of the TDBC J-aggregate film. Two experimental transmission spectra of the coupled system marked by the white dashed line in Figures 2g and 2h are presented in Figure 2p. The red line shows a transmission spectrum, where the TDBC J-aggregate film is placed close to the center of the tunable microresonator (130 nm SiO_2 spacer layer), and clearly three modes due to strong coupling of the two microresonators with the TDBC J-aggregate molecules can be resolved. On the contrary, light–matter coupling is weaker when the film is moved away from the center of the tunable microresonator (100 nm SiO_2 spacer layer, black line) and is only observable as a shoulder at ∼600 nm. Apart from the coupling strength, the damping of the coupled system is obviously altered by the position of the TDBC J-aggregate film, which can directly be seen by the larger/smaller line widths in Figures 2f,h as compared to the empty microresonator shown in Figure 1c. A parameter influencing the spectral dispersion of the modes is the ratio of the damping constants of the individual modes, which is illustrated in Figure S1 of the Supporting Information. Figure S1 shows that the maximum intensity of the transmission spectra follows more closely the mode with lower damping, while it becomes symmetric when the damping constants of both modes are the same. This dispersion behavior allows to draw the conclusion that the damping of the fixed and tunable microresonators in Figure 2f is similar, while damping of the tunable microresonator is smaller in Figure 2h. Three damped coupled harmonic oscillators are used to model the two coupled microresonators and the TDBC J-aggregate molecules. The corresponding calculations are presented in Figures 2k–o, where the resonance frequency, damping, and coupling constant of the fixed and tunable resonators are varied to reproduce the experimental data. The resonance frequency and the damping constant of the oscillator used to model the TDBC J-aggregate molecules are determined from the absorption spectrum acquired outside of the microresonator and are kept constant for all calculations. All parameters used in the calculations are summarized in Table S1. The coupling constants obtained from the calculations are presented in Figure 2q as a function of the spacer layer thickness. The data points are connected by lines as a guide to the eye. The resonator–resonator coupling constant $\kappa_{res-res}$ for an empty microresonator with a 50 nm SiO_2 spacer layer is $\kappa_{res-res}$ = 530 meV (indicated by the black dashed line in Figure 2q), and there is a small reduction to 520 meV by the presence of the TDBC J-aggregate film inside the tunable microresonator. Moving the TDBC J-aggregate film closer to the center leads to a decrease of the resonator–resonator coupling constant with a minimum of $\kappa_{res-res}$ = 450 meV, when the film is in the center of the tunable microresonator. A further increase of the spacer layer thickness is accompanied by an increase of $\kappa_{res-res}$. In contrast, the resonator–molecule coupling constant ($\kappa_{res-mol}$) increases rapidly from 250 meV at 50 nm to 450 meV at 130 nm. Interestingly, both coupling constants, $\kappa_{res-res}$ and $\kappa_{res-mol}$, are the same when the TDBC J-aggregate film is in the center of the tunable microresonator. Afterward, the resonator–molecule coupling constant steadily decreases to 100 meV for a 185 nm thick SiO_2 layer. Maximum strong coupling of the whole system (blue triangles) is shown by the sum of the molecule–molecule and molecule–resonator coupling constant, which is nearly constant for spacer layer thicknesses ranging from 70 to 160 nm. The corresponding damping constants obtained from the coupled harmonic oscillator approach for different positions of TDBC J-aggregate film in the tunable microresonator are illustrated in Figure 2r. The damping constant γ_{mol}, attributed to the TDBC J-aggregate molecules (blue triangles), is kept constant at 60 meV and is determined from the line width of the absorption spectrum of the TDBC J-aggregate molecules outside of the microresonator. The damping constants of the empty coupled microresonators are γ_{fix} = 100 meV for the fixed resonator (black dashed line) and γ_{tune} = 17 meV for the tunable resonator (red dashed line). An increase of the damping of the tunable resonator by the SiO_2 spacer layer is expected due to scattering at the SiO_2 surface, which can be assumed to be constant for the different SiO_2 spacer layer thicknesses. However, introducing a SiO_2 spacer layer of 70 nm with a TDBC J-aggregate film on top leads to strong increase of the damping constant of the tunable microresonator from γ_{tune} = 17 meV to γ_{tune} = 40 meV. This increase can be understood because the TDBC molecules mainly increase damping due to absorption and experience weaker coupling to the optical modes when they are located closer to the central mirror. Moving the film toward the center of the tunable microresonator leads to a reduction of the damping constant of the tunable resonator from γ_{tune} = 42 to 20 meV, which is quite close to the damping constant of the empty microresonator. At 130 nm the TDBC J-aggregate film is approximately located at the center of the tunable resonator, leading to the strongest coupling between the molecules and the microresonator, and results in the lowest damping. Interestingly, introducing the TDBC J-aggregate film into the tunable resonator significantly reduces the damping of the fixed resonator from γ_{fix} = 100 to 60 meV (black dots in Figure 2r), and a further increase of the SiO_2 layer thickness increases the damping constant back to 98 meV, which is close to the value obtained from the empty resonator. Hence, introducing a thin TDBC J-aggregate film in the coupled resonator structure close to the central mirror reduces the damping of the fixed resonator, while it increases the damping of the tunable one. On the other hand, there is nearly no influence on the damping of the tunable resonator when the film is in its center. This result shows that the coupled system needs to be considered as a whole, and influencing one parameter does have an impact on all other parameters.

One advantage of such a coupled microresonator structure is that all parameters can be easily and precisely adjusted by choosing different layer and mirror thicknesses. For instance, the fixed resonator can either be on or off resonance with the TDBC J-aggregate film, which is shown in Figure 3.

https://doi.org/10.1021/acs.jpcc.1c03004
J. Phys. Chem. C 2021, 125, 13024–13032

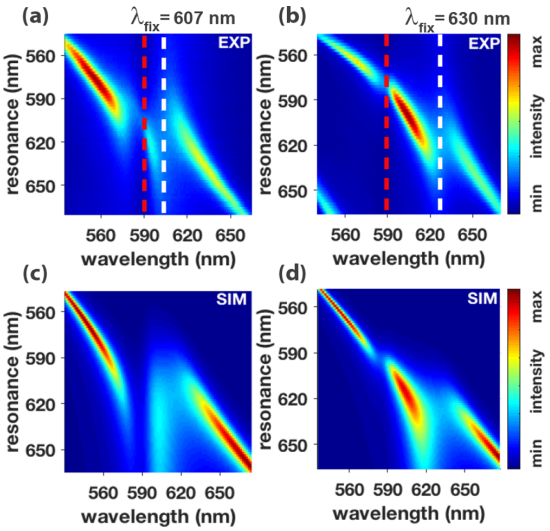

Figure 3. Experimental transmission spectra of two coupled microresonators with an additional TDBC J-aggregate film on top of a 160 nm SiO_2 spacer layer in the tunable resonator. The absorption maximum of the film is illustrated by the red dashed line. The white dashed line indicates the resonance wavelength of the fixed resonator at 607 nm in (a) and at 630 nm in (b). (c) and (d) show respective simulations for (a) and (b).

Figures 3a and 3b show experimental transmission spectra of two coupled microresonators, where the resonances of the fixed one are indicated by the white dashed line at 607 nm (a) and 630 nm (b). Hence, in the first case the resonance is closer to the absorption maximum of the TDBC molecules at 590 nm (red dashed line), while it is off resonant in the second case. The corresponding calculations based on three coupled oscillators are shown in Figures 3c,d are in good agreement with the experimental data. Similar to Figure 2, there is strong coupling between the two microresonators, which can be seen by the anticrossing at 607 and 630 nm in (a) and (b), respectively. The corresponding resonator−resonator coupling constants are $\kappa_{res-res}$ = 490 meV (a) and $\kappa_{res-res}$ = 430 meV (b). A second anticrossing dispersion can be observed close to the red dashed line, which is caused by coupling between the tunable microresonator and the TDBC J-aggregate film. Interestingly, detuning the resonance of the fixed microresonator from the TDBC J-aggregate film absorption maximum reduces coupling of the molecules to the tunable resonator from $\kappa_{res-mol}$ = 380 to 140 meV. This again shows that the coupled system needs to be considered as a whole, and strong coupling of the TDBC film to the tunable resonator can be influenced by detuning the fixed resonator.

According to the Jaynes−Cummings model, the Rabi splitting energy ΔE is proportional to the square root of the number of coherently coupled molecules n:[76]

$$\Delta E = 2\sqrt{n}\hbar g_0 \quad (1)$$

where g_0 is the coupling constant. To investigate this influence, TDBC J-aggregate films with different concentrations were deposited on the SiO_2 spacer layer. The results are presented in Figure 4.

In Figures 4a−c, thin TDBC J-aggregate films with concentrations of 10^{-2}, 10^{-3}, and 10^{-4} mol L^{-1} were spin-coated on top of a 160 nm SiO_2 spacer layer. For this experiment, the resonance of the fixed resonator (white dashed line) was slightly detuned from the absorption maximum of the TDBC J-aggregate film (red dashed line) to clearly distinguish anticrossing caused by coupling of the two resonators at 630 nm from coupling of the molecules with the resonators. The Rabi splitting caused by strong coupling of the TDBC J-aggregate molecules with the tunable resonator can be clearly observed in Figures 4a,b at 590 nm, while it is not visible anymore for the lowest concentration in Figure 4c. Corresponding simulations of the coupled systems are shown in Figures 4d−f. The damping constant of the fixed resonator is γ_{fix} = 99 meV, and the damping constants of tunable resonators γ_{tune} are 16, 17, and 17 meV in Figures 4d−f. The resonator−resonator coupling constant is $\kappa_{res-res}$ = 430, 400, and 370 meV in Figures 4d−f, respectively. As suggested by eq 1, reducing the number of coupled molecules reduces the Rabi splitting, and consequently the observed coupling of the molecules to the tunable resonator decreases from $\kappa_{res-mol}$ = 140 meV to 130 meV and 30 meV in Figures 4d−f. Figure 4g shows a similar experiment, where the resonance of the tunable resonator is kept constant (indicated by a gray dashed line in (a)) and the number of TDBC J-aggregate molecules is decreased by photobleaching. Rabi splitting due to coupling of the TDBC J-aggregate molecules with the tunable resonator can be clearly observed before photobleaching (black solid line) and decreases from 14 to 5 nm after photobleaching (black dashed line). After photobleaching, the upper polariton peak of the coupled system is hardly visible. The emission spectra before (red solid line) and after (red dashed line) photobleaching clearly show that the number of emitters was strongly reduced. The last emission spectrum is multiplied by a factor of 20 for better visibility. The whole bleaching series is shown in Figures 4h,i, where each spectrum is obtained after a 2 min bleaching interval, and in total 10 transmission and emission spectra were recorded. The emission spectra in Figure 4i are obtained directly after the acquisition of the transmission spectra in Figure 4h but before the next bleaching interval. To ensure that the spectral shift in Figure 4h is not due to a drift of the piezo actuators, transmission spectra of the coupled resonators are measured before irradiating the sample with the high-power laser, which is shown in Figure S2. These results show how the observed strong light−matter interaction can be influenced by the number of coupled molecules and illustrate the importance to control both the concentration and the spatial position of the coupled molecules to achieve efficient strong coupling.

CONCLUSIONS

In summary, we have presented the existence of two types of strong coupling existing in the same coupled system, that is, strong coupling between the optical modes of two microresonators combined with strong light−matter interaction between the coupled microresonator and TDBC J-aggregates. We have shown that the number and the spatial position of the coupled molecules have a strong impact on the coupling and damping of the coupled hybrid system. Furthermore, coupling can be tuned by adjusting the resonance of either the fixed or tunable resonator. Additionally, we have shown that the coupled system can be modeled by three damped coupled harmonic oscillators allowing to determine all important

https://doi.org/10.1021/acs.jpcc.1c03004
J. Phys. Chem. C 2021, 125, 13024−13032

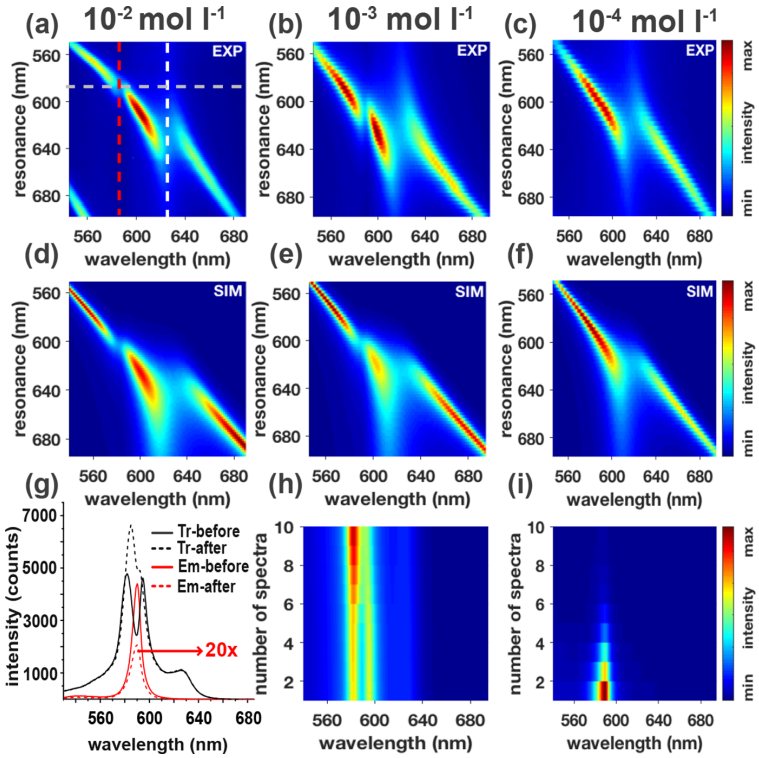

Figure 4. Experimental transmission spectra of two coupled microresonators with a thin film of TDBC J-aggregate molecules on a 160 nm SiO_2 spacer layer. The absorption maximum of the film is illustrated by the red dashed line and the white dashed line indicates the resonance wavelength of the fixed resonator at 630 nm in (a). The concentration of the TDBC J-aggregate molecules in the film is 10^{-2} mol L^{-1} in (a), 10^{-3} mol L^{-1} in (b), and 10^{-4} mol L^{-1} in (c). The Rabi splitting at 590 nm caused by strong coupling of the TDBC J-aggregate film and the tunable resonator decreases from (a) to (c). Corresponding simulations based on three coupled harmonic oscillators are shown in (d) to (f). (g) Transmission and emission spectra before (solid line) and after (dashed line) photobleaching cycles, where the resonance of the tunable resonator is kept constant (indicated by a gray dashed line in (a)). The emission spectrum after photobleaching is multiplied by a factor of 20 for better visibility. (h) Reduction of the Rabi splitting by photobleaching of the TDBC J-aggregate molecules using a laser at 470 nm. (i) Experimental emission spectra of the TDBC J-aggregate molecules corresponding to the transmission spectra shown in (h).

parameters. We find that the optimal coupling scenario is achieved with a thin film located in the center of one microresonator and when the resonance of the other resonator is matching the resonance of the coupled emitter. Interestingly, the results clearly show that the individual components of the hybrid system cannot be treated individually, but the system needs to be considered as a whole. For example, detuning the resonance of the fixed resonator reduces the coupling strength of the molecules located in the tunable resonator without a physical change of this resonator. Consequently, the system presented here is an excellent example where strong coupling between optical modes and strong light−matter coupling is combined in a single hybrid system.

These results could have important consequences for applications in optoelectronics; for example, let us assume that coupling of an emitter and a receiver over a large spatial separation shall be achieved via the optical modes of several intermediate resonators. We have shown that already a very thin film in the center of the first resonator is sufficient to achieve efficient coupling of the emitter to the optical resonator mode. However, not only efficient coupling to the resonator is needed, but also the geometry of the intermediate resonators needs to be carefully adapted to the optical properties of the emitter to achieve efficient transfer to the receiver. Additionally, the results presented here could also be exploited in the field of polaritonic chemistry, where one resonator could be a fixed and robust reaction resonator, and the optical mode density, and hence the coupling strength of the reactant, could be adjusted by an adjacent tuning resonator.

■ ASSOCIATED CONTENT

Supporting Information

The Supporting Information is available free of charge at https://pubs.acs.org/doi/10.1021/acs.jpcc.1c03004.

Details of the theoretical coupled harmonic oscillator model and used parameters to model two coupled microresonators and the molecules located in the tunable resonator; theoretical and experimental transmission spectra of two coupled microresonators (PDF)

■ AUTHOR INFORMATION

Corresponding Authors

Frank Wackenhut − *Institute of Physical and Theoretical Chemistry, Eberhard Karls University, 72076 Tübingen,*

https://doi.org/10.1021/acs.jpcc.1c03004
J. Phys. Chem. C 2021, 125, 13024−13032

Germany; orcid.org/0000-0001-6554-6600; Email: frank.wackenhut@uni-tuebingen.de

Alfred J. Meixner – *Institute of Physical and Theoretical Chemistry, Eberhard Karls University, 72076 Tübingen, Germany*; orcid.org/0000-0002-0187-2906; Email: alfred.meixner@uni-tuebingen.de

Authors

Saeed Nosrati – *Institute of Physical and Theoretical Chemistry, Eberhard Karls University, 72076 Tübingen, Germany*

Tim Rammler – *Institute of Physical and Theoretical Chemistry, Eberhard Karls University, 72076 Tübingen, Germany*

Complete contact information is available at: https://pubs.acs.org/10.1021/acs.jpcc.1c03004

Notes

The authors declare no competing financial interest.

■ ACKNOWLEDGMENTS

The authors gratefully acknowledge funding by the German Research Foundation (DFG, ME 1600/13-3).

■ REFERENCES

(1) Lidzey, D. G.; Bradley, D. D. C.; Virgili, T.; Armitage, A.; Skolnick, M. S.; Walker, S. Room temperature polariton emission from strongly coupled organic semiconductor Microcavities. *Phys. Rev. Lett.* **1999**, *82* (16), 3316−3319.

(2) Junginger, A.; Wackenhut, F.; Stuhl, A.; Blendinger, F.; Brecht, M.; Meixner, A. J. Tunable strong coupling of two adjacent optical $\lambda/2$ Fabry-Pérot microresonators. *Opt. Express* **2020**, *28* (1), 485−493.

(3) Purcell, E. M.; Torrey, H. C.; Pound, R. V. Resonance absorption by nuclear magnetic moments in a solid. *Phys. Rev.* **1946**, *69* (1−2), 37.

(4) Agranovich, V.; Litinskaia, M.; Lidzey, D. Microcavity polaritons in materials with weak intermolecular interaction. *Phys. Status Solidi B* **2002**, *234* (1), 130−138.

(5) Chizhik, A.; Schleifenbaum, F.; Gutbrod, R.; Chizhik, A.; Khoptyar, D.; Meixner, A. J.; Enderlein, J. Tuning the fluorescence emission spectra of a single molecule with a variable optical subwavelength metal microcavity. *Phys. Rev. Lett.* **2009**, *102* (7), 073002.

(6) Chizhik, A. I.; Chizhik, A. M.; Kern, A. M.; Schmidt, T.; Potrick, K.; Huisken, F.; Meixner, A. J. Measurement of vibrational modes in single SiO_2 nanoparticles using a tunable metal resonator with optical subwavelength dimensions. *Phys. Rev. Lett.* **2012**, *109* (22), 223902.

(7) Konrad, A.; Trost, A.-L.; Skandary, S.; Hussels, M.; Meixner, A. J.; Karapetyan, N. V.; Brecht, M. Manipulating the excitation transfer in Photosystem I using a Fabry-Perot metal resonator with optical subwavelength dimensions. *Phys. Chem. Chem. Phys.* **2014**, *16* (13), 6175−6181.

(8) Skolnick, M.; Fisher, T.; Whittaker, D. Strong coupling phenomena in quantum microcavity structures. *Semicond. Sci. Technol.* **1998**, *13* (7), 645.

(9) Koenderink, A. F. On the use of Purcell factors for plasmon antennas. *Opt. Lett.* **2010**, *35* (24), 4208−4210.

(10) Masenelli, B.; Gagnaire, A.; Berthelot, L.; Tardy, J.; Joseph, J. Controlled spontaneous emission of a tri (8-hydroxyquinoline) aluminum layer in a microcavity. *J. Appl. Phys.* **1999**, *85* (6), 3032−3037.

(11) Kern, A. M.; Zhang, D.; Brecht, M.; Chizhik, A. I.; Failla, A. V.; Wackenhut, F.; Meixner, A. J. Enhanced single-molecule spectroscopy in highly confined optical fields: from $\lambda/2$-Fabry-Pérot resonators to plasmonic nano-antennas. *Chem. Soc. Rev.* **2014**, *43* (4), 1263−1286.

(12) Steiner, M.; Schleifenbaum, F.; Stupperich, C.; Virgilio Failla, A.; Hartschuh, A.; Meixner, A. J. Microcavity controlled single molecule fluorescence. *ChemPhysChem* **2005**, *6* (10), 2190−2196.

(13) Canet-Ferrer, J.; Martínez, L. J.; Prieto, I.; Alen, B.; Munoz-Matutano, G.; Fuster, D.; Gonzalez, Y.; Dotor, M. L.; Gonzalez, L.; Postigo, P. A.; Martínez-Pastor, J. P. Purcell effect in photonic crystal microcavities embedding InAs/InP quantum wires. *Opt. Express* **2012**, *20* (7), 7901−7914.

(14) Noda, S.; Fujita, M.; Asano, T. Spontaneous-emission control by photonic crystals and nanocavities. *Nat. Photonics* **2007**, *1* (8), 449−458.

(15) Cang, H.; Liu, Y.; Wang, Y.; Yin, X.; Zhang, X. Giant suppression of photobleaching for single molecule detection via the Purcell effect. *Nano Lett.* **2013**, *13* (12), 5949−5953.

(16) Konrad, A.; Metzger, M.; Kern, A. M.; Brecht, M.; Meixner, A. J. Controlling the dynamics of Förster resonance energy transfer inside a tunable sub-wavelength Fabry-Pérot-resonator. *Nanoscale* **2015**, *7* (22), 10204−10209.

(17) Pelton, M. Modified spontaneous emission in nanophotonic structures. *Nat. Photonics* **2015**, *9* (7), 427−435.

(18) Schleifenbaum, F.; Kern, A. M.; Konrad, A.; Meixner, A. J. Dynamic control of Förster energy transfer in a photonic environment. *Phys. Chem. Chem. Phys.* **2014**, *16* (25), 12812−12817.

(19) Stefani, F. D.; Vasilev, K.; Bocchio, N.; Gaul, F.; Pomozzi, A.; Kreiter, M. Photonic mode density effects on single-molecule fluorescence blinking. *New J. Phys.* **2007**, *9* (2), 21.

(20) Wientjes, E.; Renger, J.; Curto, A. G.; Cogdell, R.; Van Hulst, N. F. Strong antenna-enhanced fluorescence of a single light-harvesting complex shows photon antibunching. *Nat. Commun.* **2014**, *5* (1), 1−7.

(21) Hopfield, J. J. Theory of the contribution of excitons to the complex dielectric constant of crystals. *Phys. Rev.* **1958**, *112* (5), 1555−1567.

(22) Atlasov, K. A.; Karlsson, K. F.; Rudra, A.; Dwir, B.; Kapon, E. Wavelength and loss splitting in directly coupled photonic-crystal defect microcavities. *Opt. Express* **2008**, *16* (20), 16255−16264.

(23) Dovzhenko, D. S.; Ryabchuk, S. V.; Rakovich, Y. P.; Nabiev, I. R. Light-matter interaction in the strong coupling regime: configurations, conditions, and applications. *Nanoscale* **2018**, *10* (8), 3589−3605.

(24) Norris, T. B.; Rhee, J. K.; Sung, C. Y.; Arakawa, Y.; Nishioka, M.; Weisbuch, C. Time-resolved vacuum Rabi oscillations in a semiconductor quantum microcavity. *Phys. Rev. B: Condens. Matter Mater. Phys.* **1994**, *50* (19), 14663−14666.

(25) Herrera, F.; Spano, F. C. Cavity-controlled chemistry in molecular ensembles. *Phys. Rev. Lett.* **2016**, *116* (23), 238301.

(26) Lather, J.; Bhatt, P.; Thomas, A.; Ebbesen, T. W.; George, J. Cavity catalysis by cooperative vibrational strong coupling of reactant and solvent molecules. *Angew. Chem., Int. Ed.* **2019**, *58* (31), 10635−10638.

(27) Thomas, A.; Jayachandran, A.; Lethuillier-Karl, L.; Vergauwe, R. M.; Nagarajan, K.; Devaux, E.; Genet, C.; Moran, J.; Ebbesen, T. W. Ground state chemistry under vibrational strong coupling: dependence of thermodynamic parameters on the Rabi splitting energy. *Nanophotonics* **2020**, *9* (2), 249−255.

(28) Kapon, E.; Katz, J.; Yariv, A. Supermode analysis of phase-locked arrays of semiconductor lasers. *Opt. Lett.* **1984**, *9* (4), 125−127.

(29) Guan, C.; Yuan, L.; Shi, J. Supermode analysis of multicore photonic crystal fibers. *Opt. Commun.* **2010**, *283* (13), 2686−2689.

(30) Zhou, J. Analytical formulation of super-modes inside multi-core fibers with circularly distributed cores. *Opt. Express* **2014**, *22* (1), 673−688.

(31) Atlasov, K. A.; Rudra, A.; Dwir, B.; Kapon, E. Large mode splitting and lasing in optimally coupled photonic-crystal microcavities. *Opt. Express* **2011**, *19* (3), 2619−2625.

(32) Cai, T.; Bose, R.; Solomon, G. S.; Waks, E. Controlled coupling of photonic crystal cavities using photochromic tuning. *Appl. Phys. Lett.* **2013**, *102* (14), 141118.

(33) Chalcraft, A.; Lam, S.; Jones, B.; Szymanski, D.; Oulton, R.; Thijssen, A.; Skolnick, M.; Whittaker, D.; Krauss, T.; Fox, A. Mode structure of coupled L3 photonic crystal cavities. *Opt. Express* **2011**, *19* (6), 5670−5675.
(34) Coles, D. M.; Somaschi, N.; Michetti, P.; Clark, C.; Lagoudakis, P. G.; Savvidis, P. G.; Lidzey, D. G. Polariton-mediated energy transfer between organic dyes in a strongly coupled optical microcavity. *Nat. Mater.* **2014**, *13* (7), 712−719.
(35) Dovzhenko, D.; Mochalov, K.; Vaskan, I.; Kryukova, I.; Rakovich, Y.; Nabiev, I. Polariton-assisted splitting of broadband emission spectra of strongly coupled organic dye excitons in tunable optical microcavity. *Opt. Express* **2019**, *27* (4), 4077−4089.
(36) Hobson, P. A.; Barnes, W. L.; Lidzey, D.; Gehring, G.; Whittaker, D.; Skolnick, M.; Walker, S. Strong exciton-photon coupling in a low-Q all-metal mirror microcavity. *Appl. Phys. Lett.* **2002**, *81* (19), 3519−3521.
(37) Johnson, S.; Dolan, P R.; Grange, T.; Trichet, A. A. P.; Hornecker, G.; Chen, Y. C.; Weng, L.; Hughes, G. M.; Watt, A. A. R.; Auffeves, A.; Smith, J. M. Tunable cavity coupling of the zero phonon line of a nitrogen-vacancy defect in diamond. *New J. Phys.* **2015**, *17* (12), 122003.
(38) Shalabney, A.; George, J.; Hutchison, J.; Pupillo, G.; Genet, C.; Ebbesen, T. W. Coherent coupling of molecular resonators with a microcavity mode. *Nat. Commun.* **2015**, *6* (1), 5981.
(39) Thompson, J.; Zwickl, B.; Jayich, A.; Marquardt, F.; Girvin, S.; Harris, J. Strong dispersive coupling of a high-finesse cavity to a micromechanical membrane. *Nature* **2008**, *452* (7183), 72−75.
(40) Wang, D.; Kelkar, H.; Martin-Cano, D.; Utikal, T.; Götzinger, S.; Sandoghdar, V. Coherent coupling of a single molecule to a scanning Fabry-Perot microcavity. *Phys. Rev. X* **2017**, *7* (2), 021014.
(41) Pellegrino, D.; Pagliano, F.; Genco, A.; Petruzzella, M.; Van Otten, F.; Fiore, A. Deterministic control of radiative processes by shaping the mode field. *Appl. Phys. Lett.* **2018**, *112* (16), 161110.
(42) Samutpraphoot, P.; Đorđević, T.; Ocola, P. L.; Bernien, H.; Senko, C.; Vuletić, V.; Lukin, M. D. Strong coupling of two individually controlled atoms via a nanophotonic cavity. *Phys. Rev. Lett.* **2020**, *124* (6), 063602.
(43) Yoshie, T.; Scherer, A.; Hendrickson, J.; Khitrova, G.; Gibbs, H.; Rupper, G.; Ell, C.; Shchekin, O.; Deppe, D. Vacuum Rabi splitting with a single quantum dot in a photonic crystal nanocavity. *Nature* **2004**, *432* (7014), 200−203.
(44) Hennessy, K.; Badolato, A.; Winger, M.; Gerace, D.; Atatüre, M.; Gulde, S.; Fält, S.; Hu, E. L.; Imamoßlu, A. Quantum nature of a strongly coupled single quantum dot-cavity system. *Nature* **2007**, *445* (7130), 896−899.
(45) Reithmaier, J. P.; Sęk, G.; Löffler, A.; Hofmann, C.; Kuhn, S.; Reitzenstein, S.; Keldysh, L.; Kulakovskii, V.; Reinecke, T.; Forchel, A. Strong coupling in a single quantum dot-semiconductor microcavity system. *Nature* **2004**, *432* (7014), 197−200.
(46) Peter, E.; Senellart, P.; Martrou, D.; Lemaître, A.; Hours, J.; Gérard, J. M.; Bloch, J. Exciton-photon strong-coupling regime for a single quantum dot embedded in a microcavity. *Phys. Rev. Lett.* **2005**, *95* (6), 067401.
(47) Wang, J.; Yin, Y.; Hao, Q.; Zhang, Y.; Ma, L.; Schmidt, O. G. Strong coupling in a photonic molecule formed by trapping a microsphere in a microtube cavity. *Adv. Opt. Mater.* **2018**, *6* (1), 1700842.
(48) Baranov, D. G.; Munkhbat, B.; Länk, N. O.; Verre, R.; Käll, M.; Shegai, T. Circular dichroism mode splitting and bounds to its enhancement with cavity-plasmon-polaritons. *Nanophotonics* **2020**, *9* (2), 283−293.
(49) Chikkaraddy, R.; De Nijs, B.; Benz, F.; Barrow, S. J.; Scherman, O. A.; Rosta, E.; Demetriadou, A.; Fox, P.; Hess, O.; Baumberg, J. J. Single-molecule strong coupling at room temperature in plasmonic nanocavities. *Nature* **2016**, *535* (7610), 127−130.
(50) Konrad, A.; Kern, A. M.; Brecht, M.; Meixner, A. J. Strong and coherent coupling of a plasmonic nanoparticle to a subwavelength Fabry-Pérot resonator. *Nano Lett.* **2015**, *15* (7), 4423−4428.
(51) Pelton, M.; Storm, S. D.; Leng, H. Strong coupling of emitters to single plasmonic nanoparticles: exciton-induced transparency and Rabi splitting. *Nanoscale* **2019**, *11* (31), 14540−14552.
(52) Törmä, P.; Barnes, W. L. Strong coupling between surface plasmon polaritons and emitters: a review. *Rep. Prog. Phys.* **2015**, *78* (1), 013901.
(53) Vasa, P.; Lienau, C. Strong light-matter interaction in quantum emitter/metal hybrid nanostructures. *ACS Photonics* **2018**, *5* (1), 2−23.
(54) Bisht, A.; Cuadra, J.; Wersäll, M.; Canales, A.; Antosiewicz, T. J.; Shegai, T. Collective strong light-matter coupling in Hierarchical microcavity-plasmon-exciton systems. *Nano Lett.* **2019**, *19* (1), 189−196.
(55) Bayer, M.; Gutbrod, T.; Reithmaier, J.; Forchel, A.; Reinecke, T.; Knipp, P.; Dremin, A.; Kulakovskii, V. Optical modes in photonic molecules. *Phys. Rev. Lett.* **1998**, *81* (12), 2582.
(56) Galbiati, M.; Ferrier, L.; Solnyshkov, D. D.; Tanese, D.; Wertz, E.; Amo, A.; Abbarchi, M.; Senellart, P.; Sagnes, I.; Lemaitre, A.; Galopin, E.; Malpuech, G.; Bloch, J. Polariton condensation in photonic molecules. *Phys. Rev. Lett.* **2012**, *108* (12), 126403.
(57) Rakovich, Y. P.; Donegan, J. F. Photonic atoms and molecules. *Laser Photonics Rev.* **2010**, *4* (2), 179−191.
(58) Zhang, M.; Wang, C.; Hu, Y.; Shams-Ansari, A.; Ren, T.; Fan, S.; Lončar, M. Electronically programmable photonic molecule. *Nat. Photonics* **2019**, *13* (1), 36−40.
(59) Plumhof, J. D.; Stöferle, T.; Mai, L.; Scherf, U.; Mahrt, R. F. Room-temperature Bose−Einstein condensation of cavity exciton-polaritons in a polymer. *Nat. Mater.* **2014**, *13* (3), 247−252.
(60) Takada, N.; Kamata, T.; Bradley, D. D. Polariton emission from polysilane-based organic microcavities. *Appl. Phys. Lett.* **2003**, *82* (12), 1812−1814.
(61) Christmann, G.; Butté, R.; Feltin, E.; Mouti, A.; Stadelmann, P. A.; Castiglia, A.; Carlin, J.-F.; Grandjean, N. Large vacuum Rabi splitting in a multiple quantum well GaN-based microcavity in the strong-coupling regime. *Phys. Rev. B: Condens. Matter Mater. Phys.* **2008**, *77* (8), 085310.
(62) Houdré, R.; Weisbuch, C.; Stanley, R. P.; Oesterle, U.; Pellandini, P.; Ilegems, M. Measurement of cavity-polariton dispersion curve from angle-resolved photoluminescence experiments. *Phys. Rev. Lett.* **1994**, *73* (15), 2043−2046.
(63) Pradeesh, K.; Baumberg, J.; Prakash, G. V. Strong exciton-photon coupling in inorganic-organic multiple quantum wells embedded low-Q microcavity. *Opt. Express* **2009**, *17* (24), 22171−22178.
(64) Weisbuch, C.; Nishioka, M.; Ishikawa, A.; Arakawa, Y. Observation of the coupled exciton-photon mode splitting in a semiconductor quantum microcavity. *Phys. Rev. Lett.* **1992**, *69* (23), 3314−3317.
(65) Groß, H.; Hamm, J. M.; Tufarelli, T.; Hess, O.; Hecht, B. Near-field strong coupling of single quantum dots. *Sci. Adv.* **2018**, *4* (3), No. eaar4906.
(66) Agranovich, V.; Litinskaia, M.; Lidzey, D. G. Cavity polaritons in microcavities containing disordered organic semiconductors. *Phys. Rev. B: Condens. Matter Mater. Phys.* **2003**, *67* (8), 085311.
(67) Lidzey, D. G.; Bradley, D.; Skolnick, M.; Virgili, T.; Walker, S.; Whittaker, D. Strong exciton-photon coupling in an organic semiconductor microcavity. *Nature* **1998**, *395* (6697), 53−55.
(68) Nagarajan, K.; George, J.; Thomas, A.; Devaux, E.; Chervy, T.; Azzini, S.; Joseph, K.; Jouaiti, A.; Hosseini, M. W.; Kumar, A.; et al. Conductivity and photoconductivity of a p-Type organic semiconductor under ultrastrong coupling. *ACS Nano* **2020**, *14* (8), 10219−10225.
(69) Bonnand, C.; Bellessa, J.; Plenet, J. Properties of surface plasmons strongly coupled to excitons in an organic semiconductor near a metallic surface. *Phys. Rev. B: Condens. Matter Mater. Phys.* **2006**, *73* (24), 245330.
(70) George, J.; Wang, S.; Chervy, T.; Canaguier-Durand, A.; Schaeffer, G.; Lehn, J.-M.; Hutchison, J. A.; Genet, C.; Ebbesen, T. W.

https://doi.org/10.1021/acs.jpcc.1c03004
J. Phys. Chem. C 2021, 125, 13024−13032

Ultra-strong coupling of molecular materials: spectroscopy and dynamics. *Faraday Discuss.* **2015**, *178* (0), 281−294.
(71) Kang, E. S. H.; Chen, S.; Sardar, S.; Tordera, D.; Armakavicius, N.; Darakchieva, V.; Shegai, T.; Jonsson, M. P. Strong plasmon-exciton coupling with directional absorption features in optically thin hybrid nanohole metasurfaces. *ACS Photonics* **2018**, *5* (10), 4046−4055.
(72) Munkhbat, B.; Wersäll, M.; Baranov, D. G.; Antosiewicz, T. J.; Shegai, T. Suppression of photo-oxidation of organic chromophores by strong coupling to plasmonic nanoantennas. *Sci. Adv.* **2018**, *4* (7), No. eaas9552.
(73) Tischler, J. R.; Bradley, M. S.; Zhang, Q.; Atay, T.; Nurmikko, A.; Bulović, V. Solid state cavity QED: Strong coupling in organic thin films. *Org. Electron.* **2007**, *8* (2−3), 94−113.
(74) Vasista, A. B.; Barnes, W. L. Molecular monolayer strong coupling in dielectric soft microcavities. *Nano Lett.* **2020**, *20* (3), 1766−1773.
(75) Gentile, M. J.; Núñez-Sánchez, S.; Barnes, W. L. Optical field-enhancement and subwavelength field-confinement using excitonic nanostructures. *Nano Lett.* **2014**, *14* (5), 2339−2344.
(76) Fox, M.; *Quantum Optics: An Introduction*; OUP: Oxford, 2006; Vol. *15*.

https://doi.org/10.1021/acs.jpcc.1c03004
J. Phys. Chem. C 2021, 125, 13024−13032

https://doi.org/10.1021/acs.jpcc.1c03004

Anteil an gemeinschaftlicher Veröffentlichung:

Es handelt sich hierbei um eine Nebenveröffentlichung. Wie auch diese Arbeit behandelt sie Mikroresonatoren. Die wissenschaftliche Grundidee dieser Veröffentlichung hatten Saeed Nosrati, Alfred J. Meixner und Frank Wackenhut. Die Projektplanung wurden von Saeed Nosrati durchgeführt. Bei der Datenaufnahme war ich beratend tätig. Der Aufbau einer der verwendeten Messinstrumente erfolgte durch mich. Die Datenverarbeitung wurde von Saeed Nosrati und Frank Wackenhut durchgeführt. Die Daten wurden von Saeed Nosrati und Frank Wackenhut evaluiert. Das Manuskript wurde von Saeed Nosrati, Alfred J. Meixner und Frank Wackenhut erstellt, wobei ich inhaltlich unterstützend und beratend tätig war.

7.4 Accumulation and penetration behavior of hypericin in glioma tumor spheroids studied by fluorescence microscopy and confocal fluorescence lifetime imaging microscopy (veröffentlicht)

Analytical and Bioanalytical Chemistry (2022) 414:4849–4860
https://doi.org/10.1007/s00216-022-04107-2

RESEARCH PAPER

Accumulation and penetration behavior of hypericin in glioma tumor spheroids studied by fluorescence microscopy and confocal fluorescence lifetime imaging microscopy

Miriam C. Bassler[1,2] · Tim Rammler[2] · Frank Wackenhut[1] · Sven zur Oven-Krockhaus[2] · Ivona Secic[1] · Rainer Ritz[3] · Alfred J. Meixner[2] · Marc Brecht[1,2]

Received: 18 March 2022 / Revised: 14 April 2022 / Accepted: 28 April 2022 / Published online: 10 May 2022

Abstract
Glioblastoma WHO IV belongs to a group of brain tumors that are still incurable. A promising treatment approach applies photodynamic therapy (PDT) with hypericin as a photosensitizer. To generate a comprehensive understanding of the photosensitizer-tumor interactions, the first part of our study is focused on investigating the distribution and penetration behavior of hypericin in glioma cell spheroids by fluorescence microscopy. In the second part, fluorescence lifetime imaging microscopy (FLIM) was used to correlate fluorescence lifetime (FLT) changes of hypericin to environmental effects inside the spheroids. In this context, 3D tumor spheroids are an excellent model system since they consider 3D cell–cell interactions and the extracellular matrix is similar to tumors in vivo. Our analytical approach considers hypericin as probe molecule for FLIM and as photosensitizer for PDT at the same time, making it possible to directly draw conclusions of the state and location of the drug in a biological system. The knowledge of both state and location of hypericin makes a fundamental understanding of the impact of hypericin PDT in brain tumors possible. Following different incubation conditions, the hypericin distribution in peripheral and central cryosections of the spheroids were analyzed. Both fluorescence microscopy and FLIM revealed a hypericin gradient towards the spheroid core for short incubation periods or small concentrations. On the other hand, a homogeneous hypericin distribution is observed for long incubation times and high concentrations. Especially, the observed FLT change is crucial for the PDT efficiency, since the triplet yield, and hence the O_2 activation, is directly proportional to the FLT. Based on the FLT increase inside spheroids, an incubation time > 30 min is required to achieve most suitable conditions for an effective PDT.

Keywords Hypericin · Fluorescence microscopy · Fluorescence lifetime · Photodynamic therapy · Tumor spheroid

Introduction

Cancer is still one of the most threatening diseases of humankind. In 2020, 19.3 million new cancer cases were diagnosed worldwide [1]. Promising therapeutic and treatment approaches are constantly being developed to prolong the patient's life and hopefully allow a complete cure. One of these auspicious treatments is photodynamic therapy (PDT) using various photosensitizers, including hypericin [2] that was already characterized chemically [3] and optically [4–7]. In PDT, photosensitizers that enter the excited triplet state upon irradiation either damage the biological substrate directly or generate reactive oxygen species inducing photodamage [8]. So far, PDT with hypericin has been applied to several cancer types, including dermal, colon, and

✉ Frank Wackenhut
frank.wackenhut@reutlingen-university.de

✉ Marc Brecht
marc.brecht@reutlingen-university.de

[1] Process Analysis and Technology (PA&T), Reutlingen University, Alteburgstr. 150, 72762 Reutlingen, Germany

[2] Institute of Physical and Theoretical Chemistry, University of Tübingen, Auf der Morgenstelle 18, 72076 Tübingen, Germany

[3] Department of Neurosurgery, Schwarzwald-Baar Clinic, Klinikstr. 11, 78052 Villingen-Schwenningen, Germany

bladder cancer [9, 10]. However, its applicability in glioma tumor treatment necessitates further research.

Most hypericin PDT applications are often tested in 2D cell cultures in vitro [11] after hypericin treatment of the cells. Various studies in cell monolayers showed that hypericin is mainly enriched in the endoplasmic reticulum or Golgi apparatus [12, 13], and others also observed hypericin accumulation in mitochondria or lysosomes [14]. This localization was proven to be dependent on incubation time of hypericin [14]. Cellular uptake mechanisms of hypericin in monolayer experiments were discussed to be either an energy-dependent uptake, e.g., by receptor-mediated endocytosis/pinocytosis [15], or passively driven by diffusion through the cell membrane [16]. Compared to 2D cell cultures, tumor spheroids are a more representative in vitro model, since they better reflect 3D cell–cell interactions and the extracellular matrix (ECM) of tumors in vivo (Fig. 1) [17]. Due to a decreasing nutrient and oxygen supply towards the spheroid center, tumor spheroids can be differentiated into three zones: a proliferative zone at the spheroid's margin, a transitional zone of quiescent cells, and a necrotic core [18]. Differences between these zones can be ascribed to the cell cycle, as proliferative cells participate in the cell cycle and quiescent cells have left it. Hence, the response of a drug can directly be linked to the cell cycle state of the tumor cells within each zone [19]. Often, a higher response of anticancer drugs was detected in proliferative compared to quiescent cells that are less targeted by the drugs [20]. The drug response can further depend on microenvironmental conditions, like hypoxia, acidosis, complex tumor cell–cell interactions, or the ECM constituents [21], which can be perfectly studied with tumor spheroid models.

The analysis of drug-spheroid interactions is useful for a successful therapeutic implementation, as shown in several studies [22], but only a small number of studies were performed on spheroids and hypericin [23–26]. In this context, the distribution and localization of the drug as well as the cellular uptake and transfer by the tumor spheroids are important [27]. Huygens et al. investigated hypericin penetration in bladder spheroids related to the expression of E-cadherin, a cell molecule contributing to cell–cell adhesion [25]. An additional study involving bladder spheroids concluded that the ECM might also contribute to the hypericin penetration and in this case limit the hypericin intake [24]. Hypericin's lipophilicity and binding ability to surrounding lipoproteins additionally influence its accumulation and permeation behavior [28]. A deep understanding of these intake and penetration mechanisms in spheroids is essential to realize its full potential for PDT.

An additional impact on PDT performance is expected to result from different local cellular environments throughout tumors and tumor spheroids, caused by the changing availability of nutrients, oxygen, and glucose [22, 29]. Based on the prevalent conditions, like hypoxia or starvation, within spheroids, cells can react differently in terms of metabolism, gene, and protein expression [30, 31], which might directly influence not only the hypericin accumulation but also the effectiveness of PDT. A powerful tool to detect these cellular, environmental variations is fluorescence lifetime imaging microscopy (FLIM). In FLIM, the excited state decay rate of a probe molecule, represented by the fluorescence lifetime (FLT), is measured with the spatial resolution of a confocal microscope and can be related to the local cellular environment [32]. Several studies used FLIM to measure FLT changes of NAD(P)H in 2D and 3D cell culture systems [33, 34] or to reveal the cell cycle S-phase of spheroids [35]. Recent single molecule studies of hypericin show that the local environment has a strong influence on its FLT [4, 6].

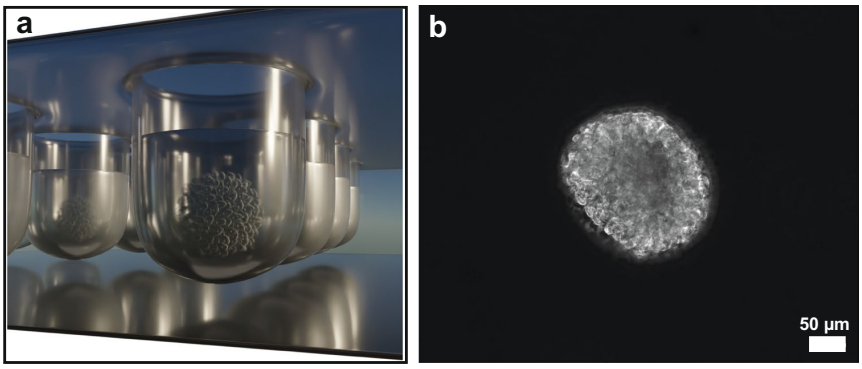

Fig. 1 **a** Schematic illustration of the tumor spheroid formation in a 96-well plate by the forced-floating method. Due to a cell-repellent coating inside the well, the included cell suspension is forced to agglomerate to a spheroid. Additionally, the round bottom of the cavities promotes and accelerates the formation of spherical tumor clusters in reproducible size and shape. **b** Phase contrast image of a U-87 MG tumor spheroid with a seeding density of 1500 cells/cm^2 and a cultivation time of 35 h + 15 min

However, applications of FLIM with hypericin in general and especially in a cellular context are rare. Nevertheless, FLIM was used to analyze the hypericin release from nanocarriers or pharmaceutical preparations into the intracellular environment [36] and the interaction and localization of hypericin in cells [37, 38]. For this reason, FLIM with hypericin can be used to investigate microenvironmental effects within tumor spheroids, particularly regarding the application of PDT. The obtained knowledge about the cellular environment is essential for the adaptation and optimization of the PDT treatment.

In our study, we use fluorescence microscopy and FLIM to investigate hypericin within glioblastoma tumor spheroids. Fluorescence microscopy allows us to study the accumulation and distribution of hypericin to better understand the extent and dynamics of its penetration into glioma spheroids. Additional analyses of spheroids by FLIM enable the detection of cellular environmental effects due to hypericin FLT changes, from which valuable information about prevalent cellular conditions can be deduced. Since hypericin functions not only as probe molecule for FLIM, but is considered as photosensitizer for PDT at the same time, the detailed analysis of hypericin's localization and its environmental characterization in the glioma spheroids allows us to understand the impact of both parameters on the hypericin PDT for brain tumors. For our investigations, spheroids are treated for variable incubation times and with different incubation concentrations to examine hypericin uptake, permeation, and FLT. For each incubation condition, spheroid cryosections are prepared and outer and inner sections are compared to study local differences. Our results generate a fundamental understanding of photosensitizer interactions with tumor spheroids as complex biological systems. This knowledge delivers vital information to improve PDT efficiency in tumors and is applicable to other photosensitizers used for PDT treatment.

Materials and methods

Cell culture

Tumor spheroids derive from the glioblastoma cell line U-87 MG (ATCC® HTB-14™). U-87 MG spheroids were generated and cultivated in round-bottom, cell-repellent 96-well plates for 24 h (Greiner bio One) at a density of 1500 cells/cm^2 using the forced-floating method (Fig. 1a). Eagle's Minimum Essential Medium (MEM, no glutamine and phenol red, Gibco™) serves as cultivation medium and is supplemented with 10% fetal bovine serum (FBS), 1% L-glutamine, 1% sodium pyruvate, and 1% penicillin–streptomycin (all purchased from Gibco™). Cultivation conditions for the U-87 MG spheroids encompassed 37 °C and a 5% CO_2 atmosphere.

Hypericin incubation for different incubation times and concentrations

All preparation steps were performed in the dark. Stock solutions of hypericin (PhytoLab GmbH & Co.KG) in DMSO (Molecular Probes™ D12345) with concentrations of 0.1 mM, 0.25 mM, 0.125 mM, 0.05 mM, and 0.005 mM were prepared and frozen at − 20 °C. Aliquots of this stock were freshly thawed for each experiment. After thawing, a 1:100 dilution of hypericin (1 µM, 2.5 µM, 1.25 µM, 0.5 µM, 0.05 µM) in complete cultivation medium and additional 10% FBS was prepared. This procedure was adopted from [15]. Excess medium was removed from each single well and the hypericin/MEM mixture was added at a final concentration of 1 µM for incubation time experiments. Spheroids were incubated for 5 min, 30 min, 125 min, 10 h + 30 min, and 35 h + 15 min in the hypericin cultivation medium, respectively. Varying hypericin concentrations (2.5 µM, 1.25 µM, 0.5 µM, 0.05 µM) were incubated for a predefined time period of 30 min. Non-hypericin-incubated control spheroids were treated with a 1:100 dilution of DMSO in complete cultivation medium and additional 10% FBS for 30 min. Afterwards, the hypericin and control incubation were disrupted by removing the incubation medium and applying three washing steps with phosphate buffered saline (PBS). Following the washing steps, U-87 MG spheroids were directly preserved by fixation. All experiments were executed in triplicate.

Spheroid fixation and nucleus staining

All preparation steps were performed in the dark. PBS of the spheroid washing steps was discarded, followed by a formaldehyde fixation (ROTI®Histofix 4%) with an incubation time of 30 min. Afterwards, the fixation solution was removed, and spheroids were washed three times with PBS. For cell nucleus staining, Hoechst 33342 was used as fluorescence dye (NucBlue™ Live ReadyProbes™ Reagent (Hoechst 33342), Invitrogen™). The Hoechst 33342 solution was diluted in PBS according to the NucBlue Reagent protocol. This dilution was added to each U-87 MG spheroid and incubated for 20 min at room temperature. Nucleus staining with Hoechst 33342 was not performed for FLIM. After fixation and Hoechst 33342 incubation, a series of three PBS washing steps was applied. Fixed tumor spheroids were stored in PBS in the dark until microtome sectioning.

Spheroid sectioning

For preparation of microtome sections, tumor spheroids were embedded in the cryoembedding medium OCT (optimal cutting temperature compound, Sakura Finetek™ Tissue-Tek™ O.C.T. Compound). Each spheroid was transferred into one embedding mold filled up with OCT and quickly cooled down with dry ice to prevent water crystal formation. The frozen OCT blocks were cut with a cryomicrotome (Leica CM3050 S cryostat) and cryosections of 5 µm thickness were produced. Temperatures of the cooling chamber and the sample holder were kept at − 30 °C. Subsequent cutting series of the whole spheroids were manufactured to obtain outer and inner sections of the tumor spheroids. All cutting sections were placed onto a coverslip and stored in the dark for further microscopic imaging experiments.

Fluorescence and brightfield microscopy

Acquisition of fluorescence images was performed with a Zeiss Axio Observer.Z1 fluorescence microscope equipped with a mercury short-arc lamp (HXP-120) and colored LEDs (Colibri light source, Zeiss). For the fluorescence excitation of Hoechst 33342, a Colibri LED with 385 nm was used. The corresponding filter cube (Zeiss filter set 49) had an excitation wavelength range of 335–383 nm, whereas emission was detected between 420 and 470 nm. LED intensity was set to 70% and the exposure time for one Hoechst image was 250 ms. Hypericin fluorescence was excited with the HXP-120 lamp in a filter wavelength region of 580–604 nm and fluorescence emission was detected between 615 and 725 nm (Zeiss filter set 71). The HXP-120 lamp intensity was defined at the highest intensity level and fluorescence images were acquired with 150 ms per image. All fluorescence images were recorded with a 20 × objective lens (Zeiss Plan-Apochromat 20 × /0.80, Ph 2, M27) and fluorescence detection was conducted with an Axiocam 506 microscope camera. Tumor spheroid sections were imaged by z-stacking. Subsequent image processing entailed the application of the extended depth-of-field fusion algorithm using wavelet transform in order to obtain a sharp composite image (Zeiss ZEN 2.3 software, blue edition). Brightfield microscopy was accomplished with a second Zeiss Axio Observer microscope (Z1/7) using a white light LED. All brightfield images were recorded with a 20 × objective lens (Zeiss LD A-Plan 20 × /0.35, Ph 1) and an Axiocam 305 microscope camera. White light LED intensity was set to 11.5% and exposure times per image were equal to 18 ms.

Fluorescence lifetime imaging microscopy

The time-resolved confocal fluorescence microscope was custom-built. The used light source was a pulsed laser diode (LDH P–C-405, PicoQuant GmbH, Germany) with an excitation wavelength of 405 nm and at a repetition frequency of 40 MHz. The pulse duration was 50 ps. The beam was focused on the sample by an oil immersion objective lens (Zeiss Plan-Apochromat, 100 ×, 1.4 Oil DIC, Carl Zeiss AG, Germany). An additional long-pass filter (EdgeBasic™ Long Wave Pass 405) separated the excitation light from the sample emission. Confocal imaging was achieved using a single photon avalanche diode (SPAD; PDM series, Micro Photon Devices, Italy). By coupling the SPAD with a time-correlated single photon counting (TCSPC) unit (HydraHarp 400, PicoQuant GmbH, Germany) and the pulsed laser diode, time-resolved measurements were performed. The scanning stage, SPAD, laser diode, and TCSPC unit were controlled by SymphoTime® software (PicoQuant GmbH, Germany). Time-resolved measurements were also analyzed and evaluated with the SymphoTime® software.

Fluorescence spectra acquisition

Fluorescence spectra were recorded using a spectrometer (Acton SP300i, Princeton Instruments, USA) with a thermoelectrically cooled CCD camera (PIXIS 100, Princeton Instruments, USA). The wavelength range of the spectrometer was set to 480–760 nm. A long-pass filter (EdgeBasic™ Long Wave Pass 405) was applied to remove the laser signal from the spectra. The acquisition time for each hypericin spectrum was 250 ms. Fluorescence spectra were acquired using Winspec® software (Princeton Instruments, USA).

Results

A first characterization of whole tumor spheroids was performed by fluorescence microscopy. Figure 2a shows a fluorescence intensity image of a 5-min-incubated tumor spheroid before sectioning. Hypericin fluorescence is shown in red, whereas the nucleus staining with Hoechst 33342 is shown in blue. Based on these colors, cell nuclei and hypericin can be identified in the spheroids (Fig. 2a). Afterwards, cryosections were prepared to analyze and compare the spatial distribution of hypericin in outer and inner spheroid regions in more detail. Figure 2b and c show fluorescence intensity images of outer and inner sections. As a consequence of spheroid cutting, section elongation, compression, and regions without cells can occur. Thus, sections might appear differently shaped or patchy compared to whole spheroids. The technically limited size of the FLIM images (24 × 24 µm) required us to stitch together successive images to cover the entire width of the spheroid sections with FLIM and superimpose them on the respective brightfield images. Figure 2d and e show the respective composite images.

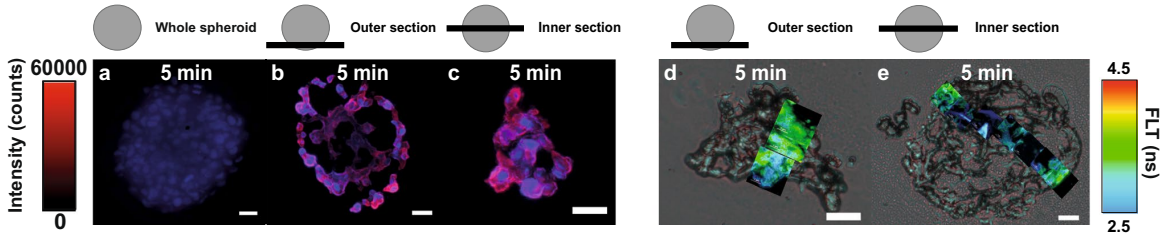

Fig. 2 Investigation of hypericin penetration into spheroids by comparing outer and inner spheroid sections. The penetration was examined with fluorescence microscopy and FLIM for an incubation time of 5 min. Fluorescence images of the whole spheroid (**a**) and spheroid sections (**b**, **c**) are displayed. The fluorescence intensity of Hoechst in the nuclei (blue) and hypericin fluorescence (red) is superimposed in **a**–**c**. The outer section reveals a homogeneous hypericin intensity (red) throughout the section compared to the inner one (**b**, **c**). In the inner section, an intensity gradient is observed (**c**). All fluorescence images have scale bars of 25 µm. To represent FLTs across the sections, FLIM images (24×24 µm) are superimposed on corresponding brightfield images to generate a composite image (**d**, **e**). Scale bars of the brightfield images represent 25 µm. Hypericin FLTs vary between 3.5 and 2.5 ns depending on the position inside the spheroid (peripheral to central area). An FLT gradient can be observed from the spheroid outside (3.5 ns) to the inside (2.5 ns) (**e**)

In Fig. 2b, hypericin appears to be homogeneously distributed across the outer spheroid section after 5 min incubation, as visualized by the homogenous fluorescence intensity (Fig. 2b; red). For the inner section, hypericin was mainly accumulated in a peripheral zone of the section and only a small portion penetrated deeper towards the spheroid center (Fig. 2c; red). All observations are corroborated by the single channel fluorescence images in Fig. S1. Control experiments on spheroids without hypericin incubation only reveal the fluorescence intensity of the cell nuclei across the sections (Fig. S2a, SI, blue).

FLIM composite images show a mostly uniform spatial distribution of hypericin FLTs (3.5 ns) throughout the outer section (Fig. 2d). Contrarily, the inner section revealed an FLT gradient across the section. The spheroid edge exhibits an FLT of 3.5 ns, which decreases to 2.5 ns towards the center of the spheroid. As both the hypericin FLT and its intensity are detected simultaneously, these experiments additionally confirm the results obtained by fluorescence microscopy. Although similar trends of hypericin fluorescence intensity and FLT are observable, reasons for both are different since FLTs are concentration-independent, but strongly influenced by the cellular environment [32, 39, 40]. For this reason, hypericin FLTs are used to deduce microenvironmental effects inside the spheroids. FLTs of non-hypericin-treated control spheroids are below 2.5 ns throughout the sections, resulting from the autofluorescence of the spheroids. This represents the untreated spheroid constitution (Fig. S2b, SI).

This behavior of hypericin in varying spheroid layers points to a difference in uptake and transfer inside the spheroid, which most likely depend on the hypericin incubation concentration. This was successfully shown in fluorescence images of four different hypericin concentrations with a constant incubation time of 30 min, summarized in Fig. 3.

This incubation time was chosen to guarantee a sufficient hypericin amount for fluorescence microscopy, especially at low incubation concentrations. Again, whole spheroids were analyzed prior to cryosectioning (Fig. 3a, c, e, g). As illustrated by the Hoechst staining, cell nuclei are evenly distributed throughout the tumor spheroids (Fig. 3a, c, e, g; blue). Additionally, the fluorescence intensity of hypericin continuously increases with increasing incubation concentration (Fig. 3a, c, e, g; red). Inner sections were prepared to investigate the accumulation and permeation of hypericin inside the spheroids as a function of incubation concentration and are shown in Fig. 3b, d, f, h. Incubation concentrations of 0.05 µM, 0.5 µM, and 1.25 µM show an annular accumulation of hypericin in the outer regions of the spheroid sections (Fig. 3b, d, f; red). Additionally, intensity gradients of hypericin occur towards the spheroid center (Fig. 3b, d, f; red). Although weak, the fluorescence of hypericin at the core is still detectable for these incubation concentrations. The presence of hypericin in central areas was proven by corresponding single channel images in Fig. S3, SI and in spectral line scans in Fig. S4, SI. Incubation with a 2.5 µM hypericin solution caused a high hypericin uptake, indicated by the high fluorescence intensity (Fig. 3h; red). Although hypericin seems to be almost uniformly spread across the whole inner section (Fig. 3h; red), an intensity gradient is also observable, as was confirmed by the single channel images in Fig. S3, SI. Most pronounced fluorescence intensities of hypericin are observed throughout the section for this incubation concentration. Two large holes, caused by the cutting procedure, preclude the innermost hypericin concentration of this section from analysis.

Besides the impact of concentration, the duration of hypericin incubation should also influence its uptake, distribution, and FLT inside the spheroids. For this purpose, tumor spheroids were incubated for five different incubation periods (5 min, 30 min, 125 min, 10 h + 30 min, and

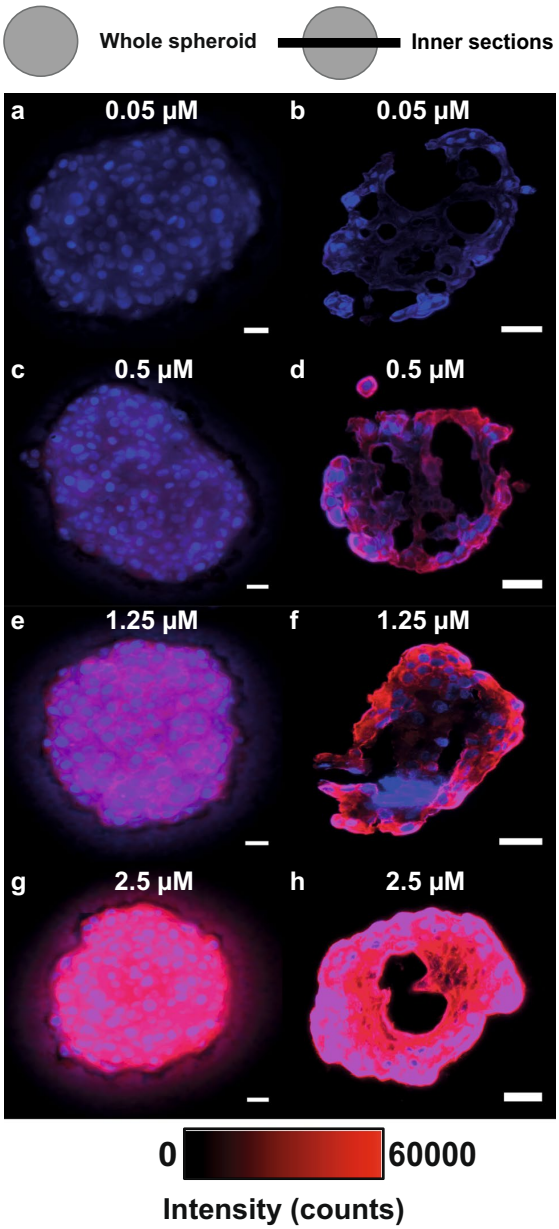

Fig. 3 Influence of different incubation concentrations on the hypericin uptake and penetration, investigated by fluorescence microscopy. Fluorescence images of whole spheroids, incubated with different hypericin concentrations (0.05 µM, 0.5 µM, 1.25 µM, 2.5 µM) for 30 min, are illustrated in **a**, **c**, **e**, and **g**. Corresponding fluorescence images of their inner sections are displayed in **b**, **d**, **f**, and **h**. The Hoechst fluorescence intensity in the nuclei (blue) proves cell occurrence throughout the whole spheroids. Hypericin fluorescence intensity (red) of whole spheroids increases with larger incubation concentrations (**a**, **c**, **e**, **g**). As shown by the inner sections, an increase in incubation concentration also results in a higher internal intensity, at least partly, in an annular area at the section edges (**b**, **d**, **f**, **h**; red). Intensity gradients occur for all investigated concentrations (**b**, **d**, **f**, **h**), although hardly visible for the 2.5 µM incubation concentration (**h**). The scale bars of all fluorescence images are 25 µm

35 h + 15 min), using a 1 µM hypericin solution. This concentration was chosen to guarantee a sufficient hypericin amount, especially at short incubation times, for fluorescence microscopy. Fluorescence intensity and FLIM composite images for inner spheroid sections after different hypericin incubation periods are depicted in Fig. 4.

A comparison of inner and outer sections is shown in Fig. S5, SI. FLIM images are again combined with the related brightfield image to create a composite image. Shorter incubation times (5 min, 30 min, 125 min) caused a mainly peripheral hypericin accumulation within the inner section, as can be observed by the higher hypericin fluorescence intensity in this area (Fig. 4a–c). At the center of the tumor spheroid, only a weak hypericin fluorescence intensity is observed, indicating a small hypericin enrichment (Fig. 4a–c). Thus, a similar penetration gradient is noticeable, as previously determined for different incubation concentrations (Fig. 3b, d, f). At even longer incubation times (10 h + 30 min and 35 h + 15 min), the uniform fluorescence intensity shows that hypericin is homogeneously accumulated throughout the whole tumor section (Fig. 4d, e).

FLIM composite images of the 5 min and 30 min incubations revealed an FLT gradient towards the center of the spheroid's inner sections (Fig. 4f, g). Here, the FLT drops from 3 to 3.5 ns in the outer region to 2.5 ns towards the central area of the sections. However, this gradient is not caused by the hypericin concentration gradient observed in the fluorescence intensity image, but by alterations of the cellular microenvironment. For longer incubation times (125 min, 10 h + 30 min, 35 h + 15 min), the FLTs of hypericin increase to 3–4.5 ns with small areas exhibiting shorter FLTs (2.5–3 ns). Compared to the 5 min and 30 min incubations, no FLT gradient can be observed. Instead, a more homogenous FLT is detected across the spheroid sections (Fig. 4h, i, j). Although similar trends of hypericin fluorescence intensity and FLT are observable, reasons for both are different since FLTs are concentration-independent, but strongly influenced by the cellular environment [32, 39, 40]. For this reason, hypericin FLTs are used to deduce microenvironmental effects inside the spheroids.

In general, the observed FLT change could occur due to chemical modifications, e.g., deprotonation or isomerization, of hypericin [5, 41, 42]. In order to exclude such effects, fluorescence spectra of hypericin are shown in Fig. 5a as line scans across inner spheroid sections and no alteration of the emission spectra can be observed throughout the sections.

The measurement of line scans additionally confirmed the presence of hypericin all over the sections (Fig. 5a). This was also particularly demonstrated in 2D surface plots for the 5 min incubation in Fig. S4, SI. Hence, a chemical reaction leading to hypericin degradation is unlikely. One factor that potentially impacts hypericin FLTs is the pH, which also shows a gradient towards the spheroid core

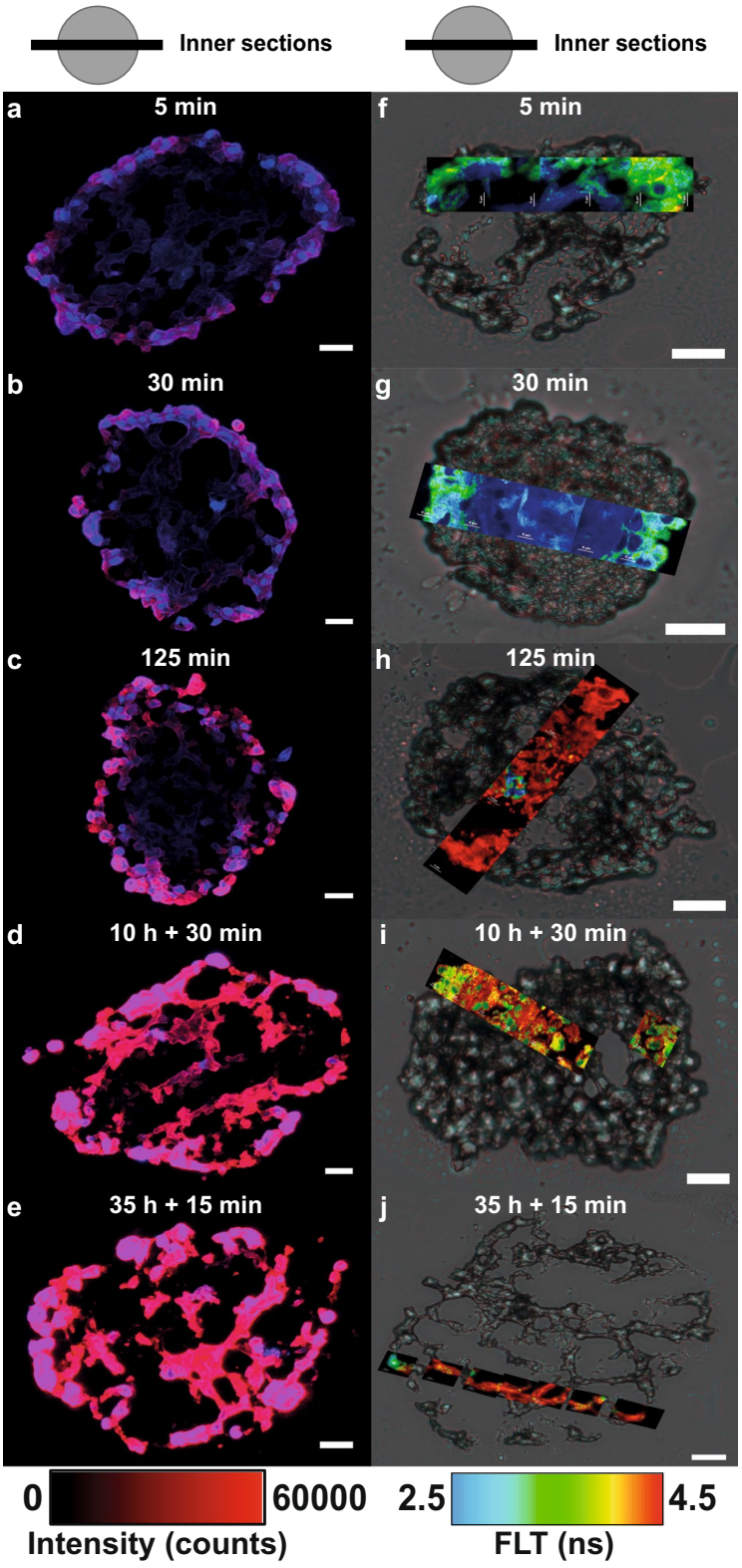

Fig. 4 Impact of different incubation times on hypericin at the spheroid center, examined by fluorescence microscopy and FLIM. Inner sections of the spheroids were investigated by both techniques after incubation times of 5 min, 30 min, 125 min, 10 h + 30 min, and 35 h + 15 min, respectively. Cell nuclei were identified by their blue Hoechst fluorescence (**a**–**e**). Fluorescence images of the sections reveal hypericin intensity gradients (red) for a 5 min, 30 min, and 125 min incubation, with decreasing intensity towards the core (**a**–**c**). An evenly distributed hypericin fluorescence intensity is observed for long incubation times of 10 h + 30 min and 35 h + 15 min (**d**, **e**). Additionally, a larger amount of hypericin penetrates deeper into the spheroid at longer incubation times. Overall, an increasing hypericin fluorescence intensity (red) is observed for increasing incubation times (**a**–**e**). The scale bars of all fluorescence images are 25 µm. Composite images were again generated by combining FLIM images (24 × 24 µm) and corresponding brightfield images (**f**–**j**). Corresponding scale bars of the brightfield images also equal 25 µm (**f**–**j**). Composite FLIM images show an FLT range of 2.5–4.5 ns for hypericin throughout the inner sections of the tumor spheroids (**f**–**j**). Gradients of hypericin FLT appear for short incubation times (**f**, **g**), whereas a mostly homogeneous FLT distribution occurs at longer incubation times (**h**–**j**)

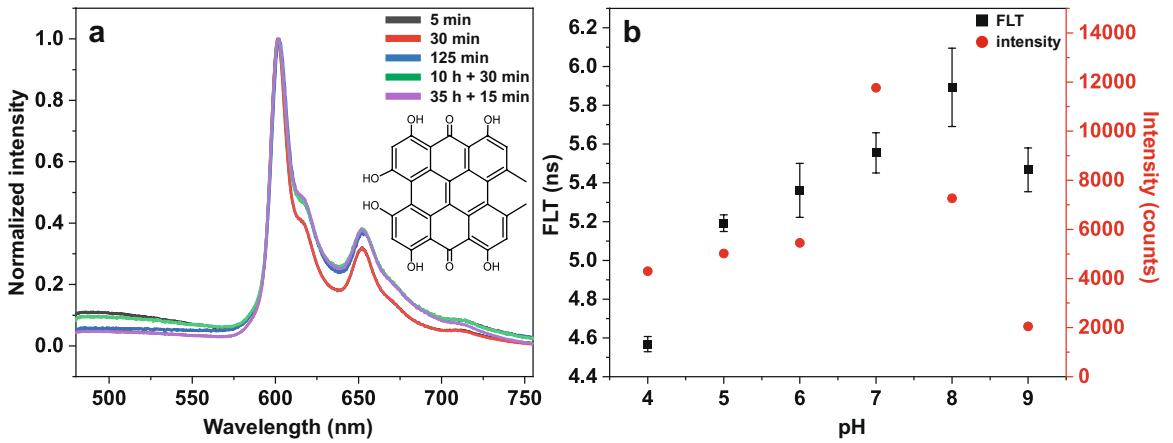

Fig. 5 Hypericin fluorescence spectra of inner spheroid sections treated for different incubation times (**a**) and FLTs as well as hypericin maxima intensities depending on pH (**b**). In **a**, fluorescence spectra are averaged line scans across the sections and normalized to maximum intensity. In **b**, FLTs of hypericin and maximum intensities of the 1st hypericin fluorescence maximum (600 nm) are shown for different pH levels (pH 4–9). The largest hypericin FLT of 5.9 ns appears at pH 8, whereas the lowest FLT of 4.5 ns is observed at pH 4. In comparison to FLTs, the highest intensity was measured at pH 7 and the lowest at pH 9

[43]. Therefore, we investigated FLTs of hypericin in incubation media with different pH levels (pH 4–9). The result is shown by the black squares in Fig. 5b. The physiological pH of the hypericin incubation medium is 8, here the largest hypericin FLT of 5.9 ns can be observed (Fig. 5b, black squares). Decreasing the pH value down to a value of 4 leads to a decrease of the hypericin FLT to 4.5 ns. However, an increase of the pH value to 9 also reduces the hypericin FLT to 5.5 ns (Fig. 5b, black squares). Besides the influence on the FLT, the pH also influences the fluorescence intensity, which is presented as red circles for the emission maximum at 600 nm (Fig. 5b). Corresponding fluorescence spectra at different pH levels are illustrated in Fig. S6, SI. The highest fluorescence intensity at 600 nm is observed at pH 7, whereas the smallest one can be identified for pH 9. Between pH 4 and 6, the fluorescence intensity does hardly change, as reported in literature [44]. Comparable trends of the FLT and the maximum intensity can be observed and highest values for both appear in a physiological pH range of 7–8, decreasing for either lower or higher pH values (pH 4–6, pH 9).

Discussion

The uptake and the accumulation of hypericin inside U-87 MG glioblastoma cell spheroids using fluorescence microscopy were studied. All results presented by fluorescence microscopy reveal two major phenomena. First, a hypericin gradient is formed from outer to inner spheroid regions for low incubation concentrations or short incubation times, causing an increased hypericin accumulation at the spheroid edge (Figs. 2, 3, 4, S1, and S4, SI). Second, hypericin distributes homogeneously throughout the spheroids for long incubation periods or high concentrations (Figs. 2, 3, 4, S1, and S4, SI). Several effects might be responsible for this accumulation and penetration behavior [23, 26]. Hypericin uptake could be affected by the different spheroid zones, as the drug response can be associated with the cell cycle state that differs in each zone [19]. In the proliferative region, cells pass through the whole cell cycle and are thus more susceptible for drugs, whereas in quiescent areas, cells have left the cell cycle and are consequently less targeted [20]. Thus, the hypericin gradient could be directly related to the cell cycle state. Additionally, metabolic activity also differs between the zones and thus either an active or passive uptake mechanism might be dominant. At the outer spheroid region, an actively driven intake of hypericin due to high cell viability is conceivable, which proceeds to a passive permeation as the metabolic activity decreases in deeper cell layers. These effects can also explain the hypericin fluorescence gradient, as the hypericin concentration continuously decreases between adjacent cell layers due to an inward passive diffusion. With increasing incubation times and concentrations, passive diffusion could cause a larger amount of hypericin to penetrate deeper into the spheroids, as was observed by its homogenous distribution for these incubation conditions. Besides, spheroid-related features, such as cell–cell contacts, ECM [24], and protein activity, e.g., for E-cadherin/P-glycoproteins, might additionally influence hypericin penetration [25]. In any case, we expect passive diffusion of hypericin to be the transfer principle in the

necrotic core. Comparable to our results, a similar uptake behavior was also observed for bladder spheroids [23].

In addition to fluorescence microscopy, FLIM was applied to study hypericin FLT differences, which allow to draw conclusions about the cellular environment within spheroids [45]. Compared to the FLT of hypericin on glass (6.34 ± 2.98 ns) or in PVA (4.23 ± 0.89 ns) [4], FLTs are overall shorter in tumor spheroids (2.5–5 ns). This only partially correlates with the refractive indices predominant in cells (nucleus: 1.355–1.365, cytosol: 1.360–1.390, mitochondria: 1.400–1.420) [46]. Since cellular refractive indices are similar to the one of PVA (1.48), comparable hypericin FLTs of approx. 4 ns would be expected [47, 48]. However, most hypericin FLTs in spheroid sections are below 4 ns, so additional factors must be considered. As FLTs are independent of local probe concentration [39], the observed FLT gradients do not result from different hypericin concentrations across the spheroid. Instead, FLTs are strongly dependent on the microenvironment, including the pH level. Based on the spheroid's structure, a diminished supply with nutrients/oxygen [49] and a hampered removal of metabolic waste [22] cause hypoxia in the core and the lactate production increases [43, 50]. This leads to a lactate-induced acidosis and the pH decreases towards the spheroid center (pH 6–7) [43]. Therefore, the pH inside the spheroid can affect the FLT of hypericin. Figure 5 clearly demonstrates that a decreasing pH is accompanied by a decline in hypericin FLT, which can, at least partly, explain the FLT gradients for short incubation times. However, the FLT decrease is larger and the average FLT is smaller in the spheroids than the ones observed in Fig. 5b, hence additional parameters need to be considered. Associated with hypoxia and acidosis, cellular metabolism changes in deeper spheroid layers, where lactate serves as an alternative substrate for ATP synthesis [51]. The altered metabolism inside the spheroids might also cause a change in microenvironment and thus influence the FLT gradient for short incubation periods. Therefore, hypericin FLTs could be utilized to reveal metabolic activity inside spheroids. However, these assumptions only seem to be true for hypericin-treated spheroids for short incubation times (5 min, 30 min). For long incubation times, a homogeneous FLT distribution with no gradient towards the center can be observed. However, the FLT is decreased in the outer layers compared to inner ones (Fig. 4i, Fig. S3s, t, SI). In part, this is also observed for the 35 h + 15 min incubation in Fig. 4j. In general, FLTs are independent of the probe concentration [39], but this is not true for excessively high concentrations, where most molecules are agglomerated [38]. Non-fluorescent hypericin aggregates are formed that cause fluorescence self-quenching and decrease the FLT at the spheroids edge. The impact of fluorescence quenching, however, might not be sufficient to describe the FLT behavior completely. The occurrence of intermolecular FRET from hypericin monomers to aggregates [38] or hypericin-hypericin excimer-like interactions [52] could additionally contribute to the FLT decrease at the spheroid's margin. Additionally, the incubation time was shown to alter the hypericin accumulation in cell organelles, causing a shift of the primary accumulation site from mitochondria to lysosomes for U-87 MG monolayers after 6 h (500 nM) [14]. Hypericin-enriched lysosomes (2 h incubation, 2.5 µM) in U-87 MG were also observed in our experiments (data not shown). In spheroids, the outer regions are incubated comparatively longer than inner ones as hypericin permeates towards the core. Thus, hypericin might predominantly accumulate in lysosomes of the outer spheroid layers, whereas it is mostly located in mitochondria in the inner spheroid. Furthermore, the metabolic activity is increased in the outer regions, which might also favor the redistribution of hypericin towards lysosome uptake. This lysosome enrichment can decrease the hypericin FLT due to an increased refractive index of 1.600 compared to 1.410 in mitochondria [46]. These effects, influencing the excited states lifetimes, have a direct impact on the PDT efficiency, since the triplet formation yield is directly proportional to the FLT [53]. Hence, long FLTs promote the transition to the triplet state, resulting in an increased O_2 activation and higher PDT efficiency. To achieve long FLTs inside glioblastoma spheroids, incubation times of at least 30 min are required to ensure appropriate conditions for PDT treatment.

Conclusion

In this study, we examined the accumulation and penetration behavior of hypericin in U-87 MG tumor spheroids and correlated FLT changes of hypericin to cellular, environmental conditions. Here, hypericin was simultaneously regarded as probe molecule for FLIM and as photosensitizer for PDT. Hypericin uptake and FLTs were studied in spheroid cryosections, as a function of hypericin concentration and incubation time. Low incubation concentrations and short incubation times caused an increased enrichment at the peripheral region of the spheroids with hypericin gradients towards the center. These FLT gradients were explained by pH or metabolism-associated influences, as the FLT is independent of the actual concentration for small hypericin concentrations. In this context, active or passive internalization mechanisms as well as other spheroid-related attributes are discussed to be the driving force in hypericin uptake and permeation. In contrast, high incubation concentrations and long incubation periods lead to a more homogeneous hypericin distribution throughout the spheroid. However, short FLTs in the peripheral spheroid regions were explained by agglomeration-based fluorescence quenching and possible FRET and excimer-like interactions as a consequence of

excessive hypericin accumulation. A further explanation was deduced from the incubation-time-dependent enrichment of hypericin in different cell organelles. The knowledge about hypericin FLTs can be used to significantly influence PDT, since the triplet formation yield, and thus the O_2 activation, is directly proportional to the FLT. Hence, small FLTs after short incubations are indicative of an insufficient PDT inside tumor spheroids. Therefore, incubation times of at least 30 min are required to achieve an increased hypericin FLT within spheroids and thus improve the efficiency of PDT. Our findings reveal important insights concerning the localization and state of hypericin in an improved in vitro tumor model, which is essential in order to understand the effects of hypericin PDT for glioma tumors.

Supplementary Information The online version contains supplementary material available at https://doi.org/10.1007/s00216-022-04107-2.

Acknowledgements We would like to express our sincere thanks to Prof. Dr. Ralf Kemkemer and Prof. Dr. Petra Kluger (Reutlingen University) for support in the cell culture experiments. Furthermore, we thank Karen Ende (Reutlingen University) for cell biological input and her revision of the manuscript.

Funding Open Access funding enabled and organized by Projekt DEAL. This study was funded by the doctoral program of the University of Tübingen and Reutlingen University "Intelligente Prozess-und Materialentwicklung in der Biomateriomics (IPMB)" which is supported by the MWK Baden-Württemberg (PhD student fellowship to MCB).

Data availability The data sets generated and/or analyzed during the current study are not publicly available since they are part of an ongoing PhD thesis. However, the data sets are available from the corresponding authors on reasonable request.

Declarations

Conflict of interest The authors declare no competing interests.

References

1. Ferlay J, Colombet M, Soerjomataram I, Parkin DM, Piñeros M, Znaor A, Bray F. Cancer statistics for the year 2020: an overview. Int J Cancer. 2021;149(4):778–89. https://doi.org/10.1002/ijc.33588.
2. Agostinis P, Vantieghem A, Merlevede W, de Witte PAM. Hypericin in cancer treatment: more light on the way. Int J Biochem Cell Biol. 2002;34(3):221–41. https://doi.org/10.1016/S1357-2725(01)00126-1.
3. Falk H. From the photosensitizer hypericin to the photoreceptor stentorin—the chemistry of phenanthroperylene quinones. Angew Chem Int Ed. 1999;38(21):3116–36. https://doi.org/10.1002/(SICI)1521-3773(19991102)38:21%3c3116::AID-ANIE3116%3e3.0.CO;2-S.
4. Liu Q, Wackenhut F, Hauler O, Scholz M, zur Oven-Krockhaus S, Ritz R, Adam P-M, Brecht M, Meixner AJ,. Hypericin: single molecule spectroscopy of an active natural drug. J Phys Chem A. 2020;124(12):2497–504. https://doi.org/10.1021/acs.jpca.9b11532.
5. Liu Q, Wackenhut F, Wang L, Hauler O, Roldao JC, Adam P-M, Brecht M, Gierschner J, Meixner AJ. Direct observation of structural heterogeneity and tautomerization of single hypericin molecules. Journal Phys Chem Lett. 2021;12(3):1025–31. https://doi.org/10.1021/acs.jpclett.0c03459.
6. Liu Q, Wang L, Roldao JC, Adam P-M, Brecht M, Gierschner J, Wackenhut F, Meixner AJ. Theoretical and experimental evidence of two-step tautomerization in hypericin. Adv Photonics Res. 2021;2(6):2000170. https://doi.org/10.1002/adpr.202000170.
7. Wang L, Liu Q, Wackenhut F, Brecht M, Adam P-M, Gierschner J, Meixner AJ. Monitoring tautomerization of single hypericin molecules in a tunable optical λ/2 microcavity. J Chem Phys. 2022;156(1): 014203. https://doi.org/10.1063/5.0078117.
8. Buytaert E, Dewaele M, Agostinis P. Molecular effectors of multiple cell death pathways initiated by photodynamic therapy. Biochim Biophys Acta. 2007;1776(1):86–107. https://doi.org/10.1016/j.bbcan.2007.07.001.
9. Kleemann B, Loos B, Scriba TJ, Lang D, Davids LM. St John's Wort (Hypericum perforatum L.) photomedicine: hypericin-photodynamic therapy induces metastatic melanoma cell death. PLoS One. 2014;9(7):e103762. https://doi.org/10.1371/journal.pone.0103762.
10. Dong X, Zeng Y, Zhang Z, Fu J, You L, He Y, Hao Y, Gu Z, Yu Z, Qu C, Yin X, Ni J, Cruz LJ. Hypericin-mediated photodynamic therapy for the treatment of cancer: a review. J Pharm Pharmacol. 2020;73(4):425–36. https://doi.org/10.1093/jpp/rgaa018.
11. Nakajima N, Kawashima N. A basic study on hypericin-PDT in vitro. Photodiagnosis Photodyn Ther. 2012;9(3):196–203. https://doi.org/10.1016/j.pdpdt.2012.01.008.
12. Ritz R, Roser F, Radomski N, Strauss WSL, Tatagiba M, Gharabaghi A. Subcellular colocalization of hypericin with respect to endoplasmic reticulum and Golgi apparatus in glioblastoma cells. Anticancer Res. 2008;28(4B):2033–8.
13. Uzdensky AB, Ma L-W, Iani V, Hjortland GO, Steen HB, Moan J. Intracellular localisation of hypericin in human glioblastoma and carcinoma cell lines. Lasers Med Sci. 2001;16(4):276–83. https://doi.org/10.1007/pl00011364.
14. Huntosova V, Nadova Z, Dzurova L, Jakusova V, Sureau F, Miskovsky P. Cell death response of U87 glioma cells on hypericin photoactivation is mediated by dynamics of hypericin subcellular distribution and its aggregation in cellular organelles. Photochem Photobiol Sci. 2012;11(9):1428–36. https://doi.org/10.1039/C2PP05409D.
15. Ritz R, Wein HT, Dietz K, Schenk M, Roser F, Tatagiba M, Strauss WSL. Photodynamic therapy of malignant glioma with hypericin: comprehensive in vitro study in human glioblastoma cell lines. Int J Oncol. 2007;30(3):659–67.
16. Saw CLL, Olivo M, Soo KC, Heng PWS. Delivery of hypericin for photodynamic applications. Cancer Lett. 2006;241(1):23–30. https://doi.org/10.1016/j.canlet.2005.10.020.

17. Frantz C, Stewart KM, Weaver VM. The extracellular matrix at a glance. J Cell Sci. 2010;123(24):4195–200. https://doi.org/10.1242/jcs.023820.
18. Edmondson R, Broglie JJ, Adcock AF, Yang L. Three-dimensional cell culture systems and their applications in drug discovery and cell-based biosensors. Assay Drug Dev Technol. 2014;12(4):207–18. https://doi.org/10.1089/adt.2014.573.
19. Olive PL, Durand RE. Drug and radiation resistance in spheroids: cell contact and kinetics. Cancer Metastasis Rev. 1994;13(2):121–38. https://doi.org/10.1007/BF00689632.
20. Mellor HR, Ferguson DJP, Callaghan R. A model of quiescent tumour microregions for evaluating multicellular resistance to chemotherapeutic drugs. Br J Cancer. 2005;93(3):302–9. https://doi.org/10.1038/sj.bjc.6602710.
21. Hoffmann OI, Ilmberger C, Magosch S, Joka M, Jauch K-W, Mayer B. Impact of the spheroid model complexity on drug response. J Biotechnol. 2015;205:14–23. https://doi.org/10.1016/j.jbiotec.2015.02.029.
22. Mehta G, Hsiao AY, Ingram M, Luker GD, Takayama S. Opportunities and challenges for use of tumor spheroids as models to test drug delivery and efficacy. J Control Release. 2012;164(2):192–204. https://doi.org/10.1016/j.jconrel.2012.04.045.
23. Kamuhabwa AAR, Huygens A, De Witte PAM. Photodynamic therapy of transitional cell carcinoma multicellular tumor spheroids with hypericin. Int J Oncol. 2003;23(5):1445–50. https://doi.org/10.3892/ijo.23.5.1445.
24. Huygens A, Huyghe D, Bormans G, Verbruggen A, Kamuhabwa AR, Roskams T, De Witte PAM. Accumulation and photocytotoxicity of hypericin and analogs in two- and three-dimensional cultures of transitional cell carcinoma cells. Photochem Photobiol. 2003;78(6):607–14. https://doi.org/10.1562/0031-8655(2003)0780607AAPOHA2.0.CO2.
25. Huygens A, Kamuhabwa AR, Roskams T, Bv C, Hv P, Witte PAMd. Permeation of hypericin in spheroids composed of different grade transitional cell carcinoma cell lines and normal human urothelial cells. J Urol. 2005;174(1):69–72. https://doi.org/10.1097/01.ju.0000162037.49102.56.
26. Roelants M, Van Cleynenbreugel B, Lerut E, Van Poppel H, de Witte PAM. Human serum albumin as key mediator of the differential accumulation of hypericin in normal urothelial cell spheroids versusurothelial cell carcinoma spheroids. Photochem Photobiol Sci. 2011;10(1):151–9. https://doi.org/10.1039/C0PP00109K.
27. Kessel D. Hypericin accumulation as a determinant of PDT efficacy. Photochem Photobiol. 2020;96(5):1144–7. https://doi.org/10.1111/php.13302.
28. Crnolatac I, Huygens A, Agostinis P, Kamuhabwa AR, Maes J, Van Aerschot A, De Witte PAM. In vitro accumulation and permeation of hypericin and lipophilic analogues in 2-D and 3-D cellular systems. Int J Oncol. 2007;30(2):319–24. https://doi.org/10.3892/ijo.30.2.319.
29. Casciari JJ, Sotirchos SV, Sutherland RM. Glucose diffusivity in multicellular tumor spheroids. Cancer Res. 1988;48(14):3905–9.
30. Riffle S, Hegde RS. Modeling tumor cell adaptations to hypoxia in multicellular tumor spheroids. J Exp Clin Cancer Res. 2017;36(1):102. https://doi.org/10.1186/s13046-017-0570-9.
31. Keith B, Simon MC. Hypoxia-inducible factors, stem cells, and cancer. Cell. 2007;129(3):465–72. https://doi.org/10.1016/j.cell.2007.04.019.
32. Bastiaens PIH, Squire A. Fluorescence lifetime imaging microscopy: spatial resolution of biochemical processes in the cell. Trends Cell Biol. 1999;9(2):48–52. https://doi.org/10.1016/S0962-8924(98)01410-X.
33. Lakner PH, Monaghan MG, Möller Y, Olayioye MA, Schenke-Layland K. Applying phasor approach analysis of multiphoton FLIM measurements to probe the metabolic activity of three-dimensional in vitro cell culture models. Sci Rep. 2017;7(1):42730. https://doi.org/10.1038/srep42730.
34. Cong A, Pimenta RML, Lee HB, Mereddy V, Holy J, Heikal AA. Two-photon fluorescence lifetime imaging of intrinsic NADH in three-dimensional tumor models. Cytometry A. 2019;95(1):80–92. https://doi.org/10.1002/cyto.a.23632.
35. Okkelman IA, Dmitriev RI, Foley T, Papkovsky DB. Use of fluorescence lifetime imaging microscopy (FLIM) as a timer of cell cycle S phase. PLoS ONE. 2016;11(12): e0167385. https://doi.org/10.1371/journal.pone.0167385.
36. Penjweini R, Deville S, D'Olieslaeger L, Berden M, Ameloot M, Ethirajan A. Intracellular localization and dynamics of hypericin loaded PLLA nanocarriers by image correlation spectroscopy. J Control Release. 2015;218:82–93. https://doi.org/10.1016/j.jconrel.2015.09.064.
37. Taroni P, Valentini G, Comelli D, D'Andrea C, Cubeddu R, Hu D-N, Roberts JE. Time-resolved microspectrofluorimetry and fluorescence lifetime imaging of hypericin in human retinal pigment epithelial cells. Photochem Photobiol. 2005;81(3):524–8. https://doi.org/10.1111/j.1751-1097.2005.tb00220.x.
38. Huntosova V, Alvarez L, Bryndzova L, Nadova Z, Jancura D, Buriankova L, Bonneau S, Brault D, Miskovsky P, Sureau F. Interaction dynamics of hypericin with low-density lipoproteins and U87-MG cells. Int J Pharm. 2010;389(1):32–40. https://doi.org/10.1016/j.ijpharm.2010.01.010.
39. Lakowicz JR, Szmacinski H, Nowaczyk K, Berndt KW, Johnson M. Fluorescence lifetime imaging. Anal Biochem. 1992;202(2):316–30. https://doi.org/10.1016/0003-2697(92)90112-K.
40. Suhling K, French PMW, Phillips D. Time-resolved fluorescence microscopy. Photochem Photobiol Sci. 2005;4(1):13–22. https://doi.org/10.1039/B412924P.
41. Chang MC, Petrich JW, McDonald DB, Fleming GR. Nonexponential fluorescence decay of tryptophan, tryptophylglycine, and glycyltryptophan. J Am Chem Soc. 1983;105(12):3819–24. https://doi.org/10.1021/ja00350a013.
42. Morsy MA, Al-Somali AM, Suwaiyan A. Fluorescence of thymine tautomers at room temperature in aqueous solutions. J Phys Chem B. 1999;103(50):11205–10. https://doi.org/10.1021/jp990858e.
43. Carlsson J, Acker H. Relations between ph, oxygen partial pressure and growth in cultured cell spheroids. Int J Cancer. 1988;42(5):715–20. https://doi.org/10.1002/ijc.2910420515.
44. Chowdhury PK, Ashby KD, Datta A, Petrich JW. Effect of pH on the fluorescence and absorption spectra of hypericin in reverse micelles. Photochem Photobiol. 2000;72(5):612–8. https://doi.org/10.1562/0031-8655(2000)0720612EOPOTF2.0.CO2.
45. Liu J, Saw C, Olivo M, Sudhaharan T, Ahmed S, Heng P, Wohland T. Study of interaction of hypericin and its pharmaceutical preparation by fluorescence techniques. J Biomed Opt. 2009;14(1): 014003.
46. Liu PY, Chin LK, Ser W, Chen HF, Hsieh CM, Lee CH, Sung KB, Ayi TC, Yap PH, Liedberg B, Wang K, Bourouina T, Leprince-Wang Y. Cell refractive index for cell biology and disease diagnosis: past, present and future. LChip. 2016;16(4):634–44. https://doi.org/10.1039/C5LC01445J.
47. Strickler SJ, Berg RA. Relationship between absorption intensity and fluorescence lifetime of molecules. J Chem Phys. 1962;37(4):814–22. https://doi.org/10.1063/1.1733166.
48. Tregidgo C, Levitt J, Suhling K. Effect of refractive index on the fluorescence lifetime of green fluorescent protein. J Biomed Opt. 2008;13(3): 031218.

49. Khaitan D, Chandna S, Arya MB, Dwarakanath BS. Establishment and characterization of multicellular spheroids from a human glioma cell line: implications for tumor therapy. J Transl Med. 2006;4:12–12. https://doi.org/10.1186/1479-5876-4-12.
50. Acker H, Holtermann G, Bölling B, Carlsson J. Influence of glucose on metabolism and growth of rat glioma cells (C6) in multicellular spheroid culture. Int J Cancer. 1992;52(2):279–85. https://doi.org/10.1002/ijc.2910520221.
51. Kunz-Schughart LA, Doetsch J, Mueller-Klieser W, Groebe K. Proliferative activity and tumorigenic conversion: impact on cellular metabolism in 3-D culture. Am J Physiol Cell Physiol. 2000;278(4):C765–80. https://doi.org/10.1152/ajpcell.2000.278.4.C765.
52. Mukherjee P, Adhikary R, Halder M, Petrich JW, Miskovsky P. Accumulation and interaction of hypericin in low-density lipoprotein—a photophysical study. Photochem Photobiol. 2008;84(3):706–12. https://doi.org/10.1111/j.1751-1097.2007.00234.x.
53. Byeon CC, McKerns MM, Sun W, Nordlund TM, Lawson CM, Gray GM. Excited state lifetime and intersystem crossing rate of asymmetric pentaazadentate porphyrin-like metal complexes. Appl Phys Lett. 2004;84(25):5174–6. https://doi.org/10.1063/1.1763983.

Bassler, M.C., Rammler, T., Wackenhut, F. *et al.* Accumulation and penetration behavior of hypericin in glioma tumor spheroids studied by fluorescence microscopy and confocal fluorescence lifetime imaging microscopy. *Anal Bioanal Chem* **414**, 4849–4860 (2022).

https://doi.org/10.1007/s00216-022-04107-2

Anteil an gemeinschaftlicher Veröffentlichung:

Es handelt sich hierbei um eine Nebenprojekt. Wie auch diese Arbeit behandelt es Fluoreszenzlebensdauern. Die wissenschaftliche Grundidee hatten Miriam C. Bassler und Marc Brecht. Die Projektplanung wurde von Miriam C. Bassler durchgeführt. Der Aufbau einer der verwendeten Messinstrumente und die Datenaufnahme wurden von Miriam C. Bassler und mir durchgeführt. Das Züchten und Schneiden der Zellverbände übernahm Ivona Secic. Für die Datenevaluation waren Miriam C. Bassler, Frank Wackenhut und ich zuständig. Das Manuskript wurde von Miriam C. Bassler, Frank Wackenhut, Alfred J. Meixner und Marc Brecht erstellt.

7.5 Periodic Fluorescence Variations of CdSe Quantum Dots Coupled to Aryleneethynylenes with Aggregation-Induced Emission (veröffentlicht)

ACS NANO

www.acsnano.org

ARTICLE

Periodic Fluorescence Variations of CdSe Quantum Dots Coupled to Aryleneethynylenes with Aggregation-Induced Emission

Krishan Kumar, Jonas Hiller, Markus Bender, Saeed Nosrati, Quan Liu, Marc Edelmann, Steffen Maier, Tim Rammler, Frank Wackenhut, Alfred J. Meixner, Kai Braun, Uwe H. F. Bunz,* and Marcus Scheele*

Cite This: *ACS Nano* 2021, 15, 480−488

Read Online

ACCESS | Metrics & More | Article Recommendations | Supporting Information

ABSTRACT: **CdSe nanocrystals and aggregates of an aryleneethynylene derivative are assembled into a hybrid thin film with dual fluorescence from both fluorophores. Under continuous excitation, the nanocrystals and the molecules exhibit anticorrelated fluorescence intensity variations, which become periodic at low temperature. We attribute this to a structure-dependent aggregation-induced emission of the aryleneethynylene derivative, which impacts the rate of excitation energy transfer between the molecules and nanocrystals. This work highlights that combining semiconductor nanocrystals with molecular aggregates, which exhibit aggregation-induced emission, can result in emerging optical properties.**

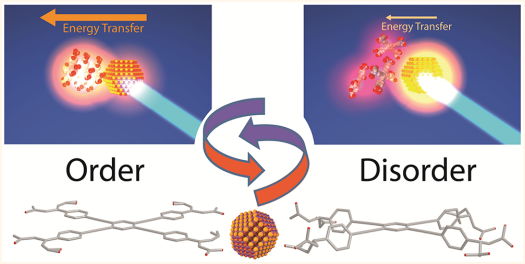

KEYWORDS: *quantum dots, organic π-systems, aggregation-induced emission, energy transfer, fluorophores*

Aggregation-induced emission (AIE) refers to enhanced and often red-shifted fluorescence of luminophores upon formation of aggregates from solution.[1] The prototypical example are organic π-systems with a large degree of structural twisting in the ground state, for example, tetraphenylethylenes[2] or aryleneethynylenes,[3] which exhibit high torsion angles between the central C═C or C≡C bond and the sterically demanding phenyl substituents. Photoexcitation weakens the double or triple bond and reduces the torsion angles with the phenyl rings.[4−6] Relaxation from this state occurs *via* three pathways: (1) radiative recombination, (2) intramolecular motion (mostly detwisting of the C═C or C≡C bond), or (3) photochemical reaction to an intermediate. AIE occurs if pathways (2) and (3) are significantly inhibited in the aggregates due to restriction of intramolecular motion.[7] The degree of this restriction depends on the solid-state structure and, thus, on temperature-induced structural transitions.[5,8,9] These transitions may be triggered photothermally *via* sufficiently strong photoexcitation and the concomitant rise in temperature.[10,11] The photoexcitation can occur either directly *via* resonant excitation of the aggregates or indirectly by excitation energy transfer (EET) *via* a sensitizer.[12,13] Inorganic semiconductor nanocrystals (NCs) are ideal as sensitizers, as they exhibit much larger extinction coefficients than most organic dyes and strong absorption at above-band gap photon energies.[14] EET between NCs and organic π-systems has been extensively investigated in both solution and solid state. However, to the best of our knowledge, no research has been committed specifically toward involving AIE molecules.[15−21]

Here, we combine aggregates of the aryleneethynylene derivative AE **1** (Figure 1a) with pronounced AIE together with CdSe NCs into a hybrid nanocomposite. We show that EET between the NCs and the molecular aggregates in combination with photothermally-induced structural changes lead to temporal fluctuations of the NC fluorescence and the degree of AIE in the aggregates, which are anticorrelated to

Received: June 19, 2020
Accepted: December 31, 2020
Published: January 13, 2021

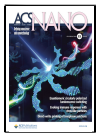

https://dx.doi.org/10.1021/acsnano.0c05121
ACS Nano 2021, 15, 480−488

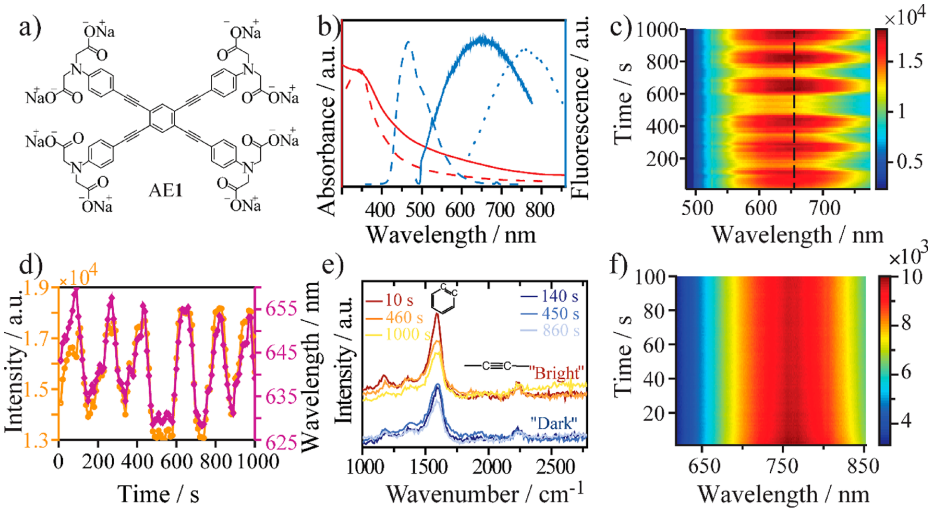

Figure 1. (a) Structural formula of the arylenephenylene derivative AE 1. (b) Optical properties of AE 1. Absorption in methanol (red dashed line), thin-film absorption (red solid line), fluorescence in methanol (blue dashed line, excitation at 350 nm), thin-film fluorescence (blue solid line, 488 nm excitation), and thin-film fluorescence at 160 K (blue dotted line, 488 nm excitation). (c) Thin-film fluorescence during 1000 s of continuous excitation at 488 nm with a binning time of 1 s. (d) Line profile (orange solid) and wavelength maxima position (purple) of (c) extracted by fitting Gaussian functions. (e) Raman spectra taken during "bright" periods (at 10, 460, and 1000 s) and "dark" periods (at 140, 450, and 860 s). Bands attributed to the phenyl-C═C breathing and the C≡C stretching mode are indicated. (f) Thin-film fluorescence at 160 K during 100 s of continuous excitation at 488 nm.

each other. At low temperature, these intensity fluctuations become periodic, and the periodicity correlates with the laser power. Hybrid materials with these properties may be interesting for application in nanothermometry.

RESULTS AND DISCUSSION

In methanolic solution, AE **1** shows a broad absorption with a maximum at 350 nm, including a small low-energy tail as well as a narrow, weak emission at 480 nm (Figure 1b, red and blue dashed lines, respectively). In the solid state, aggregates of AE **1** exhibit pronounced low-energy tailing of the absorption as well as broad, enhanced emission with a maximum at 650 nm (Figure 1b, red and blue solid lines). At 160 K, the fluorescence maximum is further red-shifted to 750 nm (Figure 1b, dotted line). These optical properties are typical for molecules with AIE and are consistent with other similar aryleneethynylenes.[6,8,22,23] Absorption and fluorescence of AE **1** are strongly dependent on the extent of conjugation of the π-electron cloud, for which the torsion angles of the five phenyl rings are an important measure.[24] For torsion angles close to 0°, the molecule is fully planarized, the degree of π-conjugation is maximized, and the energy of this rotamer is minimized.[25] In the ground state, the energy difference between rotamers of different torsion angles is low (<4 kJ/mol), and a wide range of rotational states are populated.[26] This leads to the broad absorption feature in Figure 1b. In the excited state, the torsion-angle-dependent energy profile of the rotamers becomes much steeper ($\Delta E \approx 30$ kJ/mol)[27] and, an unhindered rotation provided, radiative emission will occur from a narrow range of rotational states with relatively small torsion angles.[26] This narrows and red-shifts the fluorescence compared to the absorption. In the solid state, structural rigidity favors rotamers with small torsion angles and enforces a higher degree of planarization. This invokes the low-energy tailing of the absorption and the red-shift of the fluorescence in Figure 1b. Kinetic arrest of high-energy rotamers due to the structural rigidity prevents the fluorescence line narrowing observed in solution and leads to a broad fluorescence feature. At low temperature, structural order and, thus, the degree of planarization are enhanced further, which shifts the fluorescence to even lower energies.[28,29]

Continuous excitation at 488 nm under nitrogen atmosphere leads to substantial fluctuations (±20%) in the fluorescence intensity emitted by the AE **1** aggregates (Figure 1c,d). The time scale of seconds for the transition between an intensity maximum and minimum suggests that a macroscopic process, and not an electronic transition, is responsible for the fluctuations. Within the theory of AIE, this process needs to affect either the restriction of intramolecular motion or the rate of formation of a photochemical intermediate to result in fluorescence intensity fluctuations.[4] Photothermally-induced local structural changes are a likely cause for less restricted intramolecular motion and faster nonradiative recombination. Indeed, we observe significant local changes in the optical scattering and luminescence images of AE **1** aggregates after laser excitation, indicating an altered morphology (see Figure S1). Furthermore, we find a strong correlation between the intensity and the peak wavelength of the fluorescence, in that a lower intensity coincides with a blue-shifted fluorescence peak (Figure 1d). This is consistent with a transformation from a more planarized structure with high fluorescence quantum yield to a less planarized structure with fast nonradiative recombination. To test for the formation of a photochemical intermediate as an alternative cause for the intensity fluctuations, we compare the Raman bands of AE **1** appearing together with the fluorescence signals of different intensities

https://dx.doi.org/10.1021/acsnano.0c05121
ACS Nano 2021, 15, 480−488

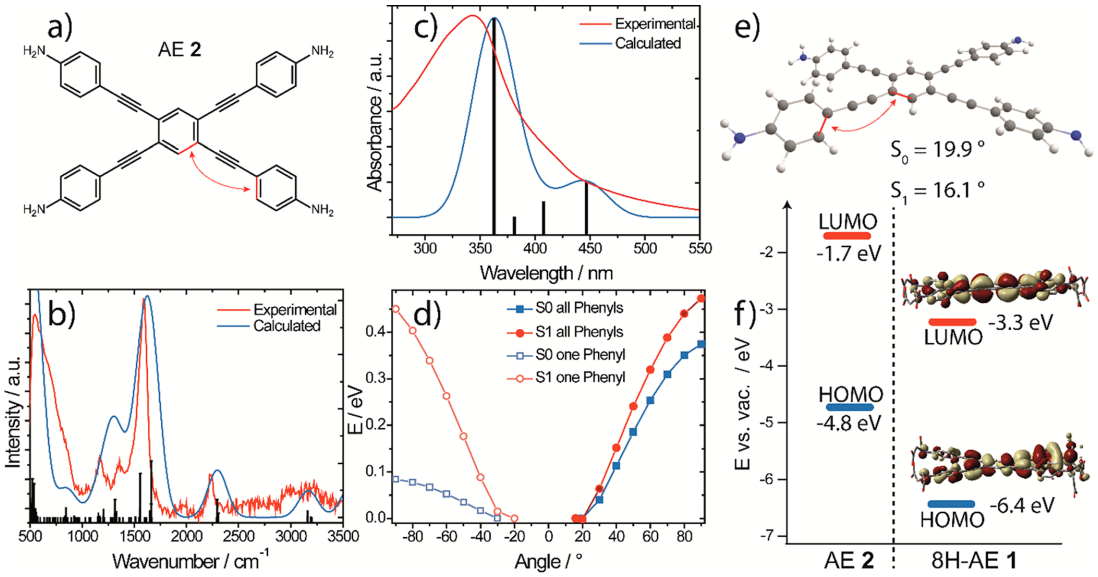

Figure 2. (a) Model compound AE 2 used for quantum chemical calculations and relevant phenyl torsion angles (red). (b) Calculated Raman spectrum of AE 2 with individual vibrations (black), the envelope spectrum (blue), and the experimental Raman spectrum of AE 1 (red). (c) Calculated absorption spectrum of AE 2 with individual transitions (black), the envelope spectrum (blue), and the experimental UV−vis spectrum of AE 1 in methanol (red). (d) Energy difference relative to the energetic minimum of the ground state (S_0, blue squares) and the first singlet state (S_1, red spheres) of AE 2 with respect to the out-of-plane torsion of one phenyl ring (open symbols, left) and of all four phenyl rings (closed symbols, right). (e) Geometry of AE 2 and indication of the most stable out-of-plane torsion of the phenyl groups for the S_0 and S_1 states. (f) HOMO and LUMO energies relative to the vacuum level of AE 2 (left) and the neutral, protonated derivative of AE 1 (right, "8H-AE 1"). For 8H-AE 1, we also show the corresponding isosurfaces.

(Figure 1e). We find a strong band at 1590 cm^{-1} and a weak signal at 2230 cm^{-1}, which we assign to the phenyl-C═C breathing and the C≡C stretching mode in agreement with earlier reports.[29,30] There are no substantial differences between Raman spectra taken during periods of fluorescence intensity minima *vs* maxima, suggesting that chemical transformations of AE **1** are not responsible for the fluorescence intensity fluctuations. Over the course of 1000 s of continuous excitation, the intensity of the phenyl-C═C breathing mode decreases in comparison with that of the C≡C stretching mode. However, this evolution progresses within periods of low and high fluorescence intensity alike.

We conclude that the fluorescence intensity fluctuations of AE **1** under continuous 488 nm laser excitation are probably caused by a photothermally-induced order/disorder transition. This transition locally increases the nonradiative recombination rate due to bond rotation and decreases the fluorescence quantum yield. In the disordered, less planarized state, the absorption of AE **1** at 488 nm is weakened (Figure 1b), which now decreases the rate of photothermal heating and allows for a recovery of the initial optical properties of the AE **1** aggregates. At 160 K, the fluorescence fluctuations disappear (Figure 1f). We suspect that photothermal heating may not be sufficient at this temperature to invoke the same structural changes that lead to the random fluorescence fluctuations in Figure 1c.

In Figure 2, we display the results of quantum chemical calculations of the simplified arylethynylene AE **2** (Figure 2a), which we choose as a model compound to resemble AE **1** but at reduced computational costs. The calculations are carried out using B3LYP-D3BJ level of theory with a def2-TZVP basis set. Our choice of the model compound AE **2** is justified by a comparison of the calculated Raman (Figure 2b) and absorption spectra (Figure 2c), which are in good agreement with the experimental data of AE **1** (taken from Figure 1b,e). Figure 2d details the energy difference arising from varying the out-of-plane torsion of the phenyl moieties in AE **2** for the S_0 (blue) and S_1 state (red). Figure 2e shows the most stable geometry of the S_0 state with a phenyl torsion of 19.9° and of the S_1 state with a reduced torsion angle of 16.1°. The HOMO and LUMO energy levels relative to the vacuum level of AE **2** in the ground state are provided in Figure 2f (−4.8 eV and −1.7 eV). In view of the potentially large effect of the eight carboxylic acid substituents of AE **1** on the position of the frontier orbitals, we also calculate the HOMO and LUMO energies of the neutral, protonated derivative (8H-AE **1**) and display the energies as well as the isosurfaces on the left side of Figure 2f. We find that the HOMO/LUMO levels in 8H-AE **1** are substantially depressed compared to AE **2** with energies of −6.4 eV/-3.3 eV *vs* vacuum, while the HOMO−LUMO gap (−3.1 eV) is unaffected by the substitution.

From these calculations, we conclude the following: (1) The excited state of AE **1** is more planar than the ground state, and (2) the torsion-angle-dependent energy landscape of the S_1 state is steeper than that of the S_0 state. This is particularly pronounced if the out-of-plane torsion of only one phenyl moiety is considered (Figure 2d, left), but also holds true (to a lesser extent) if all four phenyl substituents are taken into account (Figure 2d, right). These properties favor the

https://dx.doi.org/10.1021/acsnano.0c05121
ACS Nano 2021, 15, 480−488

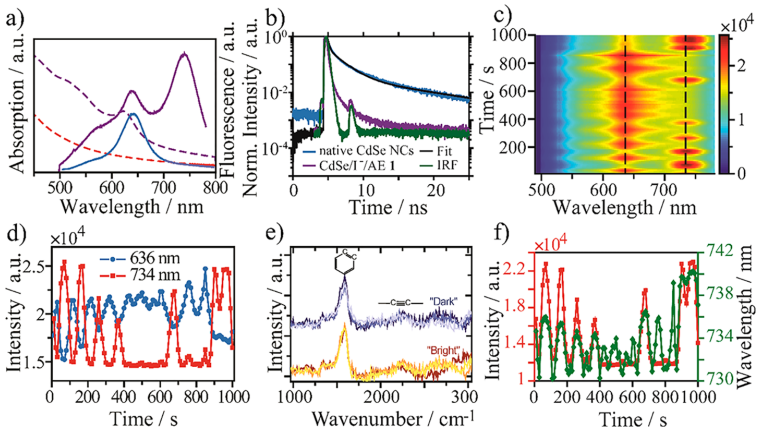

Figure 3. (a) Thin-film absorption (purple dashed line) and thin-film fluorescence (purple solid line) of CdSe/I⁻/AE 1. Excitation at 488 nm. For comparison, the fluorescence of the CdSe/I⁻ NCs (blue solid line) and the absorption of pure AE 1 (red dashed line) are also displayed. (b) Fluorescence lifetime measurements of the native CdSe NCs (blue), their fit (black), and the same NCs after functionalization with AE 1 (purple). The IRF is displayed in green. (c) Thin-film fluorescence of CdSe/I⁻/AE 1 during 1000 s of continuous excitation at 488 nm with a binning time of 1 s. (d) Line profile of (c) cut at 636 and 734 nm. (e) Raman spectra taken during "bright" and "dark" periods. (f) Peak position of the low-energy band in (c) (green) compared with the intensity of the same band (red).

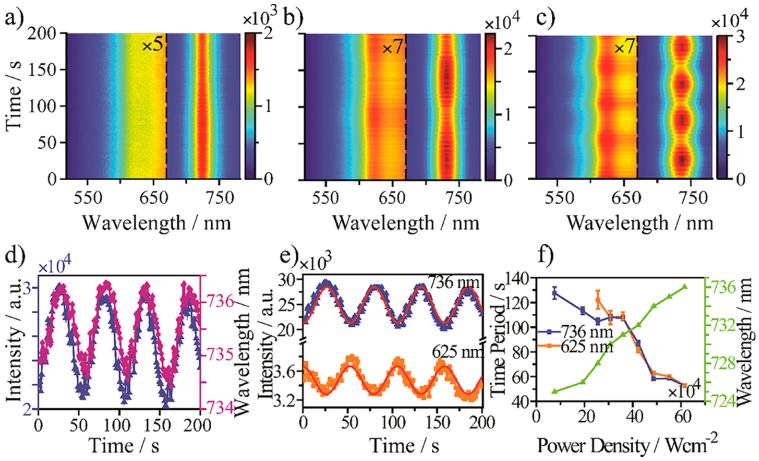

Figure 4. Thin-film fluorescence at 160 K of CdSe/I⁻/AE 1 during 200 s of continuous excitation at 488 nm with a binning time of 1 s and varying laser power. (a) 45 kW/cm², (b) 360 kW/cm², and (c) 615 kW/cm². (d) Peak position of the low-energy band in (c) (purple) compared with the intensity of the same band (blue). (e) Line profile of (c) cut at 625 and 736 nm. (f) Correlation between the laser power and the period of one complete oscillation in (e) for the fluorescence bands at 620 nm (blue) and 725 nm (orange). A concomitant redshift of the AE 1 emission peak is also displayed on the right axis.

occurrence of AIE and are consistent with the optical data in Figure 1.

In Figure 3, we analyze the solid-state fluorescence of AE **1** aggregates coupled to the surface of iodide-capped CdSe nanocrystals (CdSe/I⁻ NCs) at room temperature. The NCs were chosen based on the large spectral overlap between their fluorescence (Figure 3a, blue solid line) with the absorption of AE **1** aggregates (Figure 3a, red dashed line) to enable efficient EET. The absorption spectrum of the hybrid material (CdSe/I⁻/AE **1**) is dominated by the absorption of the CdSe NCs (purple dashed line), while the fluorescence spectrum bears two well-resolved, narrow bands at 636 and 734 nm (purple solid line). We assign the band at 636 nm to the CdSe/I⁻ NCs and the band at 734 nm to AE **1**. Fluorescence lifetime measurements reveal that the fluorescence decay of the same CdSe NCs shortens upon functionalization with AE **1** from a biexponential decay (τ_1 = 2.3 ns and τ_2 = 9.1 ns) to a decay kinetics, which is too fast to be distinguished from the resolution function (instrument response function (IRF), ~1 ns) of the instrument (Figure 3b).

Continuous excitation at 488 nm with 1−10 MW/cm², a diffraction-limited focus (few 100 nm diameter) and nitrogen atmosphere of CdSe/I⁻/AE **1** results in the temporal fluctuations in the fluorescence spectrum depicted in Figure

https://dx.doi.org/10.1021/acsnano.0c05121
ACS Nano 2021, 15, 480−488

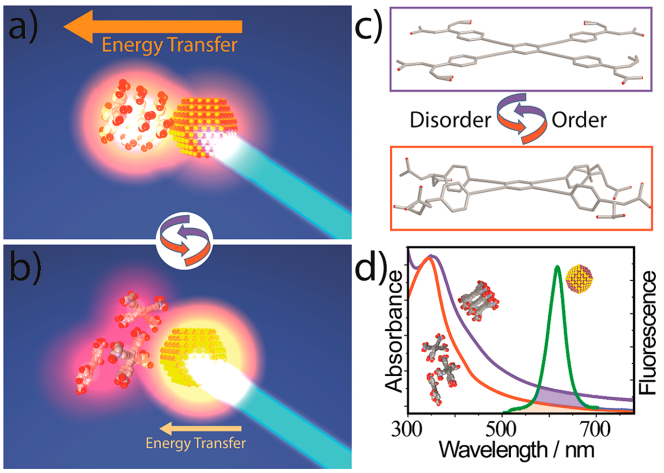

Figure 5. (a,b) Idealized schematic of the two structural scenarios proposed for CdSe/I⁻/AE 1 composites with different energy transfer efficiency. (c) Qualitative description of the proposed order/disorder transition. (d) Spectral overlap between NC emission (green) and AE 1 absorption in the ordered (blue) and disordered (red) state.

3c. We stress that these fluctuations occur only in highly selected places (roughly 1% of the total sample area). The fluctuations occur gradually over a time scale of 10−30 s with ON/OFF periods of similar duration. Most notably, the ON/OFF periods of the bands at 636 and 734 nm are mostly anticorrelated, that is, an increase of the NC fluorescence occurs together with a decrease of the AE **1** emission and *vice versa* (Figure 3d). We verify that CdSe/I⁻ NCs without AE **1** do not exhibit similar fluorescence fluctuations (Figure S2). Similar to pure AE **1**, we find the same Raman signals at 1590 and 2230 cm^{-1}, which do not change significantly during relative ON or OFF periods (Figure 3e). Here, however, the intensity of the phenyl−C≡C breathing mode remains constant, indicating a higher photostability of the hybrid composite compared to pure AE **1**. Another similarity between CdSe/I⁻/AE **1** and the pure molecule is the strong correlation of the intensity (red) and peak wavelength position (green) of the fluorescence of AE **1** (Figure 3f). In contrast, the peak wavelength position of the CdSe/I⁻ fluorescence remains constant throughout the fluctuations.

At 160 K and helium atmosphere, the temporal fluorescence fluctuations of CdSe/I⁻/AE **1** become periodic (Figure 4). At 45 kW/cm^2 excitation power density, the two fluorescence bands of the CdSe/I⁻ NCs and the AE **1** aggregates are quasi-continuous over a time scale of 200 s (Figure 4a). Increasing the excitation power density to 615 kW/cm^2 induces periodic oscillations of the intensity of both fluorescence bands by ±20%, which remain exactly anticorrelated (Figure 4b−e). The peak wavelength position of AE **1** (Figure 4d, purple) follows the intensity fluctuations (Figure 4d, blue) almost perfectly, however, the variations are significantly smaller compared to room temperature (Figure 3f). The periodicity of the fluctuations depends on the excitation power density and varies with a period of 127 s at 75.6 kW/cm^2 to 53 s at 620 kW/cm^2 (Figure 4f), as determined from the sine fits shown in Figure 4e. In addition, the peak wavelength of the AE 1 emission exhibits a redshift from 725 to 736 nm during this increase in laser power.

We suggest that changes in the EET efficiency from excited CdSe/I⁻ NCs to aggregates of AE **1** are responsible for the anticorrelated fluctuations in the CdSe/I⁻/AE **1** nanocomposite (Figure 5a,b). Under 488 nm excitation, most of the light is absorbed by the inorganic NCs, as reflected by the absorption spectrum in Figure 3a, which mimics that of the pure NCs. The NC fluorescence overlaps with the absorption of AE **1**, resulting in efficient EET, which weakens the CdSe fluorescence signal and strengthens the molecular fluorescence. In Figure 4e, this scenario applies when the fluorescence band at 736 nm is at a maximum and the band at 625 nm is at a minimum, for example, after 25 s. Simultaneously, this EET invokes photothermal heating of the AE **1** aggregates, eventually triggering an order/disorder transition to break up the aggregates. The result of this transition is a reduced degree of planarization (Figure 5c), which blueshifts the absorption spectrum, decreases the overlap with the NC fluorescence (Figure 5d), weakens the efficiency of EET, diminishes the molecular fluorescence, and brightens the emission of the NCs. In Figure 4e, this scenario applies when the fluorescence band at 736 nm is at a minimum and the band at 625 nm is at a maximum, for example, after 55 s. In the disordered state, EET is slow, and photothermal heating is weak, such that new aggregates of AE **1** may form and the initial state with efficient EET from the NCs to the aggregates is restored. An illustration of the different absorption and emission pathways underlying this picture is provided in Scheme S2 in the Supporting Information. It is supported by the quantum chemical calculations of the angle-dependent energies of the excited and the ground states (Figure 2d), which are crucial for the occurrence of AIE.

The overall interpretation in Figure 5 is consistent with the laser power-dependent period for one complete cycle (Figure 4f) as increasing the number of photons will increase the rate of heat transfer, which should shorten the cycle period. It is furthermore supported by the fluorescence fluctuations of pure AE **1** in Figure 1, which are likely due to a similar order/disorder transition of the aggregates. The fact that the fluctuations are only observed in spatially confined, highly

https://dx.doi.org/10.1021/acsnano.0c05121
ACS Nano 2021, 15, 480−488

selective places on the sample suggests that a certain structure/geometry of the molecular stacks in the vicinity of the NCs is required. This is consistent with the often complex correlation between the efficiency of energy transfer and molecular orientation, distance, or structure.

Relaxing the structural rigidity in molecular emitters with AIE increases the rate of nonradiative recombination and decreases the fluorescence intensity.[4] The higher stability of the phenyl−C═C moiety in the nanocomposite (Figure 3e) compared to the pure molecule (Figure 1e) is consistent with a mostly indirect excitation of AE **1** in the nanocomposite by EET *vs* direct excitation of the pure molecule leading to photodegradation. EET as the main electronic interaction between the CdSe NCs and AE **1** is also in line with the fluorescence lifetime data in Figure 3b. Alternatively, one may consider charge transfer and the formation of an interfacial exciton between AE **1** and CdSe. Based on the calculated HOMO/LUMO positions of the molecule (Figure 2f), a type II energy alignment scenario where the hole resides on the NC and the electron is located partially on the molecule appears energetically plausible.[31] However, the short fluorescence lifetime of the CdSe/I^-/AE **1** nanocomposite (Figure 3b) is uncharacteristic for the formation of such an interfacial exciton, as one would expect much longer lifetimes similar to those in type II core/shell NCs.[32]

CONCLUSION

Coupling organic π-systems that exhibit aggregation-induced emission to a second fluorophore can result in emergent optical properties, such as dual fluorescence with oscillating intensity fluctuations. This is realized in a hybrid thin film consisting of CdSe NCs coupled to aggregates of an aryleneethynylene derivative with fluorescence from both fluorophores, which establish a feedback loop: Excitation energy transfer from the NCs to the aggregates leads to photothermal heating and an order/disorder transition in the aggregates. This transition weakens the fluorescence intensity of the organic π-system and the rate of energy transfer, which strengthens the NC fluorescence. Simultaneously, the slower energy-transfer rate reduces photothermal heating, which gradually restores the initial structure and optical properties of the molecular aggregates. This closes the feedback loop and initiates the next cycle. The resulting optical oscillations and their temperature dependence may be of interest for application in nanothermometry.

EXPERIMENTAL SECTION

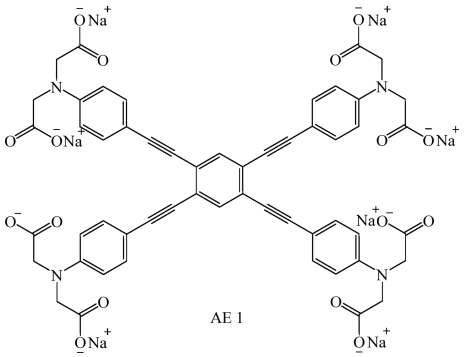

Sodium 2,2′,2″,2‴,2⁗,2⁗′,2⁗″,2⁗‴-(((benzene-1,2,4,5-tetrayltetrakis(ethyne-2,1-diyl))tetrakis(benzene-4,1-diyl))tetrakis(azanetriyl))octaacetate (AE 1). AE **1**-COOET (316 mg, 257 mmol) was dissolved in MeOH/H_2O (1:1, 10 mL/10 mL), and NaOH (515 mg, 12.9 mmol) was added. The resulting mixture was stirred at 70 °C for 2 d. The solvent was evaporated *in vacuo*. The residue was dissolved in H_2O and filtered. The resulting solution was adjusted to pH 7 and dialyzed against DI H_2O for 5 d. After filtration and freeze-drying, the title compound AE **1** was afforded as a brown fluffy solid (250 mg, 97%). ^{1}H NMR (600 MHz, D_2O): δ = 7.71−7.69 (m, 2 H), 7.48−7.44 (m, 8 H), 6.58−6.54 (m, 8 H), 3.93 (m, 16H) ppm. Due to low solubility, a ^{13}C NMR spectrum could not be obtained. IR (cm^{-1}): ν 3589, 3327, 3171, 3037, 2928, 2650, 2193, 1577, 1516, 1457, 1381, 1298, 1232, 1176, 1134, 972, 906, 817, 695, 610, 515, 456, 435.

The experimental procedures of precursors of compound AE **1** have been reported in the Supporting Information.

CdSe NCs Synthesis. *Chemicals Used.* Chemicals used were cadmium oxide (CdO, 99.99%, Aldrich), oleicacid (OA, 90%, Aldrich), trioctylphosphine (TOP, 97%, Abcr), trioctylphosphine oxide (TOPO, 99%, Aldrich), hexadecylamine(HDA, 90%, Aldrich), 1-octadecene (ODE, 90%, Acros Organics), selenium pellets (Se, 99.999%, Aldrich), ammonium iodide (99.999%,Aldrich), *N*-methylformamide (NMF, 99%, Aldrich), hexane (extra dry, 96%, Acros Organics), ethanol (extra dry, 99.5%, AcrosOrganics), acetone (extra dry, 99.8%, Acros Organics), dimethyl sulfoxide (DMSO, 99.7%, Acros Organics), and acetonitrile (extra dry, 99.9%, Acros Organics).

All chemicals, except those used in the CdSe NC synthesis, were stored and used inside a nitrogen-filled glovebox. All sample preparations for electrical or fluorescence measurements were carried out in a nitrogen-filled glovebox. The samples were inserted into a probe station for low-temperature photocurrent measurements using an airtight arm sealed inside the glovebox. Samples were kept under low pressure for at least 2 h before starting any measurements.

CdSe NCs and Device Preparation. Wurtzite CdSe NCs having ∼5 nm size were synthesized using a literature reported synthesis.[33,34] As synthesized, NCs were dispersed in hexane. CdSe NCs 5 mL, ∼10 mg/mL were taken for ligand exchange with 300 μL of a 1 M solution of NH_4I in NMF further diluted using 2.7 mL acetone. This biphasic mixture was stirred until the NCs changed their phase, then centrifuged and washed using excess of acetone. CdSe/I^- thus obtained was dispersed in NMF with a 60−100 mg/mL concentration. For device preparation, we used commercially available gold patterned Si/SiO_2 with 230 nm-thick dielectric layer and 2.5 μm × 1 cm channel provided by the Fraunhofer Institute for Photonic Microsystems, Dresden, Germany. In a typical device preparation, 70 μL of CdSe/I^- NCs was dropped on an FET substrate, mixed with 30 μL of AE **1** solution in NMF with a concentration of roughly 1 mg/mL, and kept undisturbed for 6 h. The still wet mixture of CdSe/I^-/AE **1** was then spun off at 30 rps for 1 min. Then the substrate was washed with acetonitrile multiple times and annealed at 190 °C for 35 min. A similar procedure was followed for preparing fluorescence samples on glass coverslips using a ligand-to-NC ratio of roughly 20:1, as determined by absorption spectroscopy and Lambert−Beer's law.

Electrical and Optical Measurements. Electrical measurements were carried out under nitrogen by using a Keithley 2634B source meter. The charge-carrier mobility was extracted using the gradual channel approximation in the linear regime. The error in the mobility (S) was calculated using the standard deviation error in the slope of I_d *vs* V_g curve at 5 V source−drain voltage:

$$S = \sqrt{\frac{1}{N-1}\sum_{i=1}^{N}|A_i - \bar{A}|}; \quad \bar{A} = \frac{1}{N}\sum_{i=1}^{N}A_i$$

where A is the slope from N measurements with the mean value $\bar{A}$.

Absorption measurements were acquired using a Carry 5000 UV−vis-NIR spectrophotometer on a thin glass coverslip or in methanol as stated in the text. Photocurrent low-temperature measurements were recorded using a CRX-6.5K (Lake Shore Desert) probe station operated under low pressure 5 × 10^6 mbar and a Keithley 2634B

https://dx.doi.org/10.1021/acsnano.0c05121
ACS Nano 2021, 15, 480−488

source meter. Samples were illuminated using a 408 nm LP405-SF10 laser diode manufactured by Thorlabs with a theoretical maximum output power of 11.5−30 mW. This output power decreases orders of magnitude due to beam decollimation, scattering, and inefficient coupling of optical fiber when calibrated using a test sample that comes out to be 10−18 μW.

Room-Temperature Fluorescence and Resonance Raman Measurements. The 12 ×12 mm glass coverslips were cleaned by submerging in a chromosulfuric acid cleaning solution for several hours, followed by three subsequent washing steps with triple distilled water and spectroscopy grade methanol. Fluorescence samples were then prepared on these coverslips using the drop casting method described above. The film was washed with acetonitrile and annealed at 190 °C before any measurements were taken.

The room-temperature steady-state photoluminescence and resonance stokes Raman spectral measurements as well as photoluminescence and scattering image acquisition were carried out using a home-built inverted confocal laser scanning microscope.[35] A 488 nm TOPTICA Photonics iBeam smart diode laser with a Gaussian intensity profile, operated in continuous wave mode, was employed as the light source. The laser intensity in the diffraction limited focus at maximum laser power is estimated to be 10^7 W/cm^2 operating at roughly 30−60% of maximum power. This focusing is crucial as the observed intensity fluctuations in Figures 1c, 3c, and 4a,c occur only in highly selective places and length scales of a few 100 nm. Focusing of the laser on the sample and the subsequent collection of reflected as well as scattered and emitted light was achieved through an oil immersion objective (NA = 1.25). The spectral data was recorded using an Acton SpectraPro 2300i spectrometer with a grating of 300/mm and a detector temperature of −45 °C. Extraction of Raman spectra from kinetic series spectra enables the study of correlations between vibrational and luminescence features from the same spot. Photoluminescence and scattering images were acquired by scanning the area of interest while utilizing two separate avalanche photodiodes (APDs) as detectors. The exclusion of atmospheric oxygen was achieved by nearly completely enclosing the upper part of the sample holder and passing a constant flow of nitrogen through this apparatus.

Low Temperature Fluorescence Measurements. Low temperature fluorescence was measured using a home-built confocal microscope mounted on a damped optical table and a standard microscope objective (60X DIN Achromatic objective, NA = 0.85, Edmund Optics) located inside a cryostat (SVT-200, Janis). A Cernox temperature sensor (CX-1030-SD-HT 0.3L) was positioned close to the sample to measure the temperature by a LakeShore Model 336 temperature controller. The sample holder was mounted on the scan stage. Attocube systems linear stages (ANPx320 and ANPz101eXT) and scanners (ANSxy100lr and ANSz100lr) were used to scan and position the sample.

A continuous wave 488 nm laser diode (OBIS LS 20 mW, Coherent Inc.) was used to excite the sample. The excitation intensity of the laser was measured between 0.35 mW and 4.80 mW before entering into the cryostat. The excitation light was then aligned into the objective (60X DIN Achromatic air objective, Edmund Optics) to get an optimal focus. The excitation intensity in the focus was between 5.5 × 10^4 and 7.52 × 10^5 W/cm^2.[36]

The collected fluorescence signal was passed through a dichroic mirror and a long-pass filter (488 LP Edge Basic, AHF Analysentechnik). It was detected by a single-photon counting avalanche photodiode (APD, COUNT-100C, Laser Components). Fluorescence spectra were also acquired with integration times of one second by a Shamrock 500 spectrograph in combination with an Andor Newton back illuminated deep depleted CCD camera (DU920PPR-DD). Further details for low temperature confocal imaging and spectroscopy setup can be found elsewhere.[37]

Time-resolved photoluminescence decay measurements. Time-resolved photoluminescence spectra were measured with a home-built scanning confocal microscope.[38] The sample was fixed on a piezo stage (Physik Instrumente) *via* magnets to avoid movement. A constant nitrogen flow was applied to maintain an inert atmosphere and avoid oxidation of the sample. To avoid bleaching, the lifetime was always measured before a fluorescence measurement.

A linearly polarized continuous wave laser (488 nm,0.33 mW measured before objective lens) was focused on the sample by a high numerical aperture (NA = 1.46) oil objective, the fluorescence was collected by the same objective and sent to a spectrometer (Acton SP-2500i, Princeton Instruments). For lifetime measurement, the laser was operated in the pulsed mode (5.3 × 10^3 W/cm^2,20 MHz). The signal was sent to a single photon avalanche photodiode (APD), connected to a time-correlated single photon counting module (HydraHarp 400). Decay curves were fitted and analyzed by SymPhoTime 64. See Scheme S1 for schematic of the time-resolved photoluminescence instrument.

Quantum Chemical Calculations. The computations of AE **2** were carried out with Turbomole 7.4.1. A selection of DFT functionals was considered, including M06-2X, wB97x, CAM-B3LYP, and B3LYP-D3BJ. Minimum geometries are confirmed by frequency analysis and agreed with results from RI-MP2. All values reported are obtained with the def2-TZVP basis set. We found B3LYP-D3BJ/def2-TZVP and its time-dependent variant to be superior, particularly in correctly simulating the Raman and absorption spectra. Calculations of the neutral, protonated derivative of AE **1** (8H-AE **1**) were performed by using Gaussian 16. The gas-phase ground-state equilibrium geometry of the molecules was optimized at the B3LYP/def2-SVP level of theory. Afterward, the phenylethinyl substituents were forced into specific torsion angles, and the resulting dihedral was fixed. Another geometry optimization was performed using B3LYP/def2-SVP level of theory. Fragment molecular orbital calculations were performed starting from the optimized geometries on the B3LYP/def2-SVP level of theory.

ASSOCIATED CONTENT

Supporting Information

The Supporting Information is available free of charge at https://pubs.acs.org/doi/10.1021/acsnano.0c05121.

Figure S1: Luminescence and scattering images of pure linker and CdSe/I$^-$/AE **1**. Figure S2: Fluorescence of CdSe/I$^-$. Figure S3: Gate sweeps of CdSe/I$^-$ and CdSe/I$^-$/AE **1**. Figure S4: Raman spectra of pure linker and CdSe/I$^-$/AE **1**. Figure S5: SEM micrograph of CdSe/I$^-$/AE **1**. Figure S6: Temperature-dependent electric conductivity of CdSe/I$^-$/AE **1** thin films. Scheme S1: Schematic of time-resolved photoluminescence instrument. Scheme S2: Schematic of the absorption and emission pathways in CdSe/I$^-$/AE **1** NC thin films in the ordered as well as the disordered states (PDF)

AUTHOR INFORMATION

Corresponding Authors

Marcus Scheele − *Institute for Physical and Theoretical Chemistry and Center for Light-Matter Interaction, Sensors and Analytics LISA+, University of Tübingen, 72076 Tübingen, Germany*; orcid.org/0000-0002-2704-3591; Email: marcus.scheele@uni-tuebingen.de

Uwe H. F. Bunz − *Organisch-Chemisches Institut and Centre for Advanced Materials, Ruprecht-Karls-Universität Heidelberg, 69120 Heidelberg, Germany*; orcid.org/0000-0002-9369-5387; Email: uwe.bunz@oci.uni-heidelberg.de

Authors

Krishan Kumar − *Institute for Physical and Theoretical Chemistry, University of Tübingen, 72076 Tübingen, Germany*

https://dx.doi.org/10.1021/acsnano.0c05121
ACS Nano 2021, 15, 480−488

Jonas Hiller – *Institute for Physical and Theoretical Chemistry, University of Tübingen, 72076 Tübingen, Germany*
Markus Bender – *Organisch-Chemisches Institut and Centre for Advanced Materials, Ruprecht-Karls-Universität Heidelberg, 69120 Heidelberg, Germany*
Saeed Nosrati – *Institute for Physical and Theoretical Chemistry, University of Tübingen, 72076 Tübingen, Germany*
Quan Liu – *Institute for Physical and Theoretical Chemistry, University of Tübingen, 72076 Tübingen, Germany; Charles Delaunay Institute, CNRS Light, Nanomaterials, Nanotechnologies (L2n, former "LNIO"), University of Technology of Troyes, 10004 Troyes, France*
Marc Edelmann – *Institute for Physical and Theoretical Chemistry, University of Tübingen, 72076 Tübingen, Germany*
Steffen Maier – *Organisch-Chemisches Institut and Centre for Advanced Materials, Ruprecht-Karls-Universität Heidelberg, 69120 Heidelberg, Germany*
Tim Rammler – *Institute for Physical and Theoretical Chemistry, University of Tübingen, 72076 Tübingen, Germany*
Frank Wackenhut – *Institute for Physical and Theoretical Chemistry, University of Tübingen, 72076 Tübingen, Germany;* orcid.org/0000-0001-6554-6600
Alfred J. Meixner – *Institute for Physical and Theoretical Chemistry and Center for Light-Matter Interaction, Sensors and Analytics LISA+, University of Tübingen, 72076 Tübingen, Germany;* orcid.org/0000-0002-0187-2906
Kai Braun – *Institute for Physical and Theoretical Chemistry, University of Tübingen, 72076 Tübingen, Germany;* orcid.org/0000-0003-3774-0507

Complete contact information is available at: https://pubs.acs.org/10.1021/acsnano.0c05121

Notes

The authors declare no competing financial interest.

ACKNOWLEDGMENTS

Financial support of this work has been provided by the Emmy Noether program of the DFG under grants SCHE1905/3-1 and ME 1600/13-3. We thank Andre Maier for electron microscopy imaging.

REFERENCES

(1) Luo, J.; Xie, Z.; Lam, J. W. Y.; Cheng, L.; Tang, B. Z.; Chen, H.; Qiu, C.; Kwok, H. S.; Zhan, X.; Liu, Y.; Zhu, D. Aggregation-Induced Emission of 1-Methyl-1,2,3,4,5-Pentaphenylsilole. *Chem. Commun.* **2001**, No. 18, 1740–1741.
(2) Barbara, P. F.; Rand, S. D.; Rentzepis, P. M. Direct Measurements of Tetraphenylethylene Torsional Motion by Picosecond Spectroscopy. *J. Am. Chem. Soc.* **1981**, *103*, 2156–2162.
(3) Bunz, U. H. F. Poly(aryleneethynylene)s: Syntheses, Properties, Structures, and Applications. *Chem. Rev.* **2000**, *100*, 1605–1644.
(4) Chen, Y.; Lam, J. W. Y.; Kwok, R. T. K.; Liu, B.; Tang, B. Z. Aggregation-Induced Emission: Fundamental Understanding and Future Developments. *Mater. Horiz.* **2019**, *6*, 428–433.
(5) Cai, Y.; Du, L.; Samedov, K.; Gu, X.; Qi, F.; Sung, H. H. Y.; Patrick, B. O.; Yan, Z.; Jiang, X.; Zhang, H.; Lam, J. W. Y.; Williams, I. D.; Lee Phillips, D.; Qin, A.; Tang, B. Z. Deciphering the Working Mechanism of Aggregation-Induced Emission of Tetraphenylethylene Derivatives by Ultrafast Spectroscopy. *Chem. Sci.* **2018**, *9*, 4662–4670.
(6) Bunz, U. H. F. Poly(aryleneethynylene)s. *Macromol. Rapid Commun.* **2009**, *30*, 772–805.
(7) Leung, N. L. C.; Xie, N.; Yuan, W.; Liu, Y.; Wu, Q.; Peng, Q.; Miao, Q.; Lam, J. W. Y.; Tang, B. Z. Restriction of Intramolecular Motions: The General Mechanism behind Aggregation-Induced Emission. *Chem. - Eur. J.* **2014**, *20*, 15349–15353.
(8) Parrott, E. P. J.; Tan, N. Y.; Hu, R.; Zeitler, J. A.; Tang, B. Z.; Pickwell-Macpherson, E. Direct Evidence to Support the Restriction of Intramolecular Rotation Hypothesis for the Mechanism of Aggregation-Induced Emission: Temperature Resolved Terahertz Spectra of Tetraphenylethene. *Mater. Horiz.* **2014**, *1*, 251–258.
(9) Yamamoto, N. Mechanisms of Aggregation-Induced Emission and Photo/Thermal E/Z Isomerization of a Cyanostilbene Derivative: Theoretical Insights. *J. Phys. Chem. C* **2018**, *122*, 12434–12440.
(10) Maity, S.; Wu, W. C.; Tracy, J. B.; Clarke, L. I.; Bochinski, J. R. Nanoscale Steady-State Temperature Gradients within Polymer Nanocomposites Undergoing Continuous-Wave Photothermal Heating from Gold Nanorods. *Nanoscale* **2017**, *9*, 11605–11618.
(11) Borzenkov, M.; Pallavicini, P.; Chirico, G. Photothermally Active Inorganic Nanoparticles: From Colloidal Solutions to Photothermally Active Printed Surfaces and Polymeric Nanocomposite Materials. *Eur. J. Inorg. Chem.* **2019**, *2019*, 4397–4404.
(12) Park, C. H.; Yun, H.; Yang, H.; Lee, J.; Kim, B. J. Fluorescent Block Copolymer-MoS_2 Nanocomposites for Real-Time Photothermal Heating and Imaging. *Adv. Funct. Mater.* **2017**, *27*, 1604403.
(13) Crane, M. J.; Zhou, X.; Davis, E. J.; Pauzauskie, P. J. Photothermal Heating and Cooling of Nanostructures. *Chem. - Asian J.* **2018**, *13*, 2575–2586.
(14) Resch-Genger, U.; Grabolle, M.; Cavaliere-Jaricot, S.; Nitschke, R.; Nann, T. Quantum Dots *versus* Organic Dyes as Fluorescent Labels. *Nat. Methods* **2008**, *5*, 763–775.
(15) Lutich, A. A.; Jiang, G.; Susha, A. S.; Rogach, A. L.; Stefani, F. D.; Feldmann, J. Energy Transfer *versus* Charge Separation in Type-II Hybrid Organic-Inorganic Nanocomposites. *Nano Lett.* **2009**, *9*, 2636–2640.
(16) Walker, B. J.; Nair, G. P.; Marshall, L. F.; Bulović, V.; Bawendi, M. G. Narrow-Band Absorption-Enhanced Quantum Dot/J-Aggregate Conjugates. *J. Am. Chem. Soc.* **2009**, *131*, 9624–9625.
(17) Beane, G.; Boldt, K.; Kirkwood, N.; Mulvaney, P. Energy Transfer between Quantum Dots and Conjugated Dye Molecules. *J. Phys. Chem. C* **2014**, *118*, 18079–18086.
(18) Luo, X.; Han, Y.; Chen, Z.; Li, Y.; Liang, G.; Liu, X.; Ding, T.; Nie, C.; Wang, M.; Castellano, F. N.; Wu, K. Mechanisms of Triplet Energy Transfer across the Inorganic Nanocrystal/Organic Molecule Interface. *Nat. Commun.* **2020**, *11*, 28.
(19) Freyria, F. S.; Cordero, J. M.; Caram, J. R.; Doria, S.; Dodin, A.; Chen, Y.; Willard, A. P.; Bawendi, M. G. Near-Infrared Quantum Dot Emission Enhanced by Stabilized Self-Assembled J-Aggregate Antennas. *Nano Lett.* **2017**, *17*, 7665–7674.
(20) Stöferle, T.; Scherf, U.; Mahrt, R. F. Energy Transfer in Hybrid Organic/ Inorganic Nanocomposites. *Nano Lett.* **2009**, *9*, 453–456.
(21) Guzelturk, B.; Demir, H. V. Near-Field Energy Transfer Using Nanoemitters for Optoelectronics. *Adv. Funct. Mater.* **2016**, *26*, 8158–8177.
(22) Zhang, H.; Rominger, F.; Bunz, U. H. F.; Freudenberg, J. Aggregation-Induced Emission of Triphenyl-Substituted Tristyrylbenzenes. *Chem. - Eur. J.* **2019**, *25*, 11218–11222.
(23) Zucchero, A. J.; McGrier, P. L.; Bunz, U. H. F. Cross-Conjugated Cruciform Fluorophores. *Acc. Chem. Res.* **2010**, *43*, 397–408.
(24) Li, N.; Jia, K.; Wang, S.; Xia, A. Theoretical Study of Spectroscopic Properties of Dimethoxy-*p*-Phenylene-Ethynylene Oligomers: Planarization of the Conjugated Backbone. *J. Phys. Chem. A* **2007**, *111*, 9393–9398.
(25) Miteva, T.; Palmer, L.; Kloppenburg, L.; Neher, D.; Bunz, U. H. F. Interplay of Thermochromicity and Liquid Crystalline Behavior in Poly(*p*-Phenyleneethynylene)s: Π–π Interactions or Planarization of the Conjugated Backbone? *Macromolecules* **2000**, *33*, 652–654.

https://dx.doi.org/10.1021/acsnano.0c05121
ACS Nano 2021, 15, 480–488

(26) Sluch, M. I.; Godt, A.; Bunz, U. H. F.; Berg, M. A. Excited-State Dynamics of Oligo(*p*-Phenyleneethynylene): Quadratic Coupling and Torsional Motions. *J. Am. Chem. Soc.* **2001**, *123*, 6447−6448.
(27) Wierzbicka, M.; Bylińska, I.; Czaplewski, C.; Wiczk, W. Experimental and Theoretical Studies of the Spectroscopic Properties of Simple Symmetrically Substituted Diphenylacetylene Derivatives. *RSC Adv.* **2015**, *5*, 29294−29303.
(28) Panzer, F.; Bässler, H.; Köhler, A. Temperature Induced Order-Disorder Transition in Solutions of Conjugated Polymers Probed by Optical Spectroscopy. *J. Phys. Chem. Lett.* **2017**, *8*, 114−125.
(29) Castruita, G.; Arias, E.; Moggio, I.; Pérez, F.; Medellín, D.; Torres, R.; Ziolo, R.; Olivas, A.; Giorgetti, E.; Muniz-Miranda, M. Synthesis, Optical Properties and Supramolecular Order of π-Conjugated 2,5-Di(alcoxy)Phenyleneethynylene Oligomers. *J. Mol. Struct.* **2009**, *936*, 177−186.
(30) Köhler, A.; Khan, A. L. T.; Wilson, J. S.; Dosche, C.; Al-Suti, M. K.; Shah, H. H.; Khan, M. S. The Role of C-H and C-C Stretching Modes in the Intrinsic Non-Radiative Decay of Triplet States in a Pt-Containing Conjugated Phenyleneethynylene. *J. Chem. Phys.* **2012**, *136*, No. 094905.
(31) Jasieniak, J.; Califano, M.; Watkins, S. E. Size-Dependent Valence and Conduction Band-Edge Energies of Semiconductor Nanocrystals. *ACS Nano* **2011**, *5*, 5888−5902.
(32) Kim, S.; Fisher, B.; Eisler, H.-J.; Bawendi, M. Type-II Quantum Dots: CdTe/CdSe(Core/Shell) and CdSe/ZnTe(Core/Shell) Heterostructures. *J. Am. Chem. Soc.* **2003**, *125*, 11466−11467.
(33) Sayevich, V.; Guhrenz, C.; Dzhagan, V. M.; Sin, M.; Werheid, M.; Cai, B.; Borchardt, L.; Widmer, J.; Zahn, D. R. T.; Brunner, E.; Lesnyak, V.; Gaponik, N.; Eychmüller, A. Hybrid N-Butylamine-Based Ligands for Switching the Colloidal Solubility and Regimentation of Inorganic-Capped Nanocrystals. *ACS Nano* **2017**, *11*, 1559−1571.
(34) Kumar, K.; Liu, Q.; Hiller, J.; Schedel, C.; Maier, A.; Meixner, A.; Braun, K.; Lauth, J.; Scheele, M. Fast, Infrared-Active Optical Transistors Based on Dye-Sensitized CdSe Nanocrystals. *ACS Appl. Mater. Interfaces* **2019**, *11*, 48271−48280.
(35) Wackenhut, F.; Virgilio Failla, A.; Züchner, T.; Steiner, M.; Meixner, A. J. Three-Dimensional Photoluminescence Mapping and Emission Anisotropy of Single Gold Nanorods. *Appl. Phys. Lett.* **2012**, *100*, 263102.
(36) Brecht, M.; Studier, H.; Elli, A. F.; Jelezko, F.; Bittl, R. Assignment of Red Antenna States in Photosystem I from Thermosynechoccocus Elongatus by Single-Molecule Spectroscopy. *Biochemistry* **2007**, *46*, 799−806.
(37) Hussels, M.; Konrad, A.; Brecht, M. Confocal Sample-Scanning Microscope for Single-Molecule Spectroscopy and Microscopy with Fast Sample Exchange at Cryogenic Temperatures. *Rev. Sci. Instrum.* **2012**, *83*, 123706.
(38) Wackenhut, F.; Failla, A. V.; Meixner, A. J. Multicolor Microscopy and Spectroscopy Reveals the Physics of the One-Photon Luminescence in Gold Nanorods. *J. Phys. Chem. C* **2013**, *117*, 17870−17877.

https://dx.doi.org/10.1021/acsnano.0c05121
ACS Nano 2021, 15, 480−488

https://doi.org/10.1021/acsnano.0c05121

Anteil an gemeinschaftlicher Veröffentlichung:

Es handelt sich hierbei um eine Nebenveröffentlichung. Wie auch diese Arbeit behandelt sie Fluoreszenzlebensdauern. Für das Erstellen dieser Veröffentlichung sind hauptsächlich meine Co-Autoren verantwortlich. Mein Beitrag zu dieser Arbeit war der Aufbau eines der verwendeten zeitaufgelösten Mikroskope, der Aufnahme der Fluoreszenzlebensdauern von CdSe Quanten Dots sowie die Beratung bei der Evaluation von Fluoreszenzlebensdauerdaten.

7.6 Distinguishing between Triplet-Pair State and Excimer Emission in Singlet Fission Chromophores Using Mixed Thin Films (veröffentlicht)

THE JOURNAL OF PHYSICAL CHEMISTRY C
A JOURNAL OF THE AMERICAN CHEMICAL SOCIETY

pubs.acs.org/JPCC Article

Distinguishing between Triplet-Pair State and Excimer Emission in Singlet Fission Chromophores Using Mixed Thin Films

Julian Hausch, Adam J. Berges, Clemens Zeiser, Tim Rammler, Arne Morlok, Jona Bredehöft, Sebastian Hammer, Jens Pflaum, Christopher J. Bardeen,* and Katharina Broch*

Cite This: J. Phys. Chem. C 2022, 126, 6686−6693 Read Online

ACCESS | Metrics & More | Article Recommendations | Supporting Information

ABSTRACT: In the photoluminescence spectra of thin films made of singlet fission (SF) materials emission features that are red-shifted from the free exciton emission are of particular interest. They can be fingerprints of the correlated triplet-pair state and as such offer insights into the mechanisms of the multistep SF process. However, excimer formation or trap-state population can also cause such features and a clear disentanglement of the various contributions can be challenging. Here, we use blends of anthradithiophene (ADT) and weakly interacting organic semiconductors to control the polarizability of the molecular environment and, thus, to distinguish between excimer emission and emission from the correlated triplet-pair state. Using time-resolved photoluminescence spectroscopy measurements, we clarify the relation between excimer formation and SF in ADT and find that excimer formation constitutes a parallel relaxation channel for the exciton and neither mediates nor hinders SF.

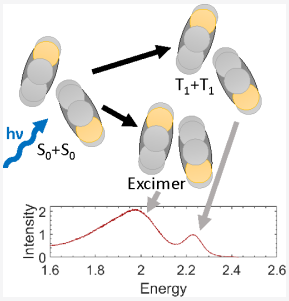

INTRODUCTION

In the optimization of organic optoelectronic devices, a crucial part is understanding the mechanism and contribution of loss channels. To obtain deeper insight into the involved processes, photoluminescence (PL) spectroscopy is a well suited method, as it not only allows the detection of nonradiative channels via quenching but also is sensitive to specific radiative channels such as the population of trap states or excimer formation, both of which can be readily identified by spectroscopic signatures red-shifted from the exciton emission.[1,2] Similar signatures are of particular importance for a specific class of organic semiconductors, namely singlet fission (SF) materials, as they can give insights into the details of this multistep, technologically relevant,[3] process. SF describes the spin-allowed fission of a singlet exciton into two triplet excitons via an electronically coupled triplet-pair state (^{1}(TT)) of singlet character[4] and has been successfully studied *inter alia*[5−7] via PL spectroscopy to elucidate the nature of the triplet-pair state intermediate and the related pathways of triplet-pair formation and triplet separation.[8−16]

However, one complication that arises in the investigation of SF materials by PL spectroscopy is the fact that the intermediate ^{1}(TT) state is a dark state[17] that becomes only emissive via Herzberg−Teller coupling.[13,15,18−20] The resulting red shift of the corresponding emission compared to the energy of the ^{1}(TT) state leads to an overlap of its spectral signature with other contributions at low photon energies such as excimers[2,11,12,14,21−26] or trap-state emission.[1,13−15] This poses the experimental challenge to disentangle the various contributions leading to emission features at low photon energies (in the following referred to as red-shifted luminescence features (RSL)) and to clarify whether the related states mediate SF[10,12,16,21,27−29] or constitute a loss channel.[11,14,15,22,23,25,30−34] This question directly relates to an ongoing debate in the literature, which concerns the role of excimer formation in the SF process.[11,12,14,21−26,31,34] Excimers as a competing channel for SF have been observed experimentally in tetracene (TET)[11,14,34,35] and antradithiophene (ADT) derivatives,[20,30] but have also been proposed as an intermediate state for SF.[10,27,36,37]

The challenges preventing a general elucidation of the nature of the many possible states which can cause RSL (X_{RSL}) in thin films of SF materials arise from the above-mentioned ambiguity in the assignment of spectral signatures[10,13,16,20,34] and the lack of a tunable parameter that affects the energetic position of trap state emission, ^{1}(TT) state emission, and excimer emission differently. Here, we address this open question in ADT, a chromophore whose derivatives have been reported to exhibit both SF and pronounced RSL.[20] ADT is codeposited with two spacer compounds to continuously change the intermolecular interactions, the number of nearest neighbors, and the polarizability of the local molecular environment. The spacer molecules TET and 6-phenacene (6PH) are chosen to have singlet energies greater than that of

Received: October 26, 2021
Revised: March 21, 2022
Published: April 8, 2022

https://doi.org/10.1021/acs.jpcc.1c09297
J. Phys. Chem. C 2022, 126, 6686−6693

ADT, making energy transfer from ADT to the spacers unlikely. The resulting changes in the dynamics of the different decay channels are probed by time-resolved PL spectroscopy (TRPL). Comparing the photoluminescence behavior of ADT in blends with spacer molecules of high and low polarizability,[38] TET and 6PH (see Figure 1a), respectively, with

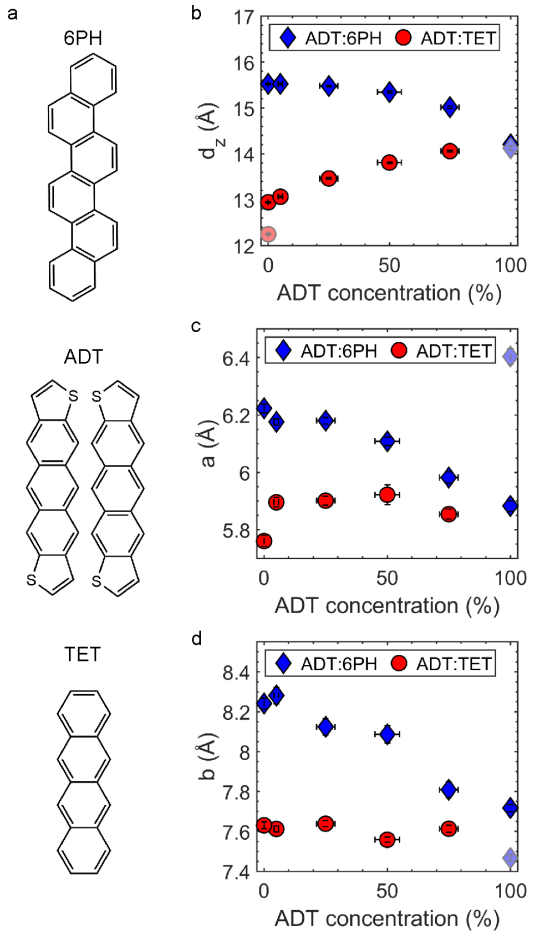

Figure 1. (a) Chemical structure of the investigated molecules. For ADT, the two isomers present in our samples are shown, see Supporting Information for details. (b) Out-of-plane lattice spacing and (c,d) in-plane unit cell parameters (c) *a* and (d) *b*, determined by X-ray diffraction. The faded data points indicate the unit cell parameters determined for the second polymorph of ADT or TET (see Supporting Information for details). Note that the in-plane unit cell parameters do not differ significantly between the two polymorphs of TET.

ADT in solution, allows us, first, to confirm the occurrence of SF in ADT and, second, to distinguish between spectral contributions of the ^{1}(TT) state, trap states and excimers. We identify the latter as a parallel pathway to SF in ADT, allowing for a refinement of current models on the role of X_{RSL} debated in the literature.[13,14]

METHODS

Anthradithiophene (ADT, Sigma-Aldrich, 97% purity, the material contains a mixture of two different isomers, anti-ADT and syn-ADT (chemical structures are displayed in Figure 1a); see Supporting Information for details), Tetracene (TET, Sigma-Aldrich, 99.99% purity), and [6]-phenacene (6PH, Lambson Japan Co. Ltd., 99% purity) were used as received. The samples were prepared by codeposition (organic molecular beam deposition) in a high vacuum chamber with a base pressure of 10^{-8} mbar. The molecules were resistively heated in individual Knudsen-cells, and the deposition rate for each molecule was controlled by a separate quartz crystal microbalance (QCM), calibrated using X-ray reflectivity (XRR) measurements. All films have a nominal thickness of 80 nm and were deposited with a total growth rate of 6 Å/min on native silicon and quartz glass substrates, which were kept at room temperature during growth. The mixing ratio of each film was calculated in molar % of ADT. XRR measurements were performed on a Ge XRD 3003TT instrument, and grazing incidence wide-angle X-ray scattering (GIWAXS) measurements, on a Xeuss 2.0 (Xenocs) in-house instrument with a Pilatus 300k detector, both using Cu K_α radiation (λ = 1.541 Å). Absorption spectra were recorded with a PerkinElmer Lambda 950 UV−vis−NIR spectrometer. The steady-state PL measurements were conducted with a pulsed laser diode LDH-P-C-470 (Pico-Quant, Germany) of 470 nm wavelength, a time-averaged power of 0.05 μW, and a repetition rate of 40 MHz. Using a Plan-NEOFLUAR 65x/NA 0.75 air-objective (Carl Zeiss AG, Germany), the laser pulses were focused on a spot with a 30 μm diameter on the sample, yielding a fluence of 1.77×10^{-4} μJ/cm^2. As the detecting unit, an Acton SP300 spectrometer with a PIXIS 100 camera (both Princeton Instruments, USA) was used.

Time-resolved photoluminescence measurements were taken with a Hamamatsu C4334 Streakscope having a time resolution of 20 ps and a spectral resolution of 2.5 nm. The 800 nm output of an 80 MHz Coherent Vitesse Ti:sapphire oscillator was frequency doubled to generate the 400 nm excitation pulse. A Pockels cell controlled by a ConOptics pulse-picking system was used to adjust the repetition rate of the oscillator to 100 kHz. A 450 nm long wave-pass filter was placed before the streak camera to minimize the contribution of laser light scatter to the signal. All measurements were performed in a vacuum cryostat (10^{-5} Torr) fitted with optical windows, and pulse fluences remained below 1.2 μJ/cm^2.

RESULTS AND DISCUSSION

The commercially available ADT used in our work contains two isomers (anti-ADT and syn-ADT; see Figure 1a for chemical structures). However, this does not significantly impact our results as both isomers show similar structural and optical properties as derived from X-ray diffraction experiments[39] and DFT calculations (see Table S1 in the Supporting Information). Consequently, we do not expect differences in the steric compatibility, the mixing behavior, or the intermolecular interactions of the two ADT isomers with the spacer molecules (TET and 6PH) studied here. Also, most previous studies on optical and electronic properties of ADT and its derivatives use a mixture of both isomers as well.[13,40−44] In the following we will thus refer to the isomerically mixed material as ADT. The structural properties of the two mixed systems (ADT:TET blends and ADT:6PH blends) are

https://doi.org/10.1021/acs.jpcc.1c09297
J. Phys. Chem. C 2022, 126, 6686−6693

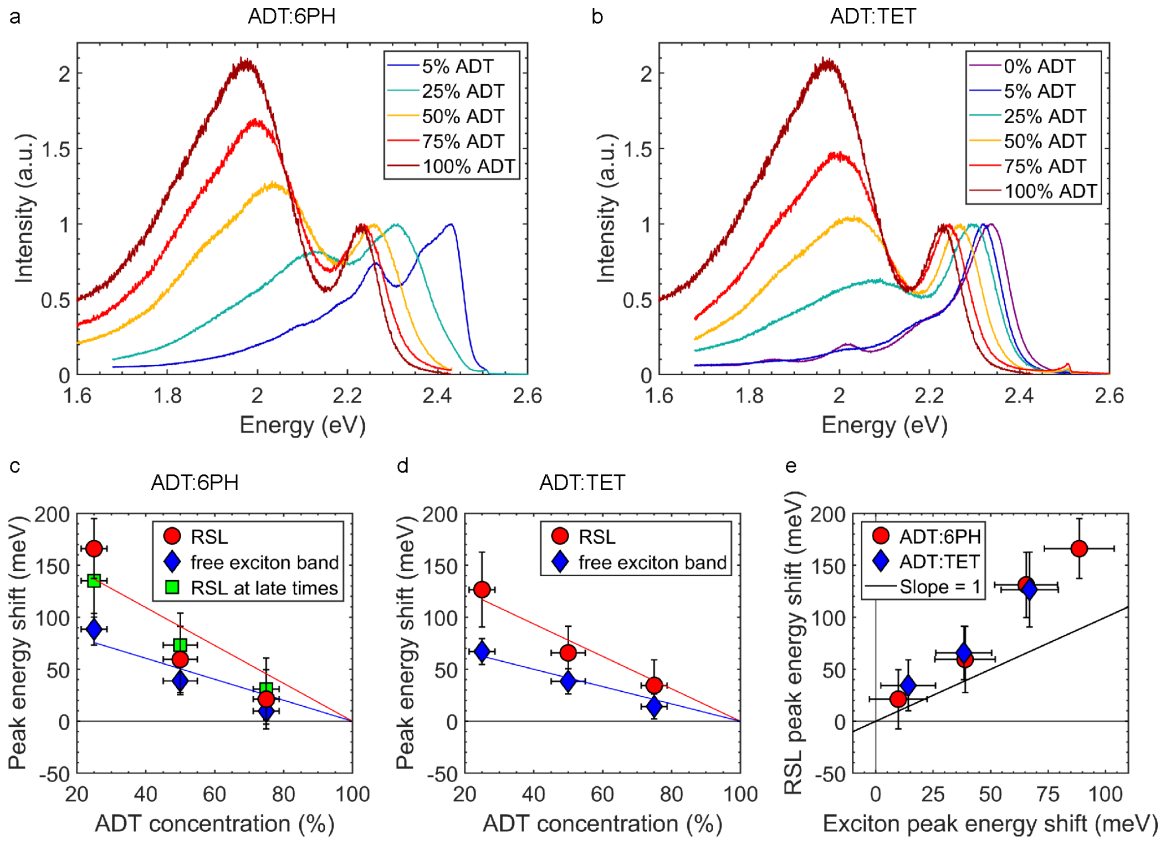

Figure 2. (a,b) Quasi-steady-state PL spectra of ADT:6PH (a) and ADT:TET blends (b) with different mixing ratios. The photon energy of the excitation was 2.54 eV. (c,d) Energetic shift of the RSL, the RSL at late times and the exciton peak position in ADT:6PH (c) and ADT:TET (d) blends compared to the respective positions for neat ADT. The red and blue lines are guide to the eye for the peak shift of the exciton (blue) and the RSL (red), respectively. (e) Energetic shift of the RSL against the shift of the free exciton emission for ADT:6PH and ADT:TET.

summarized in Figure 1b–d. For both a continuous change in the out-of-plane lattice spacing is observed, suggesting statistical intermixing[45] (see Figures S1–S3 in the Supporting Information for details), but there are clear differences in the dependence of the in-plane unit cell parameters *a* and *b* on the ADT concentration. While these parameters continuously increase with decreasing ADT concentration in blends with 6PH, they remain constant in blends of ADT with TET. This is consistent with statistical intermixing and with the fact that the neat ADT and TET films have comparable in-plane unit cell sizes, while it is clearly larger for neat 6PH (Figure 1c,d). Since the in-plane unit cell parameters describe the plane in which the molecular interactions are strongest,[46] any changes in these parameters might affect the related intermolecular electronic coupling[47−49] and, consequently, the photophysics. However, by comparing two mixed systems with different trends, we can estimate the impact of such structural changes on the PL spectra and the underlying excited state dynamics.

The steady-state PL spectra of the different samples are shown in Figure 2. The PL spectrum of neat ADT is dominated by two transitions, one at 2.21 eV, which we assign to emission of the free exciton based on the spectral shape and the small Stokes shift of 70 meV ($S_1 \leftarrow S_0$ in absorption at 2.28 eV; see Figure S4 in the Supporting Information). The second emission peak occurs at 1.95 eV, red-shifted by ΔE = 260 meV compared to the first emission peak. This spacing is too large for a vibronic progression of the free exciton, which we would expect around ΔE = 150 meV based on the vibronic progression of the absorption spectrum (see Figure S4 in the Supporting Information), and we thus assign it to the beforementioned RSL that has been observed also for other SF compounds.[10,11,13,14,16,20,30]

Now considering the PL spectra of the blends, a first interesting result is the independence of the spectral shape on the codeposited compound and the dominant ADT contribution as can be seen in Figure 2a,b. The blends with 5% ADT are the exception, with a PL spectrum that resembles the solution spectrum of ADT (Supporting Information, Figure S7b) for blends with the high band gap spacer molecule 6PH, and is dominated by TET emission in the case of ADT:TET blends (see Supporting Information for details). In the following, we will restrict the discussion to blends with ADT concentrations above 5%. Comparing the positions of the two main features in neat ADT with their positions in the PL spectra of the blends (see Figure 2c–d), we observe a continuous shift to higher photon energies with decreasing ADT concentration in all cases, which can be explained by changes in the polarizability of the local molecular environment in the blends compared to the neat film. The absolute value of the shift follows the optical band gap of the spacer

https://doi.org/10.1021/acs.jpcc.1c09297
J. Phys. Chem. C 2022, 126, 6686−6693

molecules and the related polarizability,[38] since the observed shift is larger in blends of ADT with the high band gap (low polarizability) spacer molecule 6PH compared to the low band gap (higher polarizability) spacer molecule TET. Further comparing the shift of the free exciton emission and the RSL for all blends, we find that the shift is more pronounced for the latter (see trendlines in Figure 2c,d), implying that X_{RSL} is more sensitive to changes in the polarizability of the environment than the free exciton. This increased sensitivity can be rationalized by a stronger charge transfer (CT) state admixture,[48−50] which has been observed for excimers[31,51] and gives us first insight into the nature of X_{RSL}. An additional noteworthy finding is the decrease of the intensity of the RSL relative to the free exciton emission with decreasing ADT concentration. For processes which strongly depend on interactions between neighboring molecules, like excimer formation or triplet-pair state formation, such an intensity decrease results from the replacement of nearest ADT neighbors by TET as well as 6PH.[52] Importantly, as the probability for a given number of ADT neighbors follows a binomial distribution[52] and is thus independent of the molecule (TET or 6PH) replacing ADT, this intensity decrease is identical in ADT blends with TET or 6PH. To summarize these first results, the coexistence of the RSL with emission of the free exciton makes these ADT based blends an ideal model system to investigate the origin of the RSL and its impact on SF using TRPL measurements.

Time traces extracted at the energetic position of the free exciton emission and the RSL are shown in Figure 3 and have been analyzed by fitting to a biexponential decay (see Figure 4a,b and Table S2 in the Supporting Information for decay rates and Supporting Information for details). In thin films the free exciton emission decays generally faster than the RSL and, in addition, exhibits a higher sensitivity to changes in the ADT concentration. The rates of the free exciton decay decrease linearly with decreasing ADT concentration independent of the spacer molecule (see Figure 4a,b). This, in combination with an increased decay rate of the free exciton emission of a neat ADT thin film compared to ADT in solution (see Figure 3a) gives insight into the photophysics of ADT. In solution, ADT exhibits a decay rate of 0.57 ns^{-1}, while in the polycrystalline solid state a new, much more rapid decay process with a rate of about 42 ns^{-1} appears. Furthermore, the linear dependence of this decay rate on the ADT concentration in blends demonstrates that two nearest neighbors are involved in this rapid decay and that the increase in lateral spacing with decreasing ADT concentration plays a minor role. On these time scales, SF is the most probable candidate for this system, also because SF has already been reported to occur in a variety of ADT derivatives.[13,20,30] Importantly, we can not only conclude that SF is the main decay path of the free exciton, but our results for ADT blends also allow us to elucidate its microscopic mechanism. The linear dependence of the SF rate on the chromophore concentration has been observed before for TET and referred to as the replacement effect,[52,53] indicating that SF occurs via incoherent population transfer from S_1 to ^{1}(TT). The deviation from this linear dependence found for TET blends with low ADT fractions can be explained by the similar band gaps of ADT and TET, which makes an excitation of solely ADT impossible and can also enable an energy transfer from ADT to TET. Hence the excited state dynamics of TET have to be considered for these blends as well, which is done in the Supporting Information.

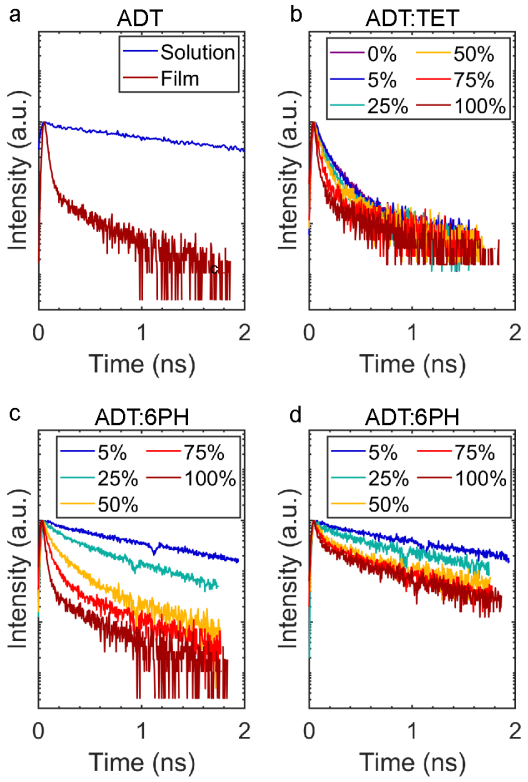

Figure 3. (a) Time traces of the singlet exciton emission of ADT in $CHCl_3$ solution and in a neat ADT film. (b,c) Time traces of the free exciton emission in (b) ADT:TET and (c) ADT:6PH blends with different ADT concentrations, (d) time traces of the RSL in ADT:6PH blends with different ADT concentrations. ADT concentrations of the blends are given in molar % in the legend. The intensity is scaled logarithmically.

Since SF is mediated by states comparable to X_{RSL} in ADT derivates,[13,20] the dynamics of the RSL also give insight into the SF mechanism. The temporal evolution of the RSL intensity (see Figure 3d and Figure S5 in the Supporting Information) allows us to conclude that X_{RSL} is formed on a time scale faster than the instrument response (<10 ps) and, furthermore, that population transfer from the exciton to X_{RSL} can be excluded as the major decay channel for the free exciton due to the lack of an increase in RSL intensity on the time scale of the free exciton emission decay. Lastly, the intensity decay of the RSL follows a similar trend with changing ADT concentration as that observed for the free exciton (see Table S2 in the Supporting Information for numeric values), although less pronounced.

In order to shed further light on the decay dynamics, PL spectra of the different ADT:6PH blends have been extracted by integrating the intensity over two time windows. For the first, short time window, a time interval between 0 and 2 ns was chosen in which both the exciton emission and the RSL are observed for blends with ADT concentrations above 5%. The starting time for the second, longer time window was chosen individually for each blend such that the decay of the exciton emission was almost complete. A noteworthy result of the comparison of the spectra in these two time windows is the

https://doi.org/10.1021/acs.jpcc.1c09297
J. Phys. Chem. C 2022, 126, 6686−6693

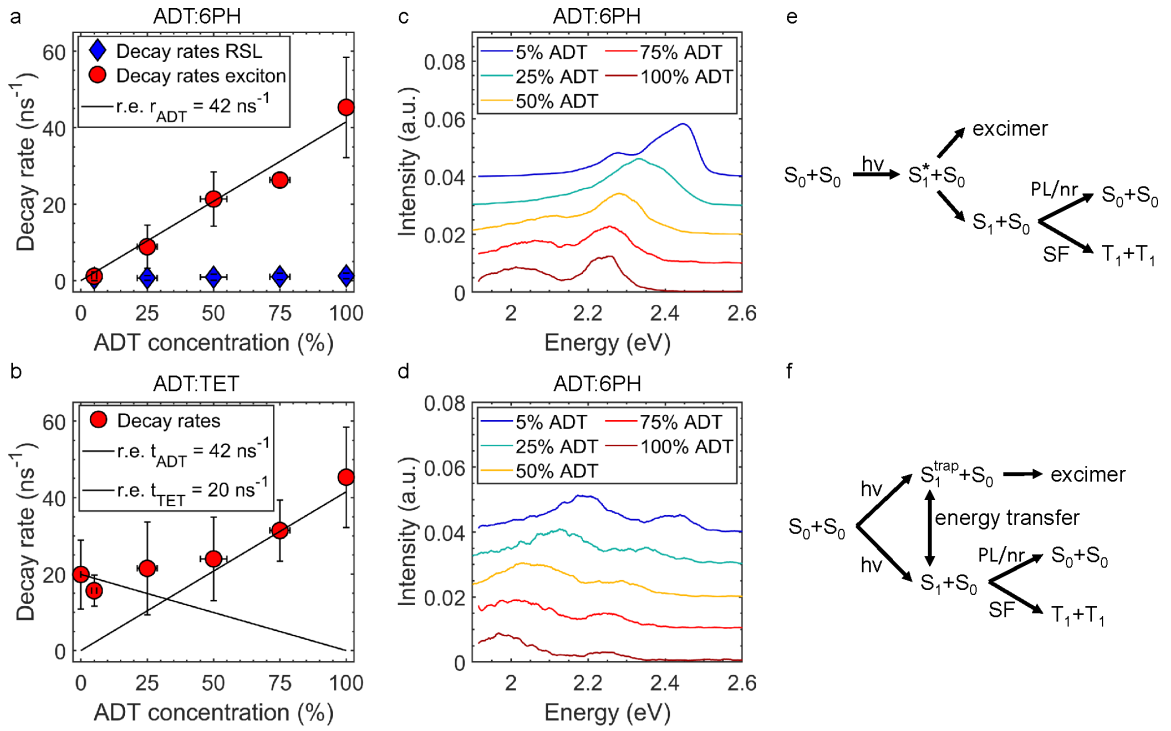

Figure 4. (a,b) Evolution of the SF rate and RSL decay rate of ADT:6PH (a) and ADT:TET (b) blends. For SF based on incoherent population transfer a linear behavior with changing ADT concentration is expected according to the replacement effect (r.e.) as sketched in the graphs. Note that the decay rate for 5% ADT in (a) might be dominated by the decay of excitons on isolated ADT molecules and that the decay rate for 100% ADT in (a,b) is close to the instrument resolution, which is 10 ps. (c,d) Time-integrated PL spectra of ADT:6PH blends in the time range (c) 0 to 2 ns and (d) >4 ns (100%, 75% ADT), >8 ns (50% ADT), >40 ns (25%, 5% ADT). Excitation at 400 nm, data noise filtered and vertically offset for clarity. (e,f) Sketches of possible decay mechanisms.

shift of the RSL to lower energies with increasing time (compare Figure 4c and Figure 4d). This points toward the existence of energetically low-lying sites such as grain boundaries where X_{RSL} is long-lived[51,54] and which are populated via exciton diffusion, dominating the spectrum at late times. Importantly, the simultaneous observation of exciton emission and RSL at short times indicates that X_{RSL} can also be formed within crystalline domains of the polycrystalline mixed films, i.e., is not unique to defect sites. However, the low-lying defect sites provide an additional decay channel via exciton diffusion, leading to the observed red shift of the RSL. This interpretation is supported by Figure 2c, where the change in peak positions of the RSL in the late time window with changing ADT concentration is also shown. We find the same trend as in the steady state PL data, suggesting that X_{RSL} exhibits the same sensitivity on changes in the polarizability of the local molecular environment, independent of the time window, and, thus, also a high CT admixture, indicating that it is the same state in both time windows.

Based on these results and in particular considering the different response of the two decay channels (exciton vs RSL) to changes in the polarizability, we can now discuss the nature of X_{RSL} and its role in the SF of ADT. The most important result is its dependence on the polarizability of the local molecular environment, for which we use the change in the energy of the free exciton emission as a measure. When Figure 2c and d are compared, clearly, both the free exciton emission and the RSL follow similar trends with decreasing ADT concentration and changes in the band gap of the codeposited compound. As discussed before, the main reason for the shift in energy of the exciton emission is a change in the polarizability of the local molecular environment, and the same reasoning has also been applied to the shift in RSL energy. However, plotting both shifts against each other gives interesting insight into the above-mentioned CT state admixture to X_{RSL}.[49,50] It allows us now to elucidate the nature of X_{RSL} and, in particular, to distinguish between an excimer and the triplet-pair state (^{1}(TT)) as possible origins. The former is expected to be highly sensitive to changes in polarizability due to a large CT admixture.[2] Consequently, the corresponding shift in the energetic position of the excimer emission with changing mixing ratio (and, thus, changing polarizability of the local molecular environment) should be larger than that of the free exciton emission and the slope in Figure 2e becomes >1. For the second case, in order to understand the sensitivity of the ^{1}(TT) state to changes in the polarizability, the exact nature of this state has to be discussed first. The ^{1}(TT) state consists of not only two triplets but also a small admixture of other states, for example of the CT state,[55,56] making the sensitivity of the ^{1}(TT) state to changes in the polarizability slightly higher than that of uncorrelated triplets.[50] However, the admixture of these states can be considered small for several reasons. From a theoretical standpoint, calculations on pentacene[37,55] and tetracene[56]

https://doi.org/10.1021/acs.jpcc.1c09297
J. Phys. Chem. C 2022, 126, 6686−6693

only showed a small admixture of these states to the ^{1}(TT) state and since SF is occurring via the coherent mechanism in pentacene,[52] while, in contrast, we showed that in ADT the incoherent SF mechanism is driving SF, it can be expected that the admixture of these states is even smaller in ADT than in pentacene.[57] Additionally, from an experimental viewpoint, a large admixture of such states to ^{1}(TT) would make the ^{1}(TT) state visible in absorption and photoluminescence spectroscopy without the need for Herzberg−Teller coupling,[55] which, however, contrasts with our results. Also, a large admixture would result in a high binding energy between the two triplets in the ^{1}(TT) state, which would result in clear differences of the excited state absorption fingerprints between ^{1}(TT) and uncorrelated triplets. However, previous studies on comparable singlet fission chromophores revealed that it is generally very challenging to find spectroscopic differences between these two.[12] For such states like ^{1}(TT), which have a dominant triplet pair contribution and only a small CT state admixture, the energetic position of the corresponding emission is expected to be more stable upon changes in the polarizability of the local molecular environment due to a stronger localization of the corresponding excitation. Hence, if X_{RSL} was of ^{1}(TT) nature, a slope ≤1 would be expected in Figure 2e. Clearly, the slope in Figure 2e is larger than 1, unambiguously demonstrating that X_{RSL}, the state related to this RSL, has a large CT state admixture and, thus, is of excimeric rather than of ^{1}(TT) character.

Now, after X_{RSL} was identified as an excimer, the remaining question is whether it mediates SF or is a loss channel. We can rule out the excimer as the mediating species based on the lack of a concomitant increase of excimer luminescence on the time scale of the exciton decay (see Figure 3c,d). Instead, two scenarios for the interrelation of excimer formation and SF are proposed (see Figure 4e,f). In the first scenario photoexcitation leads to a nonrelaxed S_1 state, from where either ultrafast exciton relaxation to the free exciton band, followed by SF, or excimer formation can occur (Figure 4e). The second scenario assumes that excimer formation is facilitated at trap sites such as grain boundaries, while for the other sites SF is the dominant decay channel (Figure 4f). Since pronounced excimer emission is also observed in single crystals (see Supporting Information, Figure S7), despite the lack of grain boundaries and presumably a lower density of trap sites, the scenario in Figure 4e is favored. Importantly, neither the formation nor the decay of this excimer directly affects the SF process, suggesting neither a direct competition between SF and excimer formation nor a mediation of SF by the excimer state in ADT, but instead the coexistence of two parallel channels at room temperature.

CONCLUSIONS

In conclusion, ADT blends with weakly interacting spacer molecules are a promising approach to clarify the origin of RSL features in PL spectra of SF materials. They allow us to clearly distinguish contributions from excimer and triplet-pair state emission based on their different response to changes in the polarizability of the local molecular environment and, thus, shed light on a current debate about the role of emissive states in molecular systems that undergo SF. Generally, this approach can be used to clarify the nature of RSL states in a variety of chromophores.

ASSOCIATED CONTENT

Supporting Information

The Supporting Information is available free of charge at https://pubs.acs.org/doi/10.1021/acs.jpcc.1c09297.

Details on the structural analysis, X-ray diffraction data, absorption spectra and details on the TRPL spectra of ADT in solution and blends with 5% ADT and 25% ADT. (PDF)

AUTHOR INFORMATION

Corresponding Authors

Christopher J. Bardeen − *Department of Chemistry, U.C. Riverside, Riverside, California 92521, United States;* orcid.org/0000-0002-5755-9476; Email: christob@ucr.edu

Katharina Broch − *Institut für Angewandte Physik, Universität Tübingen, 72076 Tübingen, Germany;* orcid.org/0000-0002-9354-292X; Email: brochkatharina@gmail.com

Authors

Julian Hausch − *Institut für Angewandte Physik, Universität Tübingen, 72076 Tübingen, Germany*

Adam J. Berges − *Department of Chemistry, U.C. Riverside, Riverside, California 92521, United States;* orcid.org/0000-0001-8586-9044

Clemens Zeiser − *Institut für Angewandte Physik, Universität Tübingen, 72076 Tübingen, Germany;* orcid.org/0000-0003-3613-2243

Tim Rammler − *Institut für Physikalische und Theoretische Chemie, 72076 Tübingen, Germany*

Arne Morlok − *Institut für Angewandte Physik, Universität Tübingen, 72076 Tübingen, Germany*

Jona Bredehöft − *Institut für Angewandte Physik, Universität Tübingen, 72076 Tübingen, Germany*

Sebastian Hammer − *Lehrstuhl für Experimentelle Physik VI, Julius-Maximilians Universität Würzburg, 97074 Würzburg, Germany;* orcid.org/0000-0002-0458-4133

Jens Pflaum − *Lehrstuhl für Experimentelle Physik VI, Julius-Maximilians Universität Würzburg, 97074 Würzburg, Germany;* orcid.org/0000-0001-5326-8244

Complete contact information is available at: https://pubs.acs.org/10.1021/acs.jpcc.1c09297

Notes

The authors declare no competing financial interest.

ACKNOWLEDGMENTS

J.H. and K.B. thank Prof. Schreiber (University of Tuebingen) for access to equipment. J.H. and K.B. acknowledge funding by the German Research Foundation (BR4869/4-1). C.J.B. acknowledges support by the U.S. National Science Foundation, Grant CHE-1800187. J.P. and S.H. acknowledge support by the Bavarian State Ministry for Science and the Arts within the collaborative research network "Solar Technologies go Hybrid" (SolTech).

REFERENCES

(1) He, R.; Chi, X.; Pinczuk, A.; Lang, D.; Ramirez, A. P. Extrinsic optical recombination in pentacene single crystals: Evidence of gap states. *Appl. Phys. Lett.* **2005**, *87*, 211117.

(2) Birks, J. B. Excimers. *Rep. Prog. Phys.* **1975**, *38*, 903.

(3) Hanna, M. C.; Nozik, A. J. Solar conversion efficiency of photovoltaic and photoelectrolysis cells with carrier multiplication absorbers. *J. Appl. Phys.* **2006**, *100*, No. 074510.
(4) Smith, M. B.; Michl, J. Recent Advances in Singlet Fission. *Annu. Rev. Phys. Chem.* **2013**, *64*, 361−386.
(5) Seiler, H.; Krynski, M.; Zahn, D.; Hammer, S.; Windsor, Y. W.; Vasileiadis, T.; Pflaum, J.; Ernstorfer, R.; Rossi, M.; Schwoerer, H. Nuclear dynamics of singlet exciton fission in pentacene single crystals. *Sci. Adv.* **2021**, *7*, No. eabg0869.
(6) Birech, Z.; Schwoerer, M.; Schmeiler, T.; Pflaum, J.; Schwoerer, H. Ultrafast dynamics of excitons in tetracene single crystals. *J. Chem. Phys.* **2014**, *140*, 114501.
(7) Wilson, M. W. B.; Rao, A.; Clark, J.; Kumar, R. S. S.; Brida, D.; Cerullo, G.; Friend, R. H. Ultrafast Dynamics of Exciton Fission in Polycrystalline Pentacene. *J. Am. Chem. Soc.* **2011**, *133*, 11830−11833.
(8) Sanders, S. N.; Pun, A. B.; Parenti, K. R.; Kumarasamy, E.; Yablon, L. M.; Sfeir, M. Y.; Campos, L. M. Understanding the Bound Triplet-Pair State in Singlet Fission. *Chem.* **2019**, *5*, 1988−2005.
(9) Burdett, J. J.; Bardeen, C. J. Quantum Beats in Crystalline Tetracene Delayed Fluorescence Due to Triplet Pair Coherences Produced by Direct Singlet Fission. *J. Am. Chem. Soc.* **2012**, *134*, 8597−8607.
(10) Burdett, J. J.; Gosztola, D.; Bardeen, C. J. The dependence of singlet exciton relaxation on excitation density and temperature in polycrystalline tetracene thin films: Kinetic evidence for a dark intermediate state and implications for singlet fission. *J. Chem. Phys.* **2011**, *135*, 214508.
(11) Piland, G. B.; Bardeen, C. J. How morphology affects singlet fission in crystalline tetracene. *J. Phys. Chem. Lett.* **2015**, *6*, 1841−1846.
(12) Stern, H. L.; Musser, A. J.; Gelinas, S.; Parkinson, P.; Herz, L. M.; Bruzek, M. J.; Anthony, J.; Friend, R. H.; Walker, B. J. Identification of a triplet pair intermediate in singlet exciton fission in solution. *P. Natl. Acad. Sci.* **2015**, *112*, 7656−7661.
(13) Bossanyi, D. G.; Matthiesen, M.; Wang, S.; Smith, J. A.; Kilbride, R. C.; Shipp, J. D.; Chekulaev, D.; Holland, E.; Anthony, J. E.; Zaumseil, J.; et al. Emissive spin-0 triplet-pairs are a direct product of triplet−triplet annihilation in pentacene single crystals and anthradithiophene films. *Nat. Chem.* **2021**, *13*, 163−171.
(14) Dover, C.; Gallaher, J.; Frazer, L.; Tapping, P.; Petty, A.; Crossley, M.; Anthony, J.; Kee, T.; Schmidt, T. Endothermic singlet fission is hindered by excimer formation. *Nat. Chem.* **2018**, *10*, 305−310.
(15) Cruz, C. D.; Chronister, E. L.; Bardeen, C. J. Using temperature dependent fluorescence to evaluate singlet fission pathways in tetracene single crystals. *J. Chem. Phys.* **2020**, *153*, 234504.
(16) Tayebjee, M. J. Y.; Clady, R. G. C. R.; Schmidt, T. W. The exciton dynamics in tetracene thin films. *Phys. Chem. Chem. Phys.* **2013**, *15*, 14797−14805.
(17) Zimmerman, P.; Bell, F.; Casanova, D.; Head-Gordon, M. Mechanism for Singlet Fission in Pentacene and Tetracene: From Single Exciton to Two Triplets. *J. Am. Chem. Soc.* **2011**, *133*, 19944−19952.
(18) Musser, A. J.; Clark, J. Triplet-Pair States in Organic Semiconductors. *Annu. Rev. Phys. Chem.* **2019**, *70*, 323−351.
(19) Thampi, A.; Stern, H. L.; Cheminal, A.; Tayebjee, M. J. Y.; Petty, A. J.; Anthony, J. E.; Rao, A. Elucidation of excitation energy dependent correlated triplet pair formation pathways in an endothermic singlet fission system. *J. Am. Chem. Soc.* **2018**, *140*, 4613−4622.
(20) Yong, C. K.; Musser, A. J.; Bayliss, S. L.; Lukman, S.; Tamura, H.; Bubnova, O.; Hallani, R. K.; Meneau, A.; Resel, R.; Maruyama, M.; et al. The entangled triplet pair state in acene and heteroacene materials. *Nat. Commun.* **2017**, *8*, 1−12.
(21) Kolata, K.; Breuer, T.; Witte, G.; Chatterjee, S. Molecular packing determines singlet exciton fission in organic semiconductors. *ACS Nano* **2014**, *8*, 7377−7383.
(22) Feng, X.; Krylov, A. I. On couplings and excimers: lessons from studies of singlet fission in covalently linked tetracene dimers. *Phys. Chem. Chem. Phys.* **2016**, *18*, 7751−7761.
(23) Liu, H.; Nichols, V. M.; Shen, L.; Jahansouz, S.; Chen, Y.; Hanson, K. M.; Bardeen, C. J.; Li, X. Synthesis and photophysical properties of a "face-to-face" stacked tetracene dimer. *Phys. Chem. Chem. Phys.* **2015**, *17*, 6523−6531.
(24) Ni, W.; Sun, L.; Gurzadyan, G. G. Ultrafast spectroscopy reveals singlet fission, ionization and excimer formation in perylene film. *Sci. Rep.* **2021**, *11*, 5220.
(25) Dron, P. I.; Michl, J.; Johnson, J. C. Singlet fission and excimer formation in disordered solids of alkyl-substituted 1,3-diphenylisobenzofurans. *J. Phys. Chem. A* **2017**, *121*, 8596−8603.
(26) Ye, C.; Gray, V.; Mårtensson, J.; Börjesson, K. Annihilation versus excimer formation by the triplet pair in triplet−triplet annihilation photon upconversion. *J. Am. Chem. Soc.* **2019**, *141*, 9578−9584.
(27) Miller, C. E.; Wasielewski, M. R.; Schatz, G. C. Modeling singlet fission in rylene and diketopyrrolopyrrole derivatives: The role of the charge transfer state in superexchange and excimer formation. *J. Phys. Chem. C* **2017**, *121*, 10345−10350.
(28) Mauck, C. M.; Hartnett, P. E.; Margulies, E. A.; Ma, L.; Miller, C. E.; Schatz, G. C.; Marks, T. J.; Wasielewski, M. R. Singlet fission via an excimer-like intermediate in 3,6-bis(thiophen-2-yl)-diketopyrrolopyrrole derivatives. *J. Am. Chem. Soc.* **2016**, *138*, 11749−11761.
(29) Walker, B. J.; Musser, A. J.; Beljonne, D.; Friend, R. H. Singlet exciton fission in solution. *Nat. Chem.* **2013**, *5*, 1019−1024.
(30) Dean, J. C.; Zhang, R.; Hallani, R. K.; Pensack, R. D.; Sanders, S. N.; Oblinsky, D. G.; Parkin, S. R.; Campos, L. M.; Anthony, J. E.; Scholes, G. D. Photophysical characterization and time-resolved spectroscopy of a anthradithiophene dimer: exploring the role of conformation in singlet fission. *Phys. Chem. Chem. Phys.* **2017**, *19*, 23162−23175.
(31) Young, R. M.; Wasielewski, M. R. Mixed electronic states in molecular dimers: Connecting singlet fission, excimer formation, and symmetry-breaking charge transfer. *Acc. Chem. Res.* **2020**, *53*, 1957−1968.
(32) Schrauben, J. N.; Ryerson, J. L.; Michl, J.; Johnson, J. C. Mechanism of singlet fission in thin films of 1,3-diphenylisobenzofuran. *J. Am. Chem. Soc.* **2014**, *136*, 7363−7373.
(33) Sandoval-Salinas, M. E.; Casanova, D. The doubly excited state in singlet fission. *ChemPhotoChem.* **2021**, *5*, 282−293.
(34) Huang, Y.; Buyanova, I. A.; Phansa, C.; Sandoval-Salinas, M. E.; Casanova, D.; Myers, W. K.; Greenham, N. C.; Rao, A.; Chen, W. M.; Puttisong, Y. Competition between triplet pair formation and excimer-like recombination controls singlet fission yield. *Cell Rep. Phys. Sci.* **2021**, *2*, 100339.
(35) Müller, U.; Roos, L.; Frank, M.; Deutsch, M.; Hammer, S.; Krumrein, M.; Friedrich, A.; Marder, T. B.; Engels, B.; Krueger, A.; et al. Role of Intermolecular Interactions in the Excited-State Photophysics of Tetracene and 2,2′-Ditetracene. *J. Phys. Chem. C* **2020**, *124*, 19435−19446.
(36) Zimmerman, P. M.; Zhang, Z.; Musgrave, C. B. Singlet fission in pentacene through multi-exciton quantum states. *Nat. Chem.* **2010**, *2*, 648−652.
(37) Zeng, T.; Hoffmann, R.; Ananth, N. The Low-Lying Electronic States of Pentacene and Their Roles in Singlet Fissions. *J. Am. Chem. Soc.* **2014**, *136*, 5755−5764.
(38) Herve, P.; Vandamme, L. General relation between refractive index and energy gap in semiconductors. *Infrared Phys. Techn.* **1994**, *35*, 609−615.
(39) Mamada, M.; Katagiri, H.; Mizukami, M.; Honda, K.; Minamiki, T.; Teraoka, R.; Uemura, T.; Tokito, S. Syn-/anti-anthradithiophene derivative isomer effects on semiconducting properties. *ACS Appl. Mater. Interfaces* **2013**, *5*, 9670−9677.
(40) Subramanian, S.; Park, S. K.; Parkin, S. R.; Podzorov, V.; Jackson, T. N.; Anthony, J. E. Chromophore Fluorination Enhances

https://doi.org/10.1021/acs.jpcc.1c09297
J. Phys. Chem. C 2022, 126, 6686−6693

Crystallization and Stability of Soluble Anthradithiophene Semiconductors. *J. Am. Chem. Soc.* **2008**, *130*, 2706−2707.
(41) Lloyd, M. T.; Mayer, A. C.; Subramanian, S.; Mourey, D. A.; Herman, D. J.; Bapat, A. V.; Anthony, J. E.; Malliaras, G. G. Efficient Solution-Processed Photovoltaic Cells Based on an Anthradithiophene/Fullerene Blend. *J. Am. Chem. Soc.* **2007**, *129*, 9144−9149.
(42) Jurchescu, O. D.; Subramanian, S.; Kline, R. J.; Hudson, S. D.; Anthony, J. E.; Jackson, T. N.; Gundlach, D. J. Organic Single-Crystal Field-Effect Transistors of a Soluble Anthradithiophene. *Chem. Mater.* **2008**, *20*, 6733−6737.
(43) Platt, A. D.; Day, J.; Subramanian, S.; Anthony, J. E.; Ostroverkhova, O. Optical, Fluorescent, and (Photo)conductive Properties of High-Performance Functionalized Pentacene and Anthradithiophene Derivatives. *J. Phys. Chem. C* **2009**, *113*, 14006−14014.
(44) Kwon, O.; Coropceanu, V.; Gruhn, N. E.; Durivage, J. C.; Laquindanum, J. G.; Katz, H. E.; Cornil, J.; Brédas, J. L. Characterization of the molecular parameters determining charge transport in anthradithiophene. *J. Chem. Phys.* **2004**, *120*, 8186−8194.
(45) Aufderheide, A.; Broch, K.; Novák, J.; Hinderhofer, A.; Nervo, R.; Gerlach, A.; Banerjee, R.; Schreiber, F. Mixing-induced anisotropic correlations in molecular crystalline systems. *Phys. Rev. Lett.* **2012**, *109*, 156102.
(46) Tanaka, S.; Miyata, K.; Sugimoto, T.; Watanabe, K.; Uemura, T.; Takeya, J.; Matsumoto, Y. Enhancement of the exciton coherence size in organic semiconductor by alkyl chain substitution. *J. Phys. Chem. C* **2016**, *120*, 7941−7948.
(47) Broch, K.; Dieterle, J.; Branchi, F.; Hestand, N. J.; Olivier, Y.; Tamura, H.; Cruz, C.; Nichols, V. M.; Hinderhofer, A.; Beljonne, D.; et al. Robust singlet fission in pentacene thin films with tuned charge transfer interactions. *Nat. Commun.* **2018**, *9*, 954.
(48) Beljonne, D.; Yamagata, H.; Brédas, J. L.; Spano, F. C.; Olivier, Y. Charge-transfer excitations steer the Davydov splitting and mediate singlet exciton fission in pentacene. *Phys. Rev. Lett.* **2013**, *110*, 226402.
(49) Yamagata, H.; Norton, J.; Hontz, E.; Olivier, Y.; Beljonne, D.; Brédas, J. L.; Silbey, R. J.; Spano, F. C. The nature of singlet excitons in oligoacene molecular crystals. *J. Chem. Phys.* **2011**, *134*, 204703.
(50) Marcus, R. A. On the theory of shifts and broadening of electronic spectra of polar solutes in polar media. *J. Chem. Phys.* **1965**, *43*, 1261−1274.
(51) Gao, Y.; Liu, H.; Zhang, S.; Gu, Q.; Shen, Y.; Ge, Y.; Yang, B. Excimer formation and evolution of excited state properties in discrete dimeric stacking of an anthracene derivative: a computational investigation. *Phys. Chem. Chem. Phys.* **2018**, *20*, 12129−12137.
(52) Zeiser, C.; Cruz, C.; Reichman, D. R.; Seitz, M.; Hagenlocher, J.; Chronister, E. L.; Bardeen, C. J.; Tempelaar, R.; Broch, K. Vacancy control in acene blends links exothermic singlet fission to coherence. *Nat. Commun.* **2021**, *12*, 5149.
(53) Arnold, S.; Alfano, R. R.; Pope, M.; Yu, W.; Ho, P.; Selsby, R.; Tharrats, J.; Swenberg, C. E. Triplet exciton caging in two dimensions. *J. Chem. Phys.* **1976**, *64*, 5104−5114.
(54) Casanova, D. Theoretical investigations of the perylene electronic structure: Monomer, dimers, and excimers. *Int. J. Quantum Chem.* **2015**, *115*, 442−452.
(55) Tempelaar, R.; Reichman, D. R. Vibronic exciton theory of singlet fission. I. Linear absorption and the anatomy of the correlated triplet pair state. *J. Chem. Phys.* **2017**, *146*, 174703.
(56) Morrison, A. F.; Herbert, J. M. Evidence for Singlet Fission Driven by Vibronic Coherence in Crystalline Tetracene. *J. Phys. Chem. Lett.* **2017**, *8*, 1442−1448.
(57) Alvertis, A. M.; Lukman, S.; Hele, T. J. H.; Fuemmeler, E. G.; Feng, J.; Wu, J.; Greenham, N. C.; Chin, A. W.; Musser, A. J. Switching between Coherent and Incoherent Singlet Fission via Solvent-Induced Symmetry Breaking. *J. Am. Chem. Soc.* **2019**, *141*, 17558−17570.

https://doi.org/10.1021/acs.jpcc.1c09297
J. Phys. Chem. C 2022, 126, 6686−6693

https://doi.org/10.1021/acs.jpcc.1c09297

Anteil an gemeinschaftlicher Veröffentlichung:

Es handelt sich hierbei um eine Nebenprojekt. Wie auch diese Arbeit behandelt es die Aufnahme von Fluoreszenzlebensdauern. Für das Erstellen dieser Veröffentlichung sind hauptsächlich meine Co-Autoren verantwortlich. Mein Beitrag zu dieser Arbeit war der Aufbau des verwendeten zeitaufgelösten Mikroskops, der Aufnahme der Fluoreszenzlebensdauern sowie die Beratung bei der Evaluation von Fluoreszenzlebensdauerdaten.

Declaration of contribution

Erklärung nach § 5 Abs. 2 Nr. 8 der Promotionsordnung der Math.-Nat. Fakultät. Anteil an gemeinschaftlichen Veröffentlichungen. Liste der Publikationen mit Erklärung:

1. *Strong coupling between an optical microcavity and photosystems in single living cyanobacteria*

Es handelt sich hierbei um die erste Hauptveröffentlichung dieser Arbeit. Die wissenschaftliche Grundidee dieser Veröffentlichung hatten Sven zur Oven-Krockhaus, Klaus Harter und Alfred J. Meixner. Die Projektplanung, der Aufbau der verwendeten Messinstrumente und die Datenaufnahme wurden von mir durchgeführt. Die Datenverarbeitung wurde von Frank Wackenhut und mir ausgeführt. Das Züchten der Cyanobakterien übernahm Johanna Rapp. Die Datenevaluation wurde von Frank Wackenhut, Karl Forchhammer, Klaus Harter, Alfred J. Meixner und mir durchgeführt. Das Manuskript wurde ebenfalls von Frank Wackenhut, Karl Forchhammer, Klaus Harter, Alfred J. Meixner und mir erstellt.

2. *Analysis of Fast Fluorescence Kinetics of a Single Cyanobacterium Trapped in an Optical Microcavity*

Es handelt sich bei diesem noch nicht veröffentlichten Manuskript um den zweiten Hauptteil dieser Arbeit. Die wissenschaftliche Grundidee stammt von mir. Anregungen dazu stammen von meinen Co-Autoren. Die Projektplanung, der Aufbau der verwendeten Messinstrumente und die Datenaufnahme wurden von mir durchgeführt. Die Daten wurden von Frank Wackenhut und mir verarbeitet. Das Züchten der Cyanobakterien übernahm Johanna Rapp. Die Datenevaluation wurde von Frank Wackenhut, Karl Forchhammer, Klaus Harter, Alfred J. Meixner und mir durchgeführt. Das Manuskript wurde ebenfalls von Frank Wackenhut, Karl Forchhammer, Klaus Harter, Alfred J. Meixner und mir erstellt.

3. *Combining Optical Strong Mode Coupling with Polaritonic Coupling in a λ/2 Fabry Pérot Microresonator*

Es handelt sich hierbei um eine Nebenveröffentlichung. Wie auch diese Arbeit behandelt sie Mikroresonatoren. Die wissenschaftliche Grundidee dieser Veröffentlichung hatten Saeed Nosrati, Alfred J. Meixner und Frank Wackenhut. Die Projektplanung wurden von Saeed Nosrati durchgeführt. Bei der Datenaufnahme war ich beratend tätig. Der Aufbau einer der verwendeten Messinstrumente erfolgte durch mich. Die Datenverarbeitung wurde von Saeed

Nosrati und Frank Wackenhut durchgeführt. Die Daten wurden von Saeed Nosrati und Frank Wackenhut evaluiert. Das Manuskript wurde von Saeed Nosrati, Alfred J. Meixner und Frank Wackenhut erstellt, wobei ich inhaltlich unterstützend und beratend tätig war.

4. *Accumulation and penetration behavior of hypericin in glioma tumor spheroids studied by fluorescence microscopy and confocal fluorescence lifetime imaging microscopy*

Es handelt sich hierbei um eine Nebenprojekt. Wie auch diese Arbeit behandelt es Fluoreszenzlebensdauern. Die wissenschaftliche Grundidee hatten Miriam C. Bassler und Marc Brecht. Die Projektplanung wurde von Miriam C. Bassler durchgeführt. Der Aufbau einer der verwendeten Messinstrumente und die Datenaufnahme wurden von Miriam C. Bassler und mir durchgeführt. Das Züchten und Schneiden der Zellverbände übernahm Ivona Secic. Für die Datenevaluation waren Miriam C. Bassler, Frank Wackenhut und ich zuständig. Das Manuskript wurde von Miriam C. Bassler, Frank Wackenhut, Alfred J. Meixner und Marc Brecht erstellt.

5. *Periodic Fluorescence Variations of CdSe Quantum Dots Coupled to Aryleneethynylenes with Aggregation-Induced Emission*

Es handelt sich hierbei um eine Nebenveröffentlichung. Wie auch diese Arbeit behandelt sie Fluoreszenzlebensdauern. Für das Erstellen dieser Veröffentlichung sind hauptsächlich meine Co-Autoren verantwortlich. Mein Beitrag zu dieser Arbeit war der Aufbau eines der verwendeten zeitaufgelösten Mikroskope, der Aufnahme der Fluoreszenzlebensdauern von CdSe Quanten Dots sowie die Beratung bei der Evaluation von Fluoreszenzlebensdauerdaten.

6. *Distinguishing between Triplet-Pair State and Excimer Emission in Singlet Fission Chromophores Using Mixed Thin Films*

Es handelt sich hierbei um eine Nebenprojekt. Wie auch diese Arbeit behandelt es die Aufnahme von Fluoreszenzlebensdauern. Für das Erstellen dieser Veröffentlichung sind hauptsächlich meine Co-Autoren verantwortlich. Mein Beitrag zu dieser Arbeit war der Aufbau des verwendeten zeitaufgelösten Mikroskops, der Aufnahme der Fluoreszenzlebensdauern sowie die Beratung bei der Evaluation von Fluoreszenzlebensdauerdaten.

Auf der folgenden Seite wird quantitativ der Anteil an meinen gemeinschaftlichen Veröffentlichungen aufgezeigt:

Nr.	Bereits akzep-tiert	Liste der Autoren	Position Autoren-liste	Wissen-schaftliche Ideen	Datener-fassung	Analyse/ Interpre-tation	Verfassen der Arbeit
1	Ja	Tim Rammler, Frank Wackenhut, Sven zur Oven-Krockhaus, Johanna Rapp, Karl Forchhammer, Klaus Harter, Alfred J. Meixner	1.	25 %	90 %	20 %	20 %
2	Ja	Tim Rammler, Frank Wackenhut, Sven zur Oven-Krockhaus, Johanna Rapp, Karl Forchhammer, Klaus Harter, Alfred J. Meixner	1.	90 %	90 %	20 %	20 %
3	Ja	Saeed Nosrati, Tim Rammler, Alfred J. Meixner, Frank Wackenhut	2.	0 %	15 %	0%	0%
4	Ja	Miriam C. Bassler, Tim Rammler, Frank Wackenhut, Sven zur Oven-Krockhaus, Ivona Secic, Rainer Ritz, Ralf Kemkemer, Alfred J. Meixner, Marc Brecht	2.	0 %	30 %	20 %	0 %
5	Ja	Krishan Kumar, Jonas Hiller, Markus Bender, Saeed Nosrati, Quan Liu, Marc Edelmann, Steffen Maier, Tim Rammler, Frank Wackenhut, Alfred J. Meixner, Kai Braun, Uwe H. F. Bunz, Marcus Scheele	8.	0 %	5 %	5 %	0 %
6	Ja	Julian Hausch, Adam J. Berges, Clemens Zeiser, Tim Rammler, Arne Morlok, Jona Bredehöft, Sebastian Hammer, Alfred J. Meixner, Jens Pflaum, Christopher J. Bardeen, Katharina Broch	4.	0 %	10 %	5 %	0 %